Magnetic field evolution in accreting neutron stars

Donald James Barclay Payne

Submitted in total fulfilment of the requirements
of the degree of Doctor of Philosophy

School of Physics
University of Melbourne

May 2005

Abstract

Observations of neutron stars in different types of binary systems indicate that their magnetic field decreases monotonically as a function of accreted mass, down to a minimum field of 10^8 Gauss. The mechanism of magnetic field reduction and the origin of the minimum field are not understood. This thesis sets out to explain these data using the ideas of magnetic burial.

The hydromagnetic structure of a neutron star accreting symmetrically at both magnetic poles is calculated numerically as a function of accreted mass, by evolving a centered magnetic dipole through a quasi-static sequence of two-dimensional Grad-Shafranov equilibria. The calculation is the first to follow the development of significant high-order magnetic multipoles, due to equatorial hydromagnetic spreading, while obeying strict mass-flux freezing. We find that it takes 10^{-5} solar masses of accreted material to significantly distort the magnetic field and consequently reduce the magnetic dipole moment. This is substantially greater than previous estimates ($\lesssim 10^{-10}$ solar masses), which neglected the magnetic stress of the compressed equatorial magnetic field. It is also shown that the distorted hydromagnetic equilibria are stable to ideal magnetohydrodynamic perturbations. However persistent global magnetohydrodynamic (Alfvén and magnetoacoustic) oscillations can be excited by the perturbations. We calculate the frequency and amplitude of these oscillations, as functions of accreted mass, using the time-dependent magnetohydrodynamics code ZEUS-3D.

The magnetic field structure resulting from burial, especially the belt of intense equatorial field, can impede thermal transport between the hemispheres of the star. It may therefore explain why millisecond oscillations detected in the tails of thermonuclear (type I) X-ray bursts in low-mass X-ray binaries are so sinusoidal.

Magnetic field burial does not just distort the magnetic field of the neu-

tron star. It also distorts the mass distribution, creating "mountains" in the star's surface layers. We find that these mountains are large enough (ellipticity $\lesssim 10^{-7}$) for accreting millisecond pulsars in low-mass X-ray binaries to emit gravitational waves at levels detectable by the next generation of long-baseline interferometers, such as LIGO II. The predicted signal-to-noise ratio is affected by the structure and orientation of the mountain, and whether the star precesses. It is shown that the predicted gravitational wave spectrum (observable, in principle) also contains information about the magnetohydrodynamic oscillations of the mountain and how they are excited.

Declaration

This is to certify that:

① This thesis entitled "Magnetic field evolution in accreting neutron stars" comprises only my original work, except where indicated in the preface.

② Due acknowledgment has been made in the text to all other material used.

③ The thesis is less than 100,000 words in length, exclusive of tables, maps, bibliographies and appendices.

.....

Donald James Barclay Payne

Preface

While most of the work presented herein is my own, there is some that is the result of collaborative work, or the result of the work of others. Specific details are listed below.

- Chapter 1 is a review of the literature. References are quoted in the text.

- Chapter 2 is based very closely on the following publication. The work is original and is my own.

  Payne, D. J. B and Melatos, A. Burial of the polar magnetic field of an accreting neutron star. I. Self-consistent analytic and numerical equilibria. *Monthly Notices of the Royal Astronomical Society*, volume 351, page 569, 2004.

- Chapter 3 is based very closely on the following publication. The work is original and is my own.

  Payne, D. J. B. & Melatos, A. Burial of the polar magnetic field of an accreting neutron star. II. Stability of axisymmetric equilibria. *Monthly Notices of the Royal Astronomical Society*, to be submitted shortly, 2005.

- Chapter 4 is based very closely on the following publication. The work is original and is my own.

  Payne, D. J. B. and Melatos, A. Magnetic burial and the harmonic content of millisecond oscillations in thermonuclear X-ray bursts. *The Astrophysical Journal*, submitted, 2005.

- The text of chapter 5 is based very closely on the following publication written in part by Dr Andrew Melatos, of which I am a co-author, viz.

Melatos, A. and Payne, D. J. B. Gravitational Radiation from an Accreting Millisecond Pulsar with a Magnetically Confined Polar Mountain. *The Astrophysical Journal*, volume 623, page 1044, 2005.

I performed the calculations of hydromagnetic equilibria in section 5.2.1, evaluated equation (5.4) for these equilibria, derived the approximate analytic formulae for ρ and ψ in section 5.2.3, prepared all the figures, and contributed to the elaboration of the ideas in section 5.3.

- Chapter 6 is based very closely on the following publication. The work is original and is my own.

  Payne, D. J. B. and Melatos, A. Frequency spectrum of gravitational radiation from global hydromagnetic oscillations of a magnetically confined mountain on an accreting neutron star. *The Astrophysical Journal*, submitted, 2005.

- The conclusions in chapter 7 have not been published elsewhere. The work is original and is my own.

Acknowledgements

It is a privilege to ponder the inner workings of the universe as one can in a Ph.D thesis. For this privilege alone, I am truly grateful.

My heartfelt thanks goes to Dr Andrew Melatos, whose supervision has far exceeded the call of duty. I have been honoured to be his first Ph.D student and hope that a good precedent is being set. His diligence and dedication to his students is highlighted by his willingness not only to guide rich research questions, peppered with physical insight, but also to get involved in the fine details. The example I will always remember personally has Andrew and myself working together late at night debugging the Grad-Shafranov code used throughout this thesis. Coupling this with his eye for the last misplaced comma leaves no doubt about his careful attention to detail.

The astrophysics group at Melbourne University is to be commended for providing a stimulating research environment. Rachel Webster deserves a special mention for paving my way into the astrophysics group for my honours year.

My family has also endured this thesis, of that there is no question. For their understanding and support, I offer thanks from the bottom of my heart to my father Edward James Barclay Payne, mother Vanessa Mary Wearing Payne, and brother Edward Morris Barclay Payne.

On my international conference travels around Europe, I was warmly welcomed everywhere I went. In particular I would like to thank Elena Amato, along with Niccolo Bucciantini and Stefano Gabici at Florence, Monica Colpi at Milan, John Kirk at Heidelberg, Ulrich Geppert at Potsdam, Simon Portegies Zwart at Amsterdam, Marten van Kerkwijk at Utrect, and Andrew Jaffe at Imperial College.

I thank Christine Chung, Brett Beeson and James Murray for their help

with ZEUS-3D, which significantly enhanced the results of this thesis. I also acknowledge the Centre for Astrophysics and Supercomputing at Swinburne University, who donated supercomputer time for some of the ZEUS-3D runs.

I thank Duncan Galloway for pointing out to us that sinusoidal light curves are a signature of hemispheric emission, the key insight that led to the work in chapter 4 of this thesis.

Contents

List of Figures

List of Tables

Chapter 1

Introduction

1.1 Accreting neutron stars

1.1.1 A giant nucleus

The existence of neutron stars was postulated in 1934, just two years after the discovery of the neutron by Chadwick (1932), a testament to the rapidity with which new discoveries can be applied. Baade and Zwicky (1934) first proposed the idea, suggesting that "a supernova represents the transition of an ordinary star into a neutron star, consisting mainly of neutrons ... packed much more closely than ordinary nuclei and electrons". Indeed, one might think of a neutron star as a gigantic nucleus, with nucleon number $\sim 10^{57}$, held together stably by gravity instead of the strong nuclear force. Later in the decade, the radial structure of a neutron star was solved for by Oppenheimer and Volkoff (1939) assuming a relativistic Fermi gas equation of state. An upper mass limit of $0.7M_{\odot}$ for a stable polytropic sphere was also calculated, now known as the Oppenheimer-Volkoff limit. It is analogous to the Chandresekhar limit for white dwarfs ($\sim 1.4M_{\odot}$). Additional equations of state, allowing for a hard core nucleon potential, were explored by Cameron (1959), leading to central densities in the range $10^{13} - 10^{19}$ g cm^{-3} and maximum stable masses up to $3M_{\odot}$.

In parallel with this theoretical research, there was spectacular progress in observational radio astronomy, pioneered in the 1930s by Karl Jansky (e.g. Jansky 1933). After World War II, military research into radars in university labs grew into a mainstream branch of civilian astronomy and larger dishes improved sensitivity and resolution. Interestingly, the possi-

bility of detecting radio pulses from rapidly rotating neutron stars (pulsars) existed as early as the 1950's. PSR B0329+54 left a clear imprint of strong pulses on several radio survey recordings by the 250-foot radio telescope at Jodrell Bank (Smith 1977).[1] However, such rapidly pulsing radio signals were put down to terrestrial interference (generated by electrical machinery, power lines, and automobile ignition) and were ignored. The first confirmed detection of a pulsar by Jocelyn Bell and Anthony Hewish came in 1967 in a scintillation study, although it was not immediately identified as such (Hewish et al. 1968). Hewish was nervous about the possibility that the signal came from an extraterrestrial civilization, until the absence of Doppler shifts, expected if the signal came from a planet, ruled out this possibility.[2] A flurry of papers followed the discovery. The identification with neutron stars was convincingly made by Gold (1969), confirming the prescient prediction of Pacini (1967), who had argued that a rapidly rotating neutron star with a dipolar magnetic field of $\sim 10^{12}$ G could act as an electric generator which powers the synchrotron radiation from a surrounding nebula, such as the Crab Nebula.

A neutron star's mass, M_*, and radius, R_*, depend solely on the central density as determined by the equation of state and the Oppenheimer-Volkoff equations; for a given equation, there is a unique mass-radius relation (Lattimer and Prakash 2001). Extensive calculations of such models have been made by Arnett and Bowers (1977) and Datta (1988) giving masses between $1.2M_\odot$ and $2M_\odot$ and radii between 8 km and 15 km (Glendenning 1998; Srinivasan 2002). The mass and radius are observationally constrained by dynamical measurements in binaries (Friedman et al. 1986) and measurements of the gravitational redshift of X-ray lines emitted from the surface of an accreting neutron star (Cottam et al. 2002). To date, the observed range is $1.25M_\odot$ to $\sim 2M_\odot$ (Lyne et al. 2004; Quaintrell et al. 2003); for a fuller discussion, see van Paradijs (1998). We adopt the canonical values of $M_* = 1.4M_\odot$ and $R_* = 10$ km throughout this thesis.

There are now more than 1600 radio pulsars known (Manchester 2004; McLaughlin et al. 2004) including over one hundred in 24 globular clusters (Ransom et al. 2005) with spin periods in the range 1.5 ms to 8.5 s and mag-

[1] A similar story is told about Jupiter's radio pulses, which were discovered in 1954 (Burke and Franklin 1955), but were found in recordings made in Australia five years prior (Shain 1955).

[2] Comment made by Anthony Hewish at the Radio Pulsars conference, Crete, 2002.

netic field strengths in the range 7×10^7 G to 9.4×10^{13} G (McLaughlin et al. 2003). Extrapolating from this detectable sample, it is estimated that there are $\sim 10^5$ pulsars in the Galaxy. The observed population fits reasonably well with the hypothesis that neutron stars are created in the aftermath of the gravitational collapse of the core of a massive star whose zero-age mass is in the range $8 - 30 M_\odot$ and possibly up to $50 M_\odot$ if the hydrogen burning shell is transferred to the companion by Roche Lobe overflow while in either the main sequence or red giant stage (Brown et al. 2001; Podsiadlowski et al. 2004).

1.1.2 Rapid rotation

Neutron stars rotate rapidly. If objects in X-ray binaries are added to the afore-mentioned sample of radio pulsars, the range of spin periods extends from 1.5 ms to 10^4 s. The origin of this rotation is not understood in detail, but it arises when the progenitor star collapses to a compact object, roughly conserving angular momentum. The final rotation rate of the core of a massive star depends on hydrodynamic and magnetic coupling to the slowly rotating envelope during the red supergiant phase, which can brake the core (Heger et al. 2004; Spruit and Phinney 1998), and wind mass loss during a subsequent Wolf-Rayet/helium star phase, which can efficiently extract angular momentum (Heger and Woosley 2003). Recently, dynamo-generated magnetic fields have also been considered in the late rotational evolution of massive stars (Spruit 2002).

A neutron star's rotation frequency f_* is limited by centrifugal break-up. For a rigid Newtonian sphere, one finds $f_* \leq (2\pi)^{-1}(GM_*/R_*)^{1/2} = 2.17(M_*/1.4M_\odot)^{1/2}(R/10\,\mathrm{km})^{-3/2}$ kHz; including deformation and general relativistic effects, f_* can be as high as 3 kHz depending on the nuclear equation of state (Cook et al. 1994; Haensel et al. 1999). Selection effects can be blamed for the absence of pulsars detected with $f_* \gtrsim 1$ kHz, but, given modern techniques such as coherent de-dispersion via baseband recording and extensive acceleration searches for submillisecond pulsars in globular clusters (Edwards et al. 2001), their absence becomes increasingly surprising. This puzzle calls into question some common equations of state and hints at other braking physics. One possibility, gravitational radiation from neutron star mountains (Bildsten 1998), is explored in chapter 5 of this thesis.

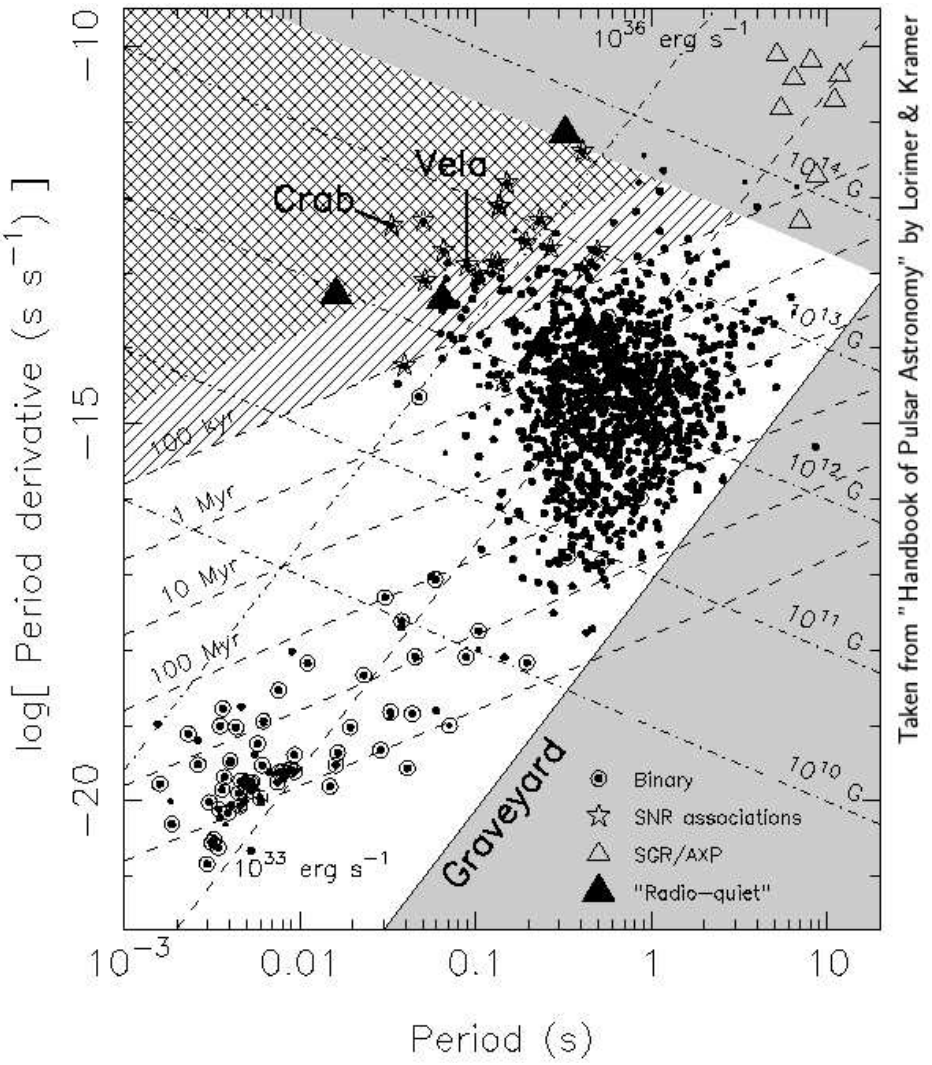

Figure 1.1: The radio pulsar P-$\dot{P}$ diagram where P is the pulsar spin period and $\dot{P}$ is the period time derivative. Binary radio pulsars are circled and pulsars with associated supernova remnants are starred (Lorimer 2001).

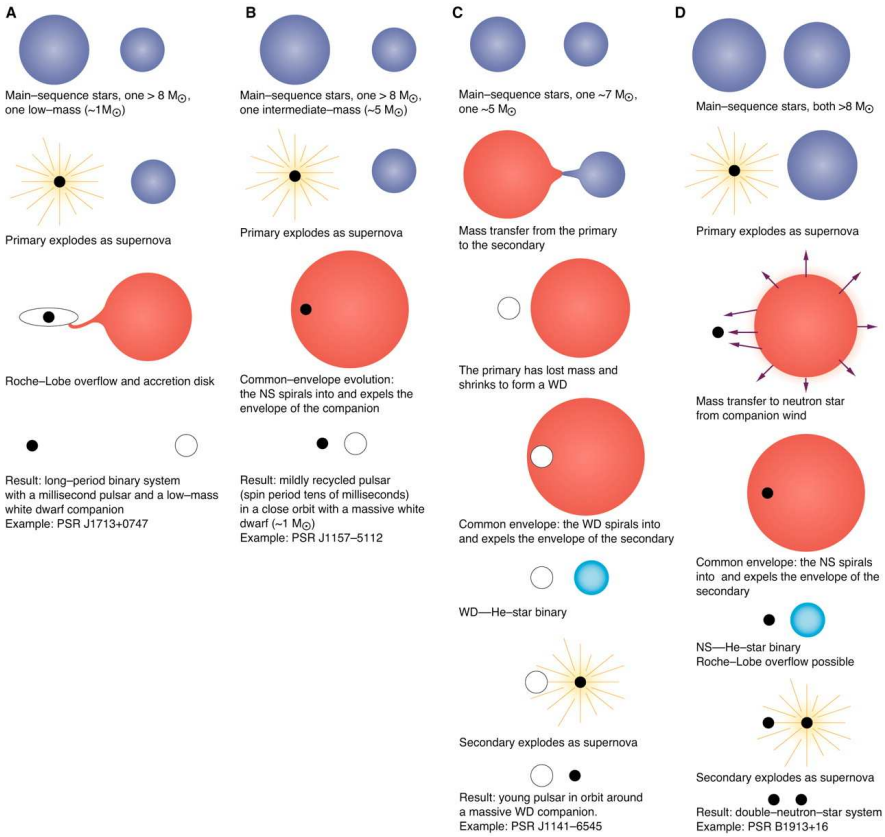

Figure 1.2: Schematic evolutionary paths leading to the largest classes of observed binary pulsars. Approximate zero-age masses for the main-sequence stars are shown. The mass-transfer stages before the explosion of the primary star in paths (A), (B), and (D) are not shown, even though large amounts of mass are transferred in path (D), but the evolution after the first supernova is described fully. The diagrams are not to scale; in particular, common-envelope evolution produces very close binary orbits. In all cases, but especially in path (A), there is great variation in final orbital separation and companion masses. [From Stairs (2004).]

1.1.3 Binary companions

Most stars are formed with at least one companion (Duquennoy and Mayor 1991; Fischer and Marcy 1992). If one of the stars has a mass between roughly $8M_{\odot}$ and $30M_{\odot}$ [though exceptions exist Ergma and van den Heuvel (1998)], a neutron star binary can be produced. If more than half the mass of a circular binary is explosively ejected during the supernova, the binary is disrupted, leaving an isolated neutron star and an OB runaway star (Blaauw 1961). Of the ~ 1600 known radio pulsars, only 101 are in binaries (Manchester et al. 2004), because binary disruption occurs frequently.

Binary evolution often involves mass transfer from the companion star to the neutron star. Such accretion can spin up the neutron star in a process known as recycling (see section 1.1.4). These systems are seen as X-ray point sources. They are often referred to as accretion-powered binary pulsars, as distinct from rotation-powered binary pulsars (see section 1.1.1). They were first detected, concentrated towards the Galactic centre, by rocket and balloon experiments when X-ray astronomy began in the 1960's (Giacconi et al. 1962). To explain the large observed X-ray luminosities (10^{34} to 10^{38} erg s^{-1}) and peak energies ($1 - 15$ keV), accretion onto a neutron star was proposed theoretically (Shklovskii 1967; Zeldovich and Guseynov 1966), even before the discovery pulsations, from Cen X-3, by the UHURU satellite (Giacconi et al. 1971; Schreier et al. 1972).

Neutron star binaries are classified by their companion type (and mass), orbital period, $P_{\rm b}$, and eccentricity, e. Rotation-powered binary pulsars are broadly divided into high-mass and low-mass systems. Accretion-powered X-ray pulsars are divided into low-mass X-ray binaries (LMXBs) and high-mass X-ray binaries (HMXBs). The population statistics and physical characteristics of each category are briefly summarised below, together with some examples. Figure 1.2 shows the evolutionary path leading to each category.

- Main-sequence star companion

  Four are known. Three have a high-mass, B- or Be-star companion: B1259−63 (Johnston et al. 2005), J0045−7319 (Kaspi et al. 1994) in the Small Magellanic Cloud, and J1740−3053 (Stairs et al. 2001). They are progenitors of HMXBs. One may have a low-mass, main-sequence companion, B1820−11 (Phinney and Verbunt 1991), making it the progenitor of a LMXB (Bhattacharya and van den Heuvel 1991),

although Lyne and McKenna (1989) argue that the companion is a neutron star. These systems all have eccentricities $e \gtrsim 0.5$ and $51 < P_{\rm b} < 1237$ days.

- Low-mass helium white dwarf companion

  This class contains ~ 40 objects, with companion masses $\lesssim 0.45 M_{\odot}$. They are in almost circular orbits ($e \lesssim 10^{-3}$, 2 hr $< P_{\rm b} <$ 1200 day), with the eccentricity set by the fluctuation-dissipation theorem during dissipative tidal circularization in the red giant phase (Phinney 1992). Their age can be estimated from the white dwarf temperature (Hansen and Phinney 1998). B0655+64 has a cool white dwarf companion (Kulkarni 1986), as does B1855+09 (Wright and Loh 1986), which independently attests to the old age ($\sim 10^{10}$ yr) of these systems. Objects in this group with degenerate, very-low-mass companions ($\lesssim 0.1 M_{\odot}$), e.g. B1957+20, are mostly found in globular clusters.

- High-mass carbon-oxygen white dwarf companion

  At least 13 objects populate this class. They are sometimes referred to as "intermediate-mass binary pulsars" and have white dwarf companions with masses between $\sim 0.5 M_{\odot}$ and $1.1 M_{\odot}$, whose main-sequence progenitors had masses between $\sim 3 M_{\odot}$ and $8 M_{\odot}$. They can be further subdivided into objects with high ($e \gtrsim 0.1$) and low ($e \lesssim 0.1$) orbital eccentricity. Two high eccentricity objects, B2303+46 and J1141−6545, contain young pulsars which have not been recycled (Davies et al. 2002). At least 11 low eccentricity objects, e.g B2145−0750, have been mildly recycled.

- Neutron star companion

  Double neutron stars are rare because the binary must survive two supernova explosions. There are 9 known, including the recently discovered double pulsar system J0737−3039A/B (Lyne et al. 2004), with pulse periods ranging from 22.7 ms to 2.77 s and eccentric ($0.1 \leq e \leq 0.83$) orbits with $0.102 < P_{\rm b} < 18.8$ days. These systems are formed in HMXBs which undergo common-envelope evolution as the less massive component becomes a giant; inspiral and envelope shedding may produce a tight binary in which mass transfer from a helium star occurs (Dewi and Pols 2003).

- Black hole companion

  No such system has been detected to date, although they are believed to exist (Narayan et al. 1991).

- Low-mass X-ray binaries (LMXBs)

  There are over 150 LMXBs known (Liu et al. 2001), e.g. Sco X-1, with companion masses $\lesssim 1M_\odot$, P_b mostly less than one day, and pulse periods between 0.46 s and 120 s. A few exhibit thermonuclear X-ray flashes from unstable nuclear burning of accreted material at the neutron star's surface, which are modulated at the spin frequency for at least 11 objects (Joss 1977; Lewin and Joss 1983; Strohmayer and Bildsten 2003). The rotation of LMXBs is discussed further in chapter 4. They are more widely distributed in the Galaxy than HMXBs because they are old ($\sim 10^{10}$ years). Mass transfer to the neutron star is typically via Roche-lobe overflow and an accretion disk, as the companion evolves through its red-giant phase, e.g. GX 1+4 (Bildsten et al. 1997). Mass transfer is efficient, with an accretion rate $\dot{M}_\mathrm{a}$ of order the Eddington rate $\dot{M}_\mathrm{Edd}$, and $\lesssim 0.1\dot{M}_\mathrm{Edd}$ for the regular bursters.

- Intermediate-mass X-ray Binaries (IMXBs)

  There are only two confirmed systems in this newly identified class, with companion masses between $1M_\odot$ and $10M_\odot$, Her X-1 and Cyg X-2 (Podsiadlowski and Rappaport 2000). They are rare because the companions are too weak to produce an observable X-ray source during wind accretion, while the mass-transfer rate during Roche-lobe overflow is so high ($\dot{M}_\mathrm{a} \sim 10^{-4}M_\odot\mathrm{yr}^{-1} \gg \dot{M}_\mathrm{Edd}$) that the phase is short-lived (Tauris et al. 2000).

- High-mass X-ray Binaries (HMXBs)

  There are 130 HMXBs (Liu et al. 2000), e.g. Cen X-1, with companion masses between $\sim 10M_\odot$ and $40M_\odot$, $0.2 < P_\mathrm{b} < 187$ days, and pulse periods between 69 ms and 835 s. HMXBs mostly contain X-ray pulsars with large magnetic fields (Nagase 1989), are concentrated in the Galactic plane, and represent a young stellar population $\lesssim 10^7$ years old. They exhibit regular pulsations with no X-ray outbursts. Mass transfer to the neutron star typically occurs via accretion from

the massive companion's stellar wind, with $\dot{M}_{\rm a} \sim 0.01\dot{M}_{\rm Edd}$; wind accretion is less efficient than disk accretion. Less mass accretes in HMXBs over their lifetimes than in LMXBs. This may explain the higher magnetic fields of the neutron stars in HMXBs; this idea is explored in chapter 2 of this thesis.

1.1.4 Recycling scenario

Isolated radio pulsars live simply. Their rotation periods increase over a few hundred million years from tens of milliseconds to seconds until they cross the pulsar "death line" (Chen and Ruderman 1993), beyond which the pulsar's magnetosphere cannot support pair production, believed to be an essential condition for radio emission (Sturrock 1971).[3] However, a dead pulsar may be revived as a rapidly rotating (millisecond) pulsar and binary systems hold the key as to how (Lipunov 1992; Pringle and Rees 1972).

Two groups of pulsars are apparent in the period-period-derivative (P-$\dot{P}$) diagram (figure 1.1). One group contains pulsars with $P \gtrsim 30$ ms and magnetic field strength $10^{11}-10^{13}$ G; the other contains pulsars with $P \lesssim 30$ ms and magnetic field strengths $10^{8}-10^{9}$ G, known as millisecond pulsars. It is striking that 80 per cent of millisecond pulsars are in binaries, whereas under seven per cent of all pulsars are in binaries. This suggests a link between binarity and millisecond pulsar formation. It is strong empirical evidence for the recycling scenario: the standard model explaining the spin-up of a slowly rotating pulsar to millisecond periods by accreted matter from a binary companion (Alpar et al. 1982; Bhattacharya and van den Heuvel 1991; Phinney and Kulkarni 1994).

The recycling scenario was vindicated when phase-coherent millisecond X-ray pulsations, unambiguously indicating a rotating neutron star, were discovered by the Rossi X-ray Timing Explorer (RXTE) in the LMXB SAX J1808.4−3658 (Chakrabarty and Morgan 1998; Wijnands and van der Klis 1998). Since then, five further examples have been found, with $40\,{\rm min} < P_{\rm b} < 4$ hr and $1.6 < P < 5.4$ ms (Galloway et al. 2002, 2005; Markwardt et al. 2003, 2002; Strohmayer et al. 2003). Quasiperiodic and burst oscillations from eleven other X-ray binaries provide further evidence

[3] Weatherall and Eilek (1997) argue against this, and a recently-discovered long-period (8.5 s) pulsar may bring this into question (Kaplan et al. 2002; Young et al. 1999; Zhang et al. 2000).

of neutron star rotation (Chakrabarty et al. 2003; Wijnands et al. 2003a). Table 1.1 summarises the salient properties of these objects. A possible explanation for the origin and harmonic content of burst oscillations — millisecond oscillations observed in the tails of thermonuclear X-ray bursts — is presented in chapter 4 of this thesis.

In the recycling scenario, material accreted from a binary companion, via a wind (in HMXBs) or a disk (in LMXBs), transfers angular momentum to the neutron star, spinning it up to millisecond periods. This occurs in stages, depending on the binary orbital parameters. The detailed fate of the accreting plasma depends on conditions at the boundary of the stellar magnetosphere which is located at the Alfvén radius,

$$r_{\rm A} = \left(\frac{\mu^4}{2GM_*\dot{M}_{\rm a}^2}\right)^{1/7} \tag{1.1}$$

$$= 3.5\times10^8 \left(\frac{\dot{M}_{\rm a}}{10^{-9}\,M_\odot\,{\rm yr}^{-1}}\right)^{-2/7} \left(\frac{\mu}{10^{30}\,{\rm G\,cm}^3}\right)^{4/7} {\rm cm}, \tag{1.2}$$

where μ is the magnetic dipole moment of the neutron star. Physically, $r_{\rm A}$ is the radius at which the ram pressure of spherically infalling matter equals the energy density of the stellar magnetic field. The plasma penetrates to the stellar surface (and is funnelled onto the magnetic poles) only if, at $r_{\rm A}$, the magnetospheric corotation speed $\Omega_* r_{\rm A}$ is less than the Keplerian speed $(GM_*/r_{\rm A})^{1/2}$, where $\Omega_* = 2\pi/P$ is the pulsar's angular velocity. Otherwise, the magnetosphere acts as a centrifugal barrier or *propeller* (Illarionov and Sunyaev 1975): the accreted plasma is forced into super-keplerian rotation and flung away, extracting angular momentum from the star. Recent simulations show that matter accumulates in the equatorial region outside the magnetosphere and accretes onto the star quasi-periodically through elongated, funnel-like streams whenever the magnetic field reconnects (Romanova et al. 2004). The field lines may also twist, inflate, and open up, if the disk conductivity is high enough (Matt and Pudritz 2005; Uzdensky et al. 2002). This continues until spin periods $\sim 10^3$ s are reached. A *wind accretion* phase follows, during which the secondary star continues its main-sequence evolution. For systems with low-mass ($\lesssim 1M_\odot$) companions, this phase can last $\sim 10^9$ yr (Jahan Miri and Bhattacharya 1994; Tauris and Savonije 1999). For systems with high-mass ($\gtrsim 10M_\odot$) companions,

this phase lasts $\sim 10^{6-7}$ yr and the system can be detected as a HMXB ($\dot{M}_{\rm a} \sim 0.01\dot{M}_{\rm Edd}$). Hydrodynamic simulations show that the stellar wind is disrupted in the vicinity of the star, forming a shock front whose interaction with the incident flow temporarily produces retrograde and prograde disks (Blondin et al. 1990; Taam et al. 1991) and hence spin-down and spin-up torques (Blondin et al. 1990; Taam et al. 1991).

When the secondary star finally evolves off the main-sequence and expands to fill its Roche lobe, a new *Roche-lobe overflow* phase of accelerated accretion begins. Low-mass systems become detectable as LMXBs, whose orbits circularize by tidal dissipation (Phinney 1992). High-mass systems undergo common-envelope evolution. In systems with $P_{\rm b} \gtrsim 2$ days, nuclear evolution of the secondary drives mass transfer (Webbink et al. 1983); for intermediate periods, $0.1 \lesssim P_{\rm b} \lesssim 2$ days, magnetic braking (Pylyser and Savonije 1989) dominates the evolution; for extremely tight systems, $P_{\rm b} \lesssim 2$ hours, gravitational radiation dominates (Faulkner 1971; Padalia 1993; Tutukov and Fedorova 2002). The outcome of this phase depends on the initial orbital periods and mass ratios.

The pulsar is spun up during the Roche-lobe overflow phase. However, an accreting X-ray pulsar does not spin up monotonically (Bildsten et al. 1997). Instead, the torque alternates in sign, with an overall spin-up trend. Angular momentum is transferred directly, when material falls onto the surface (material torque), and indirectly, by the hydromagnetic interaction of the disk and the stellar magnetic field (magnetic torque) (Ghosh and Lamb 1979; Ghosh et al. 1977).[4] The material torque is always positive while the magnetic torque is either positive or negative. Internal torques also arise from the coupling between the superfluid core and the solid outer crust (Baykal et al. 1991). If the neutron star accretes from a stable prograde disk, a positive correlation between X-ray flux and torque is expected (Ghosh and Lamb 1979; Ghosh et al. 1977); however, this is not always observed (Nelson et al. 1997).

The neutron star spins up until the magnetospheric corotation speed matches the Keplerian speed of the disk at $r_{\rm A}$. This occurs for $r_{\rm A} =$

[4] Disk-magnetosphere interactions also occur around magnetic white dwarfs and young stellar objects (Uzdensky 2004).

$(GM_*/\Omega_*^2)^{1/3}$, corresponding to the equilibrium spin period

$$P_{\rm spin-up} = 1.9 \left(\frac{\mu}{10^{27}\,{\rm G\,cm^3}}\right)^{6/7} \left(\frac{\dot{M}}{\dot{M}_{\rm Edd}}\right)^{-3/7} {\rm ms}\,. \qquad (1.3)$$

This relation is marked on figure 1.1 and is known as the spin-up line. Clearly, the extent of spin-up depends on how much μ is reduced by recycling; this issue is reviewed in section 1.2. Left over is a spun-up neutron star orbiting a helium $(0.1 - 0.5M_\odot)$ or carbon-oxygen $(0.5 - 1.1M_\odot)$ white dwarf. Once it stops accreting, the neutron star can shine as a radio millisecond radio pulsar if it lies above the death line. It can ablate (Levinson and Eichler 1991) or evaporate (Eichler 1992) its light companion, producing an isolated millisecond pulsar.

The first (and, to date, the fastest-spinning) isolated millisecond pulsar, B1937+21, was discovered by Backer et al. (1982). Millisecond pulsars, of which there are now over one hundred known, are distinguished from other radio pulsars by (i) their very short periods ($1.5 \lesssim P \lesssim 30$ ms), (ii) their lower magnetic field strengths ($\sim 10^{8-9}$ G), as deduced from their very low spin-down rates $\dot{P} \sim 10^{20}$ s s^{-1} (see section 1.2), and (iii) their old spin-down age ($P/2\dot{P} \sim 10^9$ yr), confirmed independently by cold and therefore old white dwarf companions (Kulkarni 1986; Wright and Loh 1986). As mentioned above, about eighty per cent of all millisecond pulsars have binary companions which are either white dwarfs, main sequence stars, or other neutron stars. Two special hybrid systems also exist: the so-called "planets pulsar" PSR B1257+12, a 6.2 ms pulsar orbited by at least two Earth-mass bodies (Wolszczan 1994; Wolszczan et al. 2000), and B1620−26, an 11.1 ms pulsar with a white dwarf and at least one planet (Rasio et al. 2000; Sigurdsson et al. 2003).

1.2 Magnetic burial

1.2.1 Measuring neutron star magnetic fields

The magnetic fields of rotation-powered pulsars are measured from their rate of spin down. The magnetic fields of accretion-powered pulsars are measured either from cyclotron lines or by assuming magnetocentrifugal equilibrium. We describe these measurements in this section and explain how they imply

Table 1.1: Spin frequency (f_*) and orbital period (P_b) of millisecond pulsars in X-ray binaries, detected by their persistent pulsations, or by transient pulsations during type I thermonuclear X-ray bursts.

Object	f_* (Hz)	P_b (hr)
Persistent pulsations		
XTE J0929−314	185	0.727
XTE J1807−294	191	0.683
XTE J1814−338	314	4.27
HETE J1900.1−2455	377	1.388
SAX J1808.4−3658	401	2.01
XTE J1751−305	435	0.707
IGR J00291+5934	599	2.46
Thermonuclear burst oscillations		
4U 1916−05	270	0.833
XTE J1814−338	314	4.27
4U 1702−429	330	?
4U 1728−34	363	?
SAX J1808.4−3658	401	2.01
SAX J1748.9−2021	410	?
KS 1731−260	524	?
Aql X-1	549	19.0
X1658−298	567	7.11
4U 1636−53	581	3.8
X1743−29	589	?
SAX J1750.8−2900	601	?
4U 1608−52	619	?

that the magnetic field is reduced by accretion in section 1.2.2.

In the standard rotating magnetic-dipole model (Gunn and Ostriker 1969; Pacini 1968), an isolated rotation-powered pulsar spinning in vacuo loses rotational kinetic energy, W, via electromagnetic braking at a rate

computed from classical electrodynamics,[5,6]

$$\frac{dW}{dt} = I\Omega_*\dot{\Omega}_* = -\frac{\Omega_*^4}{3c^3}\mu^2 \sin^2\alpha\,, \tag{1.4}$$

where I is the neutron star's moment of inertia, $\dot{\Omega}_* = d\Omega_*/dt$, and the magnetic axis is inclined with respect to the rotation axis by an angle α. If Ω_* and $\dot{\Omega}_*$ (or equivalently P and $\dot{P}$) are measured, μ can be estimated using this model. Assuming $\sin\alpha = 1$, $R_* = 10$ km, and $I = 10^{45}$ g cm^2, one finds

$$\mu = 3.2 \times 10^{37}(P\dot{P})^{1/2}\,\mathrm{G\,cm^3}\,. \tag{1.5}$$

From μ, the polar magnetic field strength $B_* = 2\mu/R_*^3$ can be roughly estimated, if it is assumed that there are no higher-order multipoles. Normally the field strength at the magnetic equator is quoted[7] (Shapiro and Teukolsky 1983; Usov and Melrose 1995); the field strength at the poles is ~ 2 times higher. The point dipole model can be modified (to account for an extended magnetosphere) to give a braking index $n = \ddot{\Omega}_*\Omega_*/\dot{\Omega}_*^{\,2} \neq 3$ and hence a different formula for B_* (Melatos 1997).

The magnetic field in accretion-powered X-ray pulsars is measured differently. In several HMXBs, one observes a cyclotron resonance absorption line in the hard X-ray band. The first such line was found at 35 keV in Hercules X-1 (Trümper et al. 1978), and a line and its second harmonic at 20 keV and 40 keV were found in GB880205 (Murakami et al. 1988). Cyclotron resonance features have now been detected in at least 12 X-ray binaries, with four other candidates yet to be confirmed (Coburn et al. 2002; Makishima et al. 1999). The implied magnetic field strengths, listed in table 1.2, are concentrated in the range $(1-4)\times 10^{12}$ G. The lack of higher field objects may be an instrumental selection effect, caused by the detector's high-energy cutoff ~ 50 keV, but the lack of objects with $B_* = (0.2-1)\times 10^{12}$ G is

[5] The observed pulsed emission is a small fraction of the total energy loss. For example, the rotational energy released by the Crab pulsar is $\sim 10^{38}$ erg s^{-1} while only $\sim 10^{31}$ erg s^{-1} is emitted in the radio pulses and $\sim 10^{36}$ erg s^{-1} in high-energy (gamma-ray) pulses.

[6] In reality, the neutron star is surrounded by magnetospheric plasma composed of electrons and positrons. More realistic models in which the neutron star spins down due to electromechanical stresses in a steady-state (Contopoulos et al. 1999; Goldreich and Julian 1969) or wave-like (Coroniti 1990; Lyubarsky and Kirk 2001; Melatos 1997, 2002; Melatos and Melrose 1996) relativistic wind roughly confirm the B_* estimates of the vacuum model (Reisenegger 2001).

[7] $B_* = 3.2 \times 10^{19}(P\dot{P})^{1/2}$ G.

believed to be real (Makishima et al. 1999). Theoretically, the width and depth of the cyclotron line increase with line frequency and surface temperature, but observationally, the temperature dependence is weak, perhaps indicating a small range of temperatures despite more than three orders of magnitude spread in $\dot{M}_{\rm a}$ and hence heating rate. This may indicate that the mountain of accreting matter evolves to a unique steady-state density profile, irrespective of $\dot{M}_{\rm a}$ (Coburn et al. 2002).

Isolated neutron stars are also directly observable in X-ray emission because of their high surface temperatures. Their spectra are mostly featureless (Becker and Aschenbach 2002; Pavlov et al. 2002). However, 1E 1207.4−5209 displays three distinct features, regularly spaced at 0.7, 1.4 and 2.1 keV, plus a possible fourth feature at 2.8 keV (Bignami et al. 2003), which, if interpreted as proton cyclotron lines, imply $B_* \sim 1.6 \times 10^{14}$ G, much higher than the spin-down value $B_* \sim 3 \times 10^{12}$ G (Sanwal et al. 2002; Zavlin et al. 2004). (If interpreted as electron cyclotron lines, they imply $B_* \sim 8 \times 10^{10}$ G.) Becker et al. (2003) report an emission line in the X-ray spectrum of PSR B1821−24 which may come from a corona above the pulsar's polar cap, provided one has $B_* \sim 2 \times 10^{11}$ G, well above the spin-down value $B_* \sim 2 \times 10^9$ G. Schwope et al. (2005) estimate that $B_* \sim 10^{13}$ G for the isolated, thermally emitting neutron star RBS 1223 using crustal field models of Geppert et al. (2004). Such observations suggest strong multipolar magnetic fields near the stellar surface (Bonanno et al. 2003); the spin-down model gives μ, not B_*. One explanation of multipolar surface fields is magnetic burial: the preaccretion dipolar field is distorted when accreted matter spreads from the magnetic poles towards the equator. This scenario is modelled in chapters 2 and 3 of this thesis.

The magnetic fields of binary X-ray pulsars can also be estimated from the spin-up relation (1.3), assuming centrifugal equilibrium. If the pulse period and X-ray luminosity $L = GM_*\dot{M}_{\rm a}/R_*$ are measured, then the magnetic dipole moment can be estimated as $\mu = 4.3 \times 10^{29} P^{7/6} (L/10^{37} {\rm erg\,s^{-1}})^{1/2}$ G cm^3 (Ghosh and Lamb 1979). This can be checked independently by comparing with B_* values from cyclotron absorption features (Makishima et al. 1999). Figure 1.3 shows the comparison. While there is some agreement, several objects lie far from the spin-up line. This is understandable for objects whose centrifugal equilibrium fields exceed $\sim 4 \times 10^{12}$ G, the maximum B_* that the cyclotron method can measure. However, objects below this limit

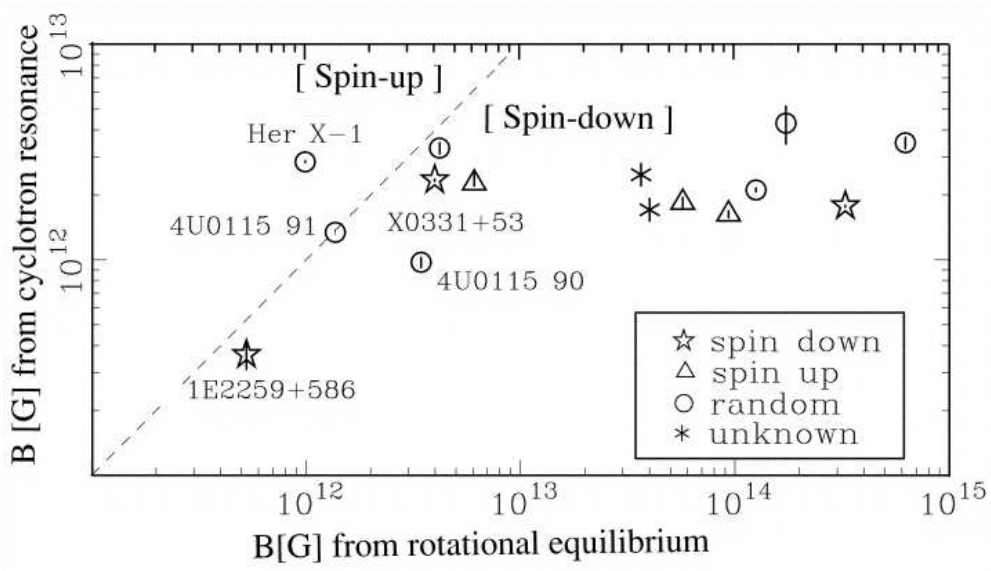

Figure 1.3: Surface magnetic field B_* for pulsars measured from cyclotron absorption features, plotted against the centrifugal equilibrium (dipole) field predicted by (1.3), using period and luminosity data from Nagase (1989). 4U 0115+63 has data points for its 1990 and 1991 observations. [From Makishima et al. (1999).]

also lie far from the spin-up line at certain epochs, like 4U 0015+63 in 1990 (but not in 1991). Many of these exhibit sporadic transitions between spin-up and spin-down (Bildsten et al. 1997; Nelson et al. 1997) and are therefore not in centrifugal equilibrium. Torque flip-flops may be caused by episodes of prograde and retrograde disk formation [e.g. GX 1+4 (Makishima et al. 1988)], a nonaxisymmetric wind-fed disk with alternating senses of rotation (Taam et al. 1991), or a transition between the bistable equilibria of a magnetosphere where diffusion balances advection of the stellar magnetic field at the inner disk boundary (Locsei and Melatos 2004).

1.2.2 Observational evidence for the link between magnetic field reduction and recycling

In the recycling scenario, a neutron star, born in a supernova with $B_* \sim 10^{12-13}$ G (Hartman et al. 1997; Regimbau and de Freitas Pacheco 2001), is spun up by accretion to form a millisecond pulsar with $B_* \sim 10^{8-9}$ G. In this section, we survey the observational evidence for whether magnetic field reduction is physically caused by accretion or incidentally associated

Table 1.2: Neutron star magnetic fields measured from cyclotron lines, ordered by magnetic field strength B_* (Coburn et al. 2002; Ibrahim et al. 2002; Makishima et al. 1999). Several types of systems are listed: Be transients, HMXBs, LMXBs and isolated pulsars. The spectral type of the binary companion is given where an identification has been made.

Name	Type	P (s)	P_b (days)	Companion (MK Type)	B_* (10^{12} G)
X2259+586		7.0			0.8
4U 0115+63	Be trans	3.6	24.3	V635 Cas (Be)	1.3
4U 1907+09	HMXB	440.4	8.38	(Be?)	2.1
GS 1843+00		29.5			2.2
4U 1538−52	HMXB	528.8	3.73	QV Nor (B0 Iab)	2.3
LMC X-4		13.5			2.3
Vela X-1	HMXB	283.2	8.96	HD 77581 (B0.5 Ib)	2.7
X0331+53		4.4			2.9
4U 0352+309	Be	837.7	250.3	X Per (09 III-Ve)	3.2
Cep X-4		66.3			3.3
Centaurus X-3	HMXB	4.8	2.09	V779 Cen (O6-8f)	3.4
XTE J1946+274	Trans	15.8	–	–	3.9
4U 1626−67	LMXB	7.7	0.03	KZ TrA	4.4
Hercules X-1	LMXB	1.2	1.70	HZ Her (A/F)	4.5
GX 301−2	HMXB	681	41.5	Wray 977 (B1.5 Ia)	4.8
A0535+26		110			5.5
1E 1207.4−5209	Isolated	0.4	–	–	~ 150
SGR 1806−20	Isolated	7.5	–	–	~ 1000

Table 1.3: Magnetic fields B_* of neutron stars for which M_a can be estimated. Radio pulsars are listed first, X-ray pulsars second. The objects are sorted by B_*, which is measured from the spin-down rate for radio pulsars (corrected for proper motion where appropriate) and the spin-up line for accretion-powered pulsars. Binary companion masses, and orbital periods P_b are taken from van den Heuvel and Bitzaraki (1995). X-ray binary parameters are taken from van Kerkwijk et al. (1995).

Name	P	P_b	Companion		$\log B_*$	M_a
	(s)	(d)	type	mass ($M_\odot$)	(G)	($M_\odot$)
J2229+2643	0.00298	93.016	He WD	0.30	7.6	0.7
J2317+1439	0.00345	2.46	He WD	0.21	7.8	0.79
J0034−05	0.00877	1.59	He WD	0.17	8.04	0.7
J2019+24m	0.00393	76.512	He WD	0.29	8.26	0.71
J1713+074	0.00457	67.8	He WD	0.28	8.30	0.72
J1855+09	0.00536	12.237	m He WD	0.25	8.49	0.75
J1045−45	0.00745	4.69	He WD	0.19	8.58	0.7
J2145−0750	0.0161	6.84	CO WD	>0.45	8.6	0.01–0.045
J0218+4232	0.00232	2.03	He WD	0.20	8.63	0.7
B1953+29	0.00613	117.35	He WD	0.21	8.63	0.03–0.8
J0437−4715	0.00576	5.74	He WD	0.23	8.69	0.77
B0021−72E	0.00354	2.22	He WD	0.19	8.77	0.7
J1022+1001	0.0165	7.8	CO WD	>0.45	8.8	0.01–0.045
B0655+64	0.1957	1.029	CO WD	0.797	10.06	0.003
B1913+16	0.059	0.323	NS	1.056	10.35	0.003
B1800−27	0.334	406.78	He WD	0.36	10.89	0.64
B1831−00	0.521	1.81	He WD	0.20?	10.94	0.80
B0820+02	0.8649	1232.4	He WD	0.45	11.48	0.005–0.04
Sco X-1	0.003	0.78	V818 Sco		8.70	0.02–0.5
1730−335			Lil 1		8.84–11.0	0.1–0.8
GX 5−1	0.01		?		9.78	0.02–0.5
Cyg X-2	0.01	9.8	F-subdwf		9.78	0.02–0.5
A0538−66	0.069	16.64	post MS	9.	11.0	0.002
4U1626−67	7.66	0.0289	He WD	0.2	11.48	0.01
GX 1+4	120.0	300.	M6 IIIe	10.	11.48	10^{-4}
Her X-1	1.24	1.7	A–FIV	2.3	11.7	6×10^{-4}
SMC X-1	0.717	3.89	B0Ib	15.	12.0	8×10^{-4}
Cen X-3	4.84	2.09	O6.5II–III	19.	12.7	1×10^{-4}
LMC X-4	13.51	1.41	O7III–V	16.	13.6	5×10^{-4}

with it.

Field at birth

Neutron stars are born with magnetic field strengths averaging $B_* = 10^{12.3\pm0.3}$ G (where $\pm$ denotes one standard deviation) (Hartman et al. 1997). This range is inferred from Monte-Carlo population synthesis studies like those performed by Hartman et al. (1997), who parametrised his simulated population by birth rate, B_* (selected from a lognormal distribution), P, beaming fraction, height above the galactic plane, projected position in the galactic disk, radio luminosity (at 400 MHz), and age (selected from a flat distribution). Several selection effects are modelled, e.g. flux cutoff, pulse broadening in the dispersive interstellar medium, and sampling rate of the detector. Similarly, Arzoumanian et al. (2002) considered a six-dimensional parameter space (P, $\dot{P}$, dispersion measure, Galactic latitude, proper motion, flux density at 300 MHz) and treated proper motion and distance selection effects. They found $B_* = 10^{12.5\pm0.4}$ G, consistent with Hartman et al. (1997), after excluding millisecond, binary, and globular cluster pulsars.

An initial field around 10^{12} G can be roughly understood as a result of magnetic flux conservation during the collapse of a main-sequence star with $B_* \sim 1-100$ G. Magnetic field strengths of white dwarfs (up to $\sim 10^6$ G) are consistent with this idea (e.g. Ferrario and Wickramasinghe 2005; Wickramasinghe and Ferrario 2005). However, flux-conserving amplification of the progenitor field cannot be the whole story because (i) massive progenitors have convective cores (as do newly born neutron stars) which tangle the primordial field by dynamo action, and (ii) we observe $B_* \lesssim 10^6$ G for most white dwarfs (Angel et al. 1981), implying $B_* \lesssim 10^{11}$ G when compressed to neutron star dimensions (Thompson and Duncan 1993; Wendell et al. 1987). Work continues on the late stages of massive main-sequence evolution in an attempt to understand the origin of the initial B_* distribution. Charbonneau and MacGregor (2001) investigated $\alpha\Omega$ dynamos in the convective core, including a magnetic diffusivity contrast between the core and radiative envelope; they ruled out thermally driven meridional circulation as a way of carrying the magnetic field to the surface. Spruit (2002) investigated stably stratified (non-convective) layers in a differentially rotating star, in which a Taylor instability of the toroidal field (wound up by differential rotation) replaces convection in closing the field amplification loop

in the dynamo. Ardeljan et al. (2005) simulated a two-dimensional, magnetorotational model of a supernova explosion and found that the growth of the toroidal magnetic field via differential rotation is quenched by the magnetorotational instability. Baumgarte and Shapiro (2003) studied the collapse of a magnetized spherical star to a black hole in general relativity. Finally, recent three-dimensional MHD simulations show that stable magnetic field configurations can develop from unstable initial fields (Braithwaite and Spruit 2004), a result that is also applicable to Ap stars and magnetic white dwarfs. It is unclear whether the conditions for the onset of a dynamo or the magneto-rotational instability are fulfilled.

Radio pulsars with ultra-strong magnetic fields $\sim 10^{14}$ G (inferred from $\dot{P}$) are now being found (McLaughlin et al. 2003). The highest known field belongs to PSR J1847−0130, a 6.7 s radio pulsar with $B_* = 9.4 \times 10^{13}$ G. Such high magnetic fields overlap the range of fields (6×10^{13} G to 5×10^{14} G) possessed by magnetars (e.g. anomalous X-ray pulsars and soft gamma-ray repeaters) (Kaspi and Gavriil 2004; Thompson and Duncan 1993, 1995), which are distinguished by their high X-ray luminosities (10^{34-36} erg s^{-1}, much greater than $I\Omega_*\dot{\Omega}_*$) and long spin periods ($6 - 12$ s). Magnetars may be analogous to the slowly rotating, high-field magnetic white dwarfs. Their unusually strong magnetization ($\mu \sim 10^{33-34}$ G cm^3) may be generated by a helical dynamo during the first few seconds after a core-collapse supernovae (Duncan and Thompson 1992) or by a magnetorotational instability (Balbus and Hawley 1991, 1998) operating tens of milliseconds after the supernova bounce (Akiyama et al. 2003).

Fields of recycled (millisecond) pulsars

Millisecond pulsars have magnetic dipole moments 10^{3-4} times smaller than young pulsars (Manchester et al. 2004), in a range from 7×10^{25} G cm^3 to 3×10^{27} G cm^3. Intermediate values of $\mu \sim 10^{28-29}$ G cm^3 are measured in some binaries, including the double neutron star binaries. These probably evolved out of HMXBs, which start with $\mu \sim 10^{29-30}$ G cm^3, and undergo common-envelope accretion as the less-massive star evolves into a giant (Dewi and Pols 2003). LMXBs have $\mu \sim 10^{26-27}$ G cm^3, derived from (1.3). The recently discovered accreting millisecond pulsars in X-ray binaries (Wijnands and van der Klis 1998) have $\mu \sim 10^{26}$ G cm^3 (Chakrabarty et al. 2003; Psaltis and Chakrabarty 1999; White and Zhang 1997). The common trait of all

these low-field neutron stars is a history of accretion in a binary.

It might be thought that low-field pulsars ($B_* < 10^{10}$ G) are born from low-field progenitors, but this idea is ruled out quantitatively by the best-fitting initial-field distribution from a recent study of isolated pulsars (Arzoumanian et al. 2002), which predicts that one in $\sim 10^9$ neutron stars in the Galaxy is born with $B_* < 10^{10}$ G. Most low-field recycled pulsars are quite old ($\gtrsim 10^9$ yr), implying that their field must be stable over such periods — it does not decay further or re-emerge (Bhattacharya and Srinivasan 1986; Kulkarni 1986; van den Heuvel et al. 1986; Verbunt et al. 1990; Wright and Loh 1986). It is puzzling that no objects have been found with $B_* \sim 10^{7-8}$ G. This may be because the inner edge of the accretion disk touches the star ($r_{\rm A} \approx R_*$) at these field strengths (Zhang 1998; Zhang and Kojima 2004; Zhang et al. 1994), so that accreted matter is no longer funneled towards the poles; or because accreted matter sinks into the superconducting core, freezing the residual field (e.g. Konar and Bhattacharya 1997); or because screening (or burial) by $\sim 0.3 M_\odot$, the maximum $M_{\rm a}$ in most binary evolution scenarios, reduces μ by $\sim 10^4$ times, (leaving a strong equatorial field). The latter idea is assessed in detail in chapters 2 and 3 of this thesis.

Field reduction during recycling: μ versus $M_{\rm a}$

Given the above observations, it is reasonable to speculate that the magnetic field is a monotonic decreasing function of $M_{\rm a}$. But is this hypothesis justified? With the help of binary evolution models, Taam and van den Heuvel (1986) showed that neutron stars with high-mass companions and a history of (inefficient) wind-fed accretion ($M_{\rm a} \lesssim 10^{-3} M_\odot$) from supergiants have $B_* \sim 10^{11-12}$ G, while those with low-mass companions and a history of (efficient) disk-fed accretion ($M_{\rm a} \gtrsim 10^{-3} M_\odot$) from red giants have $B_* \sim 10^{8-9}$ G. Non-conservative mass transfer reduces these estimates of $M_{\rm a}$ (Tauris et al. 2000). This work was followed by an analysis of 24 binary radio pulsars with nearly circular orbits and low-mass ($0.2 - 0.4 M_\odot$) companions, mostly helium white dwarfs (Van Den Heuvel and Bitzaraki 1994; van den Heuvel and Bitzaraki 1995), in which systems with long $P_{\rm b}$ (and hence lower $M_{\rm a}$) clearly exhibit higher B_*. Exceptions to this B_* versus $M_{\rm a}$ trend may be attributed to accretion-induced collapse (in which a white dwarf's mass is pushed over the Chandrasekhar limit just before accretion stops, e.g. PSR B1831−00; note that this raises a fine-tuning problem) or

to a recent capture in a globular cluster (e.g. PSR B1718−19).

Shibazaki et al. (1989) put forward an empirical scaling $B_* = B_0(1 + M_a/M_c)^{-1}$, with $B_0 = 10^{12}$ G and $M_c \sim 10^{-4} M_\odot$ (the characteristic M_a above which B_* is reduced significantly). Contradicting this, Wijers (1997) concluded that no model with B_* as a function of only M_a can fit the available data on X-ray binaries and recycled pulsars. This conclusion applies to a class of models of the form $B_* = B_0(1 + M_a/M_c)^{-\beta}$, combined with the spin-up model of Ghosh and Lamb (1979). Figure 1.4 shows theoretical curves for different values of M_c and β; PSR B1831−00 and PSR B1718−19 are exceptions for all choices of M_c and β. It is possible, of course, that M_c and β vary from object to object, but this is not appealing theoretically. More likely, there is another independent parameter in the problem, with $\dot{M}_a$ being the most popular candidate. It is surprising that Wijers (1997) arrives at a different conclusion from Taam and van den Heuvel (1986) and van den Heuvel and Bitzaraki (1995), given that similar data sets were used. One difference, however, is the interpretation of the accretion history of objects like 4U 1626−67: Taam and van den Heuvel (1986) adopt $M_a \lesssim 0.01 M_\odot$ whereas Wijers (1997) adopts $M_a \sim 0.5 M_\odot$ as clearly seen in figure 1.4. Measured neutron star masses, e.g. in relativistic binaries, suggest $\lesssim 0.1 M_\odot$ is accreted (Thorsett and Chakrabarty 1999), consistent with the amount of mass required to spin up a neutron star to millisecond periods ($0.05 M_\odot \lesssim M_a \lesssim 0.1 M_\odot$) (Burderi et al. 1999), and this is available from most donors, unless accretion is very inefficient (Tauris et al. 2000).

Interestingly, the need for a dependence on $\dot{M}_a$ besides M_a also seems indicated by theoretical modelling: Cumming et al. (2001) found that magnetic field reduction by magnetic screening (see 1.2.6) is not possible for $\dot{M}_a < 10^{-2} \dot{M}_{Edd}$, and Romani (1990) showed that $\dot{M}_a$ controls magnetic field reduction, because the rate of advection depends on the ratio of the flow and magnetic diffusion times in the crust (Romani 1995).

Exponential decay?

Theoretical models (e.g. Sang and Chanmugam 1987; Urpin and Muslimov 1992) and population studies (e.g. Bailes 1989; Narayan and Ostriker 1990; Sang and Chanmugam 1990) have been used to investigate whether the field of an isolated neutron star decays exponentially. Earlier Monte-Carlo population studies that modelled pulsar evolution with exponential magnetic

torque decay (Chevalier and Emmering 1986; Lyne et al. 1985; Stollman 1987) fitted the data available at the time, but failed when tested against a larger population; a constant field can explain the data extant today and exponential decay is unnecessary (Bailes 1989; Narayan and Ostriker 1990; Sang and Chanmugam 1990; Wakatsuki et al. 1992). Bailes (1989), who used a pulsar velocity model from the disruption of massive binary systems, found no evidence that pulsar magnetic fields decay once accretion ceases. Sang and Chanmugam (1990) showed that field decay of the form $B_*(t) = B_*(t=0)(1+t/3\mathrm{Myr})^{-1}$ is consistent with pulsar statistics.[8] Narayan and Ostriker (1990), whose model has two pulsar subpopulations with different kinematics and scale heights at birth, suggested that power-law decay is more appropriate. Wakatsuki et al. (1992), using population synthesis, found that a constant magnetic field is a better fit than a $-1/4$ power law index. The differing conclusions illustrate the difficulty of determining a seven-dimensional distribution function from only a few hundred data points (Phinney and Kulkarni 1994). Most recent studies find that a constant field better fits the statistics and this is emerging as the consensus (Arzoumanian et al. 2002; Hartman et al. 1997; Regimbau and de Freitas Pacheco 2001), though dispute lingers (Cordes and Chernoff 1998; Gonthier et al. 2002; Guseinov et al. 2004; Tauris and Konar 2001; Tauris and Manchester 1998).

1.2.3 Overview of reduction mechanisms

In view of the recycling scenario, the most natural explanation of the weaker magnetic fields of millisecond pulsars is that they are reduced during the accretion phase (Bhattacharya 1999; Konar and Bhattacharya 1997), as argued in section 1.2.2. A variety of physical models have been proposed along these lines. They relate the magnetic field evolution either to spin evolution or to the direct effects of accreting mass. Spin-coupled mechanisms include vortex-fluxoid interactions (Muslimov and Tsygan 1985; Srinivasan et al. 1990) and crustal plate tectonics (Ruderman 1991a,b,c). Accretion-induced mechanisms include accelerated Ohmic decay (Urpin and Geppert 1995; Urpin and Konenkov 1997) and magnetic screening or burial (Bisnovatyi-

[8] Coincidentally, this form is equivalent to that used by Shibazaki et al. (1989) with $M_\mathrm{a} = \dot{M}_\mathrm{a} t$, $M_\mathrm{c} = 10^{-5} M_\odot$, and $\dot{M}_\mathrm{a} \approx 3.3 \times 10^{-12} M_\odot\ \mathrm{yr}^{-1} \ll \dot{M}_\mathrm{Edd}$ (averaged over the lifetime, which includes non-accreting phases).

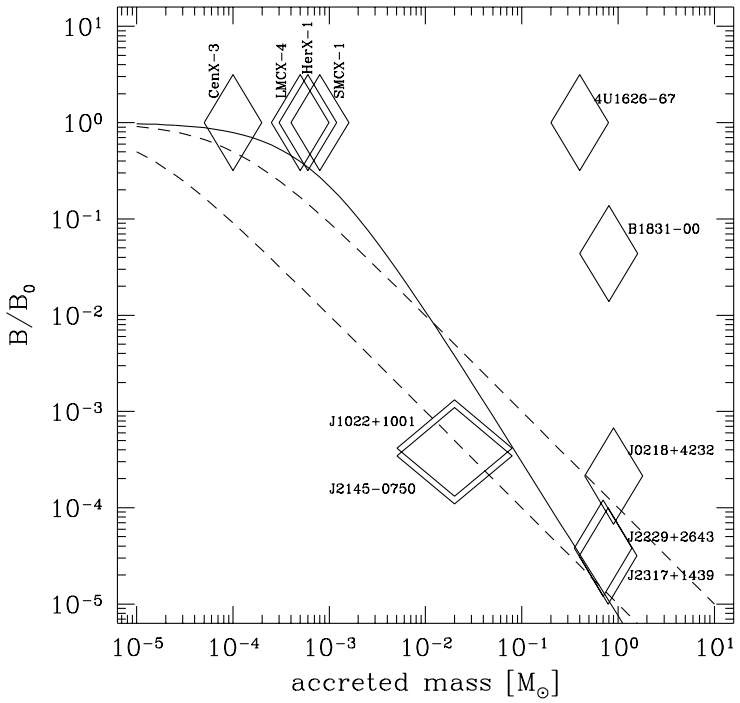

Figure 1.4: Dipole magnetic field $B_* = 2\mu/R_*^3$ as a function of accreted mass M_a for objects chosen by Wijers (1997), B_0 is the field strength before accretion. The dashed curves are decay models with $\beta = 1$, $M_\mathrm{c} = 10^{-4} M_\odot$ (*top*) and $\beta = 1$, $M_\mathrm{c} = 10^{-5} M_\odot$ (*bottom*). The solid curve is for $\beta = 1.6$ and $M_\mathrm{c} = 10^{-3.2} M_\odot$. [From Wijers (1997).]

Kogan and Komberg 1974; Romani 1990). Each mechanism is summarised below. Bhattacharya and Srinivasan (1995) and Ruderman (1995) contain detailed reviews of reduction mechanisms.

Different models assume different configurations of the initial magnetic field: spin-coupled models assume the field threads the neutron star core and is supported by proton superconductor flux tubes, while dissipative models assume the field is confined mainly to the crust. The location of magnetic fields in the stellar interior is poorly understood (section 1.2.2).

1.2.4 Accelerated Ohmic decay

Shortly after the discovery of pulsars, Ostriker and Gunn (1969) argued that neutron star magnetic fields must decay exponentially on a time-scale $t_{\rm Ohmic} \sim 10^6$ yr, in order to explain the population statistics existing at that time (e.g. the absence of long-period pulsars with $P \gtrsim 3$ s). They suggested Ohmic dissipation as the physical cause; an electrical conductivity $\sigma \sim 10^{23}$ $\rm s^{-1}$ in the crust is consistent with $t_{\rm Ohmic} = 10^6$ yr (Canuto 1970). Sang and Chanmugam (1987) showed that the magnetic field decays by a factor $\lesssim 10^2$ in a Hubble time in the crust by analysing a radial eigenfunction expansion of the field induction equation without flow and for a dipole geometry. At the time, Baym et al. (1969) pointed out that in regions below the crust, where the conductivity depends on the proton density $\rho_{\rm p}$ and the temperature T as $\sigma = 1.5 \times 10^{29}$ $(\rho_{\rm p}/10^{13}\,{\rm g\,cm^{-3}})^{3/2}(T/10^8{\rm K})^{-2}$ $\rm s^{-1}$, $t_{\rm Ohmic}$ is longer than the age of the universe. Consequently, the field evolution depends on where the magnetic flux resides. Neutron stars are either born with large magnetic fields (inherited from their progenitors), which permeate the whole star, or their fields are generated after birth, e.g. when the heat flux generates a large magnetic field by thermoelectric effects in the crust (Blandford et al. 1983; Urpin et al. 1986; Urpin and Yakovlev 1980).

Even though Ohmic decay cannot reduce the magnetic field of an isolated pulsar quickly (Sang and Chanmugam 1987; Urpin and Muslimov 1992), crustal heating during accretion reduces σ and hence $t_{\rm Ohmic}$ by several orders of magnitude, allowing crustal magnetic fields to escape outward before the crust sinks under the weight of the overburden and becomes part of the superconducting core of the star (Blondin and Freese 1986; Konar and Bhattacharya 1997, 1999a; Urpin and Geppert 1995; Urpin and Konenkov 1997). Therefore, accelerated Ohmic decay, as a result of accretion-induced heat-

ing, can reduce the magnetic field by $\sim 10^4$ times if the magnetic field is initially confined to the crust. However, if the field resides mainly in the superconducting core (e.g. if it is inherited from the progenitor), accelerated Ohmic decay cannot reduce it significantly unless the field is somehow expelled into the crust (Jahan-Miri 2002; Konar and Bhattacharya 1997), e.g. by vortex-fluxoid interactions (section 1.2.5).

As well as hastening Ohmic decay by heating, accretion can also act to stabilize the magnetic field. The accreted material forms a new crust, while the original material sinks and assimilates into the superconducting core, slowing decay. These competing effects have been modelled up to $M_{\rm a} \sim 10^{-3} M_\odot$ (Geppert and Urpin 1994; Urpin and Geppert 1995) and extended up to $M_{\rm a} \sim 4 \times 10^{-2} M_\odot$ (Konar and Bhattacharya 1997) in one dimension, assuming spherically symmetric mass flow in the crust and ignoring diamagnetic screening (section 1.2.6). Brown and Bildsten (1998), who considered aspherical accretion onto the magnetic poles, found that the flow time is always less than the Ohmic diffusion time for $\dot{M}_{\rm a} \gtrsim 3 \times 10^{-9} M_\odot$ yr^{-1}, so that field stabilization by sinking overcomes heating. The observed correlation between μ and $P_{\rm b}$ is explained by this class of models (Konar and Bhattacharya 1999b) and millisecond pulsars with $P < 1.5$ ms are predicted to exist (Possenti et al. 1998); the search for such objects continues. The effect of relativistic corrections and neutron star cooling were considered by Sengupta (1998), who found that the intense stellar gravity increases $t_{\rm Ohmic}$.

Another class of models focuses on the nonlinear Hall effect, which causes an initially dipolar field to twist and buckle, generating higher order multipoles (Cumming et al. 2004), and was first studied in neutron star crusts by Jones (1988) and Goldreich and Reisenegger (1992). Hall currents dominate Ohmic decay for magnetar field strengths $B_* \sim 10^{14-15}$ G (Arras et al. 2004; Goldreich and Reisenegger 1992), but, for $B_* \lesssim 10^{13}$ G, they are only important for very pure crusts ($Q \lesssim 0.1$)[9] at low temperatures ($T \lesssim 10^8$ K) (Cumming et al. 2004). The Hall effect is non-dissipative, but it can facilitate dissipation through a turbulent "Hall cascade" (Goldreich and Reisenegger 1992) which transports magnetic energy to small scales where Ohmic losses are rapid. Furthermore, a Hall drift instability may lead to non-local transfer of energy to small scales, on a time-scale of 10^{4-6} yr, depending on the cooling age and field strength (Rheinhardt et al. 2004). Ambipolar diffusion

[9] Q is the standard impurity factor (Itoh and Kohyama 1993).

in the neutron star interior may also be effective in allowing the magnetic field to escape from the core (Goldreich and Reisenegger 1992; Haensel et al. 1990; Pethick 1992).

1.2.5 Vortex-fluxoid interactions

Abrikosov fluxoids (in the superconducting protons) and Onsager-Feynman vortices (in the superfluid neutrons) in the core of a neutron star interact mutually via Magnus and spin-polarization forces (Bhattacharya and Srinivasan 1995; Muslimov and Tsygan 1985; Srinivasan et al. 1990). The number of vortices pre unit area is proportional to the angular velocity of the star. As the star spins down, the vortices move outward, dragging magnetic fluxoids with them. This gives $\mu \propto \Omega_*$.[10] Assuming magnetic-dipole braking, Srinivasan et al. (1990) estimated that μ decays by a factor ~ 10 in a Hubble time; a high concentration of impurities gives more decay (Konar and Bhattacharya 1999b). Jahan Miri and Bhattacharya (1994) considered extra Ohmic decay in the crust after flux has travelled there from the core, finding that the correlation of μ with $P_{\rm b}$ can be explained if the Ohmic decay time is $\sim 10^{8.5}$ yr. Jahan-Miri (2002) pointed out that the pinning force plays a crucial role in pushing the fluxoids outwards. A backreaction of the crust can considerably delay flux expulsion from the core for $B_* \gtrsim 10^{11}$ G (Konenkov and Geppert 2000).

Ruderman (1991a) suggested that shear stresses exerted by the superfluid vortices pinned to the crustal lattice break the crust before vortex unpinning occurs, dragging along magnetic fields which are tied to patches of the crust (Alpar et al. 1984; Anderson and Itoh 1975). The global magnetic axis is thereby altered, forcing the rotation and magnetic axes of millisecond pulsars to align (if spinning up, as for LMXBs) or become orthogonal (if spinning down, as for millisecond pulsars formed from accretion-induced collapse of white dwarfs) (Chen et al. 1998; Cheng and Dai 1997; van den Heuvel and Bitzaraki 1995).

[10] Jones (1991) argues that a large fraction of the original magnetic flux can remain in the superconducting interior and is subsequently trapped by the inward radial movement of neutron vortices during later spin-up episodes.

1.2.6 Magnetic burial

Crustal currents induced in the diamagnetic plasma accreted onto the stellar surface potentially neutralise the currents generating the underlying stellar magnetic field (Bisnovatyi-Kogan and Komberg 1974).[11] During the Roche-lobe overflow phase of the recycling scenario, matter is funnelled from the accretion disk by the magnetic field onto the magnetic poles, forming a mountain at the polar caps (Blandford et al. 1979). The accreted matter may be broken up by Kelvin-Helmholtz and Rayleigh-Taylor instabilities at the disk-magnetosphere boundary into blobs that strike the surface separately (Arons and Lea 1980; Zhang et al. 1994). When the hydrostatic pressure at the base of the polar mountain exceeds the magnetic tension confining the mountain (Hameury et al. 1983; Woosley and Wallace 1982), material flows equatorward across the stellar surface and neutralising currents are induced, cancelling or "burying" the original field.

The theory of magnetic burial has an extensive history. However, the problem remains unsolved. No single calculation has managed to successfully incorporate all the relevant microphysics (e.g. Ohmic dissipation, Hall effect) and hydrodynamic behaviour (e.g. flux-freezing, sinking, flow pattern), while simultaneously overcoming the computational challenges associated with steep field gradients, disparate (flow-related, diffusive and hydromagnetic) time-scales, and three-dimensional evolution (e.g. hydromagnetic instabilities). Table 1.4 summarises the elements included and excluded in magnetic burial models to date. Some models treat the accretion flow as spherical, which is more appropriate for wind accretion onto low-field ($B_* \lesssim 10^8$ G) objects (Romani et al. 1993; Romani 1990; Toropin et al. 1999); for high-field objects, a flow channelled towards the polar caps is more realistic (Brown and Bildsten 1998; Cheng and Zhang 1998; Litwin et al. 2001). Other models solve explicitly for the (radial) flow structure on long time-scales but fail to calculate the two-dimensional pole-equator structure properly. Ohmic decay affects magnetic burial significantly (Cumming et al. 2001; Konar and Bhattacharya 1997, 1999a; Romani et al. 1993; Romani 1990) because it allows buried fields to re-emerge (Young and Chanmugam 1995), but it has not been incorporated into two-dimensional pole-

[11] Such currents may cause the field to be screened or buried because of an inverse thermoelectric battery (Blandford et al. 1983; Blondin and Freese 1986; Flowers and Ruderman 1977).

equator models to date (Brown and Bildsten 1998; Hameury et al. 1983; Litwin et al. 2001; Melatos and Phinney 2001; Payne and Melatos 2004; Uchida and Low 1981).

Most work on burial assumes the accreted material is unmagnetized. In reality, this is not true. Uchida and Low (1981) found that the topology of the (axisymmetric) magnetosphere during accretion depends on whether the accreted matter is magnetized parallel or antiparallel to the star's magnetic moment. Antiparallel magnetization leads to confinement of the magnetosphere within a spherical region surrounded by the external field, with mass draining along the field lines to form an equatorial disk; parallel magnetization leads to a ring of magnetic neutral points in the equatorial plane, and opening of polar field lines, possibly leading to mass leakage. It is possible that initially magnetized material is demagnetized by the turbulent process of accretion.

During accretion onto a low-field ($B_* \lesssim 10^8$ G) neutron star, such as the six currently known accreting millisecond pulsars (Wijnands and van der Klis 1998), the disk reaches the equator and matter spreads from the equator towards the poles (Inogamov and Sunyaev 1999; Popham and Sunyaev 2001). The combined effect of the centrifugal force and radiation pressure gives rise to two rings of enhanced brightness which are symmetric about the equator in the upper and lower hemispheres (Inogamov and Sunyaev 1999).

Magnetic mountain

When accreted matter accumulates onto the magnetic poles, it is confined in a polar mountain by the magnetic tension of the stellar magnetic field. Magnetostatic equilibria have been calculated for such mountains by several authors (Brown and Bildsten 1998; Hameury et al. 1983; Litwin et al. 2001; Payne and Melatos 2004; Uchida and Low 1981). The equilibria are solutions of the cross-field force-balance equation, the Grad-Shafranov equation, including the pressure gradient, gravity, and the Lorentz force. Magnetostatic solutions are relevant to accreting neutron stars because the accretion time is long. However, by virtue of their static nature, these calculations do not involve the induction equation [unlike the models of Konar and Bhattacharya (1997); Urpin and Geppert (1995)], so flux freezing must be enforced in another way: the Grad-Shafranov equation must be supplemented by the condition that the mass-flux distribution of the final state equals that

Table 1.4: Models of magnetic burial or screening. The physics included in each model is ticked. D denotes the dimensionality of the model, $M(\psi)$ indicates that the mass-flux ratio is computed self-consistently (solutions of the induction equation with nonzero flow velocity $\mathbf{v} \neq 0$ do this automatically), $\dot{M}_{\rm a}$ indicates that the dependence of μ on the accretion rate is included, $B_{\rm a} \neq 0$ indicates that the accreted matter is magnetized, and EMS indicates that the equatorial magnetic stresses are treated self-consistently.

Model	D	Ohmic	Hall	$M(\psi)$	$\dot{M}_{\rm a}$	Sinking	$B_{\rm a} \neq 0$	EMS
UL81[a]	1	.	.	.	.	.	√	.
HBHL83[b]	1	.	.	.	.	.	.	.
R90[c]	1	√	.	.	√	.	.	.
UG95[d]	1	√	.	√	√	√	.	.
KB97[e]	1	√	.	√	.	√	.	.
BB98[f]	2	.	.	.	.	.	.	.
CZB01[g]	1	√	.	.	√	√	.	.
LBR01[h]	2	.	.	.	.	.	.	.
MP01[i]	2	.	.	.	.	.	.	√
CK02[j]	2	√	.	.	√	√	.	.
GR02[k]	1	√	√	.	.	.	.	.
CAZ04[l]	1	√	√	.	.	.	.	.
PM04[m]	2	.	.	√	.	.	.	√

[a] Uchida and Low (1981).
[b] Hameury et al. (1983).
[c] Romani (1990).
[d] Urpin and Geppert (1995).
[e] Konar and Bhattacharya (1997).
[f] Brown and Bildsten (1998). These authors do consider Ohmic dissipation, but not in their two-dimensional magnetic burial calculation.
[g] Cumming et al. (2001).
[h] Litwin et al. (2001).
[i] Melatos and Phinney (2001).
[j] Choudhuri and Konar (2002).
[k] Geppert and Rheinhardt (2002).
[l] Cumming et al. (2004).
[m] Payne and Melatos (2004).

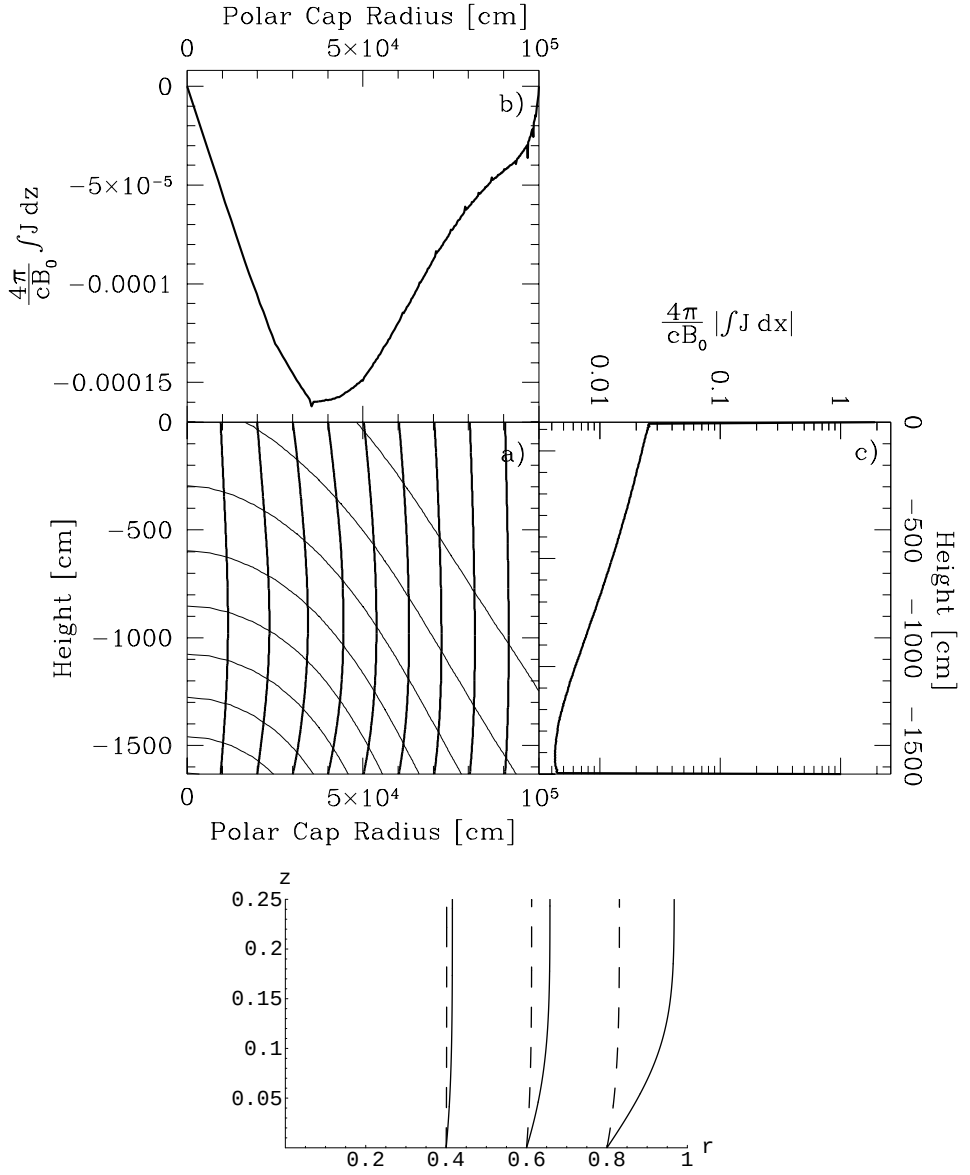

Figure 1.5: *Top*: Polar mountain confined by the magnetic field obtained by solving the Grad-Shafranov equation with a prescribed mass-flux condition. Panel (a) shows isochores (*thin lines*) and the magnetic field (*heavy lines*). Panels (b) and (c) plot the current density integrated over height and distance from the pole, respectively. [From Brown and Bildsten (1998).] *Bottom*: Magnetic field lines for two different values of $M_{\rm a}$, where r and z are the distance from the magnetic pole and the height above the surface respectively, in units of the polar cap radius $R_{\rm cap}$. [From Litwin et al. (2001).]

of the initial state (plus the accreted matter), otherwise there is no ideal-MHD route from one to the other (Gourdain and Leboeuf 2004; Payne and Melatos 2004). This point was missed by all magnetostatic calculations preceding this thesis (table 1.4). The importance of properly treating mass-flux conservation is highlighted by the example of the Parker instability in the the Galaxy (Parker 1966), where the mass-flux ratio varies inversely with the magnetic flux when calculated properly (Mouschovias 1974), contrary to naive expectations. In chapter 2, magnetostatic equilibria of accreted magnetic mountains are computed subject to mass-flux conservation.

Figure 1.5 illustrates some examples of Grad-Shafranov equilibria calculated for $M_{\rm a} \lesssim 10^{-10} M_\odot$ (Brown and Bildsten 1998; Litwin et al. 2001), without mass-flux conservation. Notice how the accreted matter pushes the magnetic field lines away from the pole. Also, the field is free at the edge of the polar cap where it matches a uniform field. Implicitly, these boundary conditions neglect the back-reaction from hydromagnetic stresses exerted by the equatorial field at the equator, likely to be important for large $M_{\rm a}$: as the accreted material spreads equatorward, the magnetic field is compressed at the equator, whereas for free boundary conditions, it slips through the equator. In chapter 2, we show that this prevents the magnetic field lines from being significantly distorted until much more mass ($M_{\rm a} \gtrsim 10^{-5} M_\odot$) has been accreted than previous analyses predicted (Brown and Bildsten 1998; Hameury et al. 1983; Litwin et al. 2001). Cheng and Zhang (1998) argued heuristically that the polar cap expands as matter accretes at the poles, but they also ignored the equatorial magnetic stresses.

Magnetic stresses are ignored completely by burial calculations in which a spherically symmetric density distribution $\rho(r)$ and quasi-dipolar magnetic field are prescribed (Konar and Bhattacharya 1997, 1999a; Romani et al. 1993; Romani 1990; Urpin and Geppert 1995). Such one-dimensional calculations employ a radial velocity field, either $v(r) = 0$ (Romani et al. 1993; Romani 1990) or $v(r) = \dot{M}_{\rm a}/4\pi r^2 \rho(r)$ (Konar and Bhattacharya 1997, 1999a). More recent, two-dimensional simulations (Choudhuri and Konar 2002; Konar and Choudhuri 2004) include a meridional flow from pole to equator, sinking radially inward at the equator and becoming spherically symmetric deeper in the crust. In all these cases, the magnetic field evolves according to the induction equation with the velocity field prescribed, i.e. it is assumed that the Lorentz force does not modify the flow, and magnetic

buoyancy is mocked up by a radial outflow in the upper crust. On the other hand, such calculations do model sinking of accreted material and ongoing crustal replacement (Choudhuri and Konar 2002; Konar and Choudhuri 2004), effects that are overlooked by most calculations of magnetostatic equilibria that include equatorward spreading and equatorial magnetic stresses (Payne and Melatos 2004).

Stability of a magnetic mountain

Instabilities and Ohmic diffusion may disrupt a polar magnetic mountain (Urpin 2005). In the buried configuration, the magnetic field components parallel to the stellar surface are buoyant (Cumming et al. 2001; Mouschovias 1974; Parker 1966) and may pop up to the surface in blisters, rendering screening ineffective (Bhattacharya 1999; Konar and Bhattacharya 1997; Young and Chanmugam 1995). Extending work by Brown and Bildsten (1998), who found that the flow time exceeds the Ohmic diffusion time for $\dot{M}_{\rm a} > \dot{M}_{\rm Edd}$, Cumming et al. (2001) showed that screening is ineffective for $\dot{M}_{\rm a} < 0.01\dot{M}_{\rm Edd}$, and that buoyancy instabilities act in the surface ocean for $B_* \gtrsim 10^{10-11}$ G. A similar conclusion is reached in the context of hypercritical ($\dot{M}_{\rm a} > \dot{M}_{\rm Edd}$) accretion onto a newly born neutron star (Geppert et al. 1999). Cumming et al. (2001) considered a one-dimensional radial accretion flow; as they point out, "the complex problem of the subsequent spreading of matter" is not tackled (Cumming 2002). In two dimensions, the magnetic Rayleigh-Taylor instability (Kruskal and Schwazschild 1954) can occur. Litwin et al. (2001) found that ballooning modes perpendicular to the magnetic field lines are unstable if the pressure at the bottom of the neutron star ocean exceeds the magnetic pressure by a factor $\sim 8R_{\rm cap}/h$, where $R_{\rm cap}$ and h denote the polar cap radius and hydrostatic scale height respectively. The effect of magnetic buoyancy on equilibria of buried magnetic fields calculated with strict mass-flux conservation and in two dimensions is addressed analytically and numerically in chapter 3: we find that, in ideal MHD, the equilibria oscillate when perturbed but are not disrupted.

Urpin (2005) recently found that the ocean of an accreting neutron star is unstable due to temperature and chemical composition gradients along the stellar surface combined with the Hall effect.

1.3 Gravitational radiation from accreting neutron stars

One of the main ideas explored in this thesis is that the mountains formed at the magnetic poles of a neutron star during accretion create a nonzero quadrupole moment of inertia ($\alpha \neq 0$ in general) and are therefore promising candidate sources of gravitational waves detectable by long-baseline interferometers. They have the advantage of being continuous-wave sources whose periods are known from radio or X-ray timing observations, so that it is possible to integrate the gravitational wave signal coherently, increasing the sensitivity by $(f_*\tau)^{1/2}$, where τ is the integration time. Several kilometer-baseline interferometers, such as the Laser Interferometer Gravitational-wave Observatory (LIGO), have begun recording data. Already, upper bounds have been placed on the gravitational wave amplitudes of 28 pulsars (The LIGO Scientific Collaboration: B. Abbott et al. 2004a,b,c), and a direct detection is expected within a decade. In this section, after introducing gravitational waves and their possible sources, the likelihood of their detection from accreting neutron stars is considered, in order to motivate the calculations in chapters 5 and 6.

1.3.1 Ripples in spacetime

Einstein's (1915) theory of general relativity predicts that gravitational waves propagate at the speed of light as ripples in the curvature of spacetime. Because gravity is nonlinear, it is impossible in general to separate the curvature contributed by large-amplitude gravitational waves from that contributed by the moving masses that are their sources. However, far from the source, one may make the linearized weak-field approximation to general relativity: the metric can be written as $g_{\mu\nu} = \eta_{\mu\nu} + h_{\mu\nu}$, with $|h_{\mu\nu}| \ll 1$, where $\eta_{\mu\nu}$ is the Minkowski metric of special relativity, and $h_{\mu\nu}$ contains both quasistatic components from local masses and an oscillatory component from gravitational waves (usually, only the wave component is considered). The waves are approximately planar when they reach the Earth and may be described by two dimensionless amplitudes h_+ and $h_\times$, one for each polarization. We call h_+ and $h_\times$ the wave strains in each polarization. The $+$ polarization distorts a ring of test masses into an ellipse along the axes of a $+$. The $\times$ polarization does the same along a cross. The coordinate system

is comoving with freely-falling particles. Introducing polarization tensors $\mathbf{e}^+$ and $\mathbf{e}^\times$, such that $e^+_{xx} = -e^+_{yy} = 1$ and $e^\times_{xy} = e^\times_{yx} = 1$ for a wave propagating in the z direction, the metric perturbation becomes $h_{\mu\nu} = h_+ e^+_{\mu\nu} + h_\times e^\times_{\mu\nu}$, a symmetric traceless tensor with zero projection along z. This expression is written in the transverse-traceless gauge.

Gravitational radiation is generated by accelerating masses, just as electromagnetic radiation is generated by accelerating charges. Conservation of linear momentum precludes dipole radiation, leaving the quadrupole as the leading order. Most predictions of source amplitudes, including those for accreting neutron stars, are based on quadrupolar emission. An exception, where higher-order multipoles must be considered, is a black hole or neutron star merger, in which the dynamics is complex (Flanagan and Hughes 1998) and fully relativistic calculations are necessary for the construction of sensitive search templates for data analysis.

1.3.2 Astrophysical sources

Gravitational wave sources can be grouped into three categories: burst (signals lasting from a fraction of a second to about 20 seconds), periodic (long term monitoring with coherent integration), and stochastic (contributing to a noisy background) (Creighton 2003). Below we list some systems in each class, ordered roughly by descending likelihood of detection, and discuss their properties.

Burst sources

- Final phase of binary black hole and/or neutron star coalescence (Flanagan and Hughes 1998). The coalescence may be divided into three epochs: inspiral (due to gravitational-wave back-reaction; wave frequency $= 2P_{\rm b}^{-1}$, $P_{\rm b}$ is the binary orbital period), merger (when the binary orbit becomes dynamically unstable), and ringdown (as the merged object settles down to a stationary state). The latter two phases are potentially detectable by LIGO I and II in neutron star mergers; the LIGO II event rate is predicted to lie between 10 and 500 per year (Belczynski et al. 2002; Kalogera et al. 2004). The first phase is detectable by the Laser Interferometer Space Antenna (LISA) in supermassive black hole mergers (wave frequency μHz – mHz) (Haehnelt

1994; Rhook and Wyithe 2005).

- Collapse of the stellar core during a supernova to form a neutron star or black hole (Fryer et al. 2002). It is very hard to estimate the asymmetry arising during collapse from first principles, although the pulsar kick velocity distribution offers a clue (Lai et al. 2001). Simulations of neutrino transport show that the infalling material bubbles and boils convectively as neutrinos stream through it (Burrows et al. 1995). The collapsed core also rotates rapidly, becoming dynamically unstable and forming a bar, which emits copious gravitational radiation (Fryer et al. 2004).

- Main-sequence stars or compact objects falling into supermassive black holes at the centres of galaxies (Cardoso and Lemos 2003; Kojima and Nakamura 1984). The characteristic wave frequency from such events is $\sim 10^{-4}$ Hz, with one occurring year per supermassive black hole. A large fraction of such captures are not resolvable individually at present because they are too distant, have unfavorable orientations, or are too far from their final plunge (Barack and Cutler 2004).

Periodic sources

- Rotating neutron stars with surface mountains. These sources are discussed in detail in section 1.3.4. Their wave frequencies are between 0.1 and 700 Hz. The quadrupole moments are generated by accretion-induced thermal instabilities (Bildsten 1998; Ushomirsky et al. 2000), toroidal magnetic fields (Cutler 2002), r-modes (Andersson 1998), or polar mountains of accreted material supported by buried magnetic fields (chapters 5 and 6 of this thesis).

  Inspiralling compact binary stars, e.g. double white dwarf binaries (Verbunt and Nelemans 2001). These sources emit gravitational waves with frequencies $\lesssim$ mHz and will be detected routinely by LISA (Flanagan and Hughes 1998).

Stochastic sources

- Gravitational radiation from the Big Bang. Primordial quantum fluctuations are amplified into gravitational waves during inflation, anal-

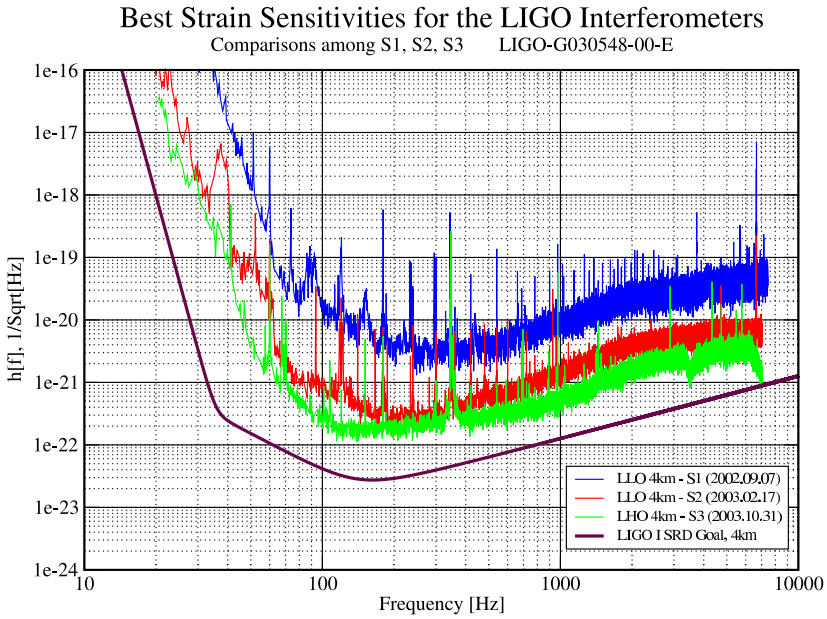

Figure 1.6: LIGO I noise sensitivity curves as a function of frequency, showing three recent science runs S1 (September, 2002), S2 (March, 2003), and S3 (January, 2004). The solid curve is the LIGO I design goal, limited by seismic (low frequency), thermal (intermediate frequency), and shot (high frequency) noise. LIGO II will be $\sim 10^2$ times more sensitive and tunable.

ogous to the amplified temperature fluctuations of cosmic microwave background radiation (Allen and Brustein 1997; Grishchuk 1975, 2005).

- Superposition of multiple galactic and extragalactic black hole, neutron star and other binaries (Farmer and Phinney 2003; Nelemans et al. 2001; Schneider et al. 2001). These are $\sim$ mHz contributions which form part of the LISA background. Coalescing supermassive black holes (e.g. during galaxy mergers) contribute at frequencies $\lesssim \mu$Hz and may be detected by a pulsar timing array (Foster and Backer 1990; Jenet et al. 2005), which searches for correlations between pulsar timing residuals at different sky positions, with widely separated pulsars in the Galaxy acting as test masses with onboard clocks.

1.3.3 Detectors

At present, almost all our information about the cosmos is carried by electromagnetic radiation, from radio waves to gamma rays. The only exception to date has been data gathered by particle detectors, e.g. cosmic rays and solar and supernova neutrinos. We can safely expect a dramatic expansion in astrophysical knowledge once gravitational waves are detected directly, opening a new window on the universe.

To date, the strongest evidence for the existence of gravitational radiation is indirect: two neutron stars in close orbit are predicted to emit gravitational radiation at twice the orbital frequency, and radio pulsar PSR 1913+16, the first of nine such systems discovered to date (Hulse and Taylor 1975),[12] provides a regular clock which allows the orbital elements to be deduced. Gravitational-radiation-induced orbital decay is observed to match the predictions of general relativity to within observational errors of less than 1 per cent (Damour 1992). Geodetic precession provides an independent test of the theory. It changes the angle between the spin axis and our line of sight. Kramer (1998) showed that the decadal changes in pulse profile of PSR 1913+16 are consistent with geodetic precession and that this pulsar will become undetectable after 2025, as its orientation changes. Similar tests have been performed on three other objects: another double neutron star system PSR B1534+12, where the uncertainties in the distance to the pulsar are limited to $\sim$ 15 per cent (Stairs et al. 1998); the closest and brightest millisecond pulsar J0437−4715, which orbits a low-mass helium white dwarf companion (van Straten et al. 2001); and PSR J1141−6545, which orbits an unidentified companion (with mass $> 0.97 M_{\odot}$, probably a white dwarf) (Bailes et al. 2003). The double pulsar system PSR J0737-3039A/B (Lyne et al. 2004), with its short orbital period ($P_{\rm b} = 2.4$ hr) and very high value of periastron advance (17 deg/yr, four times larger than for PSR 1913+16), is another excellent laboratory for testing general relativity. Observations currently underway will do so at the level of 0.1 per cent.

The first attempts to detect gravitational waves directly used bar detectors made of aluminium cylinders, whose sensitivity is due to their sharp fundamental resonance mode (bandwidth $\sim$ few Hz) (Weber 1960). Development of bar detectors continues, with cryogenic versions being developed

[12] The authors were awarded the Nobel Prize for physics in 1993 for this discovery.

in Rome, Stanford, and Australia. Their sensitivity to broadband burst sources was the best in the world until recently.

The best hope for the first direct detection of gravitational waves lies with beam detectors such as large-scale laser interferometers, including LIGO (USA), VIRGO (France and Italy), GEO600 (Germany and UK), AIGO (Australia), TAMA and JGWO (Japan). Terrestrial Michelson-Morley interferometers, such as LIGO, use high-power, recycled lasers to measure changes of the proper path lengths between mirrors along two perpendicular arms (each 4 km long in LIGO) as a gravitational wave passes. The two LIGO sites are separated geographically by ~ 3000 km, eliminating coincident perturbations, especially when data is collected in tandem with other facilities, e.g. GEO600 and AIGO. Local seismic background, electromagnetic fluctuations, acoustic noise, cosmic radiation, dust, weather, power line transients, vacuum quality, and magnetic field at several locations are monitored at each observatory.

LIGO is sensitive to gravitational wave strains $h \sim 10^{-22}$ in the frequency range 0.05 – 10 kHz, with a "sweet spot" at 100–300 Hz. Happily, this overlaps the range of spin frequencies ($f_* = 270 - 620$ Hz) of accreting millisecond pulsars, which are predicted to emit gravitational waves (e.g. due to magnetic mountains) by Bildsten (1998) and in chapters 5 and 6 of this thesis. LIGO's sensitivity is limited by seismic noise at low ($\lesssim 50$ Hz) frequencies, thermal noise in the test mass suspensions at intermediate ($\sim 50-200$ Hz) frequencies, and laser shot noise at high ($\gtrsim 200$ Hz) frequencies. These limits are delineated by the solid curve in figure 1.6, representing the LIGO I science design goal. Progress towards this goal has been steady. Figure 1.6 depicts the noise sensitivity curves achieved by LIGO I during three science runs: S1 (September, 2002), S2 (March, 2003), and S3 (January, 2004). The sensitivity is only a factor of 2 away from the design goal in the sweet spot. Lowering the noise curve to its present level has been a multi-year challenge, requiring fine control of the mirror positions and the power and frequency of the lasers; the laser radiation pressure torques the 10-kg mirrors if the beams are not centered exactly (Raab 2004). All major optics in the interferometer are suspended on a single steel wire loop, mechanically isolated from the ground by vibration isolators and controlled by multiple servo loops. The mirrors are made of fused silica and polished to within 1 nm, with homogeneous, low bulk loss, multi-layer coatings (< 50

ppm scattering losses). Seismic isolation is achieved by "stacks" formed by several layers of leg elements separated by coil springs with internal layers of damping material.

LIGO II is designed to be 100 times more sensitive than LIGO I. The upgrade will mitigate all four principal noise sources: the lasers will be upgraded from 10 W to 180 W, lowering shot noise; the test masses will be made of sapphire, which has lower mechanical losses than fused quartz; the suspension will be made out of quartz instead of steel wire, reducing thermal noise; and passive isolation and servo controls will be implemented to slave the quiet suspension platform to quiet seismometers, reducing seismic noise (Hua et al. 2004; Robertson et al. 2004). In addition, LIGO II will be tunable, using a variable reflectivity mirror, allowing experimenters to tailor the noise curve to particular sources. Given prototyping is already underway, achievement of the maximum LIGO II design sensitivity (2×10^{-24} Hz$^{-1/2}$) by 2010 is plausible. Accreting neutron stars with magnetic mountains, the sources modelled in chapters 5 and 6 of this thesis, are strong candidates for detection by LIGO II.

LIGO continuously collects data at $\sim$ 10 MB per second, which must be stored and managed in real time. LIGO has its own data management system LDAS (LIGO Data Analysis System) in a distributed computer environment, enabling data access and conditioning, signal reconstruction, coincidence analysis, database management, and archiving. The data is filtered through $\sim 10^{4-5}$ model waveforms or templates, which must be applied nearly in real time using matched filtering, to search for sources such as coalescing compact binaries and accreting neutron stars (Bose 2005; Brady et al. 1998; Cutler and Flanagan 1994; Owen 1996). These templates require accurate models of the likely sources of gravitational waves. Hierarchical Fourier searching of LIGO data increases the sensitivity by $(f_* \tau)^{1/2}$ (Brady et al. 1998). The rapid progress of LIGO (and LIGO II) instrumentation calls for more detailed theoretical models of gravitational wave sources. In chapters 5 and 6 of this thesis, detailed frequency-space models of accreting neutron stars are presented, which will serve as a useful guide when tuning LIGO II.

Three space-based detection methods also exist. Ranging radar involving spacecraft near Jupiter or Saturn allows one to monitor the return time of signals for signatures of gravitational waves (Armstrong et al. 1999). The

pulsar timing array (Hobbs 2004) exploits the regularity of pulsar signals: if one simultaneously monitors two or more pulsars over several years, the delay on Earth will be correlated in the presence of a gravitational wave, allowing long-period ($\sim$ nHz) waves to be detected (Jenet et al. 2005). The Laser Interferometer Space Antenna (LISA), which consists of three spacecraft flying freely five million kilometers apart in an equilateral triangle, orbiting the Sun at 1 AU about 20 degrees behind the Earth, exploits the fact that Earth-based gravity-gradient noise falls off as r^{-3} and aims to detect gravitational waves with frequencies between 0.1 mHz and 0.1 Hz at wave strain $h \gtrsim 10^{-20}$ (Landgraf et al. 2005).

1.3.4 Accreting neutron stars

Accreting neutron stars are arguably the most promising high-frequency (kHz) sources of gravitational radiation predicted to date. They are persistent, not transient. The harmonic content of the signal is expected to be pure (i.e. nearly sinusoidal). The period and sky position of the source are known a priori from X-ray timing observations. With the benefit of multi-detector, coherent integration, we anticipate that these sources will be detected by LIGO II. Several theoretical ideas have been put forward regarding how a quadrupole moment can be generated physically, including the one — magnetic mountains — proposed in this thesis (chapters 5 and 6).

Even without a theoretical understanding of the mechanism, observations imply strongly that such a quadrupole exists. Bildsten (1998) noted that the inferred rotation frequencies of LMXBs and accreting millisecond pulsars (table 1.1) have a frequency distribution that cuts off sharply above $f_* \approx 700$ Hz, well below the centrifugal break-up frequency ~ 1.5 kHz (Cook et al. 1994; Haensel et al. 1999), and that the fastest millisecond pulsar has $f_* = 642$ Hz. One natural way to explain this f_* gap is to say that LMXBs reach an equilibrium where the accretion torque is balanced by a gravitational-radiation torque, provided that the quadrupole moment is $\sim 10^{-7} M_* R_*^2$ (Bildsten 1998; Wagoner 1984). A wide range of accretion rates leads to a narrow range of f_*, because the gravitational radiation torque scales as f_*^5. Sco X-1, the object with the highest X-ray flux from accretion, is the most likely candidate, with $h_c \approx 2.2 \times 10^{-26}$ predicted (Bildsten 1998; Ushomirsky et al. 2000; van der Klis et al. 1997).

Below, we discuss three mechanisms for producing gravitational radiation from an accreting neutron star: precession, oscillation (e.g. r-modes), and surface mountains of magnetic or thermochemical origin.

Precession

A neutron star precesses or wobbles when its angular momentum vector is not aligned with any principal axis of inertia, consequently emitting gravitational waves at the inertial-frame precession frequency ($\approx f_*$). Amplitudes $h \sim 10^{-27}$ are possible, but dissipation quickly damps the wobble (over ~ 1 yr for a millisecond pulsar) unless something continously re-excites it (Jones and Andersson 2002). Another argument against millisecond pulsars precessing is that they have stable pulse profiles, except for the odd giant pulse (Jenet et al. 2001), e.g. PSR J1939+2134, which was monitored during LIGO S1. A few ordinary pulsars like PSR B1828−11 ($P = 0.4$ s) do precess on a 500 day time-scale (Link and Epstein 2001; Stairs et al. 2000), but they spin too slowly to be observable by LIGO as gravitational wave sources.

r-modes

Rossby waves (r-modes), mediated by the Coriolis force, are unstable due to a gravitational-wave back reaction (the Chandrasekhar-Friedman-Schutz instability): the r-mode wave pattern rotates in a retrograde (negative angular momentum) sense in the frame corotating with the star (Andersson 1998; Friedman and Morsink 1998; Kokkotas and Andersson 2002). The growth is saturated by nonlinear transfer of energy to "inertial" oscillation modes with elastic restoring forces (but negligible buoyancy) that propagate in the star; the saturation energy is roughly $E_{\rm r-mode}/(0.5 M_* R_*^2 \Omega_*^2) \sim 0.1 \nu_{\rm gr}/\Omega_* \sim 10^{-6} (f_*/10^3\,{\rm Hz})^5$, where $\nu_{\rm gr}$ is the driving rate by gravitational-wave backreaction (Arras et al. 2003). This low saturation amplitude implies the characteristic time for a newly born neutron star or LMXB to exit the region of r-mode instability is $\gtrsim 10^3 - 10^4$ yr, making them detectable in LMXBs out to $100 - 200$ kpc by LIGO II. Gravity waves from excited r-modes can balance accretion torques (Bildsten 1998) and lead to a limit cycle if r-mode damping is a decreasing function of temperature (Levin 1999). In this cycle, the instability is triggered by recycling, exciting r-modes which spin the star

down, shutting off the r-mode instability until further recycling spins up the star again.

Surface mountains

If a neutron star is permanently distorted, with ellipticity, $\epsilon = (I_{xx} - I_{yy})/I_{zz}$, and if the principal axis of the distortion is not aligned with the rotation axis, then gravitational waves are emitted. The wave strain at Earth is

$$h_0 \approx 2GI_{zz}\epsilon\Omega_*^2/dc^4 \,. \tag{1.6}$$

where d is the distance to the source, and I_{zz} is the principal moment of inertia around the rotation (z) axis. For example, if we take $\epsilon \sim 10^{-7}$ as invoked by Bildsten (1998) to explain the f_* gap in LMXBs, we obtain $h_0 \approx 8.5 \times 10^{-26}(\epsilon/10^{-7})(f_*/0.6\mathrm{kHz})^2(d/\mathrm{kpc})^{-1}$

Several mechanisms for producing mountains on the stellar surface have been proposed. (i) Crustal shear stresses may be anisotropic along an axis misaligned with the rotation axis (e.g. the magnetic axis when the crust crystallized) (Melatos 2000). In this scenario, the maximum ϵ is set by the maximum crustal breaking strain $\Sigma_{\max}$, with $\epsilon_{\max} \approx 5 \times 10^{-8}(\Sigma_{\max}/10^{-3})$ (Ushomirsky et al. 2000). If the magnetic field inside the star (generated by strong differential rotation immediately after collapse) has a toroidal topology, it can distort a neutron star into a prolate figure sufficiently to explain the f_* gap if the field measures $\sim 10^{12-13}$ G; this may also explain millisecond pulsar spin-down (Cutler 2002; Geppert et al. 2004). (iii) Accretion-induced thermo-compositional gradients, caused by electron capture in the crust, can also provide the required quadrupole (Bildsten 1998). In this scenario, crustal compression forces nuclei to undergo electron capture, the electron capture rate is temperature sensitive (hotter regions capture at lower pressures), so the associated density jump occurs at a higher altitude in the hotter parts of the crust. (iv) Finally, global reorganisation of the internal magnetic field of a magnetar, releasing sufficient energy to explain the flare in soft gamma-ray repeaters, may deform the star, leading to a burst of gravitational radiation (Ioka 2001a).

1.4 Thesis Outline

In the first two chapters (2 and 3) of the body of this thesis, we present our calculations of the hydromagnetic structure of the magnetically confined mountain accumulated at the magnetic poles of an accreting neutron star. Chapter 2 describes the numerical and analytic methods used to solve the Grad-Shafranov equation in conjunction with the mass-flux freezing constraint to find MHD equilibria of buried fields up to $M_{\rm a} \sim 10^{-4} M_{\odot}$. Chapter 3 takes the hydromagnetic equilibria generated chapter 2 and tests their stability by loading them into ZEUS-3D, a time-dependent ideal MHD code for astrophysical fluid dynamics. It is found that the equilibria are marginally stable: they oscillate when perturbed but are not disrupted.

In chapter 4, we apply our theory of magnetic burial to interpret the highly sinusoidal nature of millisecond oscillations observed in the tails of (type I) X-ray bursts.

In the next part of the thesis (chapters 5 and 6), we evaluate the promise of magnetically confined mountains on accreting neutron stars as gravitational wave sources. Chapter 5 calculates the amplitude of the gravitational wave signal using the Grad-Shafranov equilibria derived in chapter 2. The signal is found to be potentially detectable with LIGO II. Chapter 6 calculates the frequency spectrum of the gravitational waves, including the hydromagnetic oscillations revealed by the numerical stability experiments with ZEUS-3D in chapter 3. Updated signal-to-noise ratios are calculated for LIGO II.

In chapter 7 we summarise the main results of the thesis and discuss their significance to problems like magnetic dipole moment reduction in neutron-star binaries, magnetars, and the maximum spin frequency of millisecond pulsars. Some directions for future work are discussed.

Chapter 2

Theory of magnetic field burial

2.1 Introduction

Observations of low-field neutron stars in binary systems containing white-dwarf and supergiant companions, with a history of disc-fed and wind-fed accretion respectively, suggest that the magnetic dipole moment $|\boldsymbol{\mu}|$ of a neutron star decreases monotonically with accreted mass, $M_{\rm a}$ (Taam and van den Heuvel 1986; van den Heuvel and Bitzaraki 1995; see Wijers 1997 for a dissenting view). Several mechanisms have been proposed to explain why $|\boldsymbol{\mu}|$ is reduced: (i) accelerated Ohmic decay, where the electrical conductivity of the crust is lowered by accretion-induced heating (Urpin and Geppert 1995; Urpin and Konenkov 1997); (ii) interactions between superfluid neutron vortices and superconducting magnetic fluxoids in the stellar interior (Muslimov and Tsygan 1985; Srinivasan et al. 1990); and (iii) magnetic screening or burial, where the currents generating the natal magnetic field are partially neutralized by accretion-induced currents in the crust (Arons and Lea 1980; Blondin and Freese 1986). For a critical review of these mechanisms, see Melatos and Phinney (2001).

In this chapter, we study the mechanism of magnetic burial in detail. In the early stages of accretion ($M_{\rm a} \lesssim 10^{-10} M_\odot$), accreted matter accumulates in a column at the polar cap, minimally distorting the magnetic field. The mass-flux distribution in this regime has been calculated by Grad-Shafranov methods, with the prediction that $|\boldsymbol{\mu}|$ is reduced by ~ 1 per cent

for $M_{\rm a} \approx 10^{-10} M_\odot$ (Brown and Bildsten 1998; Hameury et al. 1983; Litwin et al. 2001). We show that these calculations overestimate the amount of screening; in fact, $M_{\rm a} \gtrsim 10^{-5} M_\odot$ is required to reduce $|\boldsymbol{\mu}|$ by 10 per cent when the confining stress of the compressed, equatorial magnetic field is modelled faithfully. In this regime, inaccessible to previous analyses due to numerical breakdown (Brown and Bildsten 1998; Hameury et al. 1983; Litwin et al. 2001), the latitudinal pressure gradient at the base of the polar column forces the polar magnetic field to buckle, and the accreted material spreads equatorward together with frozen-in magnetic flux (Melatos and Phinney 2001). We compute the structure of the highly distorted magnetic field, and hence $|\boldsymbol{\mu}|$ as a function of $M_{\rm a}$.

A key advance in the present work is that the mass-flux distribution in each equilibrium state is self-consistent; our equilibria are generated by a continuous deformation of the flux surfaces of the initial magnetic field (say, a dipole), in a manner which preserves flux-freezing. This is not true of previous calculations, where the mass-flux distribution is unconstrained relative to the initial state (Brown and Bildsten 1998; Hameury et al. 1983; Litwin et al. 2001; Melatos and Phinney 2001). However, several other important effects are not included to keep the problem manageable. (i) Ohmic dissipation is neglected, even though the diffusion and accretion time-scales are comparable for the smallest magnetic structures predicted by the theory (Brown and Bildsten 1998; Cumming et al. 2001). (ii) We do not investigate the stability of the hydromagnetic equilibria we compute; sharp magnetic-field gradients are potentially disrupted by Rayleigh-Taylor and interchange instabilities (Bhattacharya 1999; Cumming et al. 2001; Melatos and Phinney 2001). (iii) We treat the neutron star as a hard surface; subsidence of accreted material, and incorporation into the crust, are neglected (Bhattacharya 1999).

The chapter is structured as follows. In section 2.2, we introduce the theoretical framework for calculating the self-consistent hydromagnetic equilibrium state of an accreting neutron star. Analytic and numerical methods of solution are given in section 2.3. The properties of the equilibria are investigated in section 2.4, $|\boldsymbol{\mu}|$ is computed as a function of $M_{\rm a}$ and the radius of the polar cap, and the novel feature of magnetic bubbles is explored. The limitations of our results, with respect to time-dependent processes like hydromagnetic instabilities and ohmic dissipation, are assessed in section

2.5.

2.2 Theory of equilibria

2.2.1 Hydromagnetic force balance

The equations of non-ideal magnetohydrodynamics (MHD) in CGS units (Bernstein et al. 1958) comprise the equation of mass conservation,

$$\frac{\partial \rho}{\partial t} + \nabla \cdot (\rho \mathbf{v}) = 0\,, \tag{2.1}$$

the equation of motion,

$$\rho \frac{\partial \mathbf{v}}{\partial t} + \rho(\mathbf{v} \cdot \nabla)\mathbf{v} = -\rho \nabla \phi - \nabla p + \frac{1}{4\pi}(\nabla \times \mathbf{B}) \times \mathbf{B}\,, \tag{2.2}$$

and the induction equation (minus the displacement current),

$$\frac{\partial \mathbf{B}}{\partial t} - \nabla \times (\mathbf{v} \times \mathbf{B}) = \frac{1}{4\pi\sigma}\nabla^2 \mathbf{B}\,, \tag{2.3}$$

supplemented by $\nabla \cdot \mathbf{B} = 0$ and an adiabatic or isothermal equation of state, $d(p\rho^{-\Gamma})/dt = 0$. In this notation, $\mathbf{B}$, ρ, p, ϕ, $\mathbf{v}$ and σ represent the magnetic field, mass density, kinetic pressure, gravitational potential, plasma bulk velocity and electrical conductivity respectively. Elastic stresses are neglected (Melatos and Phinney 2001; Romani 1990), as is the Hall effect (Geppert and Rheinhardt 2002).

In the magnetostatic limit, defined by $\mathbf{v} = 0$ and $\partial/\partial t = 0$, the equation of motion reduces to

$$\nabla p + \rho \nabla \phi - \frac{1}{4\pi}(\nabla \times \mathbf{B}) \times \mathbf{B} = 0. \tag{2.4}$$

The local Alfvén time-scale, $\tau_{\rm A} = L/v_{\rm A} \lesssim 4 \times 10^{-2}$ s for ($L \lesssim 5 \times 10^4$ cm.), is much shorter than the accretion time, $\tau_{\rm a} \sim 10^7$ yr. Equations (2.1) and (2.3) are also satisfied identically (in the ideal-MHD limit $\sigma \to \infty$) and drop out of the problem. To preserve the information encoded in (2.1) and (2.3), we must impose an auxiliary constraint on the mass-flux distribution of the final state in order to connect it with the initial state and uniquely specify the problem. The constraint expresses the fact that material cannot flow across magnetic flux surfaces in the limit $\sigma \to \infty$. We delay consideration

of ohmic dissipation, where magnetic flux diffuses through the fluid at short length-scales via (2.3), to a future paper.

We define spherical polar coordinates (r, θ, ϕ) such that $\theta = 0$ defines the symmetry axis of the pre-accretion magnetic field. For an axisymmetric configuration, there exists a scalar flux function $\psi(r, \theta)$ that generates $\mathbf{B}$ via

$$\mathbf{B} = \frac{\nabla\psi}{r\sin\theta} \times \hat{\mathbf{e}}_\phi. \tag{2.5}$$

The toroidal component B_ϕ is zero at all times, if the accretion process is axisymmetric and $B_\phi = 0$ in the initial accretion state. Upon substituting (2.5) into (2.4), we obtain

$$\nabla p + \rho\nabla\phi + (\Delta^2\psi)\nabla\psi = 0\,, \tag{2.6}$$

with

$$\Delta^2 = \frac{1}{4\pi r^2\sin^2\theta}\left[\frac{\partial^2}{\partial r^2} + \frac{\sin\theta}{r^2}\frac{\partial}{\partial\theta}\left(\frac{1}{\sin\theta}\frac{\partial}{\partial\theta}\right)\right]. \tag{2.7}$$

We can then resolve (2.6) into components parallel and perpendicular to the magnetic field:

$$\rho\nabla\phi + \nabla p = 0\,, \tag{2.8}$$

$$\rho\nabla\phi + \nabla p + (\Delta^2\psi)\nabla\psi = 0\,. \tag{2.9}$$

In this chapter, we assume the accreted material forms an isothermal atmosphere, with $p = c_{\rm s}^2\rho$, where $c_{\rm s}$ denotes the isothermal sound speed. [The force equation for a general equation of state $p = p(\rho)$ is given in Appendix A of Mouschovias (1974).] The gravitational potential ϕ, determined by Poisson's equation, $\nabla^2\phi = 4\pi G\rho$, is the sum of contributions from the accreted material ($M_{\rm a}$) and the underlying neutron star (M_*), with $M_{\rm a} \ll M_*$. As the hydromagnetic length-scale $|\mathbf{B}|/|\nabla\mathbf{B}|$ is much smaller than the hydrostatic length-scale $|p|/|\rho\nabla\phi|$ (verified a posteriori), $\nabla\phi$ is approximately constant near the stellar surface for our purposes, i.e.

$$\phi = GM_* r/R_*^2\,, \tag{2.10}$$

where M_* and R_* are the mass and radius of the neutron star.

We use the method of characteristics to solve (2.6) assuming the gravitational field is radial ($M_{\rm a} \ll M_*$). The r component reads $\rho_r + (\Delta^2\psi)/c_{\rm s}^2\psi_r =$

$-\rho/c_{\rm s}^2\phi_r$ and the θ component reads $\rho_\theta = -(\Delta^2\psi)/c_{\rm s}^2\psi_\theta$, where subscripts indicate differentiation. Together these become: $\rho_r - (\psi_r/\psi_\theta)\rho_\theta = -\rho/c_{\rm s}^2\phi_r$. The characteristic equation is: $dr = -(\psi_\theta/\psi_r)d\theta = -d\rho[c_{\rm s}^2/(\phi\rho)]$. This is solved to yield the two characteristic curves: $\log\rho + \phi/c_{\rm s}^2 = C_1$ and $\psi = C_2$. Thus the characteristic solution is $\log\rho + \phi/c_{\rm s}^2 = f(\psi)$ or, equivalently,

$$p = F(\psi)\exp[-(\phi - \phi_0)/c_{\rm s}^2] \tag{2.11}$$

where $F(\psi) = \exp[f(\psi)]$ is an arbitrary positive function to be specified and $\phi_0 = GM_*/R_*$ is a reference potential. This is just the usual barometric formula with a different base pressure $F(\psi)$ for each field line. Note that ∇F is parallel to $\nabla\psi$, so ψ and hence F are constant along a field line, and one has $\nabla F = F'(\psi)\nabla\psi$. Substituting into (2.6), we obtain a second order, non-linear, elliptic partial differential equation, the Grad-Shafranov equation, for ψ:

$$\Delta^2\psi = -F'(\psi)\exp[-(\phi - \phi_0)/c_{\rm s}^2]\,. \tag{2.12}$$

Equation (2.12) can be understood as follows. The quantity F is a function of r and θ through ψ at hydrostatic equilibrium, expressing the fact that magnetic forces act only perpendicular to field lines, while pressure gradients balance gravity along field lines. If $\psi(r,\theta)$ is given, and if matter is distributed between field lines so that the forces parallel to field lines are in exact balance, then forces perpendicular to the field lines are brought into balance by the appropriate current density $(4\pi)^{-1}\nabla\times\mathbf{B}$.

2.2.2 Magnetic flux freezing and mass-flux ratio

Many authors guess $F(\psi)$ when modelling various systems, e.g. structures in the solar corona, like prominences and arcades (Dungey 1953; Low 1980), and accreting compact objects (Brown and Bildsten 1998; Hameury et al. 1983; Melatos and Phinney 2001; Uchida and Low 1981). As $F(\psi)$ does not change in passing from the initial (pre-accretion) to the final (post-accretion) state in the ideal-MHD limit, the guessed $F(\psi)$ conflicts with the initial $F(\psi)$ except under very special circumstances. In this chapter, we adopt a self-consistent approach whereby we calculate $F(\psi)$ explicitly by demanding that the mass-flux distribution of the final state equals that of the initial state, plus the accreted material, as described below.

Define a local coordinate system (s,t), with unit vectors $\hat{\mathbf{e}}_s = \mathbf{B}/|\mathbf{B}|$ and

$\hat{\mathbf{e}}_t = \nabla\psi/|\nabla\psi|$ parallel and perpendicular to the magnetic field respectively. The amount of matter between two infinitesimally separated flux surfaces ψ and $\psi + d\psi$ is $dM = 2\pi \int_C ds dt \rho r \sin\theta$, where $ds dt = |\hat{\mathbf{e}}_s ds \times \hat{\mathbf{e}}_t dt| = ds d\psi/|\nabla\psi|$ is an infinitesimal area element, and C is the curve $\psi[r(s), \theta(s)] = \psi$. Hence we can write

$$\frac{dM}{d\psi} = 2\pi \int_C ds \rho[r(s), \theta(s)] r \sin\theta |\nabla\psi|^{-1}, \tag{2.13}$$

where $dM/d\psi$ is the mass-flux ratio. Upon substituting (2.11) into (2.13), we arrive at

$$\begin{aligned} F(\psi) = & \frac{c_{\rm s}^2}{2\pi}\frac{dM}{d\psi} \\ & \times \left\{ \int_C ds\, r \sin\theta |\nabla\psi|^{-1} e^{-(\phi-\phi_0)/c_{\rm s}^2} \right\}^{-1}, \end{aligned} \tag{2.14}$$

which is to be solved simultaneously with (2.12) for $\psi(r, \theta)$ given $dM/d\psi$. For problems involving accretion, the mass-flux constraint is not conservative; $dM/d\psi$ in the final state equals $dM/d\psi$ in the initial state plus the mass-flux distribution of the accreted material.

In disc-fed accretion, mass accretes onto polar magnetic field lines that close beyond the inner edge of the accretion disc, located at a radius

$$\frac{R_{\rm a}}{R_*} \approx 270 \left(\frac{\dot{M}}{10^{-9}\, M_\odot {\rm yr}^{-1}} \right)^{-2/7} \left(\frac{|\boldsymbol{\mu}|}{10^{30} {\rm G\, cm}^3} \right)^{4/7}. \tag{2.15}$$

in the equatorial plane (Basko and Sunyaev 1976; Ghosh and Lamb 1979). The flux surface that closes at $R_{\rm a}$ is related to the flux surface at the stellar equator, $\psi_* = \psi(R_*, \pi/2)$, by $\psi_{\rm a} = \psi_* R_*/R_{\rm a}$, for a dipole. We do not model the mechanism by which plasma enters the magnetosphere (e.g. Rayleigh-Taylor and Kelvin-Helmholtz instabilities at $R \approx R_{\rm a}$), which sets the form of $dM/d\psi$ in reality, as this is an unsolved problem (Arons et al. 1984; Basko and Sunyaev 1976). Instead, we assume that the accreted mass is distributed nearly uniformly within the polar flux tube $0 \le \psi \le \psi_{\rm a}$, and that leakage onto flux surfaces $\psi_{\rm a} \le \psi \le \psi_*$ is minimal. A step change in $dM/d\psi$ at $\psi_{\rm a}$ leads to numerical problems, so we approximate the mass distribution over one hemisphere by $M(\psi) = M_{\rm a}(1-e^{-\psi/\psi_{\rm a}})/2(1-e^{-\psi_*/\psi_{\rm a}})$. We have checked that the solution of (2.12) and (2.14) is not sensitive to

the exact functional form of $dM/d\psi$. Finally, we assume that the accreted material does not transport any magnetic flux, e.g. from the accretion disc (cf. Uchida and Low 1981). If the magnetic dipole moment is less than $\approx 10^{26}$ G cm^3, we have $\psi_{\rm a} \approx \psi_*$ (Cheng and Zhang 1998) and the above functional form of $M(\psi)$ is inadequate. This occurs at the latest stages of accretion ($M_{\rm a} > 0.1 M_\odot$), outside the regime modelled in this chapter.

2.2.3 Initial and boundary conditions

In this chapter, we investigate the distortion of an initially dipolar magnetic field,

$$\psi_{\rm i}(r,\theta) = \psi_* R_* r^{-1} \sin^2\theta, \tag{2.16}$$

with $\psi_* = B_* R_*^2/2$, where B_* is the polar magnetic field before accretion. Given $dM/d\psi$ as a function of $M_{\rm a}$, we solve (2.12) and (2.14) subject to the Dirichlet boundary conditions

$$\psi(R_*,\theta) = \psi_* \sin^2\theta \quad \text{and} \quad \lim_{r\to\infty} \psi(r,\theta) = 0. \tag{2.17}$$

At the surface, i.e. the crystalline layers of density $\lesssim 4\times10^{11}$ g cm^{-3}, the field is dipolar. Far from the star, one has $\psi \propto r^{-1}$, as for any localised, static current distribution. The approximation that the surface field remains dipolar at all times is valid provided that $M_{\rm a}$ is small compared to M_*, for then the footpoints of the magnetic field lines are anchored to the highly conducting, high-inertia interior of the star. The surface field may be generated deep in the neutron star core or by a dynamo in the inner crust (Konenkov and Geppert 2001; Thompson and Duncan 1993). This line-tying boundary condition is a feature of models of magnetic loops in the solar corona (Low 1980; Zweibel and Hundhausen 1982) and earlier work on neutron star accretion (Brown and Bildsten 1998; Hameury et al. 1983; Litwin et al. 2001; Uchida and Low 1981). A drawback of preventing the accreted matter from sinking is that unrealistically high densities ($\geq 4\times10^{11}$ g cm^{-3}) are produced locally, at the base of the column, for $M_{\rm a} > 10^{-8} M_\odot$. Recent modelling of the magnetic field beneath the surface of an accreting neutron star, based on (2.3) with a velocity distribution for the fluid assumed, illustrates the effects of submergence and subsequent incorporation of accreted matter into the crust (Choudhuri and Konar 2002). Cumming

(2002) discusses a *vacuum* (like in this chapter) and a *screened* boundary condition at the surface.

In the numerical calculations presented in section 2.4, two extra grid-related boundaries are introduced: the outer radius of the grid, at $r = R_{\rm m}$, and the lines $\theta = 0$ and $\theta = \pm\pi/2$, arising when the grid is restricted to one quadrant or hemisphere. We choose $R_{\rm m}$ large enough to include the layer where the accretion-induced screening currents lie, i.e., above the greater of the hydrostatic ($c_{\rm s}^2/g$) and Alfvén ($|\mathbf{B}|/|\nabla\mathbf{B}|$) scale heights. In practice, this is achieved by increasing $R_{\rm m}$ until the dipole moment of the solution varies by less than 0.1%. At $r = R_{\rm m}$, the magnetic field is taken to be radial, with $\partial\psi/\partial r(R_{\rm m},\theta) = 0$, i.e. a free boundary. (It is outside the scope of this chapter to model the disc-magnetosphere interface in detail; (see Rastätter and Schindler 1999). Another possible way to treat the boundary condition at $r = R_{\rm m}$ is to set $\psi(R_{\rm m},\theta) = \psi_{\rm m}\sin^2\theta$ and adjust $\psi_{\rm m}$ iteratively to give the self-consistent dipole moment of the solution, but we encountered numerical difficulties with this approach.

There are two physically plausible choices for the polar and equatorial boundary conditions: (i) $\psi(r,\pi) = 0$ and $\partial\psi/\partial\theta(r,\pi/2) = 0$, as for the initial dipole, or (ii) $\partial\psi/\partial\theta(r,\pm\pi/2) = 0$, north-south symmetry. We mostly adopt (i) but explore (ii) for completeness in section 2.4.6, where it is shown that field lines on either side of the pole are peeled away, leaving the $\psi = 0$ line isolated, without affecting the dipole moment significantly. Strictly speaking, the conditions $\partial\psi/\partial\theta(r,\pi/2) = 0$ and $\partial\psi/\partial r(R_{\rm m},\pi/2) = 0$ force the magnetic field to vanish artificially at $(R_{\rm m},\pi/2)$, but $|\boldsymbol{\mu}|$ is affected by less than 0.1% (see section 2.4).

2.3 Solution methods

In this section, we discuss three ways to solve (2.12) and (2.14): analytically by Green functions (section 2.3.1), analytically in the small-$M_{\rm a}$ approximation (section 2.3.2), and numerically, by an iterative algorithm due to Mouschovias (1974) (sections 2.3.3 and 2.3.4).

2.3.1 Green functions

The Grad-Shafranov boundary value problem (2.12),

$$\Delta^2\psi(r,\theta) = Q(r,\theta), \tag{2.18}$$

with

$$\psi(R_*,\theta) = \psi_* \sin^2\theta \quad \text{and} \quad \lim_{r\to\infty}\psi(r,\theta) = 0, \tag{2.19}$$

can be solved analytically by Green functions if the source term $Q(r,\theta)$ is known as a function of r and θ. In principle, $Q(r,\theta)$ is given by (2.12) and (2.14); in practice, it is not known analytically. With ψ specified on the boundary S of the volume V, we can write (see section 2.7.1)

$$\begin{aligned}\psi(\mathbf{x}) = &\int_V d^3\mathbf{x}'\, G^* Q \\ &+ \int_S d^2\mathbf{x}'\,(\psi\nabla G^* - G^*\nabla\psi + \mathbf{b}\psi G^*),\end{aligned} \tag{2.20}$$

where G and G^* are Green functions for $L = 4\pi r^2 \sin^2\theta\,\Delta^2$ and its adjoint L^*, satisfying

$$\frac{\partial^2 G}{\partial r^2} + \frac{(1-\mu^2)}{r^2}\frac{\partial^2 G}{\partial \mu^2} = \frac{1}{r^2}\delta(r-r')\delta(\mu-\mu') \ , \tag{2.21}$$

and

$$\begin{aligned}\frac{\partial^2 G^*}{\partial r^2} + \frac{(1-\mu^2)}{r^2}\frac{\partial^2 G^*}{\partial \mu^2} + \frac{4}{r}\frac{\partial G^*}{\partial r} - \frac{4\mu}{r^2}\frac{\partial G^*}{\partial \mu} \\ = \frac{1}{r^2}\delta(r-r')\delta(\mu-\mu') \ ,\end{aligned} \tag{2.22}$$

with $\mu = \cos\theta$ and $\mathbf{b} = -2r^{-1}(\hat{\mathbf{e}}_r + \cot\theta\,\hat{\mathbf{e}}_\theta)$. Upon solving (2.21) and (2.22), we obtain

$$\begin{aligned}G(r,\mu,r',\mu') = &\sum_{\ell=0}^{\infty} N_\ell^{-1} g_{\ell+1}(r,r') \\ &\times (1-\mu^2) C_\ell^{3/2}(\mu') C_\ell^{3/2}(\mu) \ ,\end{aligned} \tag{2.23}$$

and

$$G^*(r,\mu,r',\mu') = \sum_{\ell=0}^{\infty} N_\ell^{-1} g_\ell^*(r,r') \times (1-\mu'^2) C_\ell^{3/2}(\mu') C_\ell^{3/2}(\mu) \ , \tag{2.24}$$

with

$$g_\ell(r,r') = \frac{1}{(2\ell+1)r'^2} \frac{r_<^{\ell+1}}{r_>^{\ell}} \left[\left(\frac{R_*}{r_<} \right)^{2\ell+1} - 1 \right], \tag{2.25}$$

$r_< = \min(r,r')$, $r_> = \max(r,r')$,

$$g_\ell^*(r,r') = \left(\frac{r'}{r} \right)^2 g_{\ell+1}(r,r'), \tag{2.26}$$

$$N_\ell = 2(\ell+1)(\ell+2)(2\ell+3)^{-1} \ , \tag{2.27}$$

and hence, from (2.20), we arrive at the complete solution

$$\psi(r,\mu) = \frac{\psi_* R_* (1-\mu^2)}{r} + (1-\mu^2) \sum_{\ell=0}^{\infty} N_\ell^{-1} C_\ell^{3/2}(\mu) \times \int_{-1}^{1} d\mu' \int_{R_*}^{\infty} dr' r'^2 g_\ell^*(r',r) C_\ell^{3/2}(\mu') Q(r',\mu'). \tag{2.28}$$

$C_\ell^{3/2}(\mu)$ denotes a Gegenbauer polynomial of order ℓ (see section 2.7).

2.3.2 Analytic approximation for small M_a

In the limit of small M_a, where $dM/d\psi$ and hence $Q(r,\theta)$ are small, one can show (see section 2.7.3) that the magnetic flux distribution reduces to

$$\psi(r,\theta) = \psi_\mathrm{i}(r,\theta)(1 - b^2 M_\mathrm{a}/M_\mathrm{c}) \tag{2.29}$$

far from the star ($r \to \infty$), with

$$M_\mathrm{c} = 2\pi G M_* \psi_*^2 / 4\pi c_\mathrm{s}^4 R_*^2 \tag{2.30}$$

For convenience, we write this using CGS units

$$\frac{M_\mathrm{c}}{M_\odot} = 1.2 \times 10^{-4} \left(\frac{c_\mathrm{s}}{10^8 \,\mathrm{cm\,s^{-1}}} \right)^{-4} \left(\frac{B_*}{10^{12}\mathrm{G}} \right)^2 . \tag{2.31}$$

where $M_* = 1.4M_\odot$ and $R_* = 10^6$cm.

It follows that the magnetic dipole moment scales as $|\boldsymbol{\mu}| = |\boldsymbol{\mu}_\mathrm{i}|(1 - M_\mathrm{a}/M_\mathrm{c})$. This scaling agrees, in the small-M_a limit, with empirical scalings of the form $|\boldsymbol{\mu}| = |\boldsymbol{\mu}_\mathrm{i}|(1 + M_\mathrm{a}/M_\mathrm{c})^{-1}$, with $M_\mathrm{c} \approx 10^{-5}M_\odot$, that have been proposed in the literature (Cheng and Zhang 1998; Shibazaki et al. 1989).

2.3.3 Iterative numerical scheme

To solve (2.12) and (2.14) self-consistently for $\psi(r,\theta)$ for $M_\mathrm{a} \gg M_\mathrm{c}$, we employ an iterative numerical algorithm similar to the one introduced by Mouschovias (1974) to study the Parker instability of the Galactic magnetic field. The algorithm and its performance are discussed in detail in Appendices 2.7 and 2.8 and summarized briefly here.

Given $dM/d\psi$ and an initial guess $\psi^{(0)}(r,\theta)$, we calculate the locations of N_c contours of ψ, spaced either linearly or logarithmically in ψ, capturing topologically disconnected contours and closed loops (Snyder 1978). We then compute $F[\psi^{(0)}]$ from (2.14) and hence $F'[\psi^{(0)}]$ after polynomial fitting (simple differencing causes numerical difficulties; see section 2.8.3). The Poisson equation (2.12) is solved with this source term using successive overrelaxation to obtain $\psi^{(0)}_\mathrm{new}(r,\theta)$, and the next iterate is obtained by underrelaxation: $\psi^{(n+1)} = \Theta^{(n)}\psi^{(n)} + [1 - \Theta^{(n)}]\psi^{(n)}_\mathrm{new}$, with $0 \leq \Theta^{(n)} \leq 1$. Iteration continues until the convergence criterion $|\psi^{(n+1)}_\mathrm{new} - \psi^{(n)}| < \epsilon|\psi^{(n+1)}_\mathrm{new}|$ is satisfied on average across the grid. We usually take $\epsilon = 10^{-2}$ in this chapter. Physically, the algorithm starts from a trial magnetic field (and associated current distribution), the accreted mass M_a is distributed among the flux tubes according to $dM/d\psi$, mass is allowed to slide up or down flux tubes to achieve hydrostatic equilibrium along $\mathbf{B}$, a new current distribution is computed that balances forces perpendicular to $\mathbf{B}$, and the process is repeated.

2.3.4 Numerical convergence

There is no general rule for choosing $\Theta^{(n)}$. We find, by experimentation, that one must decrease $1 - \Theta^{(n)}$ as M_a increases; a useful rule of thumb is $1 - \Theta^{(n)} \approx (M_\mathrm{a}/10^{-7}M_\odot)^{-1}(\psi_*/10\psi_\mathrm{a})^{-2}$, for $M_\mathrm{a} \geq 10^{-7}M_\odot$. More details can be found in Table 2.8.4 and section 2.8.4. At least $2/[(1 - \Theta)\log_{10}(\epsilon)]$ iterations are required for convergence; bootstrapping is recommended, i.e.

using the equilibrium solution for a lower value of $M_{\rm a}$ as the first iterate instead of the dipole. We show in section 2.8.5, that the error in ψ averaged over the grid, scales as $G^{-1.6}$, where G is the number of grid cells in each dimension.. The optimum number of contours is $N_c \approx G-1$; $F'(\psi)$ becomes jagged for $N_c \gg G$ due to grid crossings, (as demonstrated in Figure 2.13). To concentrate maximum grid resolution near the stellar surface and at the edge of the polar cap ($\psi = \psi_{\rm a}$), where screening currents predominantly reside and gradients of ρ and ψ are steepest, we scale the r and θ coordinates logarithmically as described in section 2.8.1.

Figure 2.1 displays the mean residual as a function of iteration number. Convergence is rapid for $M_{\rm a} \leq 10^{-6} M_\odot$ and poor for $M_{\rm a} \geq 10^{-4} M_\odot$. Large fluctuations in the mean residual are mainly due to the polynomial fit to $F(\psi)$ and the appearance of magnetic bubbles (see section 2.4.7).

2.4 Equatorward hydromagnetic spreading

In this section, we present the results of the analytic and numerical calculations described in section 2.3. The hydromagnetic structure of the polar 'mountain' formed by the accreted material is described in sections 2.4.1 and 2.4.3 and compared with previous calculations in which $F(\psi)$ is arbitrary (e.g. Brown and Bildsten 1998). The physics of equatorward spreading of the accreted material and the formation of an equatorial magnetic 'tutu', including a criterion for the onset of spreading, is discussed in section 2.4.4. The scalings of $|\boldsymbol{\mu}|$ with respect to $M_{\rm a}$ and $b = \psi_*/\psi_{\rm a}$ are derived analytically and numerically in sections 2.4.5 and 2.4.6. Finally, the formation of magnetic bubbles disconnected from the star — a new effect — is explored in section 2.4.7. We start from the undisturbed dipole (2.16) and adopt the following physical parameters: $M_* = 1.4 M_\odot$, $R_* = 10^6$ cm, $B_* = 10^{12}$ G (Hartman et al. 1997), $c_{\rm s} = 10^8$ cm s^{-1}, $x_0 = c_{\rm s}^2 R_*^2/GM_* = 54$ cm and hence $a = R_*/x_0 = 1.86 \times 10^4$ (Brown and Bildsten 1998). The results are mostly presented in rectangular (r, θ) plots scaled logarithmically where appropriate to emphasize the boundary layer of compressed magnetic field.

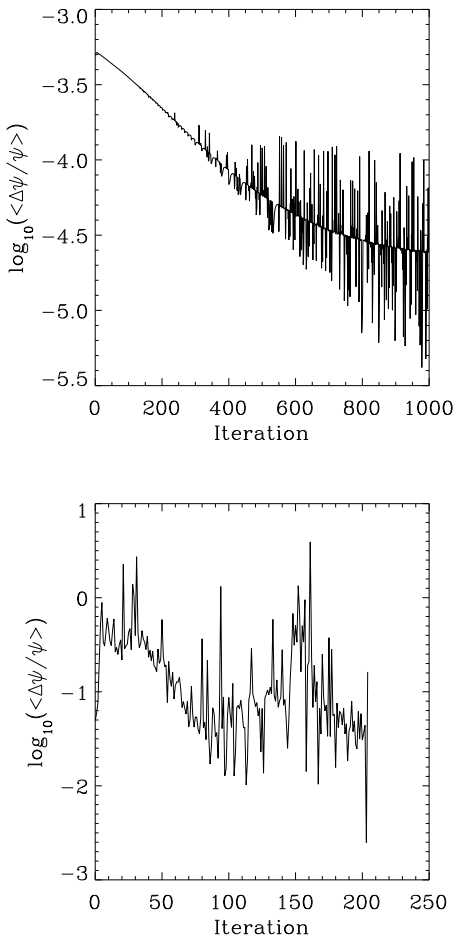

Figure 2.1: Mean residual versus iteration number. $M_{\rm a} = 10^{-6} M_\odot$, $\theta = 0.995$ (*top*). $M_{\rm a} = 10^{-5} M_\odot$, $\theta = 0.95$ (*bottom*).

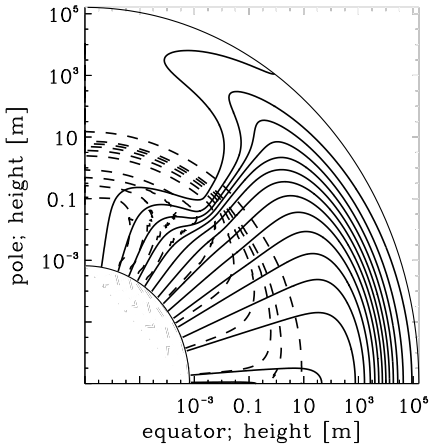

Figure 2.2: Polar plot of equilibrium magnetic field lines (solid curves) and density contours (dashed curves) for $M_{\rm a} = 10^{-5} M_\odot$. The coordinates measure altitude above the stellar surface. Density contours are drawn for $\eta\rho_{\rm max}$ (maximum at the pole and decreasing monotonically outwards, $\rho_{\rm max} = 2.52 \times 10^{14} {\rm g\,cm^{-3}}$) with $\eta =$ 0.8, 0.6, 0.4, 0.2, 0.01, 0.001, 10^{-4}, 10^{-5}, 10^{-6}, 10^{-12}.

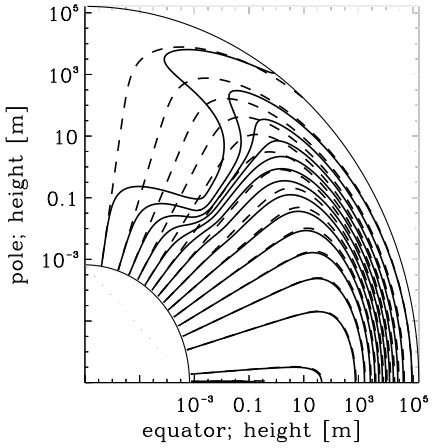

Figure 2.3: Polar plot of magnetic field lines after accretion (solid curves) and before accretion (dashed curves) for $M_{\rm a} = 10^{-5} M_\odot$. The coordinates measure altitude above the stellar surface.

2.4.1 Structure of the polar mountain and equatorial magnetic tutu

During the early stages of accretion, matter piles up on the polar cap, confined by the tension of the polar magnetic flux tube. However, for $M_{\rm a} \gtrsim 10^{-5} M_\odot$, the hydrostatic pressure at the base of the accretion column overcomes the magnetic tension and matter spreads over the stellar surface towards the equator, dragging along frozen-in polar field lines. The spreading distorts $\mathbf{B}$, generating screening currents $(4\pi)^{-1}\nabla \times \mathbf{B}$, which act to decrease the magnetic dipole moment ($|\boldsymbol{\mu}|$ is dominated by the polar field). In its turn, the spreading is also counteracted by the tension of the magnetic field lines compressed towards the equator. These equatorial stresses, neglected in previous work (Brown and Bildsten 1998; Hameury et al. 1983; Litwin et al. 2001), greatly increase the $M_{\rm a}$ required to reduce $|\boldsymbol{\mu}|$.

Figure 2.2 shows the magnetic field configuration and density profile for $M_{\rm a} = 10^{-5} M_\odot$ in cross-section (cf. schematic version in Figure 1 of Melatos and Phinney 2001). The 'polar mountain' of accreted material is readily apparent, traced out by the dashed contours. Figure 2.3 shows the distorted magnetic field configuration overlaid on the field lines of the undisturbed dipole. The distorted field exhibits a pinched, flaring geometry, termed an 'equatorial tutu' by Melatos and Phinney (2001). A more complete view of the overall hydromagnetic structure can be gained from Figure 2.4. The tutu-like field is shown again in Figures 2.4(a) and 2.4(b), while the polar mountain (ρ) is shown in Figure 2.4(c). In Figure 2.4(d), where the radius of curvature of $\mathbf{B}$ is smaller than the hydrostatic scale height x_0, the toroidal screening currents are confined below altitude x_0, and are concentrated near the polar cap. (Note that ohmic dissipation, neglected here, is important at these scales). The $\mathbf{J} \times \mathbf{B}$ force per unit volume [Figure 2.4(e)] balances the pressure gradient [Figure 2.4(f)], preventing the accreted material from spreading all the way to the equator.

The maximum density, attained at $(r, \theta) = (R_*, 0)$, is found empirically to be $\rho_{\rm max} = M_{\rm a} b^2/(2x_0^3 \pi a^2) \approx 6 \times 10^9 (b/10)^2 (M_{\rm a}/10^{-10} M_\odot)\,{\rm g\,cm^{-3}}$, in accord with analytic estimates for $\rho(r,\theta) \approx \rho_{\rm max} \exp(-x/x_0) \exp(-\psi/\psi_{\rm a})$ carried out in section 2.7. Consequently, $\rho_{\rm max}$ exceeds the neutron drip density $4 \times 10^{11}\,{\rm g\,cm^{-3}}$ for $M_{\rm a} \geq 10^{-8} M_\odot$. In reality, this overdensity is

moderated by sinking (Brown and Bildsten 1998; Choudhuri and Konar 2002), which is prevented by the hard surface in our calculation. (We can alleviate the overdensity in our model by relaxing the isothermal assumption or allowing a nonbarometric density distribution along contours.) For $M_{\rm a} \geq 10^{-6} M_\odot$, the maximum magnetic field strength becomes unrealistically large ($B_{\rm max} \gtrsim 10^{15}$ G) below an altitude x_0, in response to $\rho_{\rm max}$. Such field strengths formally exceed the yield stress of the crust (Romani 1990).

2.4.2 Sinking

The proportion of the accreted material that sinks is not well constrained. We consider a crude model of sinking in which a proportion s of the accreted matter sinks, leaving a proportion $(1-s)$ to spread. This is modelled by setting

$$dM/d\psi = (M_{\rm a}/\psi_{\rm a})[(1-s)e^{-\psi/\psi_{\rm a}}/2(1-e^{-\psi_*}) + s/(2b)]\,. \qquad (2.32)$$

We find that for $M_{\rm a} = 10^{-5} M_\odot$, for s = 0.9 (i.e. all but $10^{-6} M_\odot$ redistributed.), the resultant dipole moment increases from ≈ 0.91 to 0.96.

2.4.3 Self-consistent mass-flux distribution

In previous studies of neutron star accretion, $F(\psi)$ was chosen arbitrarily (Brown and Bildsten 1998; Hameury et al. 1983; Litwin et al. 2001; Melatos and Phinney 2001; Uchida and Low 1981). In this chapter, by contrast, we determine $F(\psi)$ self-consistently by solving (2.12) and (2.14) simultaneously for a physically plausible choice of $dM/d\psi$ that places most of the accreted material at the poles of the initial, undisturbed dipole. Figures 2.6(a) and 2.6(b) compare our self-consistent $F(\psi)$ against the functional forms guessed by previous authors for two values of $M_{\rm a}$. The differences are significant, especially near the pole ($\psi \approx 0$). [An analagous difference was discovered by Mouschovias (1974) when solving for the final states of the Parker instability in the Galaxy self-consistently, relative to the previous guess of Parker

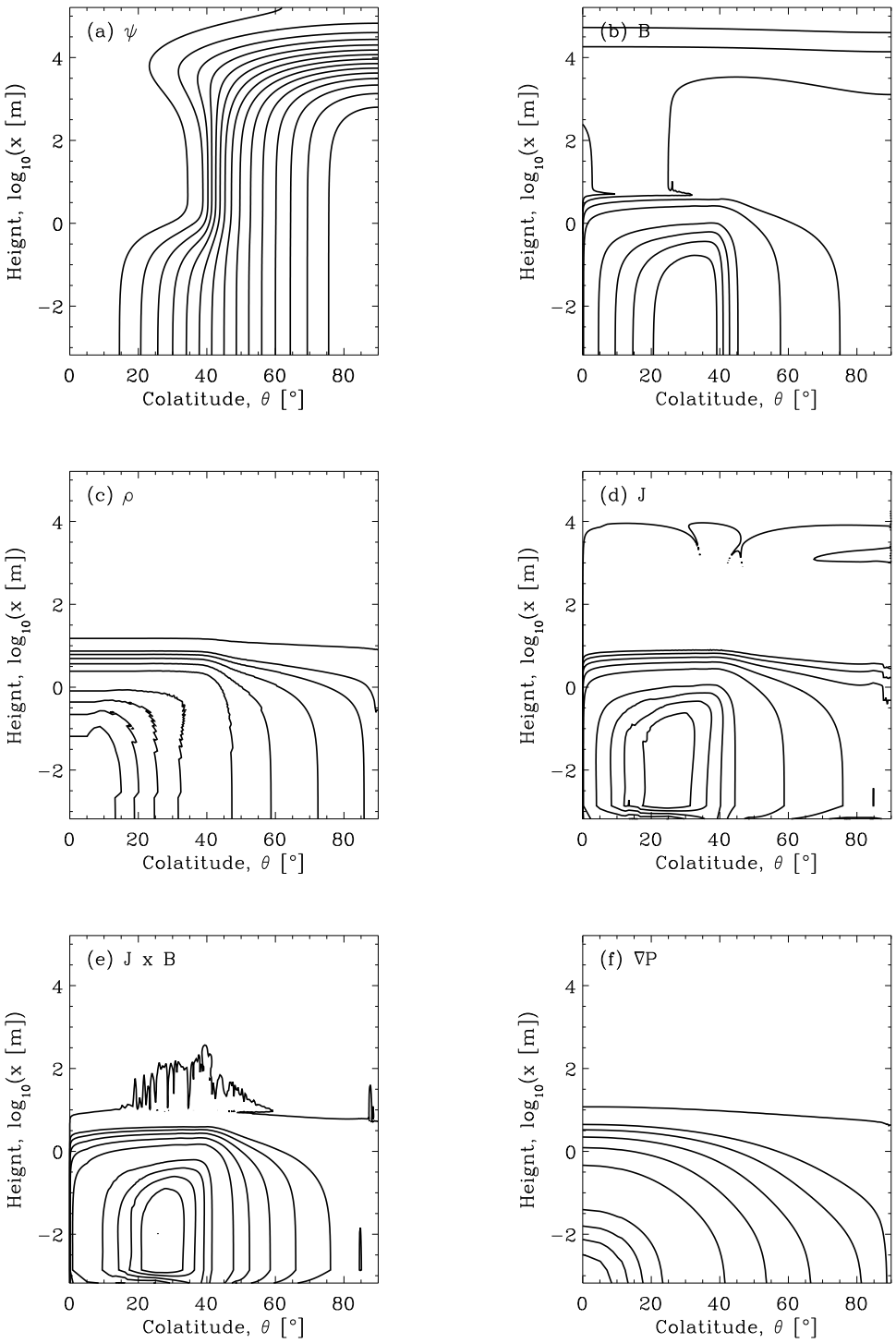

Figure 2.4: $M_a = 10^{-5} M_\odot$. (a) Magnetic field lines (ψ contours), (b) magnetic field strength ($|\mathbf{B}|$ contours), (c) density, (d) current, (e) Lorentz force, and (f) pressure gradients. For each quantity x, values ηx_{max} are plotted, with $\eta = 0.8$, 0.6, 0.4, 0.2, 0.01, 0.001, 10^{-4}, 10^{-5}, 10^{-6}, 10^{-12}. Maximum values are found to be $\rho_{max} = 1.7 \times 10^{14} \mathrm{g\,cm^{-3}}$, $|\mathbf{B}|_{max} = 3.9 \times 10^{15} \mathrm{G}$, $|\mathbf{J}|_{max} = 2.0 \times 10^{11} \mathrm{A\,cm^{-2}}$, $|\mathbf{J} \times \mathbf{B}|_{max} = 3.3 \times 10^{23} \mathrm{dyne\,cm^{-3}}$, $|\nabla P|_{max} = 1.9 \times 10^{27} \mathrm{dyne\,cm^{-3}}$.

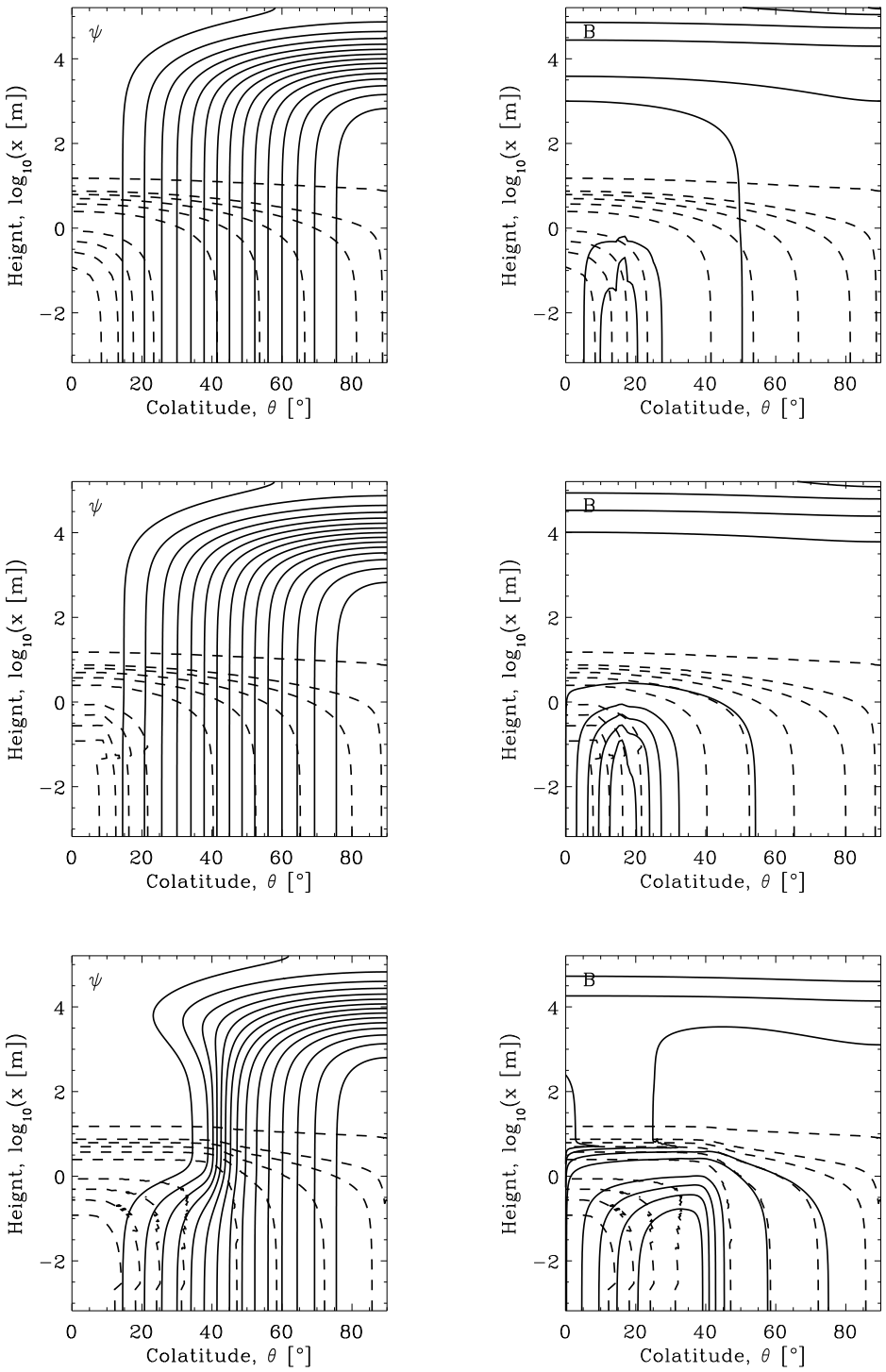

Figure 2.5: Magnetic configuration as a function of accreted mass. $M_{\rm a} = 10^{-9} M_\odot$, $\rho_{\rm max} = 4.2 \times 10^{10} {\rm g\,cm^{-3}}$, $|\mathbf{B}|_{\rm max} = 3.5 \times 10^{12}$G (*top*); $M_{\rm a} = 10^{-7} M_\odot$, $\rho_{\rm max} = 4.2 \times 10^{12} {\rm g\,cm^{-3}}$, $|\mathbf{B}|_{\rm max} = 1.1 \times 10^{14}$G (*middle*); and $M_{\rm a} = 10^{-5} M_\odot$, $\rho_{\rm max} = 1.7 \times 10^{14} {\rm g\,cm^{-3}}$, $|\mathbf{B}|_{\rm max} = 3.9 \times 10^{15}$G (*bottom*). Displayed are contours of ψ (*left, solid*), $|\mathbf{B}|$ (*right, solid*) and ρ (*left and right, dashed*). with values $\eta\rho_{\rm max}$ and $\eta|\mathbf{B}|_{\rm max}$, where $\eta = 0.8,\ 0.6,\ 0.4,\ 0.2,\ 0.01,\ 0.001,\ 10^{-4},\ 10^{-5},\ 10^{-6},\ 10^{-12}$.

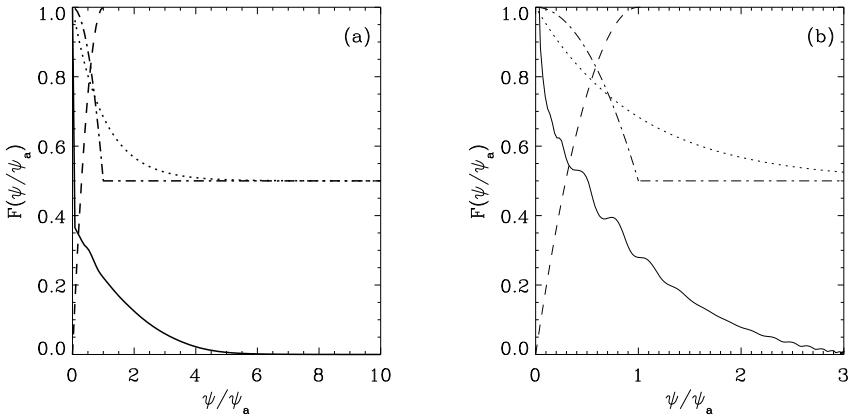

Figure 2.6: Comparison of the self-consistent $F(\psi)$ (*solid*) for (a) $M_{\rm a} = 2 \times 10^{-5} M_\odot, b = 10$ and (b) $M_{\rm a} = 1.5 \times 10^{-4} M_\odot, b = 3$ with others in the literature: Brown and Bildsten (1998) (*dotted*) Litwin et al. (2001) (*dot-dashed*), and Melatos and Phinney (2001) (*dashed*). These curves are scaled to the value at the pole, $F(0)$.

(1966).] A polynomial fit in the numerical code yields the approximate form

$$F(\tilde{\psi}) = \exp(\tilde{\psi})(0.027\tilde{\psi}^4 - 0.13\tilde{\psi}^3 + 0.21\tilde{\psi}^2 - 0.021\tilde{\psi} + 0.1333) \tag{2.33}$$

for $N_p = 4, M_{\rm a} = 1.5 \times 10^{-4} M_\odot, b = 3$, $\tilde{\psi} = \psi/\psi_{\rm a}$, and the choice of $dM/d\psi$ in section 2.2.2.

2.4.4 Onset of spreading

Brown and Bildsten (1998) showed that, for an initially vertical field and neglecting the stress from compressed equatorial flux, the condition for spreading is given by $\alpha = B^2/8\pi p \leq x_0/R_{\rm cap} \approx 0.01$, where $R_{\rm cap} = (R_*^3/R_{\rm a})^{1/2}$ is the polar cap radius. Given that $\alpha_{\rm min} = B_*^2/(8\pi p_{\rm max}) \approx 0.27(B_*/10^{12}\,{\rm G})^2(M_{\rm a}/10^{-12} M_\odot)^{-1}$, it follows that the accreted matter distorts the magnetic field negligibly for $M_{\rm a} \lesssim 3.7 \times 10^{-9} M_\odot$ (i.e. $\alpha_{\rm min} \gtrsim$

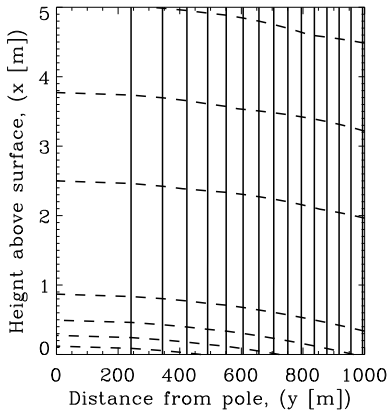

Figure 2.7: Magnetic field lines (*solid*) and density contours (*dashed*) around the polar cap for $M_{\rm a} = 10^{-13} M_\odot$ and $b = 100$; the parameters used in Figure 2 of Litwin et al. (2001).

0.01). Above this value, progressively more distortion takes place for $M_{\rm a} = 10^{-9}, 10^{-7}, 10^{-5} M_\odot$, as shown in Figure 2.5. The curved field lines have a large tangential component, previously negligible, which increases the magnetic field strength —**B**— substantially for $M_{\rm a} \gtrsim M_{\rm c}/a = 8 \times 10^{-11} M_\odot$, as predicted by the the Green function analysis in section 2.7.3. This induced magnetic pressure balances the overpressure of the accreted material. However, the effect on the magnetic dipole moment is negligible ($< 1\%$) due to countervailing magnetic stresses from the compressed field at the equator; the magnetic radius of curvature is less than x_0 until $M_{\rm a}$ exceeds $\approx 1.4 \times 10^{-6} M_\odot$, as proved in section 2.7.3. Note that the compression of field lines as $|\mathbf{B}|$ increases is imperceptible in Figure 2.5 because of the extent of the horizontal axis; $|\mathbf{B}|$ increases predominantly due to the B_θ component. The top of the boundary layer is roughly where B_θ vanishes, i.e. at an altitude $x = x_0 \ln[(a+1)/(1 - M_{\rm c}/M_{\rm a})] \approx 5.3 \times 10^2$ cm. for $M_{\rm a} < M_{\rm c}$.

We zoom in on the pole to compare with Litwin et al. (2001) in Figure 2.7. Our results differ because Litwin et al. (2001) has a free boundary at the polar cap edge and ignores the θ terms in the Grad-Shafranov equation, while we impose north-south symmetry at the equator, with no condition at the polar cap edge. This allows the compressed magnetic field equatorward of the polar cap to push back on the polar flux tube. Furthermore, we prescribe $dM/d\psi$ and calculate $F(\psi)$ instead of prescribing $F(\psi)$. We

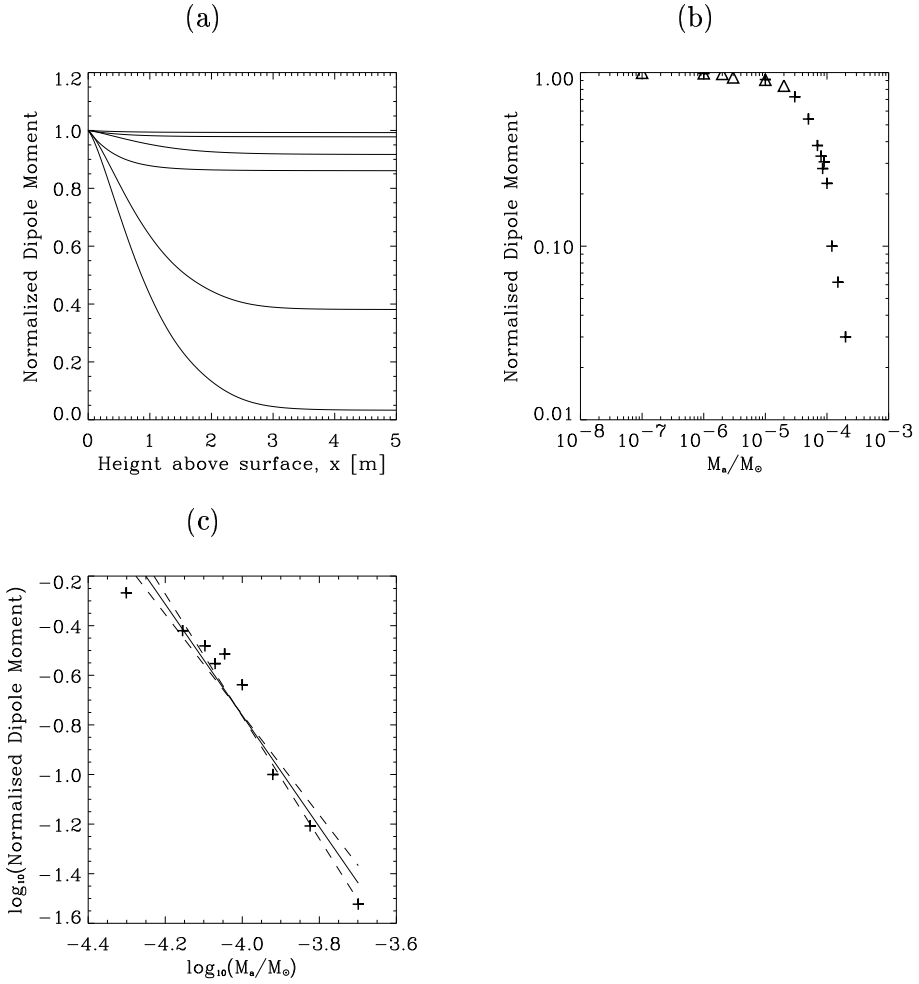

Figure 2.8: (a) Dipole moment $|\boldsymbol{\mu}|$ as a function of altitude $x = r - R_*$, normalised to $|\boldsymbol{\mu}|$ at $r = R_*$, for $M_\mathrm{a}/M_\odot = 10^{-6}$ (*top*), 3×10^{-6}, 10^{-5}, 3×10^{-5}, 10^{-4}, 3×10^{-4} (*bottom*). (b) Dipole moment $|\boldsymbol{\mu}|$ as a function of accreted mass M_a, normalized to the dipole moment $|\boldsymbol{\mu}_\mathrm{i}|$ before accretion, for $b = 3$ (*crosses*) and $b = 10$ (*triangles*). (c) Power law fit (*solid*), with 1σ errors (*dashed*), to dipole moment as a function of M_a for $M_\mathrm{a} > 2 \times 10^{-5} M_\odot$.

observe curvature comparable to Litwin et al. (2001) for $M_{\rm a} \approx 10^{-8} M_\odot$ and thus the ballooning instability may be relevant, but a detailed calculation is beyond the scope of this chapter.

An order of magnitude estimate of $M_{\rm c}$, the mass required to buckle the magnetic field, can be obtained in the following way. The hydrostatic pressure at the base of the accreted column is given by $p_{\rm max} = c_{\rm s}^2 \rho_{\rm max} = c_{\rm s}^2 M_{\rm a} b^2/(2\pi R_*^2 x_0)$, i.e. the weight per unit area of the mass $M_{\rm a}$ spread over approximately two hemispheres. This pressure is balanced by the tension of the magnetic field compressed into a layer of width $L \approx 6 \times 10^2$ cm along the surface and at the equator (see Figure 2.2). In the layer, we have $B_1 \approx B_* R_*/L \approx 10^{12}$ T by flux conservation. Hence the hydrostatic and magnetic pressures balance for $M_{\rm a} = B_*^2 R_*^4 x_0/(2\pi c_{\rm s}^2 L^2) \approx 2 \times 10^{-6} M_\odot$ in accord with the numerical results.

2.4.5 Reduction of the magnetic dipole moment

The magnetic dipole moment

$$|\boldsymbol{\mu}| = \frac{3r^3}{4} \int_{-1}^{1} d(\cos\theta)\, \cos\theta B_r(r,\theta) \tag{2.34}$$

is plotted as a function of r in Figure 2.8(a). The screening currents are confined to a thin layer above the stellar surface; $|\boldsymbol{\mu}|$ is essentially constant with r above this layer. The layer is compressed as $M_{\rm a}$ increases, with half-width comparable to x_0 for $M_{\rm a} \approx 10^{-4} M_\odot$. The asymptotic value of $|\boldsymbol{\mu}|$ also decreases as $M_{\rm a}$ increases, as expected; equatorward hydromagnetic spreading drags magnetic flux away from the pole, and $|\boldsymbol{\mu}|$ is sensitive to B_r near the pole through (2.34).

Figure 2.8(b) is a plot of $|\boldsymbol{\mu}|$ versus $M_{\rm a}$. For $M_{\rm a} \lesssim M_{\rm c} = 1.2 \times 10^{-6} M_\odot$, $|\boldsymbol{\mu}|$ decreases proportional to $(1 - M_{\rm a}/M_{\rm c})$, as predicted analytically in section 2.3.2. For $M_{\rm a} \gtrsim M_{\rm c}$, we obtain the empirical relation

$$|\boldsymbol{\mu}|/|\boldsymbol{\mu}_{\rm i}| = (M_{\rm a}/4.6 \times 10^{-5} M_\odot)^{-2.25 \pm 0.22} \tag{2.35}$$

by fitting a power law to the numerical results for $M_{\rm a} \geq 5 \times 10^{-5} M_\odot$, as in Figure 2.8(c). However, (2.35) cannot be extrapolated reliably to the regime $M_{\rm a} \gtrsim 10^{-4} M_\odot$ for two reasons. First, our numerical scheme is limited by the steepness of gradients in the source term of (2.12). Physically, these

scale as the hydrostatic pressure, with $dF/d\psi \propto M_{\rm a} b$ as shown in section 2.7. We encounter convergence errors above 50% for $M_{\rm a} b \gtrsim 3 \times 10^{-4} M_\odot$. Second, it is shown in section 2.4.7 that magnetic bubbles, disconnected from the stellar surface, are created for $M_{\rm a} b \gtrsim 10^{-4} M_\odot$, leading to the steep dependence of $|\boldsymbol{\mu}|$ on $M_{\rm a}$ in (2.35). A word of caution: when bubbles appear, it is unclear how to interpret $|\boldsymbol{\mu}| = |\boldsymbol{\mu}|_{\rm star} + |\boldsymbol{\mu}|_{\rm bubble}$. In reality, one has $|\boldsymbol{\mu}|_{\rm bubble} = 0$ as $r \to \infty$, because the flux surfaces of the bubble are closed. However, at $r = R_{\rm m}$, the ingoing and outgoing flux tubes of the bubble do not cancel perfectly and one finds $|\boldsymbol{\mu}|_{\rm bubble} \neq 0$; bubble-related currents outside the solution domain ($r > R_{\rm m}$), need to be included in order to recover $|\boldsymbol{\mu}|_{\rm bubble} = 0$.

2.4.6 Polar cap radius

We now discuss the effect on $|\boldsymbol{\mu}|$ of varying $b = \psi_{\rm a}/\psi_*$, or equivalently the polar cap radius $R_{\rm cap} = R_* \sin^{-1}(b^{-1/2})$. Although $R_{\rm cap}$ is not known exactly without a detailed model of the flow of matter from the accretion disc to the stellar surface (Arons et al. 1984), estimates of its size from (2.15) are typically of order 1 km (Litwin et al. 2001), i.e. $b \geq 100$, for $B_* = 10^8$ T (Arons et al. 1984). Figure 2.9 illustrates the magnetic configuration obtained for $b = 3$ and $b = 10$, and $|\boldsymbol{\mu}|/|\boldsymbol{\mu}_{\rm i}|$ is plotted versus $M_{\rm a}$ in Figure 2.8(b), denoting $b = 3$ by crosses and $b = 10$ by triangles. Note how the equilibrium state changes with b. The mass-flux distribution $dM/d\psi \propto \exp(-\psi/\psi_{\rm a})$ implies a surface pressure distribution $F(\psi) \propto b \exp(-\psi/\psi_{\rm a})$, so larger b means steeper pressure gradients. (Numerical difficulties set in for $b = 30$, which can be partly alleviated by stretching the coordinates around $\psi_{\rm a}$.) Importantly, however, we find $M_{\rm c}$ and the dipole moment $|\boldsymbol{\mu}|$ are independent of b. This is supported by the Green function analysis in section 2.7, except when $dM/d\psi$ depends explicitly on b, e.g. $dM/d\psi \propto b(1 - \psi/b\psi_{\rm a})^{1/2}$ implies $|\boldsymbol{\mu}| \propto b^{-1}$.

A related issue is whether $|\boldsymbol{\mu}|$ is affected in an unrealistic way by the boundary condition $\psi = 0$ at $\theta = 0$ in the examples presented so far. It is conceivable, for example, that the $\psi = 0$ line is unstable ('on a knife edge'), while neighbouring field lines are peeled away by accretion, unless it is forced to remain rectilinear artificially. As it happens, however, this is not the case.

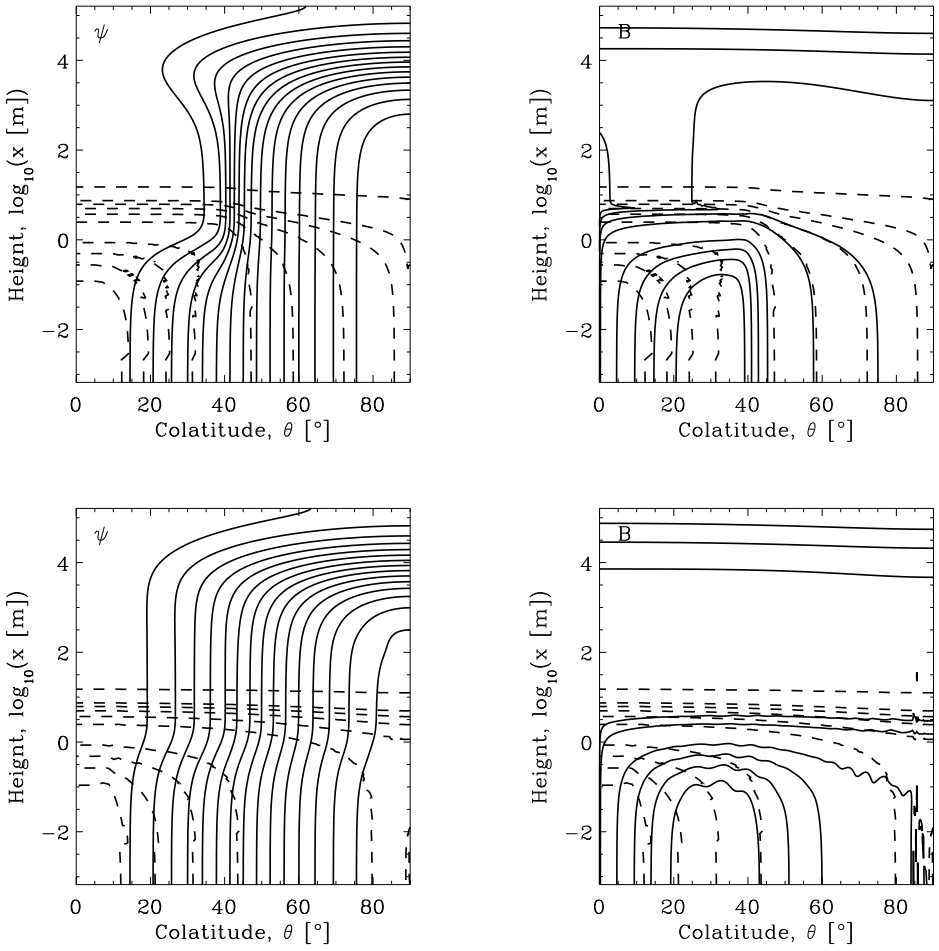

Figure 2.9: Hydromagnetic equilibria for $M_{\rm a} = 10^{-5} M_\odot$, with $b = 10$ (*top*) and $b = 3$ (*bottom*). Contours of constant ψ (*left*) and $|\mathbf{B}|$ (*right*) are displayed, with $|\mathbf{B}|_{\rm max} = 4.06 \times 10^{15}$G ($b = 10$) and 1.65×10^{15}G ($b = 3$). We find $|\boldsymbol{\mu}| \approx 0.9 |\boldsymbol{\mu}_{\rm i}|$ in both cases.

Figure 2.10 shows the output of an experiment where the grid extends from equator to equator ($|\theta| < \pi/2$), and no boundary condition is imposed at $\theta = 0$. Clearly, the magnetic field and density profiles remain symmetric about the magnetic pole, with $\psi = 0$ at $\theta = 0$ emerging naturally, while $|\boldsymbol{\mu}|$ is essentially unchanged.

2.4.7 Buoyant magnetic bubbles

From the sequence of panels in Figure 2.5 ($M_{\rm a}/M_\odot = 10^{-9}, 10^{-7}, 10^{-5}$), we observe that the magnetic field becomes increasingly distorted as $M_{\rm a}$ increases. Eventually, for $M_{\rm a} \gtrsim 10^{-5} M_\odot$, closed magnetic bubbles are created that are disconnected topologically from the surface of the star. This phenomenon is illustrated in Figure 2.11. At the value of $M_{\rm a}$ where a bubble is first created, a magnetic neutral point (Y point) is observed to form on a field line near, but not at the pole. The bubble closes at $r < R_{\rm m}$ in our simulation, but this may be a result of the approximate free boundary condition $\partial\psi/\partial\theta(R_{\rm m}, \theta) = 0$; in reality, it may connect to the accretion disc.

Bubbles correspond to a loss of equilibrium, analogous to that which occurs during eruptive solar phenomena (Klimchuk and Sturrock 1989), where no simply connected hydromagnetic equilibrium exists. In the Grad-Shafranov boundary problem, the source term $\propto F'(\psi)$ in (2.12) increases with $M_{\rm a} b$, boosting $\Delta^2\psi$ and hence ψ above the surface (to balance the weight of the added material through the Lorentz force). Above a critical value of $M_{\rm a}$, flux surfaces are created with $\psi < 0$ or $\psi > \psi_*$, which are disconnected from the star and either form closed loops or are anchored 'at infinity' (here the accretion disc). This is shown explicitly by (2.55) in the special case $F'(\psi) =$ constant. From our numerical results, we conclude that the critical $M_{\rm a}$ for bubble creation satisfies

$$M_{\rm a} \geq 10^{-4} b^{-1} M_\odot \,. \tag{2.36}$$

Note that bubble creation is a topological imperative. It is not the result of a hydromagnetic instability e.g. interchange or Rayleigh-Taylor (Bernstein et al. 1958; Mouschovias 1974; Parker 1966).

Are the bubbles merely numerical artefacts (Brown and Bildsten 1998)? No. Equation (2.55) demonstrates explicitly that flux surfaces with $\psi < 0$ or $\psi > \psi_*$ are created for $M_{\rm a}$ satisfying (2.36), at least for $F'(\psi) =$ constant.

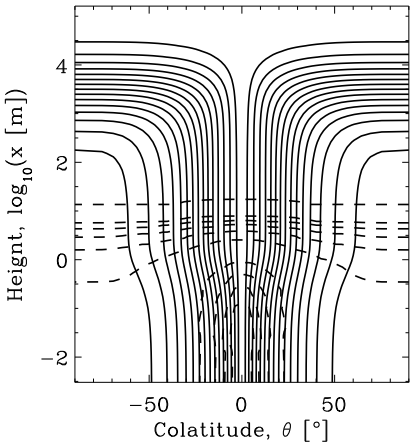

Figure 2.10: Equilibrium magnetic configuration in the northern hemisphere, showing contours of constant ψ (*solid*) and ρ (*dashed*). Equations (2.12) and (2.14) are solved in the domain $|\theta| \leq \pi/2$ here, compared to $0 \leq \theta \leq \pi/2$ in earlier figures, in order to test the validity of the $\psi = 0$ boundary condition at $\theta = 0$.

A more subtle issue is whether bubbles are the by-product of an artificial assumption in our idealized calculation. For example, if submergence of accreted material were permitted, it might reduce the pressure gradients that produce the bubbles; on the other hand, ohmic dissipation would facilitate detachment of bubbles in a pinched, Y-point configuration.

On some runs, bubbles appear and disappear during the iteration process. This happens because the mass-flux distribution is not conserved inside a bubble, although the code attempts to maintain flux freezing at the edge. If the route to convergence is a rough proxy for time-dependent behaviour, as argued by Mouschovias (1974) for iterative relaxation algorithms, the appearance and disappearance of bubbles may represent evidence — though not proof — of transient evolution in reality.

As the bubbles are disconnected topologically from flux surfaces anchored to the star and accretion disc, they do not contain any accreted material (in the ideal-MHD limit of zero cross-field transport) and are lighter than their surroundings. It is therefore possible that they rise buoyantly and ultimately escape the magnetosphere of the neutron star. This possibility cannot be investigated rigorously in the context of the equilibrium calculations in this chapter; it is considered qualitatively in section 2.5.3.

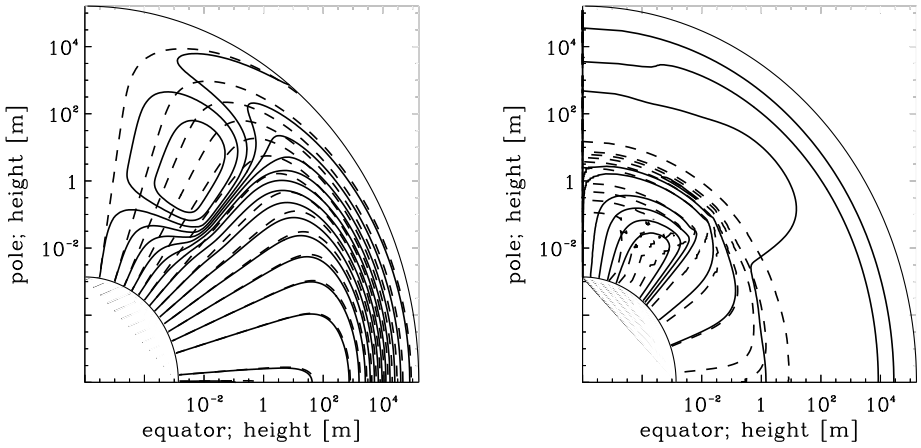

Figure 2.11: Magnetic configuration for $M_{\rm a} = 2 \times 10^{-5} M_\odot$, $b = 10$, showing the creation of a bubble. We plot contours of constant ψ (*top*) for initial (*dashed*) and final (*solid*) states, and final $|\mathbf{B}|$ contours $\eta |\mathbf{B}|_{\rm max}$ (*bottom, solid*) and ρ contours (*dashed*) $\eta \rho_{\rm max}$; $\rho_{\rm max} = 5 \times 10^{14}\,{\rm g\,cm^{-3}}$, $B_{\rm max} = 6.3 \times 10^{15}$ G, and $\eta = 0.8,\ 0.6,\ 0.4,\ 0.2,\ 0.01,\ 0.001,\ 10^{-4},\ 10^{-5},\ 10^{-6},\ 10^{-12}$.

2.5 Time-dependent effects

In this section, we discuss critically (but qualitatively) how the results of this chapter may be affected by time-dependent processes that cannot be modelled by a quasi-static sequence of hydromagnetic equilibria. We consider Parker instabilities in section 2.5.1, ohmic dissipation in section 2.5.2, and the buoyant rise of magnetic bubbles in section 2.5.3.

2.5.1 Hydromagnetic instabilities

The computed equilibria are manifestly distorted. Buoyancy of the compressed magnetic flux can drive long-wave, slow MHD modes that overturn the accreted matter on the Alfvén time-scale $\tau_{\rm A}$, as in the global Rayleigh-Taylor instability of the Galactic magnetic field (Mouschovias 1974; Parker 1966). When the accreted matter bends the polar magnetic field, there exists a significant component of magnetic field perpendicular to gravity, a condition for the onset of the Parker instability. In a plane-parallel geometry, wavelengths longer than $\Lambda = 4\pi x_0/(2\alpha + 1)$ are unstable (Mouschovias

1974), where $\alpha = B^2/(8\pi p)$. The geometry of an accreting neutron star is far from plane-parallel. Nevertheless, in hydromagnetic equilibrium, one has $\alpha \sim 1$ locally in the boundary layer, yielding $\Lambda = 2$ m. The failure to converge at large $M_{\rm a}$ is also a hint, though not a proof, that the Parker instability may operate. Mouschovias (1974) advanced a similar convergence-based argument for the stability of a stratified vertical column with periodic boundaries.

2.5.2 Ohmic dissipation

Our calculations are performed under the assumption of infinite conductivity and hence flux freezing. In reality, the accreted matter is resistive due to electron-phonon and electron-impurity scattering (Brown and Bildsten 1998; Cumming et al. 2001), potentially enhanced by accretion-induced heating (Romani 1990; Urpin and Geppert 1995).

The ohmic dissipation time-scale for a flux tube of width L is given by $\tau_{\rm d} = 4\pi\sigma L^2$, where σ is the electrical conductivity. For typical conditions, we take $\sigma \approx 10^{22}{\rm s}^{-1}$ and hence obtain $\tau_{\rm d} \approx 10^{14}(L/R_*)^2\,{\rm s}$. In comparison, the flow time-scale is given by $\tau_{\rm f} = 4\pi R_*^2 \rho L/\dot{M}_{\rm a}$, where $\dot{M}_{\rm a}$ is the accretion rate. For $\rho = 4\times10^{11}\,{\rm g\,cm^{-3}}$, $L = 6\times10^2$ cm (section 2.4.4), and $\dot{M}_{\rm a} = 1\times10^{-8}M_\odot$ yr^{-1}, we find $\tau_{\rm f} = 1\times10^2$ yr. Therefore, for the length-scales characteristic of the compressed flux layer, we have $\tau_{\rm f} > \tau_{\rm d}$ and magnetic flux diffuses through the accreted material, broadening the compressed flux layer until it is thick enough ($L \approx 6\times10^4$ cm) that $\tau_d \approx \tau_f$ and further thickening ceases. Brown and Bildsten (1998) showed that $\tau_{\rm f}/\tau_{\rm d}$ depends only on $\dot{M}_{\rm a}$ and not on depth in the crust.

Note that the buried flux is resurrected on the time-scale $\tau_{\rm d}$, after accretion stops. As the noted dipole field reasserts itself, $|\boldsymbol{\mu}|$ increases. A full analysis of this process is left to future work.

2.5.3 Buoyant bubbles

Closed magnetic bubbles have $\rho = 0$ within and are lighter than their surroundings, as discussed in section 2.4.7. They tend to rise buoyantly at the local Alfvén speed $v_{\rm A} = (B^2/4\pi\rho)^{1/2} = c_{\rm s}(2\alpha)^{1/2}$, and hence escape the magnetosphere in ≈ 2 yr. Assuming an accretion rate of $10^{-8}M_\odot\,{\rm yr}^{-1}$, it takes $\approx 10^4 b^{-1}(\dot{M}_{\rm a}/10^{-8}M_\odot\,{\rm yr}^{-1})^{-1}$ yr to accrete enough mass to create one

bubble. Moreover, a typical bubble encloses $\approx \psi_a$ of magnetic flux. Hence we conclude that magnetic flux is being expelled episodically from the magnetosphere at an average rate of $10^{19}(\psi_*/10^{24}\ \mathrm{G\,cm^2})\ (\dot{M}_a/10^{-8} M_\odot\ \mathrm{yr}^{-1})^{-1}$ G cm^2 yr^{-1}. Note that expelled flux is subsequently replenished by the current deep in the star (since ψ is fixed at the surface).

2.6 Conclusion

Observations of low-field binary neutron stars and recycled pulsars imply that the magnetic dipole moment of a neutron star is reduced by accretion. In this chapter, we undertake a self-consistent analysis (numerical and analytic) of one mechanism that may account for the reduction observed: polar magnetic burial in the ideal-magnetohydrodynamic regime. Our analysis has several new features. (i) Flux freezing is strictly enforced when connecting the final and initial magnetic configurations by solving self-consistently for the mass-flux distribution rather than specifying it ad hoc (see Figure 2.6). (ii) The Lorentz force due to equatorial magnetic field lines compressed by equatorward hydromagnetic spreading is included when calculating the confinement of the polar accreted column. (iii) Numerical methods are developed for treating accreted masses up to $\approx 10^{-4} M_\odot$, (cf. $10^{-10} M_\odot$ in previous work), where the field is dramatically distorted and high-order multipoles dominate.

We report two key results. (i) $M_a \gtrsim 10^{-5} M_\odot$ must be accreted in order to reduce significantly the magnetic dipole moment $|\boldsymbol{\mu}|$ of the star, contrary to previous estimates ($M_a \approx 10^{-10} M_\odot$) which neglected equatorial magnetic stresses. For small M_a, we find $|\boldsymbol{\mu}| = |\boldsymbol{\mu}_i|(1 - M_a/M_c)$, with $M_c = 1.2 \times 10^{-6} M_\odot$, (cf. Shibazaki et al. 1989). For $M_c \lesssim M_a \lesssim 10^{-4} M_\odot$, we find $|\boldsymbol{\mu}| = |\boldsymbol{\mu}_i|(M_a/4.6 \times 10^{-5} M_\odot)^{2.25 \pm 0.22}$. (ii) When enough mass is accreted, such that $M_a \geq 10^{-4} b^{-1} M_\odot$, the hydrostatic pressure gradient generates flux surfaces with $\psi < 0$ or $\psi > \psi_*$, creating closed magnetic bubbles that are disconnected topologically from the stellar surface. The bubbles are valid solutions of the Grad-Shafranov boundary problem, as confirmed by analytic, Green function calculations; they are not numerical artefacts or fingerprints of hydromagnetic instabilities (e.g. Parker).

Several of our assumptions need to be relaxed in future work, including (i) perfect conductivity, (ii) an impenetrable stellar surface, and (iii)

axisymmetry (which tends to suppress hydromagnetic instabilities, for example). Finally, the uniqueness of the hydromagnetic equilibria we compute numerically is yet to be established.

Our equilibria serve as useful starting points for exploring the stability of the magnetic configuration during and after accretion. Our theoretical results will be tested against observational data from binary neutron stars and recycled pulsars in chapters 5 and 6.

2.7 Appendix: Analytic solution of the Grad-Shafranov problem

In this appendix, we solve the Grad-Shafranov equation (2.12), together with the boundary conditions (2.17), by a Green function approach.

2.7.1 Green theorem for the Grad-Shafranov operator

An operator $L\psi = \nabla^2\psi + \mathbf{b}\cdot\nabla\psi + c\psi$, acting on a function ψ, possesses an adjoint $L^*\psi = \nabla^2\psi - \nabla\cdot(\mathbf{b}\psi) + c\psi$. The Grad-Shafranov operator $L = 4\pi r^2\sin^2\theta\Delta^2$, defined by (2.7) in spherical polar coordinates, has $\mathbf{b} = -2r^{-1}(\hat{\mathbf{e}}_r + \cot\theta\hat{\mathbf{e}}_\theta)$ and is not self-adjoint (cf. ∇^2). Letting G and G^* be the Green functions associated with the operators L and L^* respectively,

$$LG(\mathbf{x},\mathbf{x}') = \delta(\mathbf{x}-\mathbf{x}')\,, \tag{2.37}$$

$$L^*G^*(\mathbf{x},\mathbf{x}') = \delta(\mathbf{x}-\mathbf{x}')\,, \tag{2.38}$$

related by the reciprocity relation $G^*(\mathbf{x},\mathbf{x}') = G(\mathbf{x}',\mathbf{x})$, we arrive at the Lagrange identity

$$\psi L^*G^* - G^*L\psi = \nabla\cdot(\psi\nabla G^* - G^*\nabla\psi + \mathbf{b}\psi G^*). \tag{2.39}$$

Upon integrating (2.39) over a volume V, bounded by a surface S, and using the divergence theorem, we obtain

$$\begin{aligned}\int_V &(\psi L^*G^* - G^*L\psi)dV \\ &= \int_S(\psi\nabla G^* - G^*\nabla\psi + \mathbf{b}\psi G^*)\cdot\hat{\mathbf{n}}dS,\end{aligned} \tag{2.40}$$

where $\hat{\mathbf{n}}$ is the unit vector normal to S. Given a boundary value problem $L\psi(\mathbf{x}) = Q(\mathbf{x})$ in the volume V, with ψ given on the boundary S, we combine (2.38) and (2.40) to obtain

$$\begin{aligned}\psi(\mathbf{x}) = &\int_V d^3\mathbf{x}' G^* Q \\ &+ \int_S d^2\mathbf{x}' \hat{\mathbf{n}} \cdot (\psi \nabla G^* - G^* \nabla \psi + \mathbf{b}\psi G^*).\end{aligned} \tag{2.41}$$

2.7.2 Green function for the Grad-Shafranov equation

We wish to solve (2.12) for ψ in $r \geq R_*$ subject to Dirichlet boundary conditions (2.17) on ψ at $r = R_*$ and $r \to \infty$. In cylindrical symmetry, the volume and surface integrals in (2.20) reduce to surface and line integrals respectively. It is convenient to make the substitution $\mu = \cos\theta$, whereupon (2.12) becomes

$$\begin{aligned}\frac{\partial^2\psi}{\partial r^2} + \frac{(1-\mu^2)}{r^2}\frac{\partial^2\psi}{\partial\mu^2} &= 4\pi r^2(1-\mu^2)\frac{dF(\psi)}{d\psi} \\ &\times \exp(-\phi_0/c_{\rm s}^2 - GMr/R_*^2 c_{\rm s}^2)\end{aligned} \tag{2.42}$$

and $dF/d\psi$ is a function of r and μ through $\psi(r,\mu)$.

We redefine L to be the operator on the left-hand side of (2.42), and $Q(r,\mu)$ to be the source term on the right-hand side, known explicitly once $F(\psi)$ is known. The Green function G for L satisfies

$$\frac{\partial^2 G}{\partial r^2} + \frac{(1-\mu^2)}{r^2}\frac{\partial^2 G}{\partial\mu^2} = \frac{1}{r^2}\delta(r-r')\delta(\mu-\mu') \tag{2.43}$$

and the Green function G^* for L^* satisfies

$$\begin{aligned}\frac{\partial^2 G^*}{\partial r^2} + \frac{(1-\mu^2)}{r^2}\frac{\partial^2 G^*}{\partial\mu^2} + \frac{4}{r}\frac{\partial G^*}{\partial r} - \frac{4\mu}{r^2}\frac{\partial G^*}{\partial\mu} \\ = \frac{1}{r^2}\delta(r-r')\delta(\mu-\mu').\end{aligned} \tag{2.44}$$

Equation (2.44) is separable. We expand the solution in terms of orthogonal

Gegenbauer polynomials $C_\ell^{3/2}(\mu)$, viz.

$$G(r,\mu,r',\mu') = \sum_{\ell=0}^{\infty} g_\ell(r,r') \times (1-\mu^2) C_\ell^{3/2}(\mu') C_\ell^{3/2}(\mu), \tag{2.45}$$

with

$$\frac{d^2 g_\ell(r,r')}{dr^2} - \frac{\ell(\ell+1)}{r^2} g_\ell(r,r') = r^{-2}\delta(r-r'). \tag{2.46}$$

The Gegenbauer polynomials satisfy

$$(1-\mu^2)\frac{d^2}{d\mu^2}\left[(1-\mu^2)C_{\ell-1}^{3/2}(\mu)\right] + \ell(\ell+1)[(1-\mu^2)C_{\ell-1}^{3/2}(\mu)] = 0 \tag{2.47}$$

and are related to associated Legendre polynomials via $P_\ell^1(\mu) = -(1-\mu^2)^{1/2} C_{\ell-1}^{3/2}(\mu)$. The first few are listed for reference: $C_0^{3/2}(\mu) = 1$, $C_1^{3/2}(\mu) = 3\mu$, $C_2^{3/2}(\mu) = \frac{3}{2}(5\mu^2-1)$, $C_3^{3/2}(\mu) = \frac{5}{2}(7\mu^3-3\mu)$, $C_4^{3/2}(\mu) = \frac{15}{4}(21\mu^4 - 14\mu^2+1)$, $C_5^{3/2}(\mu) = \frac{3}{8}(231\mu^5 - 210\mu^3 + 35\mu)$. They satisfy an orthogonality condition:

$$\int_{-1}^{1} (1-\mu^2) C_\ell^{3/2}(\mu) C_{\ell'}^{3/2}(\mu) d\mu = N_\ell \delta_{\ell\ell'} \tag{2.48}$$

with

$$N_\ell = \frac{2(\ell+1)(\ell+2)}{(2\ell+3)}. \tag{2.49}$$

We solve (2.46) for $g_\ell(r,r')$ subject to the following conditions: (i) $g_\ell(r,r')$ is continuous at $r = r'$, (ii) $\lim_{\epsilon\to 0}\left[\frac{dg_\ell(r,r')}{dr}\right]_{r'-\epsilon}^{r'+\epsilon} = r'^{-2}$, (iii) $g_\ell(R_*,r') = 0$, and (iv) $\lim_{r\to\infty} g_\ell(r,r') = 0$. The result is

$$g_\ell(r,r') = \frac{1}{(2\ell+1)r'^2}\frac{r_<^{\ell+1}}{r_>^\ell}\left[\left(\frac{R_*}{r_<}\right)^{2\ell+1} - 1\right], \tag{2.50}$$

with $r_< = \min(r,r')$ and $r_> = \max(r,r')$, yielding

$$G(r,\mu,r',\mu') = \sum_{\ell=0}^{\infty} N_\ell^{-1} g_{\ell+1}(r,r') \times (1-\mu^2) C_\ell^{3/2}(\mu') C_\ell^{3/2}(\mu)\,. \tag{2.51}$$

Similarly, we obtain

$$G^*(r,\mu,r',\mu') = \sum_{\ell=0}^{\infty} N_\ell^{-1} g_\ell^*(r,r') \times (1-\mu'^2) C_\ell^{3/2}(\mu') C_\ell^{3/2}(\mu)\,, \tag{2.52}$$

with $g_\ell^*(r,r') = (\frac{r'}{r})^2 g_{\ell+1}(r,r')$. Equations (2.51) and (2.52) are consistent with the reciprocity relation. Note that basis functions for G and G^* for a non-self-adjoint operator are mutually but not individually orthogonal (Morse and Feshbach 1953).

Upon combining the Green theorem (2.40), the definition of G^* (2.52), the boundary conditions $\psi(R_*,\mu) = \psi_*(1-\mu^2)$, $\psi(r,\pm 1) = 0$, $\lim_{r\to\infty}\psi(r,\mu) = 0$, $G^*(R_*,\mu,r',\mu') = 0$, and the surface gradient $\nabla\psi(r,\pm 1)\cdot\hat{\mathbf{e}}_\mu = 0$, we find that the boundary integral over C reduces to $\int_{-1}^{1}\psi(R_*,\mu)\frac{\partial G^*}{\partial r}d\mu'$, yielding the complete solution

$$\psi(r,\mu) = \psi_* R_* \frac{(1-\mu^2)}{r} + (1-\mu^2)\sum_{\ell=0}^{\infty} N_\ell^{-1} C_\ell^{3/2}(\mu) \times \int_{-1}^{1} d\mu' \int_{R_*}^{\infty} dr' r'^2 g_\ell^*(r',r) C_\ell^{3/2}(\mu') Q(r',\mu')\,. \tag{2.53}$$

2.7.3 Small-M_a limit: Constant Source Term

To explore the form of the general solution (2.28), in the small-M_a limit, we linearise $F(\psi)$. We consider the special case $F(\psi) = Q_0(\psi_* - \psi)$, giving $Q(r,\mu) = Q_0(1-\mu^2)r^2 e^{-r}$. By orthogonality, only the $\ell = 0$ term survives. We find

$$\int_{R_*}^{\infty} g_1(r,r') r'^4 e^{-r'} dr' = -\frac{1}{r}[f_1(r) - f_1(R_*)]\,, \tag{2.54}$$

with $f_1(r) = (r^3 + 4r^2 + 8r + 8)e^{-r}$, and hence

$$\psi(r,\mu) = \psi_* R_* \frac{(1-\mu^2)}{r}\{1 - \frac{Q_0}{4\psi_* R_*}[f_1(r) - f_1(R_*)]\}\,, \tag{2.55}$$

using $N_1 = 4/3$. It is immediately clear that negative values of ψ are possible if $Q_0 > 4\psi_* R_*[f_1(r) - f_1(R_*)]$ raising the possibility of closed magnetic loops (bubbles) constructed from flux surfaces $\psi < 0$ or $\psi > \psi_*$ and hence not anchored to the stellar surface.

In dimensionless coordinates, setting $\tilde{F}(\tilde{\psi}) = k(b - \tilde{\psi})$ we arrive at

$$\begin{aligned}\tilde{\psi}(\tilde{x},\tilde{\mu}) = \; & \tilde{\psi}_{\rm i}(\tilde{x},\tilde{\mu})\ \{1 + \frac{kQ_0a^2}{b} \\ & \times [f_1(\tilde{x})e^{-\tilde{x}} - f_2(a)(1-e^{-\tilde{x}})]\},\end{aligned} \tag{2.56}$$

where $f_1(\tilde{x}) = 3\tilde{x}a^{-1} + a^{-2}(3\tilde{x}^2 + 8\tilde{x}) + \; a^{-3}(\tilde{x}^3 + 4\tilde{x}^2 + 8\tilde{x})$ and $f_2(a) = 1 + 4a^{-1} + 8a^{-2} + 8a^{-3}$. For $\tilde{x} \ll a$, where the screening currents dominate, $\tilde{\psi}$ reduces to $\tilde{\psi}_{\rm i}(\tilde{x},\tilde{\mu})\ [1 - kQ_0a^2b^{-1}(1-e^{-\tilde{x}})]$. In section 2.7.4, we show that $k \approx b/(2\pi a^2)$, so the reduction factor is $(1 - b^2M_{\rm a}/M_{\rm c})$, remembering that $Q_0 \propto M_{\rm a}$. For neutron star parameters, one has $M_{\rm c} \approx 1.2 \times 10^{-4} M_\odot$.

We can estimate the thickness of the compressed flux layer, $x_{\rm b}$, in the small-$M_{\rm a}$ regime by solving $\tilde{\psi}(x_{\rm b},\tilde{\mu}) = 0$ to give $x_{\rm b} = -\ln(1 - M_{\rm c}/M_{\rm a})$ We may also estimate when $|\mathbf{B}|$ changes significantly from its initial value $|\mathbf{B}_{\rm i}|$. Near the surface, the principal component

$$B_\mu = (B_{\rm i})_\mu[ab^2M_{\rm a}/M_{\rm c}e^{-\tilde{x}} + 1 - b^2M_{\rm a}/M_{\rm c}(1-e^{-\tilde{x}})] \tag{2.57}$$

increases significantly for $M_{\rm c}/a \geq 8 \times 10^{-11} M_\odot$, consistent the numerical results in section 2.3. Setting $B_\mu = 0$ gives an alternative estimate of the altitude below which the screening currents are confined, with $\tilde{x} = \ln[(a+1)/(1 - b^2M_{\rm c}/M_{\rm a})] = 9.8$ consistent with (2.57). Including also the radial component B_r, we obtain

$$\begin{aligned}B = & B_{\rm i}[4\mu^2(1 - b^2M_{\rm a}/M_{\rm c}(1-e^{-\tilde{x}}))^2 \\ & + (1-\mu^2)(1 + ab^2M_{\rm a}/M_{\rm c}e^{-\tilde{x}})^2]^{1/2}\,,\end{aligned} \tag{2.58}$$

which reduces to

$$B = B_{\rm i}[4\mu^2 + (1-\mu^2)(ab^2M_{\rm a}/M_{\rm c})^2]^{1/2} \tag{2.59}$$

near the surface for $10^{-10} \leq M_{\rm a}/M_{\rm c} \leq 10^{-6}$. There is also a boundary layer at the magnetic pole, where B_μ increases rapidly from zero over a short distance. The width of this polar boundary layer may be estimated by setting $B_\mu \approx B_r$, yielding $\approx \pi R_* \tan^{-1}[2M_{\rm c}/(ab^2M_{\rm a})] \approx 20$ m.

2.7.4 Dipole field

A useful analytic approximation to the source term $dF/d\psi$ can be derived for the dipole field in the early stages of accretion. In dimensionless coordinates, defined in appendix 2.8, (2.16) becomes

$$\tilde{\psi}_{\rm i}(\tilde{x},\tilde{\mu}) = b(1-\tilde{\mu}^2)(1+\tilde{x}/a)^{-1} \tag{2.60}$$

with $a = R_*/x_0$ and $b = \psi_*/\psi_{\rm a}$. From (2.14), we write $d\tilde{M}/d\tilde{\psi} = \tilde{F}(\tilde{\psi})I(\tilde{\psi})$, with

$$I(\tilde{\psi}) = 2\pi \int_C d\tilde{s}(1-\tilde{\mu}^2)^{1/2}(\tilde{x}+a)e^{-\tilde{x}}|\tilde{\nabla}\tilde{\psi}|^{-1} \tag{2.61}$$

C is a contour of constant ψ, along which we may write $\tilde{\mu} = [1-\tilde{\psi}\tilde{r}/(ab)]^{1/2}$; the integral terminates at $\tilde{x} = 0$ on the surface and $\tilde{x} = a(b/\tilde{\psi} - 1)$ above the equator. Upon rearranging we obtain

$$I(\tilde{\psi}) = \pi a^2 J(\tilde{\psi}) b^{-1/2}(b-\tilde{\psi})^{-1/2} \tag{2.62}$$

with

$$J(\tilde{\psi}) = \int_0^{a(b/\tilde{\psi}-1)} d\tilde{x}(1+\tilde{x}/a)^3 e^{-\tilde{x}} \left[1 - \frac{\tilde{x}\tilde{\psi}}{a(b-\tilde{\psi})}\right]^{-1/2} \tag{2.63}$$

The function $J(\tilde{\psi})$ is plotted in Figure 2.12. We observe that $J \approx 1$ for all $\tilde{\psi}$ except near the equator. Its limiting behaviour is $I(\tilde{\psi}) \to \pi a^2 b^{-1}$ as $\tilde{\psi} \to 0$, and $I(\tilde{\psi}) \to 2\pi a^3 (b-\tilde{\psi})^{1/2} b^{-3/2}$ as $\tilde{\psi} \to b$. If we choose $d\tilde{M}/d\tilde{\psi} = \exp(-\tilde{\psi})/2$ specifically, then from (2.61) we have

$$\tilde{F}(\tilde{\psi}) = \frac{b}{2\pi a^2} \exp(-\tilde{\psi})(1-\tilde{\psi}/b)^{1/2}[J(\tilde{\psi})]^{-1}. \tag{2.64}$$

Upon differentiating with respect to $\tilde{\psi}$, we obtain

$$\begin{aligned} \frac{d\tilde{F}}{d\tilde{\psi}} = &- \frac{be^{-\tilde{\psi}}}{2\pi a^2}\{(1-\tilde{\psi}/b)^{-1/2} \\ &\times [1+(1-2\tilde{\psi})/(2b)][J(\tilde{\psi})]^{-1} \\ &- (1-\tilde{\psi}/b)^{1/2}[J(\tilde{\psi})]^{-2}J' \\ &(\tilde{\psi})\}. \end{aligned} \tag{2.65}$$

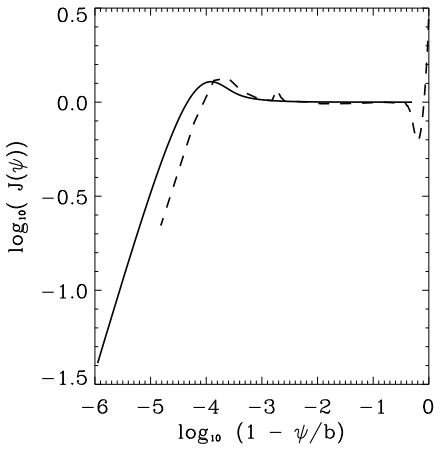

Figure 2.12: The function $J(\tilde{\psi})$ (*solid*) compared with $J(\tilde{\psi})$ calculated numerically for $M_{\rm a} = 10^{-5} M_\odot$, $b = 10$ (*dashed*).

2.8 Appendix: Iterative Numerical Scheme

2.8.1 Dimensionless equations and logarithmic coordinates

It is convenient to convert to dimensionless variables $\tilde{x} = (r - R_*)/x_0$, $\tilde{\psi} = \psi/\psi_{\rm a}$, $\tilde{M} = M/M_{\rm a}$, $\tilde{\mu} = \cos\theta$, $\tilde{F} = F/F_0$ and $\tilde{\mathbf{B}} = \mathbf{B}/B_0$ where $x_0 = c_{\rm s}^2 R_*^2/(GM_*)$ is the pressure scale height, $a = R_*/x_0$, $F_0 = M_{\rm a} c_{\rm s}^2/x_0^3$, and $B_0 = \psi_{\rm a}/r_0^2 = a^2 B_*/2b$. Equations (2.12) and (2.14) take the forms

$$\frac{\partial^2\tilde{\psi}}{\partial\tilde{x}^2} + \frac{(1-\tilde{\mu}^2)}{(\tilde{x}+a)^2}\frac{\partial^2\tilde{\psi}}{\partial\tilde{\mu}^2} = -Q_0(1-\tilde{\mu}^2)(\tilde{x}+a)^2 e^{-\tilde{x}}\frac{d\tilde{F}}{d\tilde{\psi}} \tag{2.66}$$

and

$$\frac{d\tilde{M}}{d\tilde{\psi}} = 2\pi\tilde{F}(\tilde{\psi}) \int_C d\tilde{s}(1-\tilde{\mu}^2)^{1/2}(\tilde{x}+a)e^{-\tilde{x}}|\tilde{\nabla}\tilde{\psi}|^{-1} \tag{2.67}$$

respectively, with $Q_0 = 4\pi x_0 M_{\rm a} c_{\rm s}^2/\psi_{\rm a}^2$.

As $M_{\rm a}$ increases, a thin boundary layer of screening currents forms near the surface of the neutron star (see section 2.4) (Melatos and Phinney 2001). To concentrate maximum grid resolution at the boundary layer and at the edge of the polar cap ($\psi = \psi_{\rm a}$), where the gradients of ρ and ψ are steepest, we scale the r and θ coordinates logarithmically, such that

$$\tilde{x_1} = \log(\tilde{x} + e^{-L_x}) + L_x\,, \tag{2.68}$$

$$\tilde{y_1} = -\log[1-(1-e^{-L_y})\tilde{y}]\,. \tag{2.69}$$

L_x must be chosen sufficiently small to ensure at least several nodes per hydrostatic (or hydromagnetic) scale height. To resolve steep gradients at the equator, a similar transformation exists.

2.8.2 Grid & Poisson Equation

We use a grid of (G_x, G_y) cells in (r,θ) and N_c contours of ψ, and choose $N_c \leq G_x$ to avoid zig-zags in $I(\psi)$ due to grid crossings which damage convergence, (Figure 2.13). We typically set $G_x = G_y = 256$ and $N_c = 255$, with the contour values chosen to lie between grid points at the stellar surface.

Given M_a and hence $dM/d\psi$, and starting with a guess $\psi^{(0)}(r,\theta)$, the left-hand side of (2.12), $\Delta^2\psi^{(0)}$, can be calculated at each grid point. The resulting Poisson equation is solved using a successive over-relaxation procedure with Chebychev acceleration (Press et al. 1992), stopping when the mean residual over the grid satisfies $\langle\Delta\psi/\psi\rangle \leq \epsilon = 10^{-2}$.

2.8.3 Grad-Shafranov source term and contouring

To find the source term on the right-hand side of (2.12), $F(\psi)$ is calculated from (2.14). The integral along ψ contours relies on a contouring algorithm adapted from Snyder (1978), which can follow closed loops and topologically disconnected contours. Numerical differentiation of $F(\psi)$ by first or second order differencing leads to numerical problems, magnifying small fluctuations in $I(\psi)$ and hence $F(\psi)$. We overcome this by smoothing $F(\psi)$ at each iteration step, fitting an order N_p polynomial ($N_p = 10$ typically) to $[I(\psi)]^{-1}$, viz., $[I(\psi)]^{-1} = \sum_{i=0}^{N_p} a_i(\log\psi)^i$ and then differentiating $F(\psi) = [I(\psi)]^{-1}dM/d\psi$ analytically.

2.8.4 Underrelaxation

The contour values of $dF/d\psi$ are mapped onto the grid by linear interpolation and fed into (2.12) by under-relaxation, viz.

$$\Delta^2\psi_\mathrm{new}^{(n+1)} = -F'[\psi^{(n)}]\ \exp[-(\phi-\phi_0)/c_\mathrm{s}^2]\,, \tag{2.70}$$

$$\psi^{(n+1)} = \Theta^{(n)}\psi^{(n)} + [1-\Theta^{(n)}]\psi_\mathrm{new}^{(n)}\,, \tag{2.71}$$

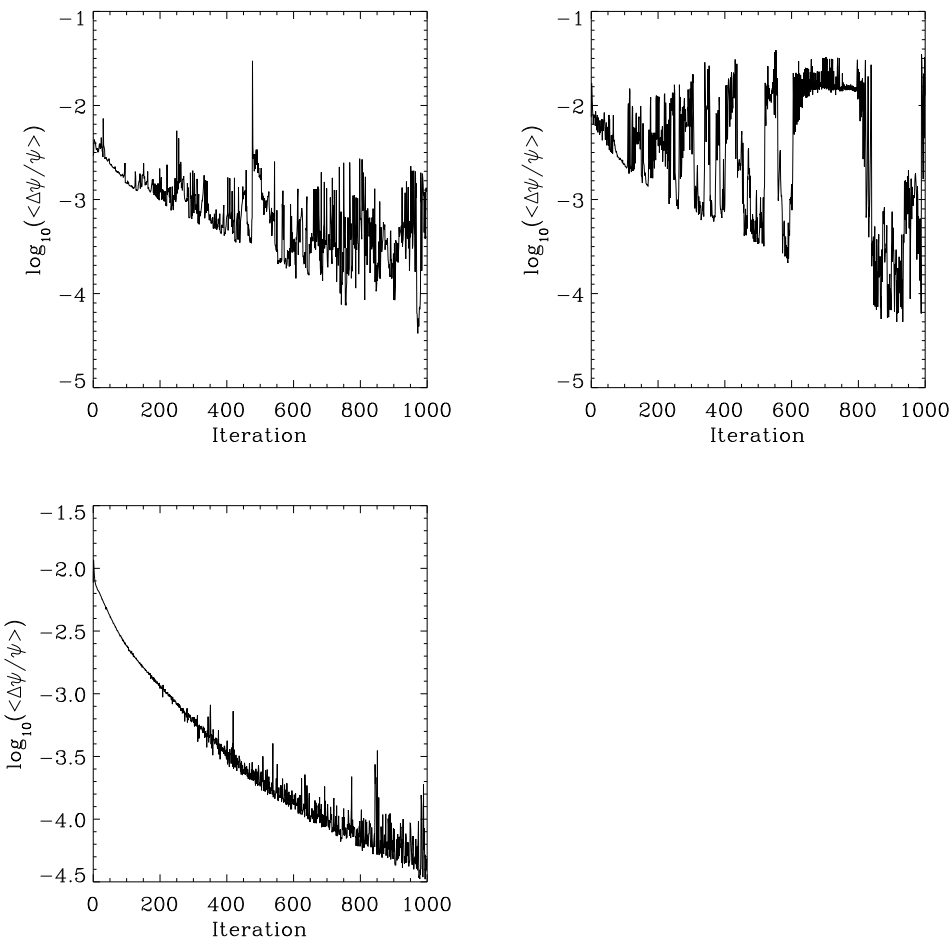

Figure 2.13: Comparison of convergence for $\Theta = 0.995$, $b = 3$, $M_{\rm a} = 8.5 \times 10^{-5} M_{\odot}$. (i) $G = 64$, $N_c = 63$ (*top*). (ii) $G = 64$, $N_c = 255$ (*middle*). (iii) $G = 256$, $N_c = 255$ (*bottom*).

b	$M_a/M_\odot$			
	10^{-10}	10^{-6}	10^{-5}	10^{-4}
3	0.0	0.5	0.9	0.995
10	0.0	0.8	0.99	0.99999
30	0.0	0.99	0.999	—

Table 2.1: Optimal $\Theta^{(n)}$ values as a function of M_a and b.

where $\psi^{(n)}_{new}$ is a provisional iterate and $0 \leq \Theta^{(n)} \leq 1$ is the under-relaxation parameter at the n^{th} iteration. Convergence is reached when

$$|\psi^{(n+1)}_{new} - \psi^{(n)}| < \epsilon |\psi^{(n+1)}_{new}| \tag{2.72}$$

is satisfied for *all* grid-points. As a rule of thumb, we take $\epsilon = 10^{-2}(M_a/10^{-6}M_\odot)$; our solutions do not converge reliably for $M_a \gtrsim 10^{-4}M_\odot$. The stability of the solution is checked by perturbing it slightly and looking for re-convergence, or by resetting $\Theta^{(n)} \approx 0$.

The optimal value of $\Theta^{(n)}$ is governed by maximum ψ gradient between grid-points, which in turn depends on M_a. We adjust $\Theta^{(n)}$ towards unity when $|\psi^{(n+1)}_{new} - \psi^{(n)}|$ tends to increase. Table 2.8.4 shows approximate optimal values of Θ for different input parameters, chosen to minimize the number of iterations while still achieving convergence.

2.8.5 Testing and convergence

We tested the code by successfully reproducing the final equilibrium states of the Parker instability, plotted in Figure 2 of Mouschovias (1974), to an accuracy of 1%. We also tested the code against the exact analytic solution (2.55) in section 2.7 for constant $dF/d\psi$. Table 2.2 shows a comparison of the mean and maximum errors as a function of grid size, relative to (2.55), when solving the Poisson equation directly [$\Theta^{(n)} = 0$].

Grid size	mean($\Delta\psi/\psi$)	max($\Delta\psi/\psi$)
8	0.0603082	0.229865
16	0.0166787	0.121939
32	0.00307997	0.0222018
64	0.00129922	0.0328857
128	0.000404714	0.00589775
256	0.000286883	0.0104630

Table 2.2: Average and maximum errors as a function of grid size.

Chapter 3

Stability of a magnetically confined mountain

3.1 Introduction

The magnetic dipole moment μ of a neutron star is observed to decrease with the accreted mass, $M_{\rm a}$, in a variety of systems, e.g. low- and high-mass X-ray binaries, and binary radio pulsars with white-dwarf and neutron-star companions (Shibazaki et al. 1989; Taam and van den Heuvel 1986; van den Heuvel and Bitzaraki 1995). In the previous chapter and in Payne and Melatos (2004) (hereafter PM04), we calculated a series of two-dimensional hydromagnetic (Grad-Shafranov) equilibria describing the structure of the magnetically confined mountain of accreted material at the magnetic poles of an accreting neutron star. These equilibrium solutions are the first of their kind to explicitly disallow cross-field transport of material as the mountain evolves from its initial to its final state (cf. Mouschovias 1974). PM04 found that μ decreases substantially once $M_{\rm a} \gtrsim 10^{-5} M_\odot$ is accreted, materially exceeding previous estimates ($\lesssim 10^{-10} M_\odot$; Brown and Bildsten 1998; Hameury et al. 1983; Litwin et al. 2001). The mountain is confined by magnetic stresses near the equator, where the field is compressed (Melatos and Phinney 2001).

PM04 calculated equilibria for $M_{\rm a} \lesssim 10^{-4} M_\odot$, falling well short of the mass required ($M_{\rm a} \sim 0.1 M_\odot$) to spin up a neutron star to millisecond periods (Burderi et al. 1999), which is supplied by a large class of mass donors including LMXBs (Strohmayer and Bildsten 2003), even given nonconser-

vative mass transfer (Tauris et al. 2000). Grad-Shafranov calculations are stymied above $M_a \sim 10^{-4} M_\odot$ by physical effects, e.g. magnetic bubbles form above the stellar surface, and numerical effects, e.g. steep magnetic gradients hinder iterative convergence. In this chapter, we extend the μ-M_a relationship to $M_a \sim 10^{-3} M_\odot$ by loading the equilibria into ZEUS-3D, a multi-purpose time-dependent, ideal-MHD code for astrophysical fluid dynamics, and adding mass quasistatically through the outer boundary.

PM04 also left open the important question of the stability of the hydromagnetic equilibria. Distorted magnetic configurations, in which the polar flux is buried beneath the accreted overburden and compressed into a narrow belt at the magnetic equator, are prima facie candidates for instability. Even in PM04, the Grad-Shafranov analysis hints at the existence of an instability (as much as a steady-state analysis can do so) by predicting the formation of magnetic bubbles.

In this chapter, we systematically explore the stability of the equilibria by evolving them in ZEUS-3D, subject to linear and nonlinear perturbations. The formalism described in section 2 of PM04 is again used here. The numerical Grad-Shafranov solver is described in appendix B of PM04 and appendix C of Mouschovias (1974).

The structure of the chapter is as follows. In section 3.2, the necessary theory is summarised and the solution method described. In section 3.3, we describe our testing of ZEUS-3D and its application to the problem of magnetic burial, after rescaling of the problem to make it tractable. In section 3.4, we explore the late stages of magnetic burial ($10^{-4} \lesssim M_a/M_\odot \lesssim 10^{-1}$) by adding mass quasistatically through the outer boundary. In section 3.5, we discuss the linear and nonlinear stability of the equilibria for all M_a. The chapter concludes with a discussion of future applications in section 3.6.

3.2 Physics of magnetic burial

3.2.1 Magnetic burial

During accretion onto a neutron star from a binary companion, matter piles up on the polar cap, constrained by the magnetic tension of the polar magnetic flux tube. Once M_a exceeds $\sim 10^{-5} M_\odot$, the hydrostatic pressure at the base of the accretion column overcomes the magnetic tension and matter spreads over the stellar surface towards the equator, dragging along frozen-

in polar field lines (PM04). The distorted magnetic field leads to screening currents which act to decrease the magnetic dipole moment. Figure 3.1(a) illustrates the magnetic 'tutu' formed for $M_{\rm a} = 10^{-5} M_{\odot}$, cut off at ten density scale heights. The polar mountain of accreted material (dashed contours) and the pinched, flaring, equatorial magnetic belt (solid contours) are plainly seen. At first glance, one might expect such equilibria, with their steep density and magnetic field gradients, to be unstable.

3.2.2 Grad-Shafranov equation

The equations of magnetohydrodynamics (MHD) (Bernstein et al. 1958) in SI units include the equation of mass continuity,

$$\frac{\partial \rho}{\partial t} + \nabla \cdot (\rho \mathbf{v}) = 0, \tag{3.1}$$

the equation of motion,

$$\rho \frac{\partial \mathbf{v}}{\partial t} + \rho(\mathbf{v} \cdot \nabla)\mathbf{v} = -\rho \nabla \phi - \nabla p + \frac{1}{4\pi}(\nabla \times \mathbf{B}) \times \mathbf{B}, \tag{3.2}$$

and the induction equation (ignoring displacement current),

$$\frac{\partial \mathbf{B}}{\partial t} - \nabla \times (\mathbf{v} \times \mathbf{B}) = \frac{1}{4\pi\sigma} \nabla^2 \mathbf{B} \tag{3.3}$$

supplemented by $\nabla \cdot \mathbf{B} = 0$ and an isothermal equation of state, $p = \rho c_{\rm s}^2$, where $\mathbf{B}$, ρ, p, ϕ, $\mathbf{v}$, $c_{\rm s}$, and σ denote the magnetic field, matter density, pressure, gravitational potential, plasma bulk velocity, sound speed, and conductivity respectively.

In the magnetostatic limit, $\mathbf{v} = 0$ and $\partial/\partial t = 0$, the force equation becomes

$$\nabla p + \rho \nabla \phi - \frac{1}{4\pi}(\nabla \times \mathbf{B}) \times \mathbf{B} = 0. \tag{3.4}$$

Equations (3.1) and (3.3) are also satisfied identically (in the limit $\sigma \to \infty$) and drop out of the problem. Consequently, we are obliged to impose a constraint on the mass-flux distribution of the final state to connect it with the initial state, preserve the physical information in (3.1) and (3.3), and hence uniquely specify the solution to (3.4). The constraint, stated in section 3.2.3, expresses the fact that material cannot flow across magnetic field lines in the ideal-MHD limit (flux-freezing). As in Melatos and Phinney

(2001) and PM04, this limit is justified because the local Alfvén time-scale $\tau_A \sim 10^{-2}$ s is much less than the Ohmic diffusion time-scale. We restrict our stability experiments to ideal MHD ($\sigma \to \infty$) in this chapter, delaying consideration of Ohmic dissipation to a future paper.

3.2.3 Axisymmetric equilibria

We define spherical polar coordinates (r, θ, ϕ) such that $\theta = 0$ defines the symmetry axis of the pre-accretion magnetic field. For an axisymmetric configuration, there exists a scalar flux function $\psi(r, \theta)$ that generates $\mathbf{B}$ via

$$\mathbf{B} = \frac{\nabla\psi}{r\sin\theta} \times \hat{\mathbf{e}}_\phi. \tag{3.5}$$

Contours of ψ, which describe flux surfaces when rotated about the axis of symmetry $\theta = 0$, are projections of the magnetic field lines onto the $r - \theta$ plane. The toroidal component B_ϕ is zero at all times if the accretion process is axisymmetric and $B_\phi = 0$ in the initial accretion state. The flux surfaces are directly related to the toroidal component of the magnetic vector potential via $A_\phi = \psi/(r\sin\theta)$. Substituting (3.5) into (3.4) yields

$$\nabla p + \rho\nabla\phi - (\Delta^2\psi)\nabla\psi = 0, \tag{3.6}$$

with

$$\Delta^2 = \frac{1}{4\pi r^2\sin^2\theta}\left[\frac{\partial^2}{\partial r^2} + \frac{\sin\theta}{r^2}\frac{\partial}{\partial\theta}\left(\frac{1}{\sin\theta}\frac{\partial}{\partial\theta}\right)\right]. \tag{3.7}$$

We resolve (3.6) into components parallel and perpendicular to the magnetic field, respectively:

$$\rho\nabla\phi + \nabla p = 0, \tag{3.8}$$

$$\rho\nabla\phi + \nabla p - (\Delta^2\psi)\nabla\psi = 0. \tag{3.9}$$

The gravitational potential above the surface of the neutron star in the limit $h_0 = c_{\rm s}^2 R_*^2/(GM_*) \ll R_*$ is approximately

$$\phi = GM_* r/R_*^2, \tag{3.10}$$

where M_* is the mass of the neutron star and R_* is its radius. This leads to the Grad-Shafranov equation

$$\Delta^2\psi = \frac{dF}{d\psi}\exp[-(\phi-\phi_0)/c_s^2], \tag{3.11}$$

with the accompanying mass-flux condition

$$\frac{dM}{d\psi} = 2\pi\int_C ds\,\rho[r(s,t),\theta(s,t)]\frac{r\sin\theta}{|\nabla\psi|}\,, \tag{3.12}$$

where (s,t) are local coordinates parallel and perpendicular to the magnetic field respectively. F is a function which traces the base pressure at the stellar surface and is given by

$$F(\psi) = c_s^2\frac{dM}{d\psi}\left\{2\pi\int_C ds\,r\sin\theta|\nabla\psi|^{-1}\exp[-(\phi-\phi_0)/c_s^2]\right\}^{-1}\,, \tag{3.13}$$

where C is any magnetic field line. The initial state in this problem is the magnetic dipole,

$$\psi_{\rm d}(r,\theta) = \psi_* R_* r^{-1}\sin^2\theta\,, \tag{3.14}$$

where $\psi_* = \frac{1}{2}B_*R_*^2$, and B_* denotes the polar magnetic field before accretion. For the boundary conditions, we take

$$\psi(R_*,\theta) = \psi_*\sin^2\theta, \quad \lim_{r\to\infty}\psi(r,\theta) = 0\,, \tag{3.15}$$

$$\psi(r,0) = 0, \quad \frac{\partial\psi}{\partial\theta}(r,\pi/2) = 0\,. \tag{3.16}$$

The magnetic field lines are tied to the stellar surface at all times. In appendix 3.7 we discuss how to implement the outer ($r\to\infty$) boundary condition at $r = r_{\rm m}$ numerically.

Equations (3.11) and (3.13) are solved numerically using an iterative relaxation scheme (Mouschovias 1974; Payne and Melatos 2004). The mean residual as a function of iteration number is shown in figure 3.1(b), corresponding to the Grad-Shafranov equilibrium for $M_{\rm a}/M_{\rm c} = 0.16$ in figure 3.1(a). The form of $F(\psi)$, found from (3.13), varies from $M_{\rm a} = 0$ to $M_{\rm a} = 0.16M_{\rm c}$ in the manner displayed in figure 3.1(c). We take $dM/d\psi = M_{\rm a}e^{-\psi/\psi_{\rm a}}[2\psi_{\rm a}(1-e^{-\psi_*/\psi_{\rm a}})]^{-1}$, with $\psi_{\rm a} = \psi_* R_*/R_{\rm a}$, where $R_{\rm a}$, the magnetospheric radius, is set by the global accretion geometry. Equation (3.13)

yields different functional forms of $F(\psi)$ than those trialled by other authors (Brown and Bildsten 1998; Hameury et al. 1983; Litwin et al. 2001; Melatos and Phinney 2001).

3.2.4 Critical accreted mass $M_{\rm c}$

According to naive estimates based on hydromagnetic force balance between $(4\pi)^{-1}(\nabla \times \mathbf{B}) \times \mathbf{B}$ and ∇p at the polar cap, the magnetic field (and hence μ) is distorted appreciably away from its initial configuration for $M_{\rm a} \geq M_{\rm c} \sim 10^{-8} M_\odot$ (Brown and Bildsten 1998; Litwin et al. 2001). However, self-consistent solutions of (3.7) and (3.13), in which mass does not migrate across flux surfaces and the back-reaction from equatorial magnetic stresses is included (PM04), predict a larger value of $M_{\rm c}$, given by

$$\begin{aligned} \frac{M_{\rm c}}{M_\odot} &= GM_* B_*^2 R_*^2/(8c_{\rm s}^4 M_\odot) \\ &= 1.2 \times 10^{-4} \left(\frac{M_*}{1.4M_\odot}\right) \left(\frac{R_*}{10^6 {\rm cm}}\right)^2 \left(\frac{B_*}{10^{12}{\rm G}}\right)^2 \left(\frac{c_{\rm s}}{10^8\ {\rm cm\,s^{-1}}}\right)^{-4}, \end{aligned} \tag{3.17}$$

In the regime $M_{\rm a} \lesssim M_{\rm c}$, the Green function analysis in PM04 gives

$$\psi(r,\theta) = \psi_{\rm d}(r,\theta)[1 - mb^2(1 - e^{-x/h_0})]\,, \tag{3.18}$$

with $m = M_{\rm a}/M_{\rm c}$. The distorted field lines develop a large tangential component as mass is added, such that $|\mathbf{B}|$ increases substantially for $M_{\rm a} \gtrsim M_{\rm c}/a$;[1] The self-consistent density distribution associated with (3.18) is given by

$$\rho(r,\theta) = \rho_0 \tilde{F}[\tilde{\psi}(r,\theta)]e^{-x/h_0} \tag{3.19}$$

with

$$\tilde{F}(\tilde{\psi}) = \frac{b}{2\pi a^2} \exp(-\tilde{\psi})(1 - \tilde{\psi}/b)^{1/2}[J(\tilde{\psi})]^{-1}, \tag{3.20}$$

where we write $\tilde{F} = Fh_0^3 c_{\rm s}^2/M_{\rm a}$, $\rho_0 = M_{\rm a}/h_0^3$, $\tilde{\psi} = \psi/\psi_{\rm a}$, and $b = \psi_*/\psi_{\rm a}$, and the form factor satisfies $J(\tilde{\psi}) \approx 1$ to better than 10 per cent for all θ except near the equator, $89.5^\circ \leq \theta \leq 90^\circ$ (see figure A1 of PM04). In the small-$M_{\rm a}$ limit, F is calculated by setting ψ to a dipole and evaluating the correction from (3.7) using Green functions.

[1] The extra factor or a comes from the differentiation of ψ.

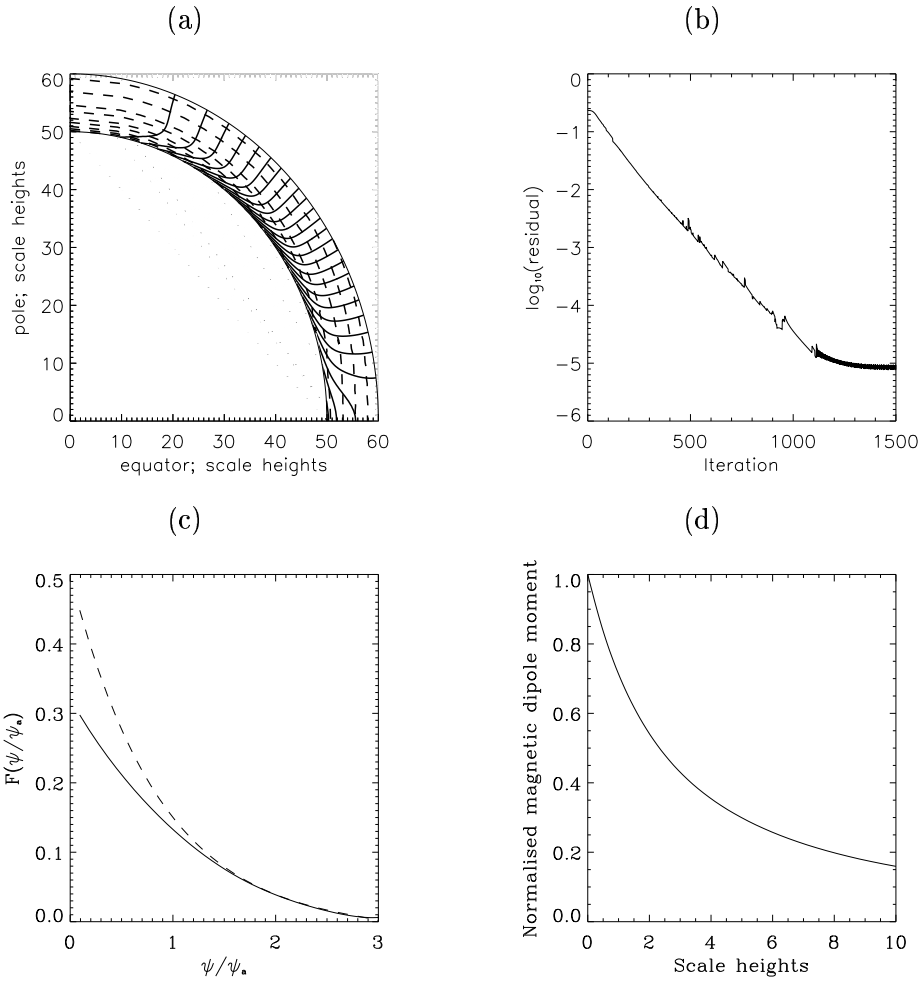

Figure 3.1: Hydromagnetic equilibrium for $a = 50$ (scaled from real stellar dimensions as discussed in section 3.3.3) and $M_a/M_c = 0.16$, with $G_x = G_y = 64$, showing (a) magnetic field lines (*solid*) and density contours (*dashed*) and (b) the corresponding mean residual versus iteration number for an underrelaxation parameter $\Theta = 0.99$. (c) Final $F(\psi)$ (*solid*) and initial $F(\psi)$ (*dashed*) vs ψ. (d) Magnetic dipole moment (normalised by its surface value) as a function of height above the stellar surface (in scale heights).

3.2.5 Screening the magnetic dipole

The magnetic dipole moment is defined in terms of the radial component of the magnetic field by

$$\mu = \frac{3}{4} r^3 \int_{-1}^{1} d(\cos\theta)\, \cos\theta B_r(r,\theta) \ . \tag{3.21}$$

We calculate it as a function of $M_{\rm a}$ from ψ (PM04). In the regime $M_{\rm a} \lesssim M_{\rm c}$, we obtain

$$\mu/\mu_{\rm i} = (1 - M_{\rm a}/M_{\rm c}) \,, \tag{3.22}$$

where $\mu_{\rm i}$ is the initial magnetic dipole moment. Equation (3.22) depends only on $m = M_{\rm a}/M_{\rm c}$, not $M_{\rm a}$ and $M_{\rm c}$ individually, as in (3.18). Figure 3.1(d) shows how μ decreases as a function of height due to the screening currents within the first few density scale heights. It is very important to note that ψ deviates substantially from its dipole form for $M_{\rm a}/M_{\rm c} \gtrsim b^{-2}$, whereas μ deviates from $\mu_{\rm i}$ for $M_{\rm a}/M_{\rm c}$, at a much later stage of accretion ($b \gg 1$).

3.3 Numerical simulations of magnetic burial

Distorted MHD equilibria like the one pictured in figure 3.1(a) are notoriously unstable. In the language of plasma confinement in tokamaks (fusion reactors), they have a large q factor. In this section, we describe how the astrophysical MHD code ZEUS-3D can be used to investigate the stability of our equilibria. We discuss the set up of ZEUS-3D in section 3.3.1 and appendix 3.7, some verification experiments in section 3.3.2 and appendix 3.7, and the curvature rescaling required to render the magnetic burial problem tractable in section 3.3.3.

3.3.1 ZEUS-3D

ZEUS-3D is a multipurpose, time-dependent, ideal-MHD code for astrophysical fluid dynamics which uses staggered-mesh finite differencing and operator splitting in three dimensions (Stone and Norman 1992a). In this chapter, we restrict the dynamics to two dimensions, disabling the third, but employ a spherical polar grid, appropriate for an axisymmetric stellar atmosphere. Previous numerical work focused on the magnetic poles of

the accreting star (Brown and Bildsten 1998; Cumming et al. 2001); here, by contrast, equatorial magnetic stresses are treated fully by simulating a complete hemisphere. The density and magnetic field strengths are read into ZEUS-3D from the output of our Grad-Shafranov code (PM04). The time-step $\Delta t_{\rm Z}$ is set by the Courant condition satisfied by the fastest MHD wave modes. Details regarding the parameters, initial conditions, boundary conditions, verification tests, and coordinate choices in the runs are given in appendix 3.7.

3.3.2 Verification

Before implementing the burial problem in ZEUS-3D, we ran a sequence of simpler verification cases. First, we reproduced the classical results for the nonlinear evolution of the Parker instability of a plane-parallel field in rectangular geometry (Mouschovias 1974). We obtained agreement on the minimum stable wavelength $\lambda_{\rm crit} = 4\pi h_0 [B^2/(4\pi p) + 1]^{-1/2}$ and reproduced the final nonlinearly evolved equilibrium state to an accuracy of 5 per cent. Second, to test spherical coordinates in ZEUS-3D, we evolved a spherical isothermal atmosphere containing zero magnetic field, followed by a dipolar magnetic field, both force-free equilibria [$(\nabla \times \mathbf{B}) \times \mathbf{B} = 0$)]. ZEUS-3D confirmed that these are indeed equilibria; they do not alter significantly even after several thousand Alfvén times. The condition at the outer boundary is chosen to suit the problem at hand. Outflow does not interfere with the magnetic field at all; however, it allows some mass loss, which we minimize by keeping $r_{\rm m}$, the outer grid radius, large, to prevent the atmosphere from evaporating over (very) long time-scales. Inflow artificially pins the magnetic field. It is used as a stage in the bootstrap algorithm (described in section 3.4.2) for adding mass in the $M_{\rm a} \gg M_{\rm c}$ regime. A radial magnetic field at the outer boundary (when inflow conditions are imposed) causes an artificial increase in μ integrated at $r_{\rm m}$.

3.3.3 Curvature rescaling

The characteristic radial (h_0) and latitudinal (R_*) length scales are very different in a neutron star, creating numerical difficulties which must be handled by rescaling the problem. For a typical neutron star with $c_{\rm s} = 10^8$ cm s^{-1} (Brown and Bildsten 1998), we find $h_0 = 54$ cm, $a = R_*/h_0 =$

1.9×10^4, and $\tau_0 = h_0/c_s = 5.4 \times 10^{-7}$ s, where τ_0 is the sound crossing time over a hydrostatic scale height.

Two input parameters are varied in the simulations: M_a and b. In the regime $M_a \lesssim M_c$ described by (3.18), ψ and consequently μ depend only on $m = M_a/M_c$ and not explicitly on M_a, suggesting that we can artificially reduce $a = R_*/h_0$ by reducing M_* and R_* as long as we keep $h_0 \propto R_*^2/M_*$ fixed. The minimum density increases as a decreases (because the atmosphere extends further), decreasing the Alfvén speed and hence the ZEUS-3D time step Δt_Z. We set $a = 50$, a good compromise that ensures $a \gg 1$ while maintaining good grid resolution in ZEUS-3D. This choice corresponds to a model star with $M_*' = 10^{-5} M_\odot$ and $R_*' = 27$ m. Our numerical results confirm that μ is independent of a (see section 3.4.1), as predicted analytically, and as illustrated in figure 3.2, where $\mu(M_a)$ is plotted for several a values; even for $M_a < M_c$, the deviations are less than ten per cent.

Our ZEUS-3D grid reaches an altitude $x_m = r_m - R_* = 10 h_0$ (cf. $> 10^3 h_0$ in PM04). We adopt a restricted domain for two reasons: (i) to maximize grid resolution near the surface of the star, where gradients are steepest; and (ii) to stop the time-step, Δt_Z, from becoming so small that runtime and numerical dissipation become excessive (as discussed in appendix 3.7). According to the Courant condition, Δt_Z scales as $1/v_{A,max} \propto \rho_{min} \propto e^{-x_m/h_0}$. Reducing a also changes the pole-to-equator sound and Alfvén crossing times ($a h_0/c_s$ and $a h_0/v_A$ respectively) in a predictable way.

3.4 Late stages of magnetic burial ($M_a \gg M_c$)

In this section, we investigate the time-dependent evolution of the highly distorted Grad-Shafranov equilibria that arise for $M_a \gg M_c$. In other words, we aim to discover what happens when $M_a > 10^{-4} M_\odot$ is added at a rate slow compared with the Alfvén time and instability oscillation period. To do this, we employ a bootstrap approach as follows: a Grad-Shafranov equilibrium for $M_a > M_c$ is loaded into ZEUS-3D; M_a is doubled quasistatically over 250 Alfvén times with inflow (and hence radial $\mathbf{B}$) at the outer boundary; the inflow is stopped and $\mathbf{B}$ is allowed to relax to a dipole at large r; this is repeated until $M_a \sim 10^{-3} M_\odot$.

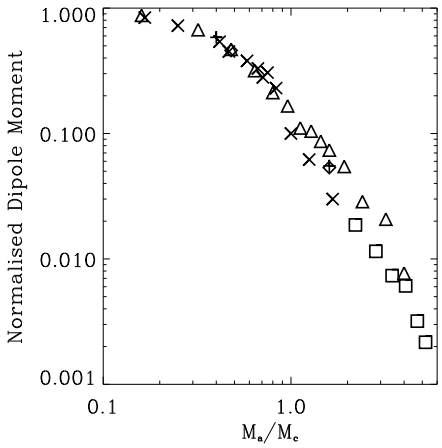

Figure 3.2: Magnetic dipole moment, μ, as a function of accreted mass, M_a/M_c, for $b = 3$ and $a = 1.86 \times 10^4$ (*crosses*), $a = 50$ (*triangles*), $a = 100$ (*pluses*), $a = 500$ (*diamonds*), and $a = 50$ with mass added through the outer boundary in ZEUS-3D (*squares*).

3.4.1 μ versus M_a

The numerical results confirm that the magnetic dipole moment is essentially independent of a. Figure 3.2 displays $\mu(M_a)$ for several a values, with $M_a > M_c$ achieved by adding mass through the outer boundary of the simulation box (squares). As predicted analytically, there is negligible dependence on a for $M_a < M_c$. For $M_a > M_c$, deviations of less than 10 per cent occur. For $x_m = 10h_0$, the outer boundary condition (radial **B**) artificially increases μ, integrated at x_m, by about 10 per cent; this is considered further below [figure 3.7(f)]. Hence the magnetic dipole moments presented in figure 3.2 are upper bounds. The dipole moment is plotted as a function of altitude x in figure 3.7(f) (dotted) for $m = 0.16$ to illustrate this. Errors are $\lesssim 1\%$ when compared against other runs with $x_m > 10h_0$. For example, for $m = 0.16$ and $G_x = G_y = 128$, the minimum dipole moment is 0.8695 and 0.8555 for $\tilde{x}_m = 10$ and $\tilde{x}_m = 20$ respectively. (A 64×64 grid gives similar results, with 0.875 for $\tilde{x}_m = 10$.)

3.4.2 Bootstrap accretion: $M_a \gg M_c$

The results in figure 3.2 extend to $M_a \approx 5M_c$, yet the Grad-Shafranov code only produces equilibria for $M_a \lesssim 10^{-4} M_\odot$, and breaks down when

magnetic bubbles first appear at $M_{\rm a} \gtrsim M_{\rm c} b^{-1}$ (section 3.4.3). This state of affairs is unsatisfactory because, in many real accreting systems (e.g. LMXBs), $M_{\rm a}$ exceeds substantially the critical mass for bubbles to form (Taam and van den Heuvel 1986; van den Heuvel and Bitzaraki 1995). For such systems, previous calculations are useful for the early stages of accretion, $\tau_{\rm a} = M_{\rm a}/\dot{M}_{\rm a} \leq 10^4 b^{-1}$ yr, but teach us little about the final stages of accretion and hence the relic magnetic structure once accretion stops. In this section, we perform a numerical experiment to address this issue. We begin with a hydromagnetic equilibrium configuration for ρ and ψ for $M_{\rm a}$ just below the critical value for bubbles, calculated using the previous Grad-Shafranov method (PM04). We load this configuration into ZEUS-3D. We then add mass on the polar flux tube $0 \leq \psi \leq \psi_{\rm a}$ at a rate slower than all the hydromagnetic time-scales involved in the process of coming to equilibrium, including the Alfvén time-scale and the period of the global Parker oscillations discussed in section 3.5, but at a rate faster than the real accretion rate $\dot{M}_{\rm a}$, so as to make the computation tractable. We then see what the final magnetic structure we get after a realistic amount of mass is accreted, e.g. $M_{\rm a} \sim 0.1 M_\odot$ for LMXBs.

This approach does not follow properly the evolution of processes that operate on intermediate time-scales between the hydromagnetic ones and $\tau_{\rm a}$, such as Hall drift (Cumming et al. 2004) and Ohmic diffusion (Romani 1990). However, it does include all time-dependent ideal hydromagnetic effects in the context of polar ($0 \leq \psi \leq \psi_{\rm a}$) magnetic burial for the first time. Note that this experiment would be completely impractical without the Grad-Shafranov equilibria previously computed for $M_{\rm a} b \lesssim 10^{-4} M_\odot$ (PM04), because the separation of the hydromagnetic and accretion time-scales is too great if one starts from $M_{\rm a} = 0$, even when the accretion is accelerated artificially.

Figure 3.3 illustrates one bootstrapping cycle; it is also a good illustration of the dynamics of magnetic burial and spreading for $M_{\rm a} \gg M_{\rm c}$. Beginning with the steady state equilibrium for $m = 1.6$, we add mass to the outer boundary, with inflow boundary conditions. The magnetic field lines are tied to the outer boundary by this condition in ZEUS-3D, preventing μ from decreasing there, and unnaturally raising μ closer to the star. To overcome this, we change the outer boundary condition from inflow ($\mathbf{B}$ pinned) to outflow ($\mathbf{B}$ free) after adding progressively more mass. Mass

is added through the polar flux tube, with $\dot{M}_{\rm a}(\theta) = \dot{M}_{\rm a,max} e^{-b\sin^2\theta}$ and $\dot{M}_{\rm a,max} \approx 2 \times 10^{-6} M_\odot/\tau_0$ when scaled up from the model ($a = 50$) to a realistic neutron star. Mass falls along field lines [figure 3.3(a)] towards the stellar surface and flattens the 'tutu' until the magnetic tension matches the hydrostatic pressure. Matter subsequently flows equatorward, dragging magnetic field lines with it [figure 3.3(c)]. Superposed on this process are sound and Alfvén oscillations, discussed in section 3.5, which leave wiggles in the field lines, visible above the spreading matter ($2-3$ m above the surface). The oscillations show up clearly in the time evolution of the magnetic dipole moment and mass quadrupole moment in figure 3.4. [Further discussion of the mass distribution appears in Melatos and Payne (2005).] Finally, the mass inflow is stopped and the outer boundary condition is switched to outflow, allowing the magnetic field lines to relax [figure 3.3(e)].

The configuration in figure 3.3(e) becomes the initial state for further mass to be added. The dipole moment attained after adding a further $3 \times 10^{-4} M_\odot$ with a 128×128 grid is shown in figure 3.8. A minimum dipole moment of $\approx 3 \times 10^{-3}$ times the surface value is obtained for $m = 4.76$ at an altitude $\sim h_0$. Results for larger $M_{\rm a}$ values may be obtained by improving the grid resolution nearer the equator.

One might be tempted to ask whether the intermediate step of relaxing the field at $r_{\rm m}$ is really necessary. It is, and figures 3.3 and 3.7 illustrate why. If too much mass is added, it is found numerically that the field lines break off the underlying magnetic dipole and, when allowed to relax, remain pinned to the outer boundary. Figure 3.4 shows μ as a function of time, measured ~ 1.5 m above the stellar surface because this is where the spreading occurs, above the tutu and below the influence of line-tying at the outer boundary. μ reaches a minimum after $\sim 100\tau_0$, even when more mass is added, because of line-tying at $r_{\rm m}$. Adding more mass is ineffective because closed magnetic loops form. They are apparent in figure 3.5 which shows the configuration after $t = 400$ (starting from the $m = 1.6$ equilibrium). This configuration cannot be used as the initial state for the next bootstrapping iteration because the magnetic field lines remain fixed at the outer boundary.

To validate this method, we take an equilibrium, well below the onset of magnetic bubbles (i.e. $m \ll 1$), and add mass up to a value of $M_{\rm a}$ for which the Grad-Shafranov equilibrium is already known. We find agreement in μ

to better than 5 per cent. We begin with the equilibrium for $m = 0.16$ and add mass $\dot{M}_{\rm a}(\theta) = \dot{M}_{\rm a,max} e^{-b\sin^2\theta}$, with $\dot{M}_{\rm a,max} \approx 7 \times 10^{-8} M_\odot/\tau_0$. Figure 3.7 shows the results of such a test, beginning with $m = 0.16$. There are several important features. (i) The initial dipole moment in figure 3.7(f) rises towards the outer boundary (see section 3.3.2). (ii) μ is unchanged at the outer boundary because of line-tying. This is because the magnetic field lines are tied there by the flux-freezing condition, to accomodate the inflowing mass; magnetic field lines bend towards the equator and decrease μ closer to the stellar surface. (iii) Closer to the surface, μ reaches a minimum value within 5 per cent of that obtained from the Grad-Shafranov equilibrium. (iv) The kinks apparent in the magnetic field lines are a result of numerical dissipation on the grid scale.

3.4.3 Bubbles

When the Grad-Shafranov equation is solved with an outer (Neumann) boundary for $M_{\rm a} \geq M_{\rm c} b^{-1}$, bubbles of magnetic field, disconnected from the inner (Dirichlet) boundary, can arise (PM04). Physically, they are generated by toroidal currents above the polar caps. However, given that the field lines must be deformed continuously from a simply connected initial state in ideal MHD, these bubbles are not realisable even though they are admissible mathematical solutions to the boundary value problem. Instead, the bubbles point to a loss of equilibrium, analogous to that which occurs during eruptive solar phenomena (Klimchuk and Sturrock 1989), where no simply connected hydromagnetic equilibrium exists. In the Grad-Shafranov boundary problem, the source term $\propto F'(\psi)$ in (3.11) increases with $M_{\rm a} b$, boosting $\Delta^2\psi$ and hence ψ above the surface, creating flux surfaces with $\psi < 0$ or $\psi > \psi_*$, which are disconnected from the star and either form closed loops or are anchored 'at infinity' (here, the accretion disk).

How does a bubble evolve in ZEUS-3D? We import a Grad-Shafranov equilibrium for $M_{\rm a} = 1.6 M_{\rm c}$ into ZEUS-3D, retaining the self-consistent $\rho = F[\psi(r,\theta)]e^{-x/h_0}$ in the region $0 \leq \psi \leq \psi_*$ but replacing it with an isothermal atmosphere inside the bubble ($\psi < 0, \psi > \psi_*$), where strict flux-freezing would imply $\rho = 0$ (matter cannot flow into this region). Figure 3.6 shows part of the evolution. Shallow bubbles rise to $r_{\rm m}$ during the first Alfvén oscillation at the Alfvén speed. Deep bubbles oscillate about an equilibrium point rather than rising buoyantly, as ρ is isothermally distributed inside

them. During the rise of the shallow bubble, 0.5 per cent of the accreted mass ($4.4 \times 10^{-7} M_\odot$ when converted back to the real neutron star parameters; see section 3.7.6) is ejected through the outer boundary on the Alfvén time-scale. This compares with evaporation of less than 0.001 per cent in the same time, resulting from the outflow boundary condition discussed below in appendix 3.7.

3.4.4 Uniform density increase method

Another means of accessing equilibria with $M_\mathrm{a} > 10^{-4} M_\odot$ is to take a Grad-Shafranov equilibrium and increase the density by a constant factor uniformly across the grid, while leaving the magnetic field strength and geometry fixed. Starting from the initial dipole ($M_\mathrm{a} = 0$), this experiment leads to excessive numerical dissipation and mass loss. However, starting from $M_\mathrm{a} = 10^{-5} M_\odot$, the readjustment is gentler. If ρ is multiplied everywhere by a factor $\gtrsim 4$, some classic examples of the Parker instability are observed. Figure 3.10 shows the initial state $m = 1.12$, with the density increased uniformly five-fold to $m = 5.6$. The magnetic field is squashed on an Alfvén time-scale perpendicular to the density gradient — ripe conditions for the Parker instability. μ settles down to $\approx 0.06 \mu_\mathrm{i}$ which is larger than we expect for $m = 5.6$, given that we found $\mu(m = 4.7) < 0.01$ using the bootstrapping method.

3.4.5 Size of the polar cap

We discuss here the effect of varying b and hence the polar cap radius, set by the disk-magnetosphere boundary at $R_\mathrm{a} = bR_*$. With $b = 3$, which we have used for all of the results displayed above, the effective polar cap radius is $R_\mathrm{cap} = R_* \theta_\mathrm{cap} = R_* \arcsin(b^{-1/2}) = 6.2$ km (17 m for $a = 50$). We choose r_cap relatively large because (i) it allows the Grad-Shafranov solution to converge numerically while still capturing the essential idea of a polar mountain, and (ii) it raises the minimum density $\rho_\mathrm{min} \propto e^{-b}$ on the grid, preventing Δt_Z from becoming too small via the Courant condition. Note that, while we assume here that matter is tied to magnetic field lines all the way from the accretion disk to the stellar surface, in reality, the plasma flow can be perturbed by Rayleigh-Taylor and Kelvin-Helmholtz instabilities (Arons et al. 1984), increasing the effective polar cap radius to ~ 1 km.

3.4.6 Equatorial magnetic belt

Melatos and Phinney (2001) predicted that the magnetic field at the equator is intensified by hydromagnetic spreading and flux conservation. The results presented here confirm this. Most of the increase in $|\mathbf{B}|$ comes from B_θ rather than B_r. At the equator, B_r is limited because the condition of north-south symmetry allows magnetic field lines to connect across the magnetic equator except right on the surface (where there is insufficient grid resolution). As seen in e.g. figure 3.1(a), B_r is reduced at the pole, with the flux (which is conserved) instead running over the surface towards the equator, increasing B_θ. Note that the analytic approximation in the limit of small M_a captures the equatorial belt provided that $J(\psi)$ is calculated properly (PM04).

An equatorial magnetic belt can impede thermal transport. It may explain why the oscillations observed in the tails of thermonuclear X-ray bursts linger for tens of seconds, much longer than the time taken by the thermonuclear flare to cover the star (Payne and Melatos 2005b).

3.5 Stability

In this section, we investigate whether the Grad-Shafranov equilibria of magnetically confined mountains calculated in this chapter and PM04 are stable to small and large perturbations. To do this, we load the numerical output from our Grad-Shafranov code into ZEUS-3D, evolve it forward in time, and report on the nature of any instabilities observed. In ideal MHD, any instabilities manifest themselves as slow, Alfvén, or fast, magnetosonic waves.

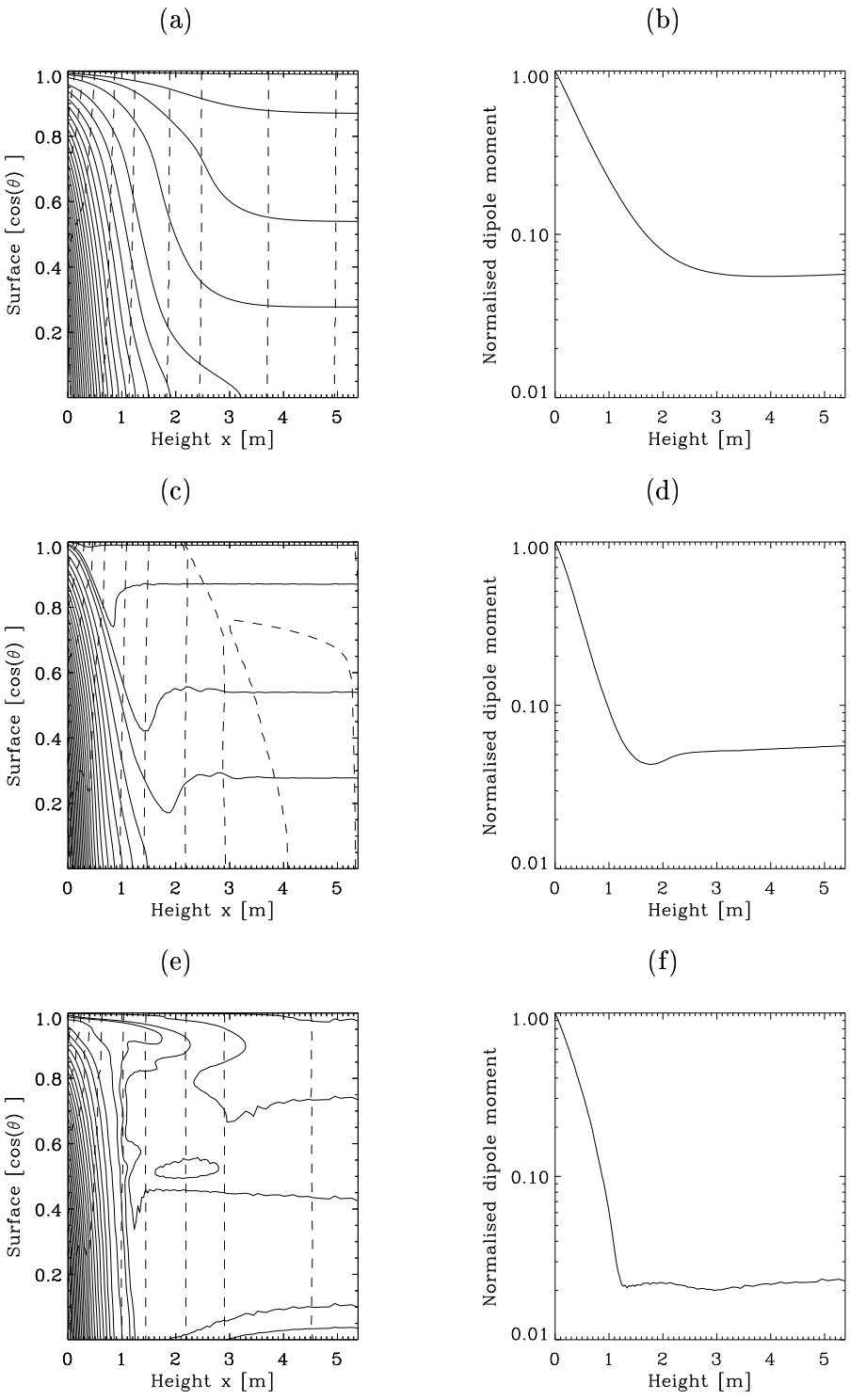

Figure 3.3: Illustration of one step in the bootstrapping algorithm. Magnetic field lines (*solid*) and density contours (*dashed*) (*left*) and the magnetic dipole moment as a function of height (*right*) for $m = 1.6$ at $t = 0$ (*top*) $m = 2.2$ at $t = 100$ (*middle*), attained by adding mass at the outer boundary, and $m = 4.1$ at $t = 100$ (*middle*) and $t = 400$ (*bottom*).

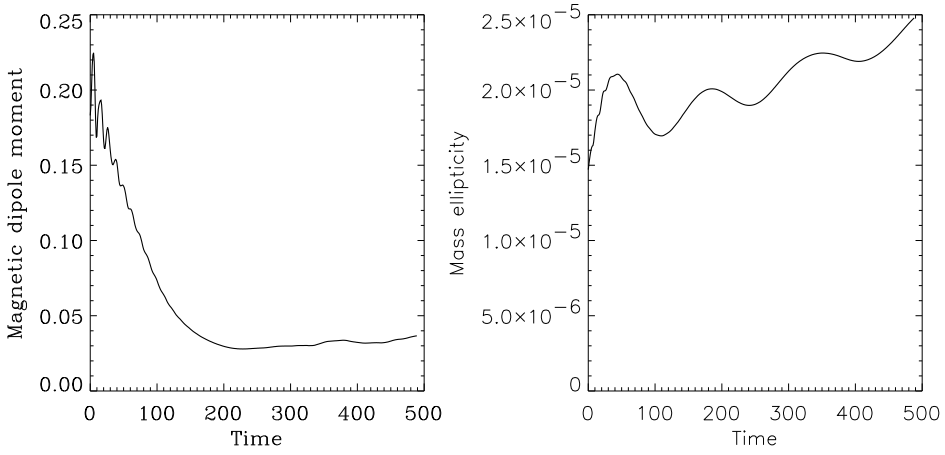

Figure 3.4: Evolution of the magnetic dipole moment, as measured 150 cm above the stellar surface (*left*), and the mass ellipticity (*right*), when mass is added to a $m = 0.16$ equilibrium.

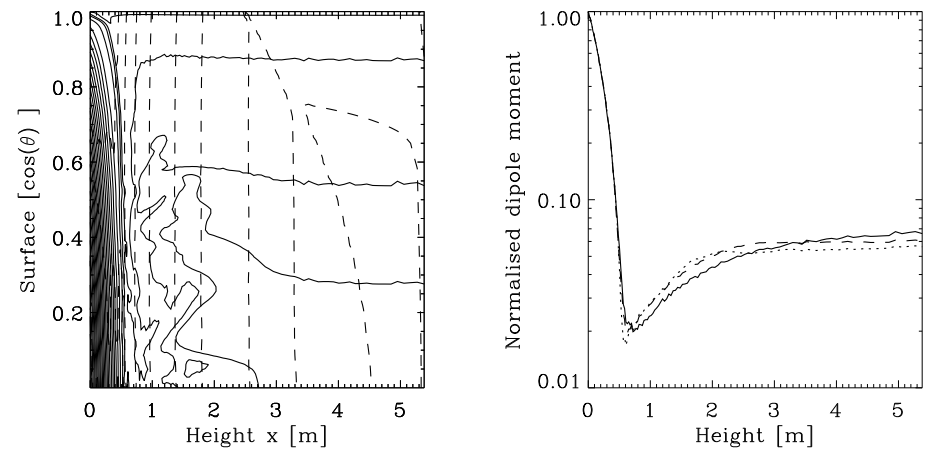

Figure 3.5: (*Left.*) Magnetic field lines (*solid*) and density contours (*dashed*) when mass is added to a $m = 0.16$ equilibrium, reaching $m = 4.1$ at $t = 400$. (*Right.*) Magnetic dipole moment as a function of altitude when the $m = 4.1$ configuration (*dotted*) relaxes in the presence of an outflow outer boundary condition, at $t = 500$ (*dashed*) and $t = 900$ (*solid*).

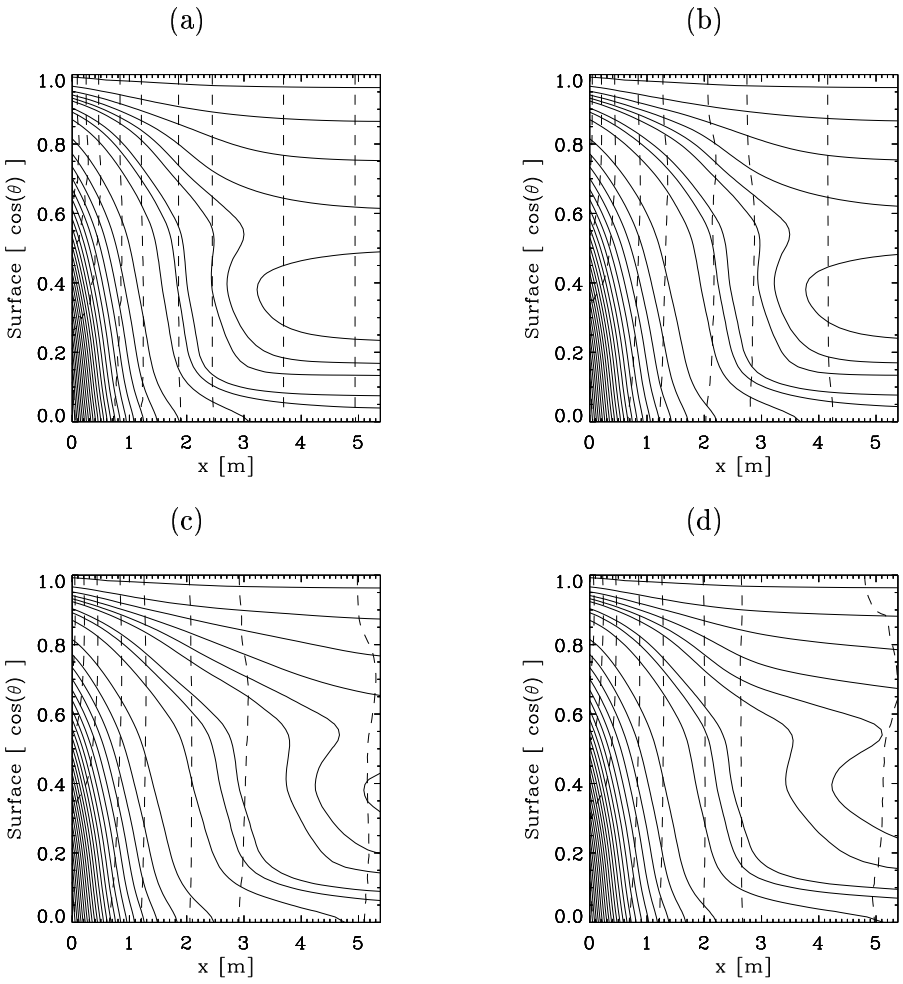

Figure 3.6: Evolution of a bubble ($3 \leq x \leq 5$ m, $0.2 \leq \cos(\theta) \leq 0.5$) with $m = 1.6$ initially, after a uniform density increase at $t = 0$ to $m = 3.2$, plotted for $t = 0, 3, 6, 9$ [(a) - (d)].

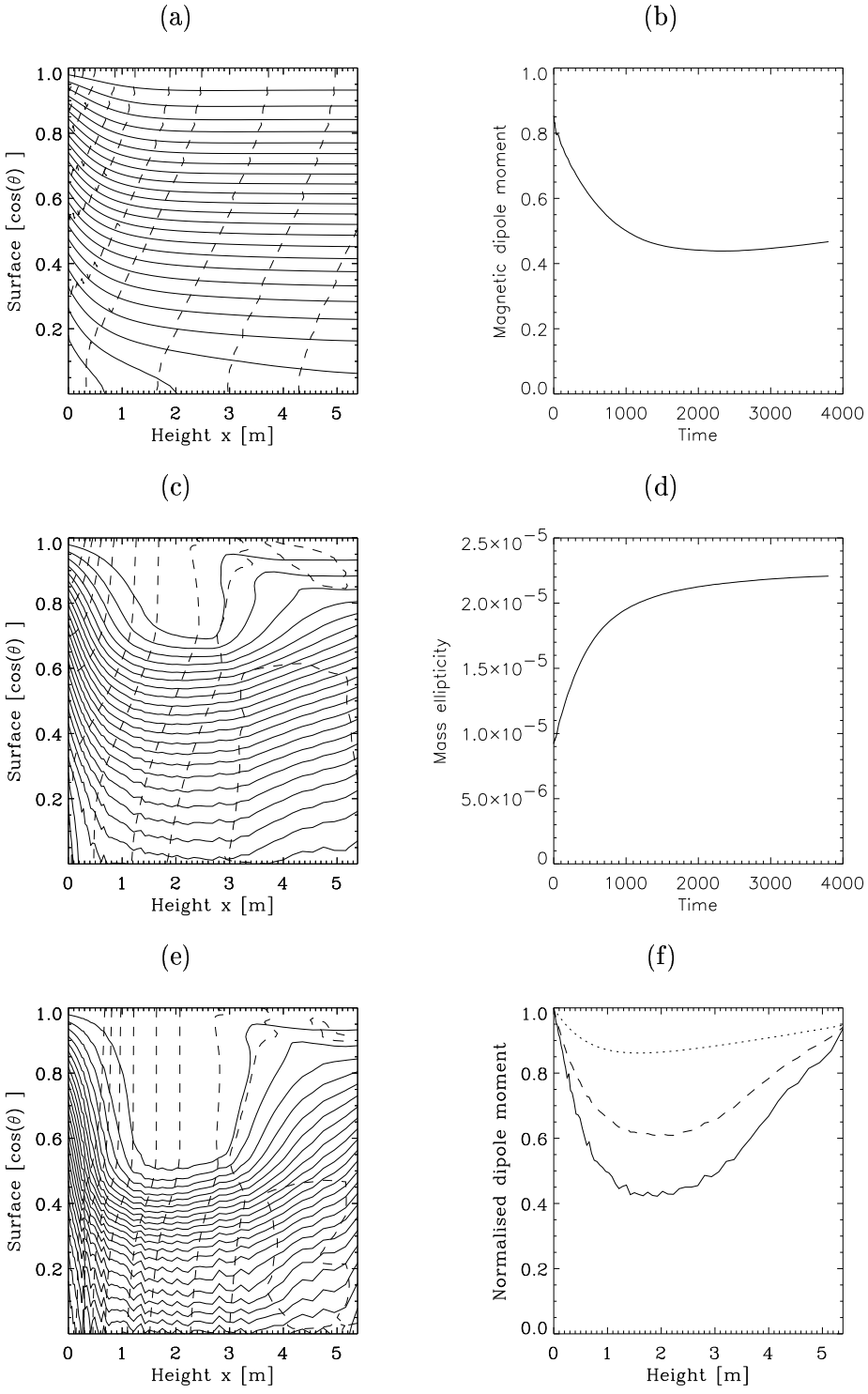

Figure 3.7: Magnetic field evolution with mass added to the outer boundary. (a), (c), (e): Magnetic field lines (*solid*) and density contours (*dashed*) for t = 0, 500, 2000 corresponding to $m = 0.16, 0.22, 0.4$ respectively. (b) Dipole moment as a function of time, measured at 300 cm above the stellar surface. (d) Quadrupole moment as a function of time. (f) Dipole moment as a function of height for t = 0 (*dotted*), 500 (*dashed*) and 2000 (*solid*).

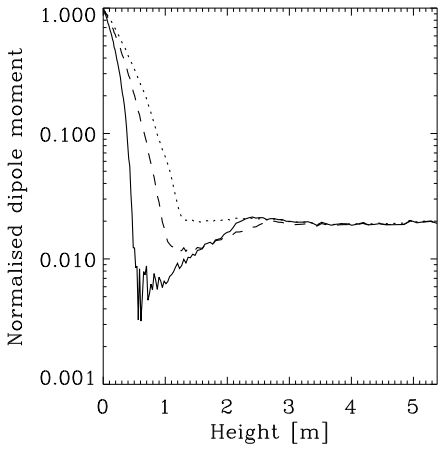

Figure 3.8: Dipole moment versus altitude when mass is added to the configuration in figure 3.3(c), at $t = 0$ (*dotted*), $t = 100$ (*dashed*) and $t = 500$ (*solid*), corresponding to $m = 2.23, 2.86$, and 4.76 respectively.

We explore the stability in the context of several experiments: (i) we load the equilibria into ZEUS-3D subject to the small numerical perturbation converting between the two grids; (ii) we identify any unstable modes aided by the Bernstein et al. (1958) stability criterion; and (iii) we consider the fate of large perturbations.

3.5.1 Linear stability: numerical experiment

Equilibria of the kind depicted in figure 3.1(a), where the magnetic field is distorted by steep gradients, are usually expected to be unstable. To assess this here, we track the evolution of $W_{\rm g}$, $W_{\rm k}$, and W_B, the gravitational, kinetic and magnetic potential energies respectively, as the magnetic mountain evolves in ZEUS-3D,

$$W = W_B + W_{\rm g} + W_{\rm k},$$

where we define

$$W_{\rm g} = \int d^3\mathbf{x}\,\rho\phi, \quad W_{\rm k} = \int d^3\mathbf{x}\,(\rho v^2/2),$$

and

$$W_B = \int d^3\mathbf{x}\,(B^2/8\pi).$$

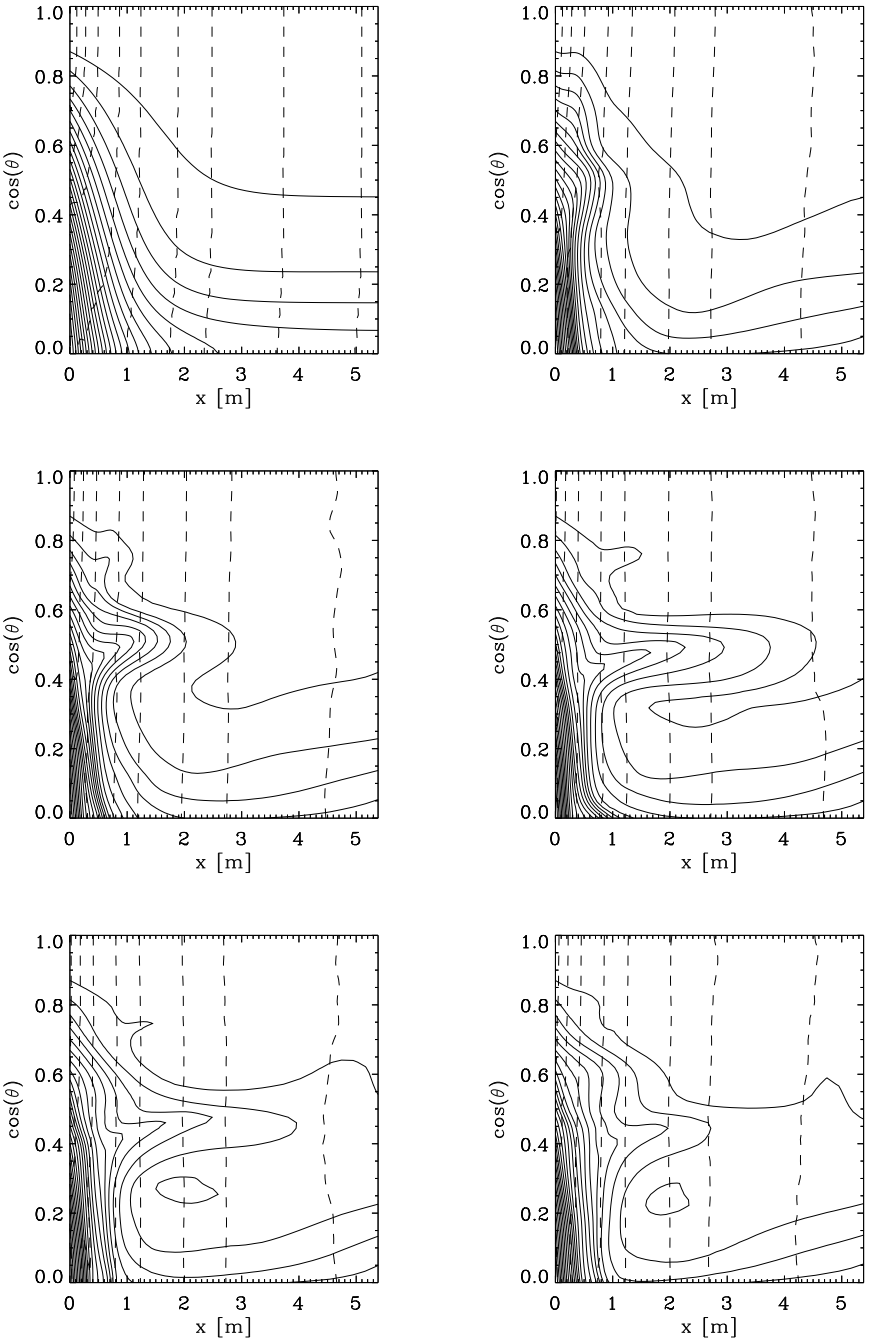

Figure 3.9: Evolution of the Parker instability for $M_a = 1.12 M_c$ with the density increased uniformly across the grid by a factor of 5. Snapshots of the magnetic field lines are shown at $t = 0, 120, 160, 200, 240$ and 280 Alfvén times (top left to bottom right).

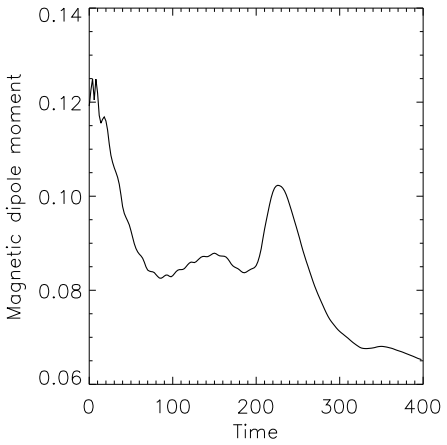

Figure 3.10: Magnetic dipole moment as a function of time during the blistering of the Parker instability displayed in figure 3.9.

Key observables of the system, such as the magnetic dipole moment μ, defined in (3.21), and the mass ellipticity ϵ, are also tracked. We neglect the pressure term $W_{\rm p} = \int d^3\mathbf{x}\, P \log P$ in what follows.

We begin, as an example, with the equilibrium for $m = 1.6$ [figure 3.3 (a)], our starting point for adding mass through the outer boundary in section 3.4.2. Figure 3.11 displays $W_{\rm g}$, $W_{\rm k}$ and W_B a function of t for this case. The evolution proceeds as follows. The equilibrium imported into ZEUS-3D is not exact due to grid resolution, imperfect convergence in the Grad-Shafranov code, and numerical discrepancies when translating between the codes (see appendix 3.7). Initially, during the first oscillation, $W_{\rm g}$ and W_B are converted to $W_{\rm k}$. When the oscillation overshoots, the energy flow reverses direction. In ideal MHD, where there is no dissipation, the oscillation persists. In ZEUS-3D, where there is still numerical dissipation and energy is radiated through the outer boundary, the oscillations are damped, as in figure 3.11. (Experiments demonstrating this numerical dissipation are reported in appendix 3.7.) Note that $W_{\rm k}$ oscillates at twice the frequency of $W_{\rm g}$ and W_B, because the leading term in $W_{\rm k}$ is quadratic in perturbed quantities ($\propto \delta v^2$) whereas $W_{\rm g}$ ($\propto \delta\rho$) and W_B ($\propto B\delta B$) are linear.

The dipole moment, normalised to its value at the stellar surface, is plotted in figure 3.12 for $m = 1.6$. The oscillation period equals that of W_B for the reason above. The kinks in the curve occur when the magnetic

field reflects off the boundaries at the pole and equator. The oscillations are identified as acoustic modes (see section 3.5.2).

3.5.2 Global MHD oscillations

We explore here the physical nature of the oscillations and how their amplitude and period depend on $M_{\rm a}$.

Figure 3.13 shows the time evolution of μ for several $M_{\rm a}$ values. The key result is that the equilibria are marginally stable: the buried field is not disrupted significantly but the configuration oscillates about its equilibrium state. Two modes are clearly present: (i) a short period oscillation, with fixed period $13\tau_0$ for all $M_{\rm a}$ (and thus ρ), which is an acoustic mode with velocity $c_{\rm s}$; and (ii) a longer period oscillation, with period increasing with $M_{\rm a}$ as displayed in figure 3.15, which is an Alfvén mode. The Alfvén oscillation frequency is fit by $f_{\rm A} \approx 0.003\tau_0^{-1}(M_{\rm a}/M_{\rm c})^{-1/2}$ Hz for $a = 50$, which, when scaled to a realistic neutron star, yields $f_{\rm A} \approx 17(M_{\rm a}/M_{\rm c})^{-1/2}$ Hz.

There are a few numerical considerations. The magnetic dipole moment artificially rises from its equilibrium value towards the surface value for $0.2 \lesssim m \lesssim 1.6$. under the following conditions. (i) There is insufficient resolution close to the stellar surface, e.g. a linear grid in r with G_x is not good enough. A comparison of figures 3.13 (logarithmic r grid) and 3.14 (linear r grid) brings out this point. μ and the quadrupole moment exhibit oscillations whose amplitude grows and mean values change substantially for a linear grid, whereas the amplitudes are damped and the mean remains constant for a logarithmic grid. (ii) The outer boundary condition is set to *outflow*, leading to a small amount of mass loss. While the mass loss amounts to $\lesssim 2\%$ by $t = 10^3$, it allows the field lines at the magnetic equator to flare up towards the pole and destabilize the equilibrium. These problems are overcome by (i) using a logarithmic scale in r to increase the grid resolution near the stellar surface, (ii) managing carefully the translation from logarithmic scaling in the Grad-Shafranov grid to the ZEUS-3D grid (see appendix 3.7), and (iii) setting the outer boundary condition to *inflow*.

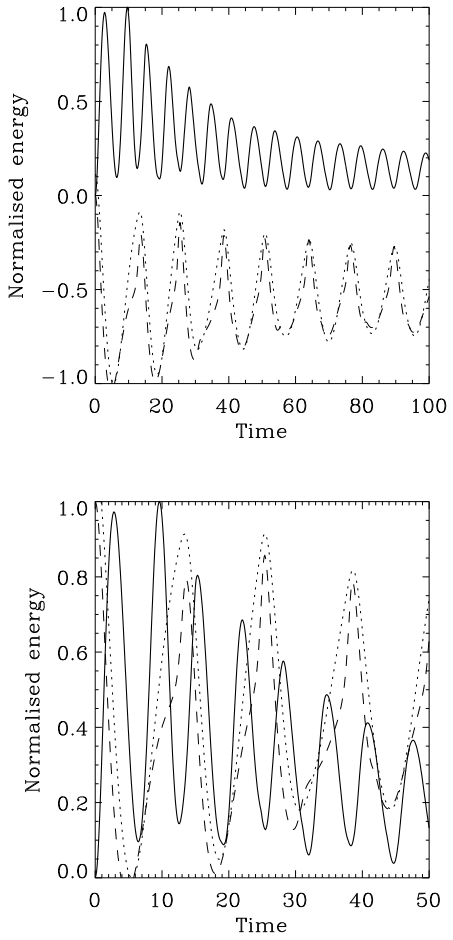

Figure 3.11: Kinetic (*solid*), magnetic (*dashed*) and gravitational potential (*dotted*) energies, normalised to their maximum values as a function of time for $m = 1.6$, $G_x = G_y = 128$. The oscillation amplitudes are scaled and the bottom panel zooms in for clarity.

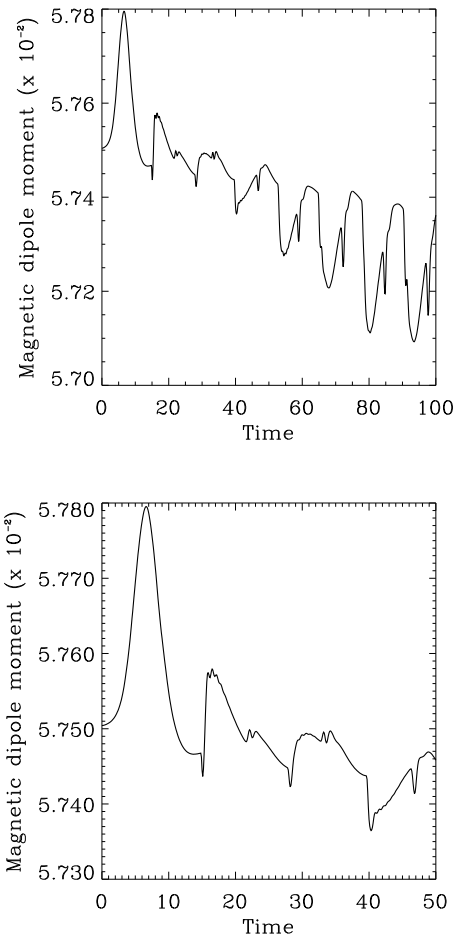

Figure 3.12: Magnetic dipole moment normalised to its surface value, plotted as a function of time for $m = 1.6$, $G_x = G_y = 128$. The bottom panel zooms in.

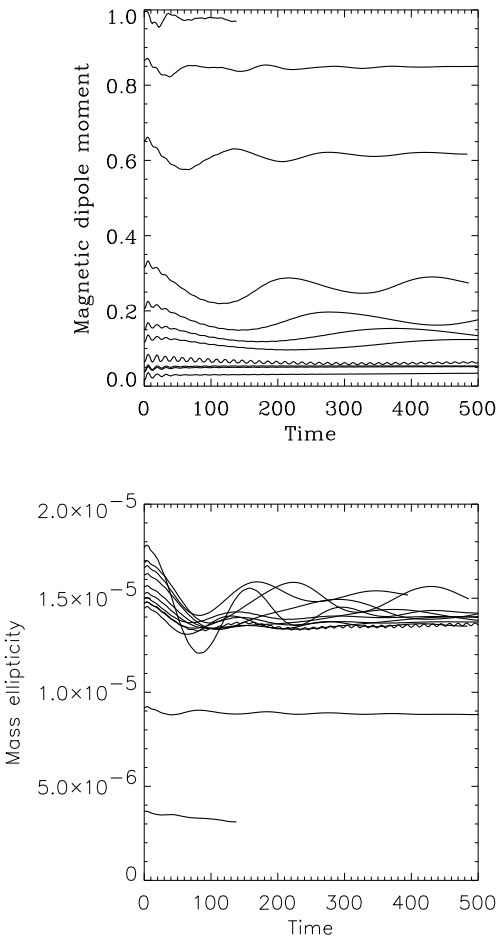

Figure 3.13: Magnetic dipole moment (*top*) and mass quadrupole moment (*bottom*) as a function of time for M_a/M_c = 0.053, 0.16, 0.32, 0.48, 0.64, 0.8, 0.96, 1.12, 1.6, 2.4, 3.2, and 4.0 (top to bottom for μ, and bottom to top for the quadrupole moment). Grid resolution: $G_{x,y}$ = 128, with logarithmic scaling in altitude.

Identifying MHD modes

To classify the oscillation modes discovered in the previous section, we need the dispersion relation of small-amplitude MHD waves in the limit (verified by the simulations) where the wavelength of the ρ and $\mathbf{B}$ perturbations is large compared with k^{-1}. Upon analysing the perturbation in Fourier modes, $\boldsymbol{\xi}(\mathbf{r},t) \propto \boldsymbol{\xi}(\mathbf{k},\omega)e^{-i(\mathbf{k}\cdot\mathbf{r}-\omega t)}$, the momentum balance equation reads

$$\rho_0\omega^2\boldsymbol{\xi} = \mathbf{k}c_{\rm s}^2\rho_0\boldsymbol{\xi}(\mathbf{k},\omega) + \ (4\pi)^{-1}\{[\mathbf{k}\times(\mathbf{k}\times(\boldsymbol{\xi}\times\mathbf{B}_0))]\times\mathbf{B}_0\}\,, \qquad (3.23)$$

yielding the dispersion relation is

$$(\omega^2 - k_\parallel^2 v_{\rm A}^2)[\omega^4 \ - k^2(c_{\rm s}^2+v_{\rm A}^2)\omega^2 \ + k^2k_\parallel^2c_{\rm s}^2v_{\rm A}^2] = 0 \qquad (3.24)$$

with solutions

$$\omega^2 = k_\parallel^2 v_{\rm A}^2 \qquad (3.25)$$

for shear Alfvén waves, and

$$\omega^2 = \tfrac{1}{2}k^2(c_{\rm s}^2+v_{\rm A}^2)\ [1\pm(1-\delta)^{1/2}] \qquad (3.26)$$

for fast $(+)$ and slow $(-)$ magnetosonic waves, with

$$\delta = \ \frac{4k_\parallel^2c_{\rm s}^2v_{\rm A}^2}{k^2(c_{\rm s}^2+v_{\rm A}^2)^2}\,, \qquad (3.27)$$

The Alfvén wave is incompressible ($\mathbf{k}\cdot\boldsymbol{\xi}=0$). It propagates analogously to a transverse wave along a string under tension, the magnetic field lines playing the role of the string.

Figure 3.15 shows the oscillation period as a function of m. When analyzing the time-evolution of the MHD configurations, the phase velocity of the waves is used to distinguish which mode is acting. For the Alfvén mode, as the average density increases (with m), $v_{\rm A}\propto M_{\rm a}^{-1/2}$ decreases, and thus the oscillation period increases. The Alfvén period (in units of the Alfvén

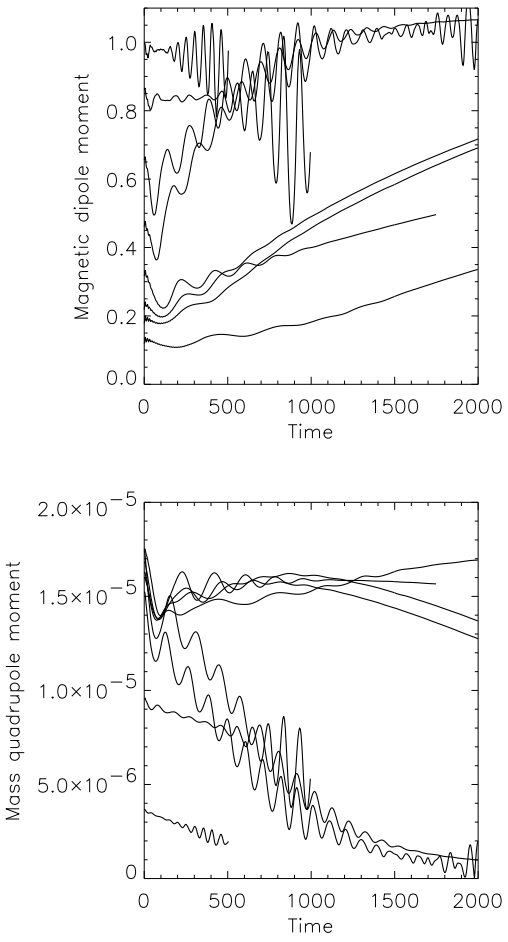

Figure 3.14: Magnetic dipole moment (*top*) and mass quadrupole moment (*bottom*) as a function of time for $M_a/M_c = 0.053,\ 0.16,\ 0.32,\ 0.48,\ 0.64,\ 0.96,\ 1.12$ (top to bottom for μ, and bottom to top for the quadrupole moment). Grid resolution: $G_{x,y} = 64$, with linear scaling in altitude.

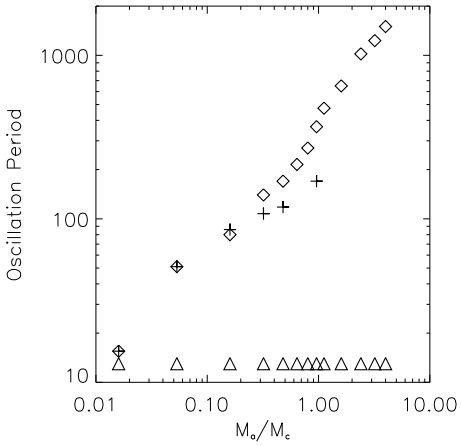

Figure 3.15: Oscillation period (in units of the Alfvén time) as a function of $M_{\rm a}$, with linear (*crosses*) and logarithmic (*diamonds*) grid sampling in altitude. The Alfvén period is well fit by $300\tau_0(M_{\rm a}/M_{\rm c})^{1/2}$. The period of the sound mode (*triangles*) is also plotted.

time) is well fit by $300\tau_0(M_{\rm a}/M_{\rm c})^{-1/2}$. The sound speed remains constant throughout all the simulations we perform.

To quantify which modes propagate when a magnetic mountain is perturbed, we estimate the Alfvén velocity across the grid. From the analytic solutions in PM04, we find that the Alfvén speed is

$$\frac{v_{\rm A}}{c_{\rm s}} \approx 9.8\times10^{-4}\left(\frac{M_{\rm a}}{10^5 M_\odot}\right)^{-1/2}\left(\frac{b}{3}\right)^{-1}\left(\frac{a}{2\times10^4}\right)^{2}\left(\frac{B_*}{10^12\,{\rm G}}\right)^{3/2} \times\exp(b\sin^2\theta)\exp(x/h_0)\,. \tag{3.28}$$

For $m = 0.16$, the corner values for $v_{\rm A}(x,y)$ (in units of $c_{\rm s}$) are $v_{\rm A}(0,0) \approx 6\times10^{-3}$, $v_{\rm A}(0,1) \approx 6.13\times10^{-4}$, $v_{\rm A}(10,0) \approx 135$, and $v_{\rm A}(10,1) \approx 14$. The plasma thus varies with density (and $M_{\rm a}$) from being high-β at the stellar surface to low-β far from the star, given that $c_{\rm s}$ is uniform. For comparison, the numerical, equilibrium values for $v_{\rm A}(x,y)$ are $v_{\rm A}(0,0) = 0.024$, $v_{\rm A}(0,1) = 5.3\times10^{-3}$, $v_{\rm A}(10,0) = 110$, and $v_{\rm A}(10,1) = 3.77$. They are given within 20 per cent by (3.28), which provides theoretical support for the observed MHD oscillations. Immediately above the surface, the magnetic field strength and hence $v_{\rm A}$ are enhanced.

Bernstein energy principle

Another perspective on stability is afforded by the MHD energy principle (Bernstein et al. 1958). This test is quick to apply if the system is unstable: one needs to find just one perturbation whose energy variation satisfies $\delta W < 0$. On the other hand, to prove stability, it must be shown that every perturbation has $\delta W > 0$, which is impractical in our problem.

3.5.3 Transient Parker instability

In the experiments described in section 3.4.4, it is observed that increasing the density uniformly by a factor $\gtrsim 4$ causes Parker instabilities to occur. Figure 3.9 consists of a sequence of frames illustrating the evolution of the Parker instability for an equilibrium state whose density is uniformly increased five-fold. The wavelength λ of the instability subtends ≈ 1 radian, i.e. $\lambda \approx 0.3 R_*$. The density profile is exponential, while the magnetic field is mostly confined to a layer of thickness $\sim h_0$, directed perpendicular to ∇P. This is the the classic situation in which Parker instabilities are expected (Mouschovias 1974).

The evolution of μ, as measured at $x = 10 h_0$, is displayed in figure 3.10. Note that, after the Parker blister subsides, μ returns to its original value. The equilibrium is not disrupted permanently; indeed, less than $\sim 1\%$ of the accreted layer and frozen-in magnetic flux is expelled from the simulation domain. In this respect, the instability can be considered transient.

The Grad-Shafranov equilibria imported from PM04 are generated by an algorithm that can follow, by successive relaxation, the full nonlinear evolution of the Parker instability (Mouschovias 1974; Parker 1966). Therefore it is unsurprising that the equilibria are stable; as explained in section 3.5.5, the relaxation algorithm evolves the magnetic field quasistatically through a sequence of intermediate "states" quite close to those that the real solution to the time-dependent MHD equations would pass through. True, the final state is distorted, and one might ask why the buoyancy of the compressed magnetic flux does not drive long-wavelength, slow MHD modes that overturn the accreted matter on the Alfvén time-scale — something that does not occur in the ZEUS-3D runs (except for the transient in figure 3.9). The explanation is that the equatorial magnetic 'tutu' represents the end state of a Parker instability that occurs quasistatically as we add material. The

tutu is the analogue of the stable magnetic 'blisters' which form when the plane-parallel Parker instability saturates, while the polar mountain is the analogue of the material that drains into the magnetic valleys.

3.5.4 Large perturbations

Next, we investigate what happens when the Grad-Shafranov equilibria are perturbed far from equilibrium, i.e. $\delta B/B \sim 1$; the perturbations considered thus far are small, arising mainly from imperfect translation between the grids of the two codes. We perturb the magnetic field, while simultaneously respecting the boundary conditions, by setting

$$\mathbf{B} \mapsto \mathbf{B}\{1 + \delta \sin[\pi(r - R_*)/(r_\mathrm{m} - R_*)] \sin\theta\}\,. \tag{3.29}$$

Figure 3.16(a) shows the fate of this perturbation for different amplitudes δ. Note that the perturbation does not strictly respect flux-freezing because it changes $dM/d\psi$ slightly. Nonetheless, even for significant perturbations, the equilibria are not disrupted — a significant and robust result. For $\delta < 0.2$, μ settles back to within 20 per cent of its initial value. For $\delta > 0.2$, μ does not settle back to its initial value, but it does settle down to some steady value. The evolution also depends on the sign of δ. The perturbation is a low-order spatial mode (in r and θ) and either compresses ($\delta > 0$) or relaxes ($\delta < 0$) the magnetic field, with compression causing a back-reaction which increases μ [as can be seen in figure 3.16].

The above perturbation (3.29) induces an effective redistribution of mass in flux tubes. To test this, we perturb the magnetic potential ψ in the Grad-Shafranov code according to

$$\psi \mapsto \psi\{1 + \delta \sin[\pi(r - R_*)/(r_\mathrm{m} - R_*)] \sin\theta\} \tag{3.30}$$

and iterate once to calculate ρ self-consistently without changing $dM/d\psi$, so that the above mass redistribution is performed self-consistently. We then load the *self-consistent* perturbed equilibrium into ZEUS-3D as before. The results are shown in figure 3.16(b). For a given δ, the amplitude of the oscillations is reduced, confirming that the mass-redistribution contributes to back-reaction. The main effect is to bring the final value of μ closer to its initial value for $\delta \geq 0.5$. The evolution still depends on the sign of δ,

suggesting that mass-flux redistribution remains somewhat important.

3.5.5 Comparison with Grad-Shafranov relaxation algorithm

Finally, we test the assertion made in PM04 that the iterative solution of the Grad-Shafranov equation coupled to a flux-freezing condition provides a good proxy for the true time-dependent behaviour. A similar assertion was made by Mouschovias (1974) concerning the plane-parallel Parker instability. We begin with a magnetic dipole with excess mass loaded into the polar flux tube in both the Grad-Shafranov code and in ZEUS-3D. In ZEUS-3D, this is effectively the same as applying a uniform density increase (section 3.4.4) to the $m = 0$ equilibrium, ending up with $m = 1.6$ in this example. We plot μ as a function of time (ZEUS-3D) and iteration number (Grad-Shafranov) in figure 3.17. An underrelaxation parameter $\Theta = 0.99$ is selected by trial and error to give a comparable rate of convergence in the two codes. The initial progress to equilibrium is similar in both cases. However, after 100 iterations (or equivalently $t \geq 100$), μ fluctuates more in ZEUS-3D than in the converging Grad-Shafranov code. In ZEUS-3D, the added mass initially squashes the field into a layer $\sim 1/4$ the thickness of the equilibrium layer [Figure 3.3(a)]. The field then bounces back and transient Parker-like instabilities occur, as we expect (ρ increases by a factor $\gtrsim 4$). This is best illustrated in figure 3.18, which shows a snapshot of the configurations at $t = 100$ (in ZEUS-3D) and iteration 100 (in the Grad-Shafranov code). Notice how the field lines are bent by the transient instabilities in ZEUS-3D but remain smooth in the Grad-Shafranov code. This comparison also illustrates why Grad-Shafranov equilibria are a necessary starting point for ZEUS-3D when aiming to reach stable equilibria for large $M_{\rm a} \gtrsim 10^{-4} M_{\odot}$.

3.6 Conclusions

We find that, when the MHD equilibria computed in PM04 are perturbed, they are marginally stable. The magnetic field remains essentially undisrupted, with the exception of transients that expel a tiny fraction of flux

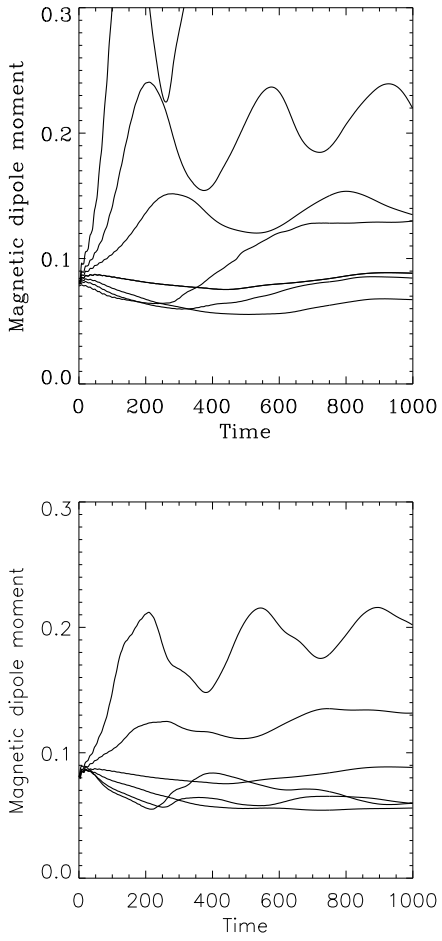

Figure 3.16: (*Top.*) Magnetic dipole moment as a function of time for perturbation amplitudes $\delta = -1.0, -0.5, -0.25, 0, 0.25, 0.5, 1.0$ (*bottom to top*), when the magnetic field is perturbed as described in (3.29) but ρ is not altered. (*Bottom.*) As above, but with the magnetic field perturbed via (3.30) and then iterated once through the Grad-Shafranov code to obtain the self-consistent ρ, for $\delta = -0.2, -0.1, 0, 0.1, 0.25, 0.5$ (*bottom to top*).

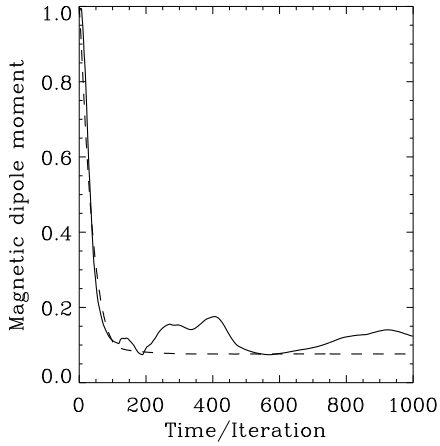

Figure 3.17: Magnetic dipole moment as a function of time in ZEUS-3D (*solid*) and as a function of iteration number in the Grad-Shafranov code with underrelaxation parameter $\Theta = 0.99$ (*dashed*).

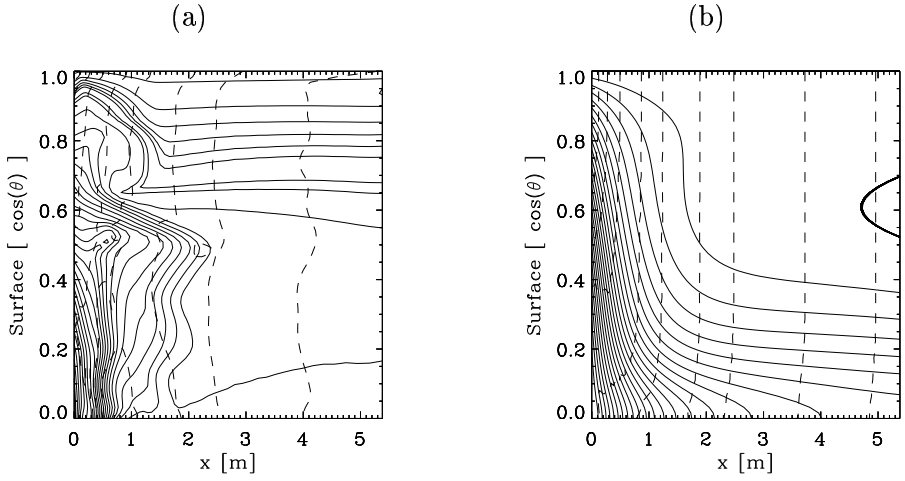

Figure 3.18: Magnetic field lines (*solid*) and density contours (*dashed*) for $t = 100$ in ZEUS-3D (*left*) and the 100^{th} iteration in the Grad-Shafranov code (*right*). The initial state is a magnetic dipole with excess mass ($m = 1.6$) in the polar flux tubes ($\psi_*/\psi_{\text{a}} = 3$).

and matter. MHD oscillations, including both acoustic and Alfvén modes, cause μ and ϵ to oscillate about their mean values. Using ZEUS-3D, we extend the results of PM04 to larger $M_{\rm a}$ in two ways. (i) We add mass through the outer boundary at an artificially accelerated rate which is still slow compared to the MHD equilibration time-scale and oscillation period (as in a real neutron star). We use a bootstrapping method in which the mass is progressively added then allowed to settle to equilibrium. (ii) We increase the density instantaneously uniformly, and then allow the configuration to settle to equilibrium. The equilibria we obtain are stable to Parker modes, as one might expect given that they are the output of a Grad-Shafranov code which follows the full nonlinear evolution of Parker instabilities. The MHD oscillations have potentially interesting observational consequences, some of which are taken up in chapters 4, 5, and 6 of this thesis, e.g. for type I X-ray bursts and gravitational waves.

3.6.1 Limitations

The work presented above and in PM04 and chapter 2 can be generalised by relaxing certain key assumptions. Some areas to explore include resistive effects (e.g. Ohmic diffusion) (e.g. Konar and Bhattacharya 1997), sinking of accreted material through a "soft" stellar surface (e.g. Konar and Choudhuri 2004), Hall currents (e.g. Rheinhardt et al. 2004), nonaxisymmetry, and other equations of state. For example, by assuming a hard surface, we end up with densities at the base of the accreted layer that can be unphysically high. It is well known that MHD equilibria can be stable in two dimensions yet unstable in three dimensions. The magnetization of the accreted plasma also warrants inclusion; it has been ignored by all authors except Uchida and Low (1981). Thermomagnetic drifts in the field, which are important in the lower-density H and He envelope, could produce strong temperature gradients which may affect the stability of the accreted mound.

The main bottleneck hindering progress towards Grad-Shafranov equilibria for $M_{\rm a} \gtrsim 10^{-3} M_\odot$ is grid resolution at the magnetic equator. At present, we believe that the only way to alleviate this is by appropriate logarithmic gridding in θ.

Ohmic dissipation due to electron-phonon and electron-impurity scattering (e.g. Bhattacharya and Srinivasan 1995) is not modelled in this chapter, to keep the problem manageable. Ultimately, it should be. It is important

for magnetic structures ~ 100 cm in size, which develop for $M_{\rm a} > 10^{-2} M_\odot$ (Brown and Bildsten 1998; Cumming et al. 2001; Melatos and Payne 2005). Note, however, that nonideal effects are already present in our calculations accidentally: the grid introduces numerical dissipation, because a field line is defined by linear interpolation between grid points and the error in this interpolation effectively allows matter to move across field lines.

3.6.2 Instabilities in three dimensions

This chapter must be generalised to three dimensions before the stability question is truly settled. As a trivial example, by restricting ourselves to two-dimensional equilibria with $B_\phi = 0$, we suppress unstable modes involving the toroidal magnetic field. The Parker instability in the galactic disc has been studied in three dimensions by Kim et al. (1998), and many simulations of toroidal and nonaxisymmetric field structures appear in the plasma physics literature. These can be studied in ZEUS-3D and will be explored in a future paper.

The existence of stable magnetic mountains with persistent (albeit oscillating) mass quadrupole moments ($\epsilon \lesssim 10^{-6}$) raises the prospect that accreting millisecond pulsars (Wijnands and van der Klis 1998) are sources of gravitational radiation. This application is pursued in chapters 5 and 6 of this thesis. Likewise, the existence of a stable equatorial magnetic belt of intense magnetic field, with its ability to impede thermal transport, has interesting implications for the persistence of millisecond oscillations in the tails of type I thermonuclear X-ray bursts in LMXBs (Muno et al. 2002). This application is pursued in chapter 4 of this thesis.

3.7 Appendix: Magnetic burial in ZEUS-3D

In this appendix, we explain briefly how to simulate the problem of magnetic burial in ZEUS-3D, so that the reader can reproduce and generalize our results.[2] For details on the general design and operation of ZEUS-3D, please consult Stone and Norman (1992a,c).

[2]This work also serves as a prototype of a simulation pipeline being developed by the Australian Virtual Observatory. We have demonstrated a preliminary version of this pipeline in which hydromagnetic equilibria generated by the time-independent, Grad-Shafranov code described in PM04 are output in a standard format (VOTable) and fed into ZEUS-3D to be evolved in time.

After discussing the control variables in ZEUS-3D, we provide several test cases for reference. The Parker instability in rectangular coordinates, whose nonlinear evolution was computed by Mouschovias (1974, 1996), tests the basic functionality of ZEUS-3D. An unmagnetized, isothermal atmosphere in spherical coordinates tests the boundary conditions on ρ and $\mathbf{v}$. A magnetized, isothermal atmosphere in spherical coordinates tests the boundary conditions on $\mathbf{B}$ and yields the equilibrium state for $M_{\rm a} = 0$.

3.7.1 Control variables

The number of active grid zones in each coordinate, `ggen1:nbl` and `ggen2:nbl` for `i` and `j` respectively, is $G_x \times G_y$ (typically 128×128). In addition, there are two ghost zones at each edge of the grid, for setting boundary conditions. The zones in, say, the `i` direction (r in spherical coordinates) can scale geometrically using `ggen1:x1rat`, such that the width of zone `(i+1)` is `x1rat` times zone `i`. This is how we implement logarithmic coordinates to increase grid resolution near the stellar surface, and to match input data from the Grad-Shafranov code in PM04 (section 3.7.7). There are several conditional compilation switches which control the geometry. To implement two dimensions, enable `KSYM`, and set the number of zones in the third ordinate, `ggen3:nbl` to one. For Cartesian coordinates, enable `XYZ`; for spherical polar coordinates, enable `RTP`. When printing out the grids, we use `nxpx` = `nypx` = 400 pixels and suppress the third dimension (z or ϕ) by setting `pixcon:ipixdir` = 3.

The results in this chapter assume an isothermal equation of state for simplicity, thus `ISO` is enabled. Self-gravity, `GRAV`, is disabled. Dimensionless quantities are chosen as follows: $\tilde{\mu}_0 = 1$ (automatic in ZEUS-3D), $\tilde{G} = 1$ (set `grvcon:g`=1), $\tilde{c}_{\rm s} = 1$ (set `eqos:ciso`=1), and $\tilde{h}_0 = 1$ ($h_0 = c_{\rm s}^2 R_*^2/GM_*$). With these choices, the basic units of mass, magnetic field and time become $M_0 = h_0 c_{\rm s}^2/G$, $B_0 = [4\pi c_{\rm s}^4/(Gh_0^2)]^{1/2}$, and $\tau_0 = h_0/c_{\rm s}$. In ideal MHD, the evolution is controlled by the geometry as well as the ratio of magnetic to thermal pressure, $\alpha = B^2/(4\pi c_{\rm s}^2 \rho)$; the physical units of B and ρ do not enter separately. Varying $\tilde{G}$, set to one by default, changes the unit conversions but not the physics. ZEUS-3D may be run as a hydrodynamic code without magnetic fields by disabling `MHD`, reducing the runtime.

The time-step $\Delta t_{\rm Z}$ is adjusted adaptively so that the Courant-Friedrichs-Lewy stability condition is satisfied in every zone, with the tolerance deter-

mined by the Courant number (`hycon:courno` = 0.5 by default). In the case of an isothermal atmosphere and subsonic fluid motions, it is set by $\max(c_s, v_A)$. Since one has $v_A \propto 1/\rho \propto e^{\tilde{x}}$ in a typical isothermal atmosphere, the code is limited in the range of altitudes and densities that it can faithfully simulate. The grid is dumped at times separated by `pixcon:dtpix` and the code runs for a maximum time `pcon:tlim`.

3.7.2 Verifying the Parker instability in a rectangular geometry

A test case which is easy to implement (and relevant to the problem of magnetic burial) is the Parker or magnetic Rayleigh-Taylor instability (Mouschovias 1974, 1996; Parker 1966). The initial equilibrium state is a semi-infinite, exponentially stratified atmosphere in a uniform gravitational field, with a magnetic field perpendicular to the gravitational force. This configuration is unstable to overturn (slow MHD) modes longer than a critical wavelength $\lambda_{\rm crit}$.

We simulate the Parker instability in the region $-X \le \tilde{x} \le X$, $0 \le \tilde{y} \le Y$. A uniform gravitational acceleration g_y in the y direction is implemented in ZEUS-3D by placing a point mass far from the simulation box, at $\tilde{y} = \tilde{R}_{\rm eff} \gg Y$. The boundary conditions are set to be periodic at $\tilde{x} = \pm X$ (`niib, noib` = 4) and reflecting at $\tilde{y} = 0, Y$ (`nijb` = `nojb` = 1).

In dimensionless units, the equilibrium initial conditions are

$$\tilde{\rho}(\tilde{x}, \tilde{y}) = 0.5 \exp[-\tilde{y}/(1+\alpha)] \tag{3.31}$$

and

$$\tilde{A}_z(\tilde{x}, \tilde{y}) = 2(1+\alpha) \exp[-\tilde{y}/2(1+\alpha)]\,, \tag{3.32}$$

with $\tilde{B}_x = (\nabla \times \tilde{A})_x = -e^{-\tilde{y}/2(1+\alpha)}$. The initial velocity perturbation is taken as $\tilde{v}_y = \epsilon \sin(\pi\tilde{y}/Y)\cos(\pi\tilde{x}/X)$, where, for $\epsilon = 0.3$, the kinetic energy equals 0.23% of the magnetic energy; cf. Mouschovias (1996).

The stability condition is tested by importing a stable equilibrium state, with $X < \lambda_{\rm crit}/2$, and checking that the kinetic energy remains negligible compared to the magnetic and gravitational potential energies. The ratio of the kinetic energy to the total energy is given in table 3.1, scaling as $\tilde{R}_{\rm eff}^{-2}$ for $\tilde{R}_{\rm eff} \lesssim 10^5$. We choose $\tilde{R}_{\rm eff} = 7.6 \times 10^4$ for most runs. This test

$\tilde{R}_{\rm eff}$	$\tilde{W}_{\rm g}$	$\tilde{W}_B$	$\tilde{W}_{\rm k}$
7.6×10^2	-1.03×10^3	12.9	1.03×10^{-1}
7.6×10^2	-1.06×10^4	14.0	1.75×10^{-3}
7.6×10^3	-1.06×10^5	14.0	1.32×10^{-5}
7.6×10^4	-1.06×10^6	14.0	1.22×10^{-6}
7.6×10^5	-1.06×10^7	14.0	1.69×10^{-6}
7.6×10^6	-1.06×10^8	14.0	1.75×10^{-6}

Table 3.1: Gravitational, magnetic and kinetic energies (dimensionless units) resulting from a point mass located at $R_{\rm eff}$ such that $\tilde{M}/\tilde{R}_{\rm eff}^2 = 1$. The initial state is the equilibrium given by (3.31) and (3.32), with $\tilde{\tau} = 10$ and $(X, Y) = (7, 25)$, perturbed as described in the text.

also confirms that the equilibrium is stable for $(X, Y) = (7, 25)$, just below the critical value $\lambda_{\rm crit}/2 = 7.26$ (Mouschovias 1974), and is unstable for $(X, Y) = (8, 25)$.

We also set (X,Y) = (12,25) and verify the output against the results given in figure 3 of Mouschovias (1996). We choose the same units, namely $c_{\rm s} = 6.2\ {\rm km\ s^{-1}}$, $h_0 = 1.3{\times}10^{20}$ cm, $\tau_0 = r_0/c_{\rm s} = 6.5{\times}10^6$ yr, $M_0 = 5.8{\times}10^{20}$ g, $\rho_0 = 2.9 \times 10^{-34}$ g cm^{-3}, $B_0 = 3.7 \times 10^{-14}$ G. (To have exactly the same units as Mouschovias (1996) choose $\tilde{G} = 6.67 \times 10^{-17}$ in ZEUS-3D.) Figure 3.19 shows the ZEUS-3D results at the three times displayed in figure 3 of Mouschovias (1996). The results are in good accord, differing by less than 5 per cent. A mountain is clearly present where the magnetic field bends down in the negative y direction.

3.7.3 Spherical, isothermal atmosphere, zero magnetic field

Having verified a known solution, we now move closer to our goal and consider spherical geometry (`RTP`). We consider first an isothermal atmosphere with no magnetic field to test the effect of the boundary conditions. In spherical geometry, the curvature of the star, characterized by $a = R_*/h_0 \sim 2 \times 10^4$, enters the problem. To cope with this large value, we scale coordinates in ZEUS-3D logarithmically (section 3.7.1). However, the code halts prematurely when the time-step $\Delta t_{\rm Z}$ becomes too small; for $a > 10^3$, it does not run at all. The problem is most severe far from the surface, where ρ is small, $v_{\rm A}$ is large, and $\Delta t_{\rm Z}$ is small. As an initial test

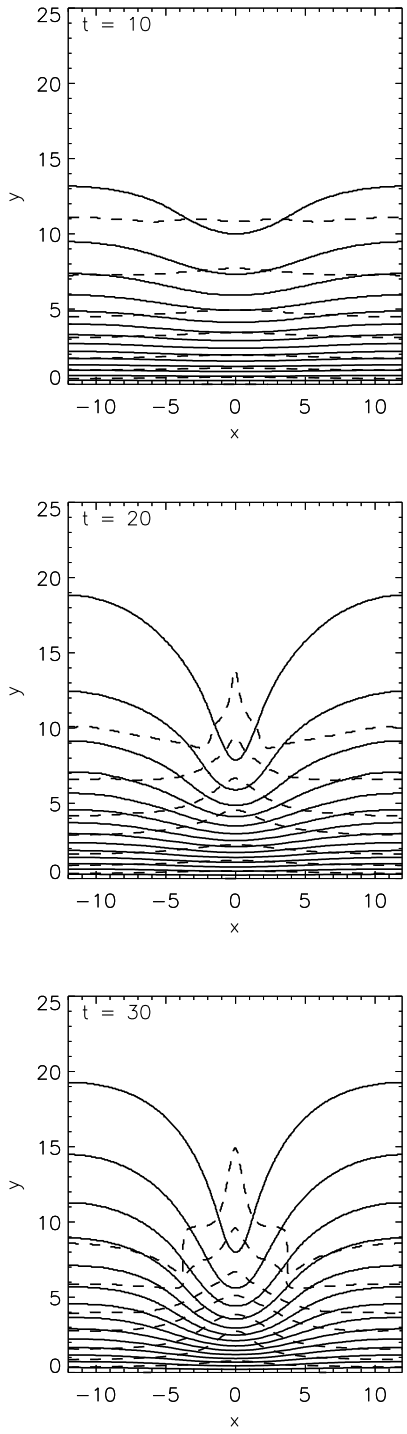

Figure 3.19: Nonlinear evolution of the Parker instability, showing magnetic flux surfaces (*solid*) and isodensity contours (*dashed*) for $(X, Y) = (12, 25)$, $\tilde{\tau} = 10$, 20, 30, and $G_x = G_y = 64$

case in spherical coordinates, we set up a spherical isothermal atmosphere with a negligible magnetic field ($\alpha = 4 \times 10^{-8}$) in 2D (single quadrant). The initial condition is an exponential isothermal atmosphere

$$\tilde{\rho}(\tilde{r}, \theta) = \exp[-a(\tilde{r} - a)/\tilde{r}] \approx \exp(-\tilde{x}) \tag{3.33}$$

threaded by a dipolar magnetic vector potential

$$\tilde{A}_\phi(\tilde{r}, \theta) = 10^{-10} \tilde{r}^{-2} \sin\theta \tag{3.34}$$

The boundary conditions are reflecting at the pole ($B_\theta = 0$, `nijb = 1`) and at the equator ($B_r = 0$, `nijb = 5`), dipolar at the surface (`niib = 3`, i.e. inward flow at zero velocity, fixed density, dipolar magnetic field), and free at the outer boundary ($\tilde{r} = \tilde{r}_{\rm m}$) (`niob = 2`, outward flow). Note that, in ZEUS-3D, a fixed magnetic field must be accompanied by inflow, even if the inflow is at zero speed.

The experiment described in this section aims to calibrate the role of the outer boundary condition. Equations (3.33) and (3.34) almost describe a force-free equilibrium except that matter can evaporate through the outer boundary. However, alternative boundary conditions offered in ZEUS-3D are not appropriate, e.g. inflow artificially pins the magnetic field lines at the boundary. The amount of mass loss is monitored and $\tilde{r}_{\rm m}$ is chosen large to minimize it. There is a trade off between minimizing mass loss as well as simulation runtime (determined primarily by $\Delta t_{\rm Z}$), as illustrated in table 3.2. Logarithmic grid scaling has little effect on the amount of mass which evaporates through the outer boundary. The outer boundary condition artificially increases the dipole moment at large r, as discussed in the main text and illustrated in figure 3.7 (f). The run time is reduced if the magnetic calculations are switched off by disabling `MHD`; the results are indistinguishable. The results in table 3.2 are for $R_* = 6.4 \times 10^8$ cm, $M_* = 6.0 \times 10^{27}$ g, $c_{\rm s} = 2.9 \times 10^4$ cm s^{-1}, $h_0 = 8.4 \times 10^5$ cm. With these choices, the basic units become $M_0 = c_{\rm s}^2/G = 1.2 \times 10^{18}$ g, $\rho_0 = M_0/r_0^3 = 2.1$ g cm^{-3}, $B_0 = [4\pi c_{\rm s}^4/(G r_0^3)]^{1/2} = 1.5 \times 10^5$ G , $\tau_0 = r_0/c_{\rm s} = 29$ s; the alert reader will note that these parameters describe the Earth!

3.7.4 Spherical, isothermal atmosphere, dipole magnetic field

As a prelude to testing the stability of the Grad-Shafranov equilibria found by PM04, we consider the simpler situation of the spherical, isothermal atmosphere (section 3.7.3) threaded by a substantial dipolar magnetic field. Note that this is a valid force-free equilibrium state [$(\nabla \times \mathbf{B}) \times \mathbf{B} = 0$ in (3.4) except at $r = 0$], except for evaporation. This configuration corresponds to the pre-accretion neutron star with $M_{\rm a} = 0$. It serves to calibrate ZEUS-3D and estimate the magnitude of numerical errors.

The relevant neutron star parameters are $R_* = 10^4$ m, $M_* = 1.4 M_\odot$, $c_{\rm s} = 10^8$ cm s^{-1}. With these choices, the basic units become $M_0 = c_{\rm s}^2/G = 1.5 \times 10^{25}$ g, $\rho_0 = M_0/r_0^3 = 9.5 \times 10^{18}$ g cm^{-3}, $B_0 = [4\pi c_{\rm s}^4/(G r_0^3)]^{1/2} = 3.5 \times 10^{18}$ G , $\tau_0 = r_0/c_{\rm s} = 5.4 \times 10^{-7}$ s. However, as discussed in section 3.3.3, we consider a scaled version of the real star with $a = 50$, leaving the physical scale height, $h_0 = c_{\rm s}^2 R_*^2/(GM_*) = 54$ cm, unchanged.

To estimate the errors in the code, we calculate the magnetic dipole moment and mass quadrupole moment and compare to the theoretical values $\mu = 0.5 a^3 \tilde{B}_*$ and $\epsilon = 0$ in table 3.3. For $b = 1$, we obtain $\epsilon = 1.02619$; for $b = 3$, $\epsilon = 1.23373$. The errors are less than 1 per cent. Figure 3.20 shows how the dipole and mass ellipticity vary with time for these cases. The dipole moment is accurate to $< 0.2\%$. The minor variations are caused by numerical jitter (also see figure 3.23) and evaporation at the outer boundary (section 3.5.5. The dependence of the error on grid size is tabulated in table 3.3.

3.7.5 Outer boundary

The outflow condition at the outer boundary has minimal effect on the evolution if the outer boundary is sufficiently far away. To test this, we try several values of $\tilde{r}_{\rm m}$, keeping $\tilde{r}_{\rm m}$ small enough so that the Alfvén time-step, set by the Courant condition with $v_{\rm A} \propto B^2/\rho$, is not too short.

Numerical dissipation occurs in ZEUS-3D for runs longer than $\gtrsim 10^5$ time-steps. Kinks in the magnetic field appear at grid points, as illustrated

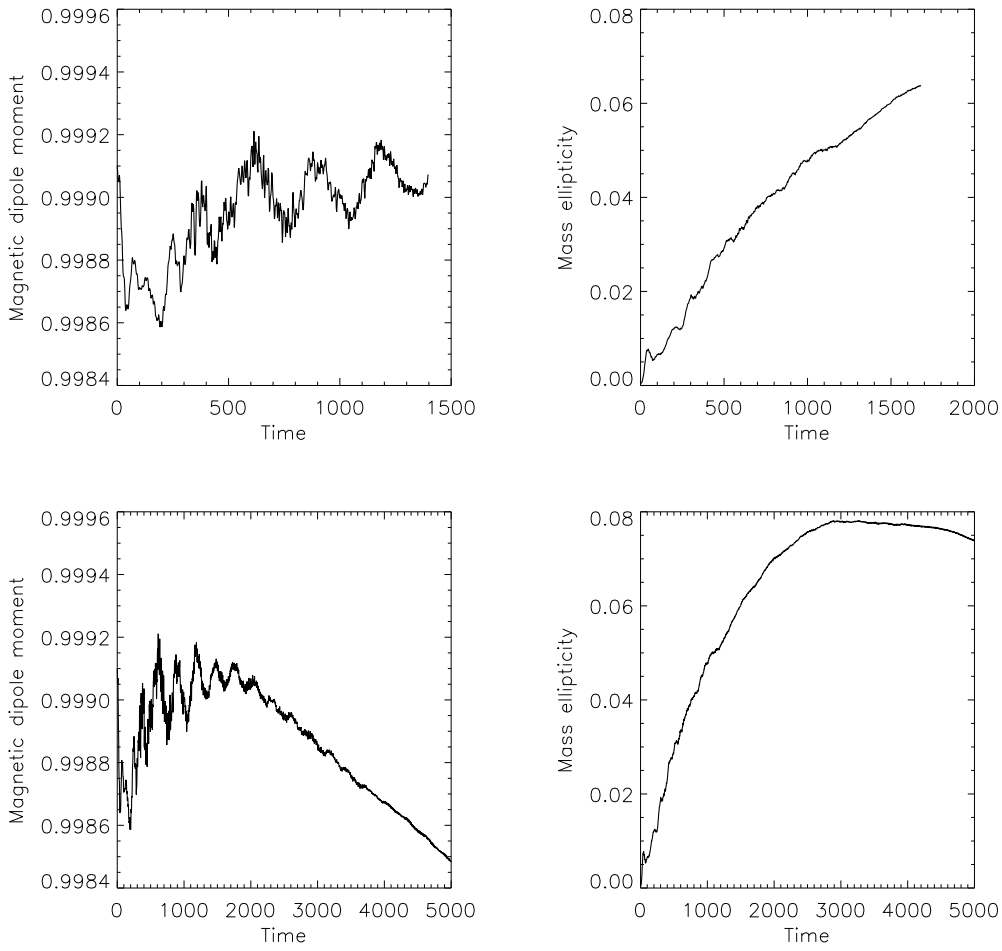

Figure 3.20: The dipole (*left*) and mass ellipticity (*right*) as a function of time for an isothermal atmosphere with $a = 100$ and $\tilde{r}_{\rm m} = 110$ in a 64×64 grid. Parameters: $\rho_0 = 1$ and $B_0 = 0.1$, `x1rat = 1.03`.

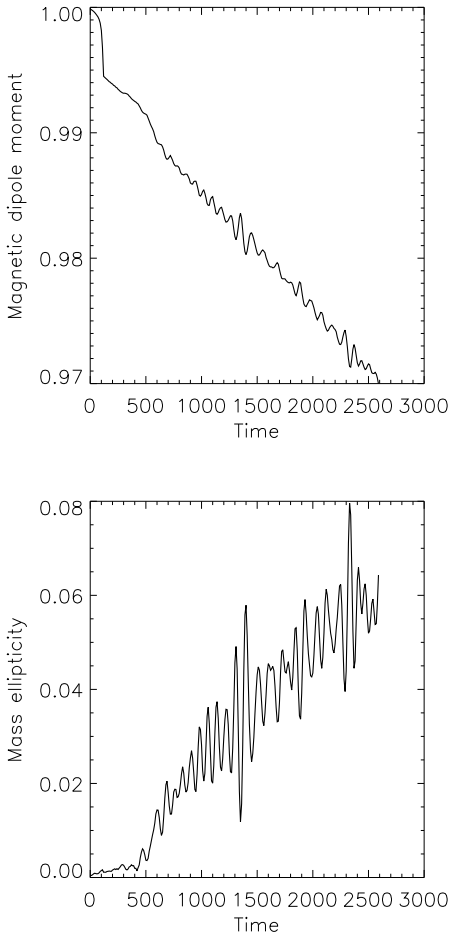

Figure 3.21: The dipole (*left*) and mass ellipticity (*right*) as a function of time for an isothermal atmosphere with $a = 500$ and $\tilde{r}_{\rm m} = 510$ in a 64×64 grid. Parameters: $\rho_0 = 1$ and $B_0 = 0.1$, `x1rat = 1.03`.

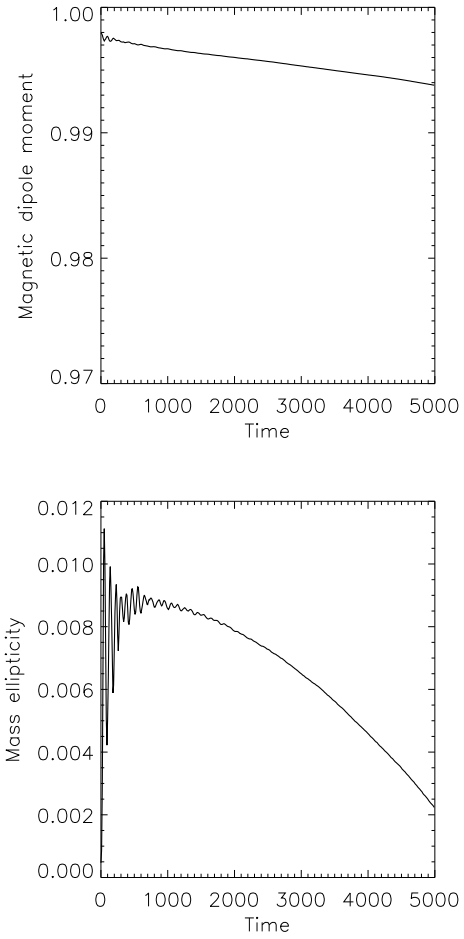

Figure 3.22: The dipole (*left*) and mass ellipticity (*right*) as a function of time for an isothermal atmosphere with $a = 40$ and $\tilde{r}_{\rm m} = 50$ in a 64×64 grid. Parameters: $\rho_0 = 1$ and $B_0 = 0.1$, `x1rat = 1.03`.

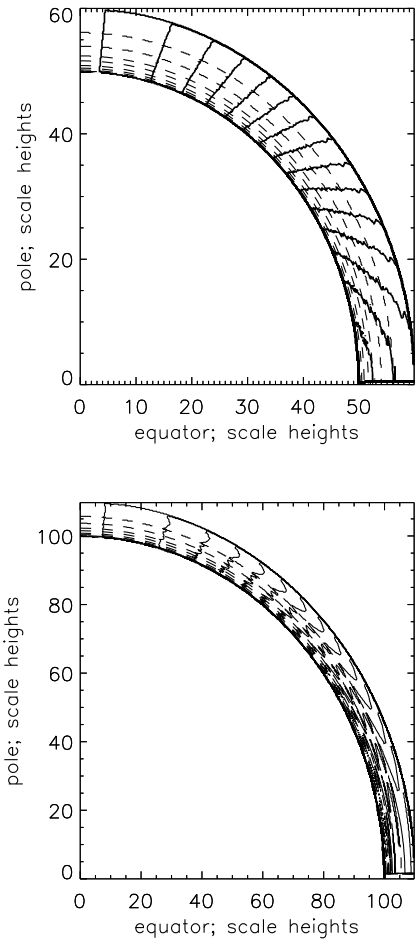

Figure 3.23: Isothermal atmosphere with dipolar magnetic field. The kinks in the magnetic field lines (*solid*) are due to numerical dissipation. Parameters: $a = 50, \tilde{r}_{\rm m} = 60, \tilde{\tau} = 66, 150 \times 150$ grid (*left*); $a = 100, \tilde{r}_{\rm m} = 110, \tilde{\tau} = 66, 50 \times 100$ grid `x1rat = 1.1` (*right*).

a	$\tilde{r}_{\rm m}$	% mass loss	runtime (min)
50	60	0.5	5
50	55	14.1	5
50	52	17.0	5
20	30	1.72	3
40	50	1.2	4
100	110	0.3	10
500	510	0.1	20

Table 3.2: Proportion of the initial mass lost from the simulation volume, and runtime for $\tilde{t} = 100$, as functions of the dimensionless hydrostatic scale height a^{-1}. The grid size used was 50×100. Naturally, the relative runtimes are more useful than the absolute.

grid size	$\mu/\mu_{\rm t}$	ϵ
64×64	0.999101	4.32268×10^{-4}
50×100	1.003032	2.63789×10^{-4}
150×150	1.001214	4.52317×10^{-4}
300×300	1.000302	1.26503×10^{-4}

Table 3.3: Errors as a function of grid size as measured by the deviation of μ and ϵ from theoretical values for $\mu_{\rm t}$ and $\epsilon_{\rm t} = 0$ for $a = 100$, $\tilde{r}_{\rm m} = 110$ and $\tilde{t} = 0$.

in figure 3.23. If the outer boundary is set too many scale heights away, the minimum density across the grid is very low, the maximum Alfvén velocity is very high, and the time-step, $\Delta t_{\rm Z}$, determined by the Courant condition, is very short. This means that (i) the simulation takes a very long time to run, and (ii) the numerical dissipation causes the simulation to stop. For $a = 50$ and $\tilde{r}_{\rm m} = 70$, the code stops at $\tilde{\tau} < 2$; for $\tilde{r}_{\rm m} = 80$, it stops at $\tilde{\tau} < 0.2$. For $a = 100$ and $\tilde{r}_{\rm m} = 110$, the code stops at $\tilde{\tau} = 10.26$, but with `ggen1:x1rat = 1.03` instead of 1, it continues until $\tilde{\tau} = 27.22$. For $a = 1000$ and $\tilde{r}_{\rm m} = 1010$, the code stops immediately. Throughout the chapter, we use $\tilde{r}_{\rm m} = 60$, so that the runs are long enough to give sufficient time to assess the stability of the equilibria. Table 3.4 shows how the grid ratio affects the time to halt.

`x1rat`	$\Delta t_{\rm A}$	$\Delta t_{\rm s}$	time to halt (τ_0)
1	2.93714×10^{-3}	0.20	10.26
1.02	4.64149×10^{-3}	0.31	17.28
1.03	5.77838×10^{-3}	0.38	27.22
1.05	8.12472×10^{-3}	0.52	55.62
1.10	9.67961×10^{-3}	0.01	66.71
1.102	9.63428×10^{-3}	0.01	43.48

Table 3.4: The time taken for numerical dissipation to halt the simulation for $a = 100$ $\tilde{r}_{\rm m} = 110$, and a 50×100 grid, as a function of `ggen1:x1rat`, the geometric ratio in the rescaled coordinate r.

3.7.6 Converting to realistic a values and between codes

Here we give the formulae for converting between the Grad-Shafranov code and ZEUS-3D. Furthermore, we detail the effects of converting from a small ($a = 50$) to a realistic ($a \approx 10^4$) star. With h_0 fixed, but allowing a to vary, we have $R_* = ah_0 = 2.7 \times 10^3 (a/50)$ cm, $M_*/M_\odot = a^2 h_0 c_{\rm s}^2/(GM_\odot) = 1.0138 \times 10^{-5}(a/50)^2$, and

$$\frac{M_{\rm c}}{M_\odot} = 6.1 \times 10^{-15} \left(\frac{a}{50}\right)^4 \left(\frac{B_*}{10^{12}{\rm G}}\right)^2 \left(\frac{c_{\rm s}}{10^8\,{\rm cm\,s^{-1}}}\right)^{-4} . \qquad (3.35)$$

h_0 is the dimensionless unit of length. The dimensionless units in the Grad-Shafranov code (subscript 'G') are $\rho_{0,{\rm G}} = M_{\rm a}/h_0^3 = 9.8{\times}10^{-13}(m/0.16)(a/50)^4$ g cm^{-3}, $B_{0,{\rm G}} = B_* a^2/(2b) = 4.2{\times}10^{14}(a/50)^2(b/3)^{-1}$ G. In ZEUS-3D (subscript 'Z'), $\rho_{0,{\rm Z}} = c_{\rm s}^2/(Gh_0^3) = 9.6 \times 10^{19}{\rm g\,cm^{-3}}$, $B_{0,{\rm Z}} = (4\pi/Gh_0^3)^{1/2} c_{\rm s}^2 = 3.5 \times 10^{18}$ G. For conversion from the equilibrium code to ZEUS-3D, the factors are $\rho_{\rm G,Z} = \rho_{0,{\rm G}}/\rho_{0,{\rm Z}} = GM_{\rm a}/c_{\rm s}^2 = 1.3 \times 10^{-7}(m/0.16)(a/50)^4$, and $B_{\rm G,Z} = B_{0,{\rm G}}/B_{0,{\rm Z}} = B_* a^2/(2bc_{\rm s}^2)(Gh_0^3/4\pi)^{1/2} = 1.2 \times 10^{-4}(a/50)^2(b/3)^{-1}$.

3.7.7 Logarithmic coordinates

PM04 concentrated maximum grid resolution near the equator and stellar surface where $\nabla\rho$ and $\nabla\psi$ are greatest, by employing logarithmic stretching:

$$\tilde{x_1} = \log(\tilde{x} + e^{-L_x}) + L_x\,, \qquad (3.36)$$

$$\tilde{y_1} = -\log[1 - (1 - e^{-L_y})\tilde{y}]\,. \qquad (3.37)$$

To implement these coordinates in ZEUS-3D, set `ggen1:x1rat` to $(Xe^{L_x} + 1)^{(G_x-1)^{-1}}$, where $0 \leq \tilde{x} \leq X$ and L_x controls the 'zoom'. Radial logarithmic scaling gives less grid resolution near the outer boundary where the density is least and thus $\Delta t_{\rm Z}$ is greater and ZEUS-3D runs for a longer time.

When importing a Grad-Shafranov equilibrium (PM04), whose grid is linear in $y = \cos\theta$, into ZEUS-3D, whose grid is (in many cases) logarithmic in y, there is no trivial multiplicative factor relating $\tilde{y}_1$ and the required logarithmic θ scaling through `ggen1:x2rat`. The problem can be overcome by rewriting the Grad-Shafranov code such that its grid is logarithmic in θ. This problem is an obstacle in certain sorts of numerical experiments e.g. the bootstrapping method in section 4.2.

Chapter 4

Millisecond oscillations in type I X-ray bursts

4.1 Introduction

Thermonuclear (type I) X-ray bursts are observed from 70 of the 160 low-mass X-ray binaries (LMXBs) discovered to date (Strohmayer and Bildsten 2003). They recur every few hours to days, when the accreted surface layer of the neutron star ignites and is incinerated by runaway *rp*-process burning. Brightness oscillations with millisecond periods are observed during thermonuclear X-ray bursts in 13 LMXBs (Muno et al. 2002; Piro and Bildsten 2004). They arise because the stellar photosphere is temporarily patchy while the thermonuclear flame spreads from its ignition point to cover the star.

A surprising property of the burst oscillations is that they often persist into the tails of bursts, after the flame is expected to have engulfed the star (Strohmayer et al. 1997). Equally surprising is how sinusoidal the oscillations are. Muno et al. (2002) analysed the harmonic content of 59 oscillations from six sources, observed with the *Rossi X-Ray Timing Explorer* (*RXTE*), and found that the Fourier amplitudes of integer and half-integer harmonics are 5 and 10 per cent of the maximum signal respectively. These data imply that if there is one hot spot on the surface, it must lie near the rotational pole or cover an entire hemisphere, whereas if there are two, antipodal hot spots, they must lie near the rotational equator (Muno et al. 2002). Most theories that explain why the oscillations persist into the tails of the bursts,

e.g. uneven heating/cooling during photospheric uplift (Strohmayer et al. 1997), or cyclones driven by zonal shear in a geostrophic flow (Spitkovsky et al. 2002), are hard pressed to account for the pattern of hot spots implied by the Fourier data. Global r-modes in the neutron star ocean can divide the photosphere into symmetric halves (Heyl 2004), but the physical mechanism converting r-mode density perturbations to brightness oscillations is unclear (Muno et al. 2002).

In this chapter, we show that an equatorial belt of intense magnetic field, compressed by accreted material spreading away from the magnetic poles, can impede thermal transport between the hemispheres of the star. In section 4.2, we review the physics of magnetic burial and compute the maximum field strength and width of the equatorial magnetic barrier. In section 4.3, we estimate the efficiency of thermal transport across the barrier by conduction, convection, radiation and ageostrophic shear, and investigate whether cyclonic flows can disrupt the barrier. The implications for the harmonic content of burst oscillations are explored in section 4.4.

4.2 Magnetic burial

4.2.1 Grad-Shafranov equilibria

In the process of magnetic burial, material accreting onto a neutron star accumulates in a column at the magnetic polar cap, until the hydrostatic pressure at the base of the column overcomes the magnetic tension and matter spreads equatorward, dragging along frozen-in polar magnetic field lines to form an equatorial magnetic belt or 'tutu'. Figure 4.1 illustrates the equilibrium configuration obtained for $M_{\rm a} = 10^{-5} M_{\odot}$, where $M_{\rm a}$ is the total accreted mass. The polar mountain of accreted material (dashed contours) and the pinched, flaring, equatorial magnetic belt are evident (Melatos and Phinney 2001; Payne and Melatos 2004). The equatorial magnetic field strength increases in inverse proportion to the surface area of the equatorial belt, by flux conservation.

In the steady state, the equations of ideal magnetohydrodynamics (MHD) reduce to the force balance equation (CGS units)

$$\nabla p + \rho \nabla \phi - (4\pi)^{-1} (\nabla \times \mathbf{B}) \times \mathbf{B} = 0, \tag{4.1}$$

where $\mathbf{B}$, ρ, $p = c_{\rm s}^2\rho$, and $\phi(r) = GM_*r/R_*^2$ denote the magnetic field, fluid density, pressure, and gravitational potential respectively, $c_{\rm s}$ is the isothermal sound speed, M_* is the mass of the star, and R_* is the stellar radius. In spherical polar coordinates (r, θ, ϕ), for an axisymmetric field $\mathbf{B} = \nabla\psi(r,\theta)/(r\sin\theta) \times \hat{\mathbf{e}}_\phi$, equation (4.1) reduces to the Grad-Shafranov equation

$$\Delta^2\psi = F'(\psi)\exp[-(\phi - \phi_0)/c_{\rm s}^2], \tag{4.2}$$

where Δ^2 is the Grad-Shafranov operator, $F(\psi)$ is an arbitrary function of the magnetic flux ψ, and we set $\phi_0 = \phi(R_*)$. In this chapter, as in Payne and Melatos (2004) and chapter 2, we fix $F(\psi)$ uniquely by connecting the initial and final states via the integral form of the flux freezing condition of ideal MHD, viz.

$$\frac{dM}{d\psi} = 2\pi\int_C \frac{ds\,\rho}{|\mathbf{B}|}, \tag{4.3}$$

where C is any magnetic field line and the mass-flux distribution $dM/d\psi$ is chosen to capture the magnetospheric geometry, e.g. the accretion stream is funneled magnetically onto the pole, with $dM/d\psi \propto \exp(-\psi/\psi_{\rm a})$, where $\psi_{\rm a}$ is the polar flux. We also assume north-south symmetry and adopt the boundary conditions ψ = dipole at $r = R_*$ (line tying), $\psi = 0$ at $\theta = 0$, and $\partial\psi/\partial r = 0$ at large r. The line-tying approximation artificially prevents accreted material from sinking, so the computed ρ is an upper limit. Equations (2) and (3) are solved numerically using an iterative relaxation scheme and analytically by Green functions (Figure 4.1).

4.2.2 Equatorial magnetic belt

The compressed magnetic field in the equatorial belt emerges approximately perpendicular to the stellar surface, with opposite sign in the two hemispheres. Near the equator, B falls off roughly as $\exp[-0.69(\pi/2 - \theta)/\Delta\theta]$ $\exp[-(r-R_*)/h]$, where $h = c_{\rm s}^2R_*^2/GM_*$ is the hydrostatic scale height. The maximum magnetic field strength in the belt, $B_{\rm max}$, computed numerically as a function of $M_{\rm a}$, is plotted in Figure 4.2. It is fitted by

$$B_{\rm max} = \begin{cases} 2.0\times10^{16}(M_{\rm a}/M_{\rm c})^{0.91\pm0.06}{\rm G} & M_{\rm a} \lesssim M_{\rm c} \\ 6.3\times10^{15}(M_{\rm a}/M_{\rm c})^{0.32\pm0.01}{\rm G} & M_{\rm a} \gtrsim M_{\rm c} \end{cases} \tag{4.4}$$

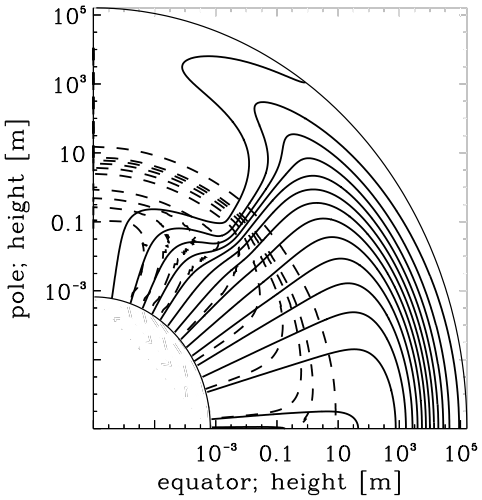

Figure 4.1: Equilibrium magnetic field lines (solid curves) and density contours (dashed curves) for $M_{\rm a} = 10^{-5} M_\odot$ and $\psi_{\rm a} = 0.1\psi_*$. Coordinates measure altitude. Density contours are drawn for $\eta\rho_{\rm max}$ ($\rho_{\rm max} = 2.52 \times 10^{14}\,{\rm g\,cm^{-3}}$), with $\eta = 0.8$, 0.6, 0.4, 0.2, 10^{-2}, 10^{-3}, 10^{-4}, 10^{-5}, 10^{-6}, 10^{-12}. Convergence residuals are less than 10^{-3}.

with $M_{\rm c} = GM_* B_0^2 R_*^2 / 8 c_{\rm s}^4 \sim 10^{-4} M_\odot$, where B_0 is the polar magnetic field strength prior to accretion. The scaling (4.4) agrees with analytic theory for small $M_{\rm a}$ (Payne and Melatos 2004). Also plotted in Figure 4.2 is the half-width half-maximum thickness of the belt, fitted by $\Delta\theta = 3^\circ (M_{\rm a}/M_{\rm c})^{-1.5\pm0.03}$. We find that $\Delta\theta$ decreases as $B_{\rm max}$ increases, as expected from magnetic flux conservation, but not exactly as $\Delta\theta \propto B_{\rm max}^{-1}$, because B_r is underestimated numerically at the equator by ~ 10 per cent (flux loss due to finite grid resolution).

Grad-Shafranov equilibria are difficult to compute directly from (4.2) and (4.3) for $M_{\rm a} \gtrsim 1.6 M_{\rm c}$, because the magnetic topology changes abruptly: magnetic bubbles form which are disconnected from the surface, hinting at time-dependent processes which the steady-state theory cannot describe. In addition, the iterative relaxation scheme struggles to handle steep field gradients. Therefore the results in Figure 4.2 for $M_{\rm a} \geq 1.6 M_{\rm c}$ are computed by direct numerical simulation using ZEUS-3D, a multipurpose, time-dependent, ideal-MHD code for astrophysical fluid dynamics which uses staggered-mesh finite differencing and operator splitting in three dimensions (Stone and Norman 1992b). We load the Grad-Shafranov equilibrium for $M_{\rm a} = 1.6 M_{\rm c}$ into ZEUS-3D; double $M_{\rm a}$ quasistatically over 250 Alfvén times with inflow (and

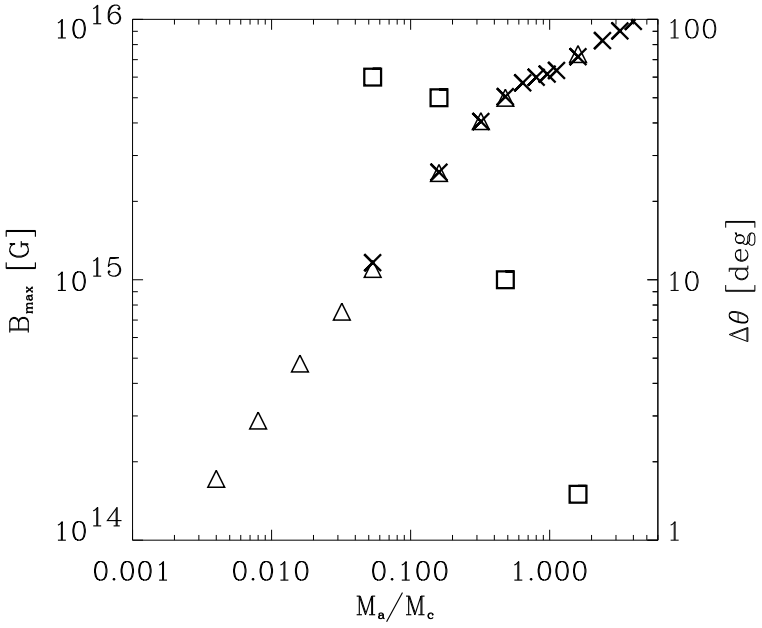

Figure 4.2: Maximum magnetic field in the equatorial belt, $B_{\max}$, computed numerically for $h/R_* = 2\times10^{-2}$ (*crosses*) and $h/R_* = 5\times10^{-5}$ (*triangles*) and scaled using $B_{\max} \propto h^{-1}$, plotted together with the half-width half-maximum thickness, $\Delta\theta$ (*squares*), as a function of accreted mass, $M_{\rm a}$.

hence radial **B**) boundary conditions; stop the inflow and allow **B** to relax to a dipole at large r; then iterate to reach $M_{\rm a} \sim 10^{-3}M_\odot$ (Payne and Melatos 2005a). An isothermal equation of state is chosen and self-gravity is switched off. The experiment is performed for $h/R_* = 2\times10^{-2}$ (for computational efficiency) and scaled to neutron star conditions ($h/R_* = 5\times10^{-5}$) according to $B_{\max} \propto R_*/h$; this scaling is verified numerically for the range of $M_{\rm a}$ in Figure 4.2.

4.2.3 Stability

Distorted ideal-MHD equilibria are often disrupted by Parker and interchange instabilities. Remarkably, however, this is not true for the equilibrium in Figure 4.1. Figure 4.3 shows the results of an experiment in which the equilibrium is loaded into ZEUS-3D, perturbed, and evolved for 500 Alfvén times (Payne and Melatos 2005a). It is marginally stable; $B_{\max}$ oscillates via magnetosonic (phase speed $\approx c_{\rm s}$) and Alfvén (phase speed $\approx v_{\rm A}$) modes which are damped by numerical dissipation. The configuration *already* represents the end point (reached quasistatically) of the nonlinear

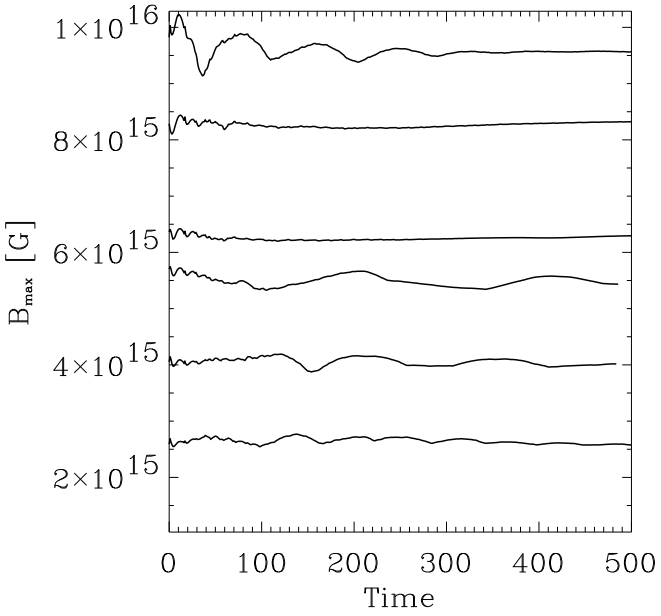

Figure 4.3: Maximum magnetic field strength, $B_{\max}$, as a function of time (in units of the Alfvén time) for $M_{\rm a}/M_{\rm c} = 0.16, 0.32, 0.64, 1.12, 2.4, 4.0$ (*bottom* to *top*) when the equilibrium in Figure 4.1 is loaded into ZEUS-3D and perturbed slightly. The configuration is stable.

Parker instability of an initially dipolar field overlaid with accreted material. It is not interchange unstable because line tying prevents flux tubes from squeezing past each other.

During a thermonuclear burst, the temperature of the crust rises isobarically until the radiation pressure dominates the hydrostatic pressure, at a maximum temperature $T \approx 2 \times 10^9$ K for a typical ignition column. The elevated temperature lowers the electrical conductivity and accelerates ohmic diffusion. In the relaxation time approximation, with Coulomb logarithms set to 10, the electron-phonon conductivity for a hydrogen-helium mixture is $\sigma = 6.3 \times 10^{24} (\rho/10^{11}\,{\rm g\,cm^{-3}})\,{\rm s^{-1}}$, the density at the base of the accreted layer is $\rho = 6.2 \times 10^{10} (M_{\rm a}/10^{-5} M_\odot)^{3/4}\,{\rm g\,cm^{-3}}$ (Brown and Bildsten 1998), and hence the Ohmic diffusion time-scale across the equatorial belt is $t_{\rm d} = 4\pi\sigma R_*^2 \Delta\theta^2/c^2 = 2.6 \times 10^6 (M_{\rm a}/10^{-5} M_\odot)^{-9/4} (T/10^9\,{\rm K})^{-1}{\rm yr}$, where we rewrite $\Delta\theta$ in terms of $M_{\rm a}$. Therefore Ohmic diffusion is negligible during the burst.

4.3 Thermal transport across the equator

Does the equatorial magnetic belt impede thermal transport enough to stop the thermonuclear flame in a type I X-ray burst from spreading from one hemisphere to another? A burst is initiated locally by a thin shell thermal instability (Schwarzschild and Härm 1965). As the nuclear burning time-scale is much shorter than the time to accrete the minimum column for ignition, the accreted layer ignites at a single point, most likely at the equator where gravity is rotationally reduced, and the thermonuclear flame spreads away either as a deflagration front (Bildsten 1995; Fryxell and Woosley 1982), by detonation (Fryxell and Woosley 1982; Zingale et al. 2001), or as a cyclone driven by zonal shear (Spitkovsky et al. 2002). Detonation, which occurs when the nuclear burning time-scale is less than the vertical sound crossing time-scale, requires a thick ($\sim 10^4$ cm) column of fuel and hence a low accretion rate ($\lesssim 10^{-11.5} M_\odot$ yr^{-1}). Deflagration occurs most commonly, with the front propagating at a speed set by the heat flux and convection (Fryxell and Woosley 1982). We estimate below how the equatorial magnetic belt modifies heat transport in these scenarios.

4.3.1 Conduction

The thermal conductivity κ of degenerate electrons at the atmosphere-ocean boundary of a magnetized neutron star, where H/He burning occurs, was calculated by Potekhin (1999). We extract approximate values for the conductivity perpendicular to the magnetic field from Figures 5 and 6 of that paper, obtaining $\kappa_\perp \approx 10^{7.5} (\rho/10^6 \mathrm{g\,cm^{-3}})\ (T/10^8\mathrm{K})^2 (B/10^{15}\mathrm{G})^{-2}$ in units of erg s^{-1}cm^{-1}K^{-1} in the regime 10^4 g cm^{-3} $\lesssim \rho \lesssim 10^9$ g cm^{-3}, 10^{12} G $\lesssim B \lesssim 10^{15}$ G, and 10^6 K $\lesssim T \lesssim 10^8$ K. Note that $\kappa_\perp$ at the equator is reduced 10^6 times relative to its value before accretion commences ($\propto B^{-2}$) and, for reference, one has $\kappa_\perp/\kappa_\parallel \sim 10^{-5}$ at $T = 10^8$ K, $B = 10^{12}$ G (Potekhin 1999). We estimate the conduction time-scale across the magnetic barrier from $t_{\rm cond} = R_*^2 \Delta\theta^2 C\rho/\kappa_\perp$, where $C = 10^4 (T/10^8\mathrm{K})\,\mathrm{erg\ g^{-1}\,K^{-1}}$ is the specific heat capacity of a degenerate Fermi gas (Brown and Bildsten 1998), finding

$$t_{\rm cond} = 27 (M_{\rm a}/M_{\rm c})^{-3} (T/10^8\mathrm{K})^{-1} (B/10^{15}\mathrm{G})^2\,\mathrm{yr}\,, \qquad (4.5)$$

which is safely longer than the duration of the burst.

4.3.2 Radiation

In a strong magnetic field, photons polarized perpendicular to **B** dominate radiative transport. In the burning (helium) layer, where Thomson scattering dominates, the Rosseland mean opacity $\perp$ **B** is given by $\kappa_{\rm R} = 1.3 \times 10^{-6} (T/10^8{\rm K})^2 (B/10^{15}{\rm G})^{-2} {\rm g}^{-1}\,{\rm cm}^2$, decreasing in inverse proportion to the square of the cyclotron frequency (Fryxell and Woosley 1982; Joss and Li 1980). Hence the optical depth of the barrier is $\tau_{\rm R} = \kappa_{\rm R} \rho R_* \Delta\theta$, i.e.

$$\tau_{\rm R} = 6.8 \times 10^4 \ (M_{\rm a}/M_{\rm c})^{-3/2} (T/10^8{\rm K})^2 (B/10^{15}{\rm G})^{-2}. \qquad (4.6)$$

The optical depth (4.6) is a lower limit obtained by assuming that radiation is transported from one hemisphere to the other near the surface, at the depth of the burning layer ($\rho \sim 10^6 {\rm g\,cm}^{-3}$) rather than at the base of the accreted column ($\rho \sim 10^{11} {\rm g\,cm}^{-3}$). Hence the peak flux penetrating the barrier is $F_{\rm burst} = L_{\rm burst} e^{-\tau_{\rm R}} / 4\pi R_*^2 = 8 \times 10^{25} e^{-\tau_{\rm R}}$ erg s^{-1} cm^{-2} (for $L_{\rm burst} = 10^{39} {\rm erg\,s}^{-1}$), which is insufficient to heat the other (quiescent) hemisphere above its ignition temperature ($\sim 10^7$ K) (assuming thermal equilibrium and applying the Stefan-Boltzmann law). Interestingly, once $B_{\rm max}$ exceeds 10^{17} G, we find $\tau_{\rm R} \lesssim 1$ and the magnetic belt becomes optically thin.

4.3.3 Convection

Bildsten (1995) estimated the convective speed in the burning layer in terms of the mixing length, $l_{\rm m}$, and thermal time-scale, $t_{\rm th}$, finding $v_{\rm c} \approx c_{\rm s} (l_{\rm m}/h)^{1/3}$ $(c_{\rm s} R_*^2 / G M_* t_{\rm th})^{1/3} \approx 10^6$ cm s^{-1}. This is consistent with the upper bound $10^7 {\rm cm\,s}^{-1}$ obtained if $L_{\rm burst}$ is transported entirely by the mechanical flux $\rho v_{\rm c}^3$. It is also consistent with the observed burst rise time $R_*/v_{\rm c} \lesssim 1$ s (Spitkovsky et al. 2002). Convection is stabilized magnetically if the magnetic tension exceeds the ram pressure $\rho v_{\rm c}^2$, which occurs for $B_{\rm max} \gtrsim (8\pi\rho v_{\rm c}^2)^{1/2} \approx 5 \times 10^9$ G. This condition is met comfortably in the equatorial belt.

4.3.4 Ageostrophic shear flow

Spitkovsky et al. (2002) suggested that inhomogeneous cooling drives zonal currents which are unstable to the formation of cyclones, as in planetary atmospheres. This may explain why the coherent oscillations observed in the tails of some type I X-ray bursts persist for many rise times. The drift in oscillation frequency ($\sim$ Hz) during the burst is attributed to the Coriolis drift of the cyclone in the frame of the star, although theory predicts larger frequency drifts ($\sim$ 10 Hz) than those observed.

Ageostrophic shear flow moves hot material ahead of the burning front and draws fresh fuel into it at the flame speed $v_{\rm flame} \approx 2 \times 10^7\ (h_{\rm hot}/10^3{\rm cm})\ (f/0.32{\rm kHz})^{-1}(t_{\rm nuc}/0.1\,{\rm s})^{-1}$, cm s^{-1} where $h_{\rm hot}$ is the scale height of the incinerated ocean, $f = 2\Omega\cos\theta$ is the local Coriolis parameter, Ω is the angular frequency of the star, and $t_{\rm nuc}$ is the nuclear burning time-scale. Magnetic tension stabilizes ageostrophic shear for $B \gtrsim (8\pi\rho v_{\rm flame}^2)^{1/2} \approx 4.5 \times 10^{10}$ G $\ll B_{\rm max}$. In other words, when the cyclonic flame runs into the equatorial magnetic belt, it is reflected; conversely, ageostrophic shear cannot disrupt the belt. Interestingly, small-scale magnetic fields, generated by a dynamo in the burning front, can couple the top and bottom of the cooling ocean, enforcing the rigid rotation necessary for burst coherence (Spitkovsky et al. 2002).

4.4 Discussion

Polar magnetic burial creates an intense, equatorial belt of magnetic field which can thermally isolate the magnetic hemispheres of an accreting neutron star. The maximum magnetic field strength in the belt, $B_{\rm max} = 5.6 \times 10^{15}(M_{\rm a}/10^{-4}M_\odot)^{0.32}$ G, is sufficient to prevent heat transport by conduction, radiation, convection, and ageostrophic shear. The conduction time-scale $t_{\rm cond} \sim 27$ yr exceeds the cooling time of the incinerated material, the magnetic belt is opaque (optical depth $\sim 7 \times 10^4$), convection is stabilized magnetically ($\rho v_{\rm c}^2 \ll B_{\rm max}^2/8\pi$), and so is ageostrophic shear ($\rho v_{\rm flame}^2 \ll B_{\rm max}^2/8\pi$).

Thermal isolation of the magnetic hemispheres is consistent with the highly sinusoidal light curves of millisecond oscillations in thermonuclear bursts in LMXBs (Muno et al. 2002). During the rise of the burst, oscillations are caused by the spreading of a hot spot, probably in the form of

a cyclone (Spitkovsky et al. 2002). In the tail of the burst, the hot spot is sequestered in one hemisphere (Muno et al. 2002), and misalignment of the magnetic and spin axes guarantees that we observe persistent oscillations at the spin frequency.

Only 70 out of 160 LMXBs undergo bursts, and only 13 exhibit millisecond oscillations. Does the equatorial belt model respect these statistics? If accretion occurs at the Eddington rate, $\dot{M}_{\rm a} \approx 10^{-8} M_\odot {\rm yr}^{-1}$, it takes less than 10^4 yr to achieve $M_{\rm a} > M_{\rm c}$ and screen the polar magnetic field, allowing bursts to ignite and creating a thermally insulating equatorial belt. However, for $M_{\rm a} \gtrsim 2\times10^3 M_{\rm c}$, the belt becomes optically thin to X-rays and $t_{\rm cond}$ drops below the duration of the burst, potentially allowing the flame to engulf the entire star in LMXBs older than a few times 10^7 yr. If accretion occurs at $\dot{M}_{\rm a} \sim 10^{-11} M_\odot {\rm yr}^{-1}$, as in accreting millisecond pulsars (Chakrabarty et al. 2003), it takes 10^7 yr to achieve $M_{\rm a} > M_{\rm c}$, screen the polar magnetic field, and allow bursts to ignite. Therefore, we do not expect bursts from all accreting millisecond pulsars, but when bursts do occur, we expect to detect oscillations at some level because we have $\tau_{\rm R} \gg 1$ and $t_{\rm cond} \gg$ (burst time-scale) for $M_{\rm a} \lesssim 10^{-3} M_\odot$. Such is the case, within current observational sensitivity, for SAX J1808.4-3658 and XTE J1814-338. Sources like XTE J1814-338, whose oscillations contain harmonics exceeding 25 per cent of the peak amplitude (Strohmayer et al. 2003), may have semi-transparent equatorial belts. Note that, for $\dot{M}_{\rm a} \lesssim 10^{-10} M_\odot\,{\rm yr}^{-1}$, ohmic diffusion may magnetize the freshly accreted material (Cumming et al. 2001), increasing the polar magnetic field strength and suppressing bursts. Also, ignition is more likely near the equator, where gravity is rotationally reduced, but this is where the magnetic field is strongest.

Chapter 5

Gravitational waves from accreting neutron stars

5.1 Introduction

The current generations of resonant bar antennas and long baseline interferometers are capable of detecting gravitational wave signals from incoherent sources with strain amplitudes h exceeding $\sim 10^{-20}$ and $\sim 10^{-21}$ respectively at frequencies near $f \approx 0.6\,\mathrm{kHz}$ (Schutz 1999). The sensitivity can be improved by a factor $(f\tau)^{1/2}$ for periodic sources of known f by integrating coherently for a total observing time τ, as in heirarchical Fourier searches (Brady and Creighton 2000; Brady et al. 1998; Dhurandhar et al. 1996). Several classes of sources with promising event rates have been identified in the kilohertz regime: coalescing neutron-star binaries (Phinney and Verbunt 1991), r-modes in young, hot neutron stars (Andersson 1998; Lindblom et al. 1998), and neutron stars in low-mass X-ray binaries whose crusts are deformed by temperature gradients (Bildsten 1998; Ushomirsky et al. 2000). More generally, every isolated and accreting millisecond pulsar is potentially a kilohertz source, because the stellar magnetic field, which is usually not symmetric about the rotation axis, deforms the crust and interior hydromagnetically. It is presently believed that hydromagnetic deformations are too small to produce gravitational waves detectable by the current generation of interferometers, with $h \sim 10^{-31}(B/10^{12}\,\mathrm{G})^2(f/0.6\,\mathrm{kHz})^2(d/1\,\mathrm{kpc})^{-1}$ for an object with surface magnetic field B, situated at a distance d from Earth (Bonazzola and Gourgoulhon 1996; Katz 1989). Magnetars, with

$B \gtrsim 10^{15}$ G, are invoked as a possible exception (Ioka 2001b; Konno et al. 2000; Palomba 2001), as are objects whose internal toroidal fields are many times greater than B (Cutler 2002), or whose macroscopically averaged Maxwell stress tensor is enhanced relative to uniform magnetization because the internal field is concentrated in flux tubes, e.g. in a type II superconductor (Bonazzola and Gourgoulhon 1996; Jones 1975).

In this chapter, we show that previous calculations materially underestimate the hydromagnetic deformation of recycled pulsars, e.g. accreting millisecond pulsars such as SAX J1808.4−3658 (Chakrabarty and Morgan 1998; Galloway et al. 2002; Markwardt et al. 2002; Wijnands and van der Klis 1998). During accretion, in a process termed *magnetic burial*, material spreads equatorward from the polar cap, compressing the magnetic field into a narrow belt at the magnetic equator and increasing the field strength locally while reducing the global dipole moment μ (Melatos and Phinney 2000, 2001; Payne and Melatos 2004), in accord with observations of low- and high-mass X-ray binaries and binary radio pulsars (Taam and van den Heuvel 1986; van den Heuvel and Bitzaraki 1995). In turn, the compressed equatorial magnetic field reacts back on the accreted material, confining it in a polar mountain which is misaligned with the rotation axis in general (Melatos and Phinney 2000, 2001). The gravitational ellipticity ϵ (Brady et al. 1998) of the mountain, calculated here self-consistently, can approach $\epsilon \sim 10^{-7}$, materially greater than for an undistorted dipole [$\epsilon \approx 6 \times 10^{-13} (B/10^{12}\,\mathrm{G})^2$, e.g. Katz (1989)] due to the enhanced stress from the compressed field. A mountain of this size generates gravitational waves at levels detectable by the current generation of interferometers and can explain the observed clustering of the spin periods of accreting millisecond pulsars through the stalling effect discovered by Bildsten (1998).

In section 5.2, we review the physics of magnetic burial and calculate the hydromagnetic structure of the polar mountain as a function of accreted mass M_a by solving an appropriate Grad-Shafranov boundary value problem, connecting the initial and final states self-consistently, and treating Ohmic diffusion semiquantitatively (Melatos and Phinney 2001; Payne and Melatos 2004). In section 5.3, we predict the orientation- and polarization-averaged gravitational wave strain $h_\mathrm{c}(M_\mathrm{a})$ and compare it against the sensitivity of the Laser Interferometer Gravitational-Wave Observatory (LIGO). We also combine $h_\mathrm{c}(M_\mathrm{a})$ with $\mu(M_\mathrm{a})$ from previous work (Payne and Melatos

2004) to deduce a novel, observationally testable scaling $h_{\rm c}(\mu)$ for accreting millisecond pulsars (Melatos and Phinney 2000). In section 5.4, we discuss the implications of magnetic burial for the sign of the net torque acting on an X-ray millisecond pulsar and the evolution of $h_{\rm c}$ and μ after accretion ends (e.g. in radio millisecond pulsars). Our conclusions rely on the assumption that the polar mountain is not disrupted by hydromagnetic (e.g. Parker) instabilities; the justification of this assumption is postponed to future work. Deformation by magnetic burial also occurs in white dwarfs (Cumming 2002; Heyl 2000; Katz 1989).

5.2 Polar magnetic burial

5.2.1 Equilibrium hydromagnetic structure of the polar mountain

The equilibrium mass density $\rho(\mathbf{x})$ and magnetic field intensity $\mathbf{B}(\mathbf{x})$ in the polar mountain are determined by the equation of hydromagnetic force balance,

$$\nabla p + \rho\nabla\phi - (4\pi)^{-1}(\nabla\times\mathbf{B})\times\mathbf{B} = 0\ , \tag{5.1}$$

supplemented by (i) the condition $\nabla\cdot\mathbf{B}=0$, (ii) the gravitational potential ϕ (with $|\nabla\phi|\approx GM_*/R_*^2$, where M_* and R_* are the stellar mass and radius, because the mountain is much shorter than R_*), and (iii) an equation of state for the pressure p (isothermal for simplicity, i.e. $p=c_{\rm s}^2\rho$, where $c_{\rm s}$ is the sound speed). We define spherical polar coordinates (r,θ,ϕ), such that $\theta=0$ coincides with the magnetic axis before accretion, and we seek solutions to (5.1) that are symmetric about this axis, such that $\mathbf{B}$ can be constructed from a scalar flux function $\psi(r,\theta)$ according to $\mathbf{B}=(r\sin\theta)^{-1}\nabla\psi\times\hat{\mathbf{e}}_\phi$. Upon resolving (5.1) into components parallel and perpendicular to $\mathbf{B}$, we arrive respectively at the barometric formula $\rho=c_{\rm s}^{-2}F(\psi)\exp[-(\phi-\phi_0)/c_{\rm s}^2]$, with $\phi_0=GM_*/R_*$, and the Grad-Shafranov equation describing cross-field force balance (Brown and Bildsten 1998; Hameury et al. 1983; Litwin et al. 2001; Melatos and Phinney 2001; Payne and Melatos 2004),

$$\frac{\partial^2\psi}{\partial r^2}+\frac{\sin\theta}{r^2}\frac{\partial}{\partial\theta}\left(\frac{1}{\sin\theta}\frac{\partial\psi}{\partial\theta}\right) = -4\pi r^2\sin^2\theta F'(\psi) \times\exp[-(\phi-\phi_0)/c_{\rm s}^2]\ . \tag{5.2}$$

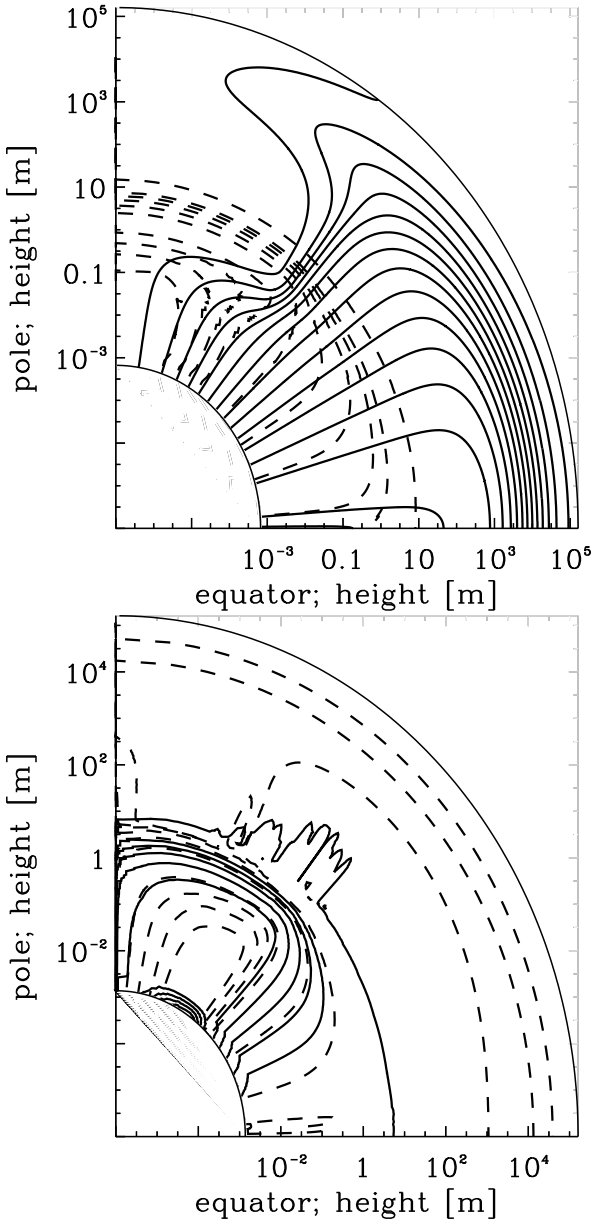

Figure 5.1: (*a*) Numerical calculation of the hydromagnetic structure of the accreted layer, showing contours of ψ (solid) and ρ (dashed). (*b*) Contours of Lorentz force density (solid) and magnetic field intensity (dashed). Parameters: $M_{\rm a} = 10^{-5} M_\odot$, $b = 10$. The contours are at fractions $\eta = 0.8$, 0.6, 0.4, 0.2, 10^{-2}, 10^{-3}, 10^{-4}, 10^{-5}, 10^{-6}, and 10^{-12} of the respective maxima.

It is customary to choose an arbitrary (albeit physically plausible) functional form of $F(\psi)$ in order to solve (5.2) (Brown and Bildsten 1998; Hameury et al. 1983; Litwin et al. 2001; Uchida and Low 1981). However, this approach leads to an inconsistency. In the perfectly conducting limit, material is frozen to magnetic field lines. Hence the mass $dM = 2\pi d\psi \int ds\, \rho[r(s), \theta(s)] r \sin\theta |\nabla\psi|^{-1}$ enclosed between two adjacent flux surfaces ψ and $\psi + d\psi$ (where the integral is along a field line) equals the mass enclosed before accretion plus any mass added during accretion, *without any cross-field transport of material* (Melatos and Phinney 2001; Mouschovias 1974; Payne and Melatos 2004). To calculate ψ correctly, one must specify $dM/d\psi$ according to the global accretion physics, with $F(\psi)$ following from

$$F(\psi) = \frac{c_{\rm s}^2}{2\pi}\frac{dM}{d\psi}\left\{\int ds\, r\sin\theta|\nabla\psi|^{-1}\exp[-(\phi-\phi_0)/c_{\rm s}^2]\right\}^{-1}; \qquad (5.3)$$

otherwise, if $F(\psi)$ is specified, $dM/d\psi$ changes as a function of $M_{\rm a}$ in a manner that inconsistently leads to cross-field transport. The functional form of $F(\psi)$, determined self-consistently through (5.3), changes as $M_{\rm a}$ increases. This property, newly recognized in the context of magnetic burial (Melatos and Phinney 2001; Payne and Melatos 2004), has an important astrophysical consequence: it produces a greater hydromagnetic deformation than predicted by previous authors, because polar (accreting) and equatorial (nonaccreting) flux tubes maintain strictly separate identities through (5.3), without exchanging material, and hence the equatorial magnetic field is highly compressed.

We solve (5.2) and (5.3) simultaneously for $\psi(r,\theta)$ and $\rho(r,\theta)$ subject to the line-tying (Dirichlet) boundary condition $\psi(R_*,\theta) = \psi_* \sin^2\theta$ at the stellar surface, such that the footpoints of magnetic field lines are anchored to the heavy, highly conducting crust (Melatos and Phinney 2001; Payne and Melatos 2004). We adopt a mass-flux distribution, $M(\psi) = \frac{1}{2}M_{\rm a}(1 - e^{-\psi/\psi_{\rm a}})(1-e^{-\psi_*/\psi_{\rm a}})^{-1}$, that embodies the essence of disk accretion, namely that the accreted mass is distributed rather evenly within the polar flux tube $0 \le \psi \le \psi_{\rm a}$, with minimal leakage onto equatorial flux surfaces $\psi_{\rm a} \le \psi \le \psi_*$, where $\psi_* = \psi(R_*, \pi/2)$ denotes the hemispheric flux and $\psi_{\rm a}$ is the flux surface touching the inner edge of the accretion disk (radius $R_{\rm a}$). Payne and Melatos (2004) verified that the results do not depend sensitively on the exact form of $M(\psi)$, only on the ratio $\psi_{\rm a}/\psi_*$.

The boundary value problem (5.2) and (5.3) with surface line-tying can be solved analytically, in the small-$M_{\rm a}$ limit, by Green functions[1] after approximating the source term on the right-hand side of (5.2) to sever the coupling between (5.2) and (5.3) (Payne and Melatos 2004). It can also be solved numerically by an iterative scheme that solves the Poisson equation (5.2) for a trial source term by successive overrelaxation then updates $F(\psi)$ from (5.3) by integrating numerically along a set of contours (including closed and edge-interrupted loops) (Mouschovias 1974; Payne and Melatos 2004). The numerical scheme is valid for arbitrarily large $M_{\rm a}$, although convergence deteriorates as $M_{\rm a}$ increases. Typically, we use a 256×256 grid and 255 contours (linearly or logarithmically spaced) and target an accuracy of $|\Delta\psi/\psi| \leq 10^{-2}$ after $\sim 10^3$ iterations. We rescale the r and θ coordinates logarithmically in the regions where steep gradients develop, e.g. $\theta \approx \pi/2$ (Payne and Melatos 2004).

5.2.2 Ohmic diffusion

The structure of the polar mountain evolves quasistatically, over many Alfvén times, in response to (i) accretion, which builds up the mountain against the confining stress of the compressed equatorial magnetic field, and (ii) Ohmic diffusion, which enables the mountain to relax equatorward as magnetic field lines slip through the resistive fluid. The competition between accretion and Ohmic diffusion has been studied in detail in the context of neutron stars (Brown and Bildsten 1998; Cumming et al. 2001; Litwin et al. 2001) and white dwarfs (Cumming 2002). In these papers, steady-state, one-dimensional profiles of the magnetic field are computed as functions of depth, from the ocean down to the outer crust, and the Ohmic ($t_{\rm d}$) and accretion ($t_{\rm a}$) time-scales are compared, under the assumptions that the magnetic field is flattened parallel to the surface by polar magnetic burial, the accreted material is unmagnetized, and the accretion is spherical; 'the complex problem of the subsequent spreading of matter' is not tackled (Cumming 2002). The field penetrates the accreted layer if the accretion rate satisfies $\dot{M}_{\rm a} \lesssim 0.1\dot{M}_{\rm Edd}$, where $\dot{M}_{\rm Edd}$ is the Eddington rate, but it is screened diamagnetically (i.e. buried) if $\dot{M}_{\rm a} \gtrsim 0.1\dot{M}_{\rm Edd}$, such that the surface field is reduced $\approx (\dot{M}_{\rm a}/0.002\dot{M}_{\rm Edd})$-fold relative to the base of the crust

[1] The Grad-Shafranov operator is not self-adjoint.

(Cumming et al. 2001).[2]

In the regime $t_{\rm d} \lesssim t_{\rm a}$, Ohmic diffusion outpaces accretion. As material is added, it does not compress the equatorial magnetic field further; instead, it diffuses across field gradients and distributes itself uniformly over the stellar surface. Hence the polar mountain (i.e. the asymmetric component of ρ) 'stagnates' at the structure attained when $t_{\rm d} \sim t_{\rm a}$. The accretion time-scale is defined as $t_{\rm a} = M_{\rm a}/\dot{M}_{\rm a}$. The Ohmic diffusion time-scale is given by $t_{\rm d} = 4\pi\sigma L^2/c^2$, where σ denotes the electrical conductivity and $L = (|\psi|/|\nabla\psi|)_{\rm min}$ is the characteristic length-scale of the steepest field gradients; L reduces to the hydrostatic scale-height in the one-dimensional geometry employed in earlier work (Brown and Bildsten 1998; Cumming 2002; Cumming et al. 2001) but is dominated by latitudinal gradients here. Following Cumming et al. (2001), we assume that the electrical resistivity is dominated by electron-phonon scattering in the outer crust ($M_{\rm a} \gtrsim 10^{-10} M_\odot$), as expected if the crustal composition is primordial, although electron-impurity scattering may dominate if the products of hydrogen/helium burning leach into the crust. In the relaxation time approximation, with all Coulomb logarithms set to unity, the electron-phonon conductivity is given by $\sigma = 7.6 \times 10^{26} (\rho/10^{11}\,{\rm g\,cm^{-3}})(\nu_{\rm c}/10^{16}\,{\rm s^{-1}})^{-1}(m_{\rm eff}/m_{\rm e})^{-1}(A/2)^{-1}\,{\rm s^{-1}}$, where A and Z denote the mean molecular weight and atomic number per electron, $m_{\rm eff}$ is the effective electron mass, $\nu_{\rm c} = 1.2 \times 10^{18} (T/10^8\,{\rm K})\,{\rm s^{-1}}$ is the electron-phonon collision frequency, T is the temperature of the crust, and $\rho = 6.2 \times 10^{10} A Z^{-1} (M_{\rm a}/10^{-5} M_\odot)^{3/4}\,{\rm g\,cm^{-3}}$ is the density at the base of the accreted layer (Brown and Bildsten 1998; Cumming et al. 2001). Ohmic diffusion therefore arrests the growth of the polar mountain for

$$\frac{|\psi|}{|\nabla\psi|} \lesssim 4.2 \times 10^2 Z^{1/2} \left(\frac{M_{\rm a}}{10^{-5} M_\odot}\right)^{1/8} \left(\frac{T}{10^8\,{\rm K}}\right)^{1/2} \times \left(\frac{m_{\rm eff}}{m_{\rm e}}\right)^{1/2} \left(\frac{\dot{M}_{\rm a}}{\dot{M}_{\rm Edd}}\right)^{-1/2} {\rm cm}\,, \tag{5.4}$$

corresponding to the condition $t_{\rm d} \leq t_{\rm a}$. The left-hand side of (5.4) is computed directly from the numerical solution, by scanning over the grid, or

[2] SAX J1808.4−3658 is presumed to possess an ordered magnetic field at its surface because it pulsates (Chakrabarty and Morgan 1998; Wijnands and van der Klis 1998). Due to the low accretion rate, $\dot{M}_{\rm a} \approx 10^{-11} M_\odot\,{\rm yr^{-1}}$, either the field has penetrated to the surface by Ohmic diffusion (Cumming et al. 2001), or polar magnetic burial and equatorward spreading have not proceeded far enough (Payne and Melatos 2004).

from the approximate analytic solution in section S5.2.3; it depends implicitly on $M_{\rm a}$. We denote by $M_{\rm d}$ the minimum accreted mass for which (5.4) is satisfied. Note that $t_{\rm d}/t_{\rm a}$ is constant with depth for electron-phonon scattering but decreases with depth for electron-impurity scattering (Brown and Bildsten 1998; Cumming et al. 2001).

Several second-order effects, neglected in (5.4), are postponed to future work. The Hall conductivity vanishes in plane-parallel geometry (Cumming et al. 2001) but more generally amounts to a fraction $1.8\times10^{-3}\ (B/10^8\,{\rm G})\ (\nu_{\rm c}/10^{18}\,{\rm s}^{-1})^{-1}\ (m_{\rm eff}/m_{\rm e})^{-1}$ of σ (Cumming et al. 2004, 2001), i.e. the electron cyclotron frequency divided by $\nu_{\rm c}$. It may therefore dominate near the equator, where the compressed field can reach $B\sim10^{15}\,{\rm G}$. In addition, the process of thermomagnetic drift is negligible in the ocean and outer crust, but it can dominate in the thin hydrogen/helium skin overlying the ocean (Cumming et al. 2001; Geppert and Urpin 1994). Neither the Hall nor the thermomagnetic drifts are diffusive; they do not smooth out field gradients as σ does. Indeed, the Hall drift tends to intensify field gradients by twisting the magnetic field in regions where the velocity of the electron fluid is sheared. The time-scale of this process is sensitive to the field geometry (as well as the radial profiles of the electron density and elastic shear modulus in the crust) (Cumming et al. 2004); it will be interesting to evaluate it for the distorted field produced by magnetic burial.

5.2.3 Mass quadrupole and magnetic dipole moments

Figure 5.1*a* depicts the density profile of the polar mountain (dashed ρ contours) and the flaring geometry of the magnetic field (solid ψ contours), for $M_{\rm a}=10^{-5}M_\odot$ and $\psi_{\rm a}/\psi_*=10^{-1}$. The accreted material spreads equatorward under its own weight until its advance is halted near the equator by the stress of the compressed (and hence amplified, by flux conservation) magnetic field. Figure 5.1*b* illustrates this balance of forces; the Lorentz force per unit volume, $(4\pi)^{-1}(\nabla\times\mathbf{B})\times\mathbf{B}$ (solid contours), peaks at the boundary $\psi_{\rm a}$ of the polar flux tube that receives accreted material, while the local magnetic field intensity, $|\mathbf{B}|$ (dashed contours), is amplified $\approx4\times10^3$ times above its initial polar value.

In Figure 5.2*a*, we plot the gravitational ellipticity $\epsilon=|I_1-I_3|/I_1$, where I_1 and I_3 denote principal moments of inertia, as a function of $M_{\rm a}$ for several values of $\psi_{\rm a}/\psi_*$. The reduced mass quadrupole moment is then given

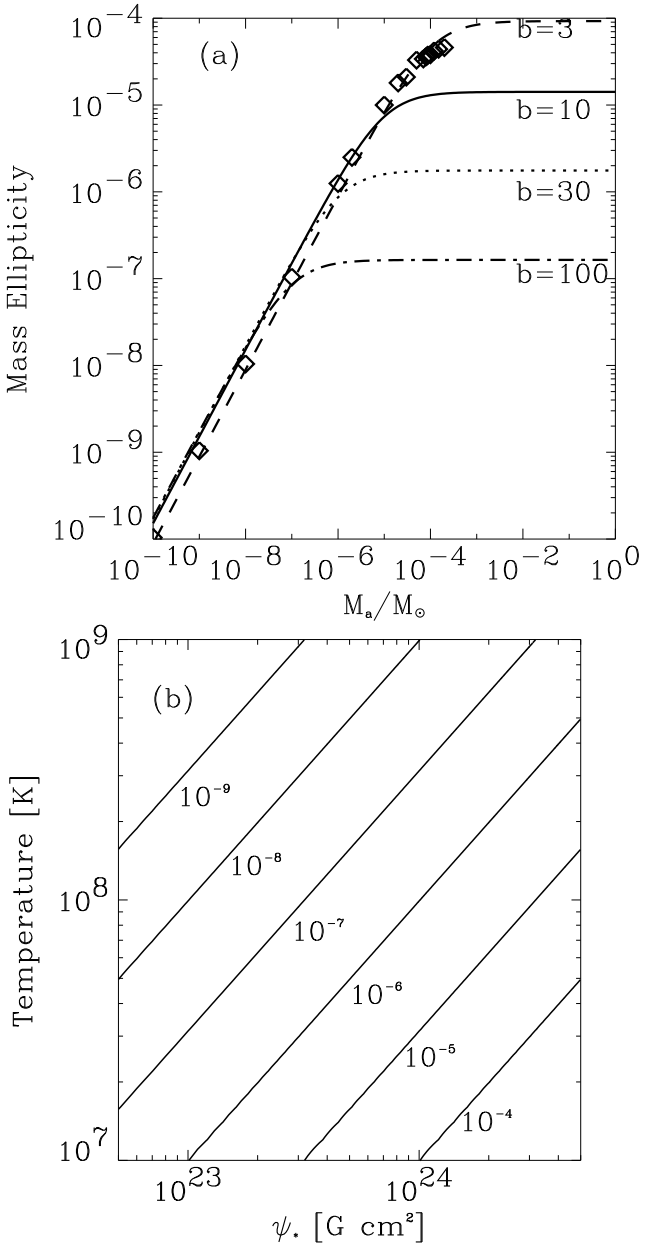

Figure 5.2: (*a*) Ellipticity $\epsilon = |I_1 - I_3|/I_1$ as a function of accreted mass M_a, for $b = \psi_*/\psi_\mathrm{a} = 3,\ 10,\ 30,\ 100$. The curves are theoretical, based on the expressions (5.5)–(5.10). The points are numerical results for $b = 3$. Parameters: $\psi_* = 10^{24}\,\mathrm{G\,cm^2}$, $T = 10^8\,\mathrm{K}$. (*b*) Contours of maximum ellipticity $\epsilon_\mathrm{max} = 20M_\mathrm{c}/(M_* b^2)$, from (5.8) and (5.10), as a function of total magnetic flux ψ_* and crustal temperature T. Contours are spaced logarithmically in the range $10^{-9} \leq M_\mathrm{c}/M_\odot \leq 10^{-4}$. In both panels, the regime $t_\mathrm{d} > t_\mathrm{a}$ is considered to highlight the effects of burial in isolation.

by $2\epsilon I_{zz}/3$, with $I_{zz} \approx 0.4 M_* R_*^2$ (Bonazzola and Gourgoulhon 1996; Shapiro and Teukolsky 1983). There is good agreement between the numerical and analytic results for $\psi_\mathrm{a}/\psi_* = 0.3$, where the gradients are manageable and the code converges reliably. The analytic results follow from a Green function analysis in the small-M_a limit, where the source term on the right-hand side of (5.2) is evaluated for a dipole, yielding (Payne and Melatos 2004)

$$\psi(x,y) = \psi_*(1-y^2)(1+x/a)^{-1}[1-(M_\mathrm{a}/M_\mathrm{c})b^2 y g(y) f(x)] \; , \tag{5.5}$$

$$\begin{aligned} \rho(x,y) &= M_\mathrm{a} a b [2\pi R_*^3 f(b)]^{-1} && (5.6)\\ &\quad \times [y^2 + (1-y^2)(M_\mathrm{a}/M_\mathrm{c}) b^2 y g(y) f(x)]^{1/2} && (5.7)\\ &\quad \times \exp[-b(1-y^2) - x + (M_\mathrm{a}/M_\mathrm{c}) b^3 y g(y) f(x)] \; , \end{aligned}$$

$$\mu = \psi_* R_* (1 + 3M_\mathrm{a}/4M_\mathrm{c})^{-1} \; , \tag{5.8}$$

$$\epsilon = (5M_\mathrm{a}/2M_*)(1-3/2b)(1 + M_\mathrm{a} b^2/8M_\mathrm{c})^{-1} \; , \tag{5.9}$$

to leading order in $M_\mathrm{a}/M_\mathrm{c}$, with

$$M_\mathrm{c} = G M_* \psi_*^2 / 4 c_\mathrm{s}^4 R_*^2 \; . \tag{5.10}$$

We define the dimensionless quantities $x = a(r/R_* - 1)$, $y = \cos\theta$, $f(x) = 1 - \exp(-x)$, $g(y) = \exp[-b(1-y^2)]$, $a = GM_*/c_\mathrm{s}^2 R_*$, and $b = \psi_*/\psi_\mathrm{a}$. Typically, the hydrostatic scale height is small compared to R_*, as is the polar fraction of the hemispheric flux, implying $a \gg 1$ and $b \gg 1$ respectively. The critical accreted mass M_c depends on the natal magnetic flux and crustal temperature through (5.10), with $M_\mathrm{c}/M_\odot = 3 \times 10^{-4} (\psi_*/10^{24}\,\mathrm{G\,cm^2})^2 (T/10^8\,\mathrm{K})^{-2}$ and $T = \bar{m} c_\mathrm{s}^2 / k_\mathrm{B}$ ($\bar{m}$ is the mean particle mass and k_B is the Bolzmann constant).

The dipole moment and mass ellipticity saturate at $\mu(M_\mathrm{d})$ and $\epsilon(M_\mathrm{d})$ respectively when Ohmic diffusion dominates ($M_\mathrm{a} > M_\mathrm{d}$; see section 5.2.2). From (5.4), (5.5), and (5.10), we obtain

$$\begin{aligned} \frac{M_\mathrm{d}}{M_\odot} = 3.4 \times 10^{-7} Z^{-4/9} &\left(\frac{\psi_\mathrm{a}}{0.1\psi_*}\right)^{16/9} \left(\frac{T}{10^8\,\mathrm{K}}\right)^{-20/9} \\ &\times \left(\frac{\psi_*}{10^{24}\,\mathrm{G\,cm^2}}\right)^{16/9} \left(\frac{\dot{M}_\mathrm{a}}{\dot{M}_\mathrm{Edd}}\right)^{4/9} . \end{aligned} \tag{5.11}$$

Contours of $M_{\rm d}$ in the $\dot{M}_{\rm a}$-T plane are displayed in Figure 5.3.

The $\epsilon(M_{\rm a})$ relation (5.9) associated with magnetic burial is new, while the $\mu(M_{\rm a})$ relation (5.8) is closely related to the phenomenological scaling invoked by Shibazaki et al. (1989) to model observations of binary and millisecond radio pulsars (Taam and van den Heuvel 1986; van den Heuvel and Bitzaraki 1995). It is important to note that magnetic burial affects ϵ and μ in different ways. The accreted mass above which ϵ saturates, $8M_{\rm c}b^{-2}$, and the saturation ellipticity, $\epsilon_{\rm max} = 20(M_{\rm c}/M_*)b^{-2}(1-3/2b)$, are inversely proportional to b^2 (for $b \gg 1$), whereas the accreted mass above which μ is screened, $4M_{\rm c}/3$, is independent of b. This theoretical prediction conforms with observations in two key respects. First, most accreting millisecond pulsars have $b \gtrsim 10$ (Litwin et al. 2001) and hence $\epsilon_{\rm max} \lesssim 10^{-7}$ from (5.9), consistent with the upper limit $\epsilon \lesssim 10^{-5}$ inferred from spin down (Brady et al. 1998; Dhurandhar et al. 1996) and the failure of bar antennas and interferometers to detect gravitational waves so far (Schutz 1999). Contours of $\epsilon_{\rm max}$ are plotted in the ψ_*-T plane in Figure 5.2*b*. Second, the floor magnetic moment of recycled neutron stars, which is observed to be 'universal', is given by $\mu_{\rm min} \sim 10^{26}\,{\rm G\,cm^{-3}}$ (for $M_{\rm a} \sim 10^{-1}M_\odot$) from (5.8). Theoretically, it is independent of b (and hence $\dot{M}_{\rm a}$) in the regime $t_{\rm d} \gtrsim t_{\rm a}$, and weakly dependent on $\dot{M}_{\rm a}$ in the regime $t_{\rm d} \lesssim t_{\rm a}$ (Melatos and Phinney 2001; Shibazaki et al. 1989). ϵ is probably exaggerated by the assumption of an impenetrable surface in the Grad-Shafranov model presented in chapter 2.

The distorted magnetic field in Figure 5.1*a* may be disrupted by interchange, Parker, and doubly diffusive instabilities wherever the local field strength exceeds $B \sim 10^{10}\,{\rm G}$ (Cumming et al. 2001; Litwin et al. 2001; Payne and Melatos 2004). However, more work is required to settle this issue; existing stability calculations are linear and plane-parallel, unlike the situation in Figure 5.1*a*. The equilibrium field may not be disrupted completely if the instability saturates promptly in the nonlinear regime; for example, the interchange instability is inhibited topologically by the line-tying boundary condition, which constrains the mobility of closely packed flux tubes.[3] In a separate effect, Payne and Melatos (2004) proved analytically that the magnetic field develops bubbles for $M_{\rm a} \gtrsim 10^{-4}M_\odot$; the source term on the

[3]Indeed, the numerical solution in Figure 5.1*a* represents the endpoint of a *convergent* sequence of iterations in a relaxation scheme. Convergence is cited by Mouschovias (1974) as evidence of stability because the relaxation process 'mimics' (albeit imperfectly) the true time-dependent evolution.

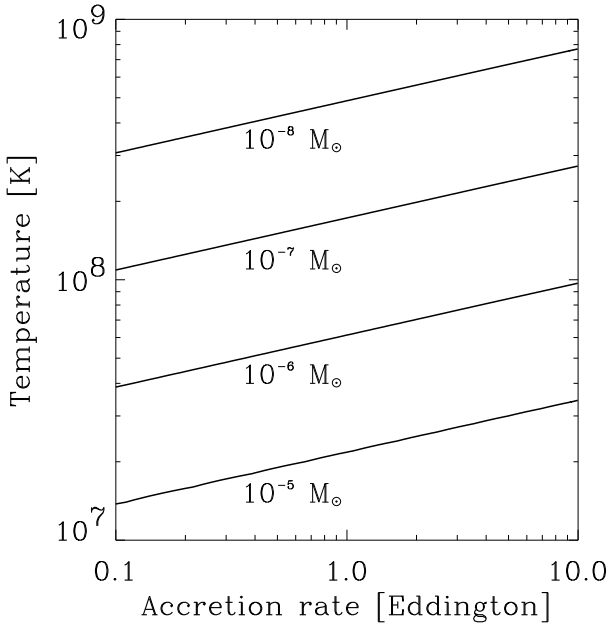

Figure 5.3: Contours of $M_{\rm d}$, the minimum accreted mass for which Ohmic diffusion arrests the growth of the polar mountain ($t_{\rm d} \leq t_{\rm a}$). The plot shows the variation of $M_{\rm d}$ with accretion rate $\dot{M}_{\rm a}$ (in units of $\dot{M}_{\rm Edd}$) and crustal temperature T (in kelvins), in the range $10^{-8} \leq M_{\rm d}/M_\odot \leq 10^{-5}$, with $\psi_{\rm a}/\psi_* = 0.1$, $Z = 1$, and $\psi_* = 10^{24}\,{\rm G\,cm^2}$. $M_{\rm d}$ is calculated from (5.4), (5.5), and (5.10).

right-hand side of (5.2) creates flux surfaces $\propto F'(\psi) \propto M_{\rm a}$ that are disconnected from the star ($\psi < 0$, $\psi > \psi_*$). Further work is required to determine how the bubbles evolve in the large-$M_{\rm a}$ regime (e.g. $M_{\rm a} \sim 10^{-1} M_\odot$), where the theory in section 5.2.1 breaks down.

5.3 Gravitational radiation

5.3.1 Detectability

The mass distribution resulting from polar magnetic burial is not rotationally symmetric in general; the principal axis of inertia $\mathbf{e}_3$ (i.e. the dipole axis of the natal magnetic field) is inclined at an angle α to the rotation axis. Gravitational waves are emitted by the deformed star at the spin frequency $\Omega = f/2$ and its first harmonic $2\Omega = f$ (unless $\alpha = \pi/2$, when there is no $f/2$ component), and the spin-down luminosity is proportional to $(16\sin^2\alpha + \cos^2\alpha)\sin^2\alpha$ (Bonazzola and Gourgoulhon 1996;

Shapiro and Teukolsky 1983). Upon averaging over α, polarization, and orientation (the position angle of the rotation axis on the sky cannot normally be measured), one can define the characteristic gravitational wave strain $h_{\rm c} = (128\pi^4/15)^{1/2} G I_{zz} f^2 \epsilon/(dc^4)$ (Brady et al. 1998), which reduces to

$$h_{\rm c} = 7.7 \times 10^{-19} \left(\frac{M_{\rm a}}{M_*}\right) \left(1 - \frac{3}{2b}\right) \left(1 + \frac{M_{\rm a} b^2}{8 M_{\rm c}}\right)^{-1} \times \left(\frac{f}{0.6\,{\rm kHz}}\right)^2 \left(\frac{d}{1\,{\rm kpc}}\right)^{-1} \tag{5.12}$$

upon substituting (5.9). Polar magnetic burial therefore generates gravitational radiation whose amplitude $h_{\rm c} \approx 6 \times 10^{-26}$ (for typical parameters $M_{\rm a} \gtrsim M_{\rm c} \sim 10^{-5} M_*$ and $b = 30$) is $\sim 10^5$ times greater than that produced by the natal, undistorted magnetic dipole, $h_{\rm c} \approx 10^{-31}\ (B/10^{12}\,{\rm G})^2 (f/0.6\,{\rm kHz})^2 (d/1\,{\rm kpc})^{-1}$ (Bonazzola and Gourgoulhon 1996; Katz 1989), due to the enhanced Maxwell stress from the compressed equatorial magnetic field. The self-consistent form of $F(\psi)$ defined by (5.3) is needed to calculate this stress properly; cf. Melatos and Phinney (2001).

Figure 5.4*a* is a plot of $h_{\rm c}$ versus f for $10^{-8} \leq M_{\rm a}/M_\odot \leq 10^{-2}$ and $10 \leq b \leq 10^2$. The sensitivity curves for initial LIGO (L) and advanced LIGO (AL) are superimposed, corresponding to the weakest source detectable with 99 per cent confidence in $\tau = 10^7$ s of integration time, if the frequency and phase of the signal at the detector are known in advance (Brady et al. 1998; Schutz 1999). The plot suggests that the prospects of detecting objects with $M_{\rm a} \gtrsim 10^{-5} M_\odot$ are encouraging, a point first made in the context of magnetic burial by Melatos and Phinney (2000). Such objects include the five accreting X-ray millisecond pulsars discovered at the time of writing, SAX J1808.4−3658, XTE J1751−305, XTE J0929−314, XTE J1807−294, and XTE J1814−338 (Campana et al. 2003; Chakrabarty and Morgan 1998; Galloway et al. 2002; Markwardt et al. 2002; Strohmayer and Bildsten 2003; Wijnands and van der Klis 1998). Detectability is facilitated if the time-dependent Doppler shift from the binary orbit is known well enough to be subtracted, but this is only practical for some objects of known f, not for an all-sky search (Brady et al. 1998).

The characteristic gravitational wave strain $h_{\rm c}$ is a lower limit in an important sense: it contains the assumption that, after averaging over polarization and orientation, the bulk of the gravitational wave signal is emitted

at $f = 2\Omega$. This is true when the observer views the system along its rotation axis, measuring $h^+ \propto h^\times \propto e^{2i\Omega t} \sin^2 \alpha$ in the two polarizations. It is *not* true when the observer views the system perpendicular to its rotation axis, measuring $h^+ \propto e^{2i\Omega t} \sin^2 \alpha$ and $h^\times \propto e^{i\Omega t} \sin \alpha \cos \alpha$, for example (Bonazzola and Gourgoulhon 1996; Shapiro and Teukolsky 1983). One certainly expects, as a matter of chance, to observe some systems in the latter orientation, or close to it. For these sources, the average quantity h_c substantially underestimates the true wave strain (which is dominated by $h^\times$ in the above example), especially if α is small.[4] (The observed pulse modulation indices of accreting millisecond pulsars imply a range of α values.) The effect on detectability is even greater when one takes into account the shape of the interferometer's noise curve; for example, LIGO is 1.5–2.5 times more sensitive at $\Omega \sim 0.3\,\mathrm{kHz}$ than at $2\Omega \sim 0.6\,\mathrm{kHz}$.

5.3.2 h_c versus μ

Polar magnetic burial is not the only mechanism whereby accreting neutron stars with $M_a \gtrsim 10^{-5} M_\odot$ can act as gravitational wave sources detectable by long baseline interferometers. Crustal deformation due to temperature gradients (section 5.4) is one of several alternatives (Bildsten 1998; Ushomirsky et al. 2000). In principle, we can distinguish between these mechanisms by eliminating M_a from (5.8) and (5.9) to derive a unique — and testable — scaling $h_c(\mu)$ for magnetic burial that relates observable quantities only, unlike (5.12), which features M_a (usually inferred from evolutionary models) (van den Heuvel and Bitzaraki 1995). The scaling,

$$h_c \propto (1 - 3/2b)[\mu/(\psi_* R_* - \mu) + b^2/6]^{-1}, \tag{5.13}$$

is graphed in Figure 5.4*b* for $3 \leq b \leq 100$. The vertical segments of all the curves represent the regime $M_a \ll M_c$, where μ retains its natal value while the ellipticity grows as M_a. The horizontal segments represent the regime $M_a \gg M_c$, where ϵ saturates while μ decreases, with the turn-off mass and $\epsilon_{\max}$ scaling as b^{-2}. The proportionality (5.13) does depend on b and ψ_*, neither of which can be measured, but the relevant scalings are moderately weak (e.g. $b \propto \dot{M}_a^{-2/7} \psi_*^{4/7}$). Consequently, the overall trend in Figure 5.4*b*

[4] We note in passing that h_c also underestimates the true wave strain substantially for precessing radio pulsars, e.g. PSR B1828−11, whose wobble angle is known to be small ($\lesssim 3°$) (Link and Epstein 2001).

may emerge statistically, once many gravitational wave sources have been detected, provided that the range of neutron star magnetic fields at birth is relatively narrow. Drawing upon population synthesis simulations, Hartman et al. (1997) inferred that $\approx$ 90 per cent of radio pulsars are born with $10^{23.5}\,\mathrm{G\,cm^2} \leq \psi_* \leq 10^{24.5}\,\mathrm{G\,cm^2}$, but the existence of anomalous X-ray pulsars implies a wider range of ψ_* in a subset of the neutron star population (Regimbau and de Freitas Pacheco 2001).

5.4 Discussion

In this chapter, we report on two new results concerning the gravitational radiation emitted by accreting neutron stars undergoing polar magnetic burial. First, upon calculating rigorously the hydromagnetic structure of the polar mountain, by solving a Grad-Shafranov boundary value problem with the correct flux freezing condition connecting the initial and final states, we find that the ellipticity of the star materially exceeds previous estimates, due to the enhanced Maxwell stress exerted by the compressed equatorial magnetic field, with $\epsilon \approx 20 M_\mathrm{c}/M_* b^2$ for $M_\mathrm{a} \gtrsim M_\mathrm{c} \sim 10^{-5} M_\odot$, as given by (5.10). The associated gravitational wave strain at Earth, $h_\mathrm{c} = 6 \times 10^{-24} (M_\mathrm{a}/M_\mathrm{c})(1 + M_\mathrm{a} b^2/8M_\mathrm{c})^{-1} (f/0.6\,\mathrm{kHz})^2 (d/1\,\mathrm{kpc})^{-1}$, averaged over polarization and orientation, is detectable in principle by the current generation of long baseline interferometers, e.g. LIGO. (The wave strain at $f/2 = \Omega$ in one polarization can exceed h_c for many orientations and α values.) Second, the stellar magnetic moment μ decreases as the polar mountain grows and spreads equatorward, implying a distinctive, observable scaling $h_\mathrm{c}(\mu)$, displayed in Figure 5.4*b*, which can be used to test the magnetic burial hypothesis. Accreting neutron stars are easier to detect as gravitational wave sources than other kilohertz sources like coalescing neutron star binaries: they are persistent rather than transient, the waveform is approximately sinusoidal, and, if X-ray pulsations or thermonuclear burst oscillations are observed in advance (e.g. SAX J1808.4−3658), extra sensitivity can be achieved by integrating coherently.

The range of ϵ predicted by the theory of magnetic burial is consistent with that invoked by Bildsten (1998) to explain the clustering of spin frequencies (within 40 per cent of 0.45 kHz) of weakly magnetized, accreting neutron stars (Chakrabarty et al. 2003) in terms of a stalling effect

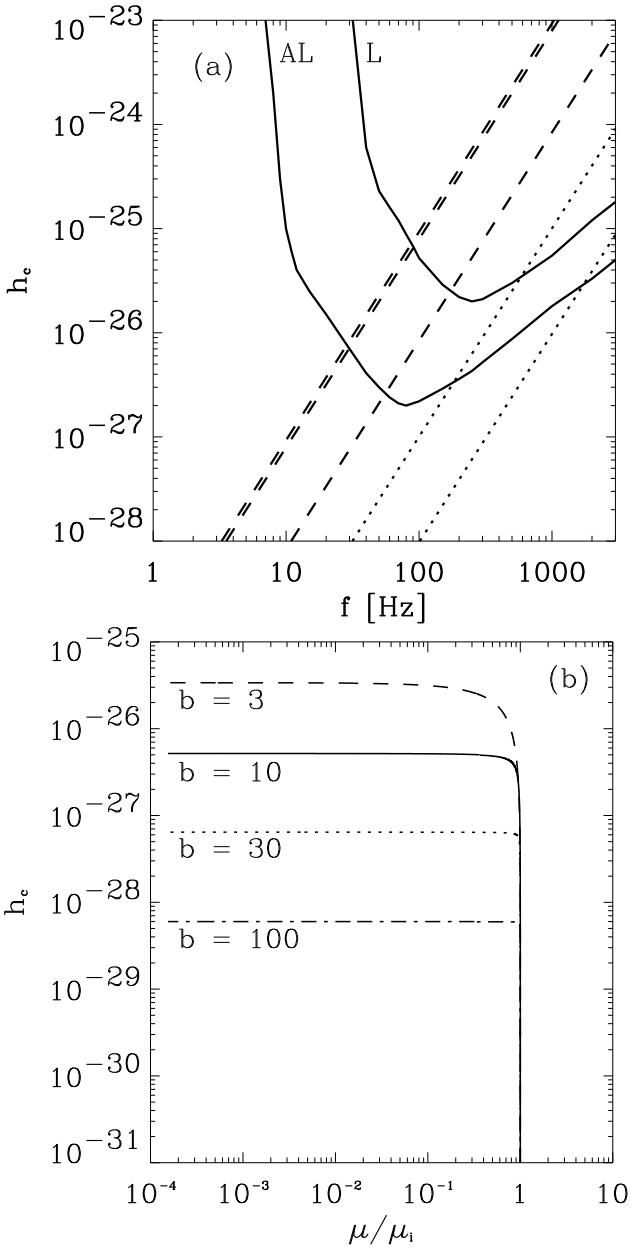

Figure 5.4: (a) Polarization- and orientation-averaged gravitational wave strain h_c as a function of wave frequency f. The initial and advanced LIGO noise curves (solid) correspond to detection with 99 per cent confidence after 10^7 s of coherent integration (Schutz 1999). Theoretical curves are shown for $b = 10$, $M_a/M_\odot = 10^{-2}$, 10^{-4}, 10^{-6} (dashed, top to bottom) and $b = 10^2$, $M_a/M_\odot = 10^{-4}$, 10^{-8} (dotted, top to bottom). (b) Gravitational wave strain h_c versus magnetic moment μ (scaled to the natal magnetic moment $\mu_i = \psi_* R_*$) for $b = 3$, 10, 30, 100, from (5.8) and (5.9).

where the gravitational wave torque ($\propto \Omega^5$) balances the accretion torque ($\propto \dot{M}_{\rm a} R_{\rm a}^{1/2} \propto \dot{M}_{\rm a}^{6/7} \mu^{2/7}$). Importantly, the theory of magnetic burial predicts that ϵ increases monotonically with $M_{\rm a}$ — a key precondition for the stalling effect to operate properly, otherwise the stall frequency Ω would not be a stable fixed point. In an alternative scenario, Bildsten (1998) and Ushomirsky et al. (2000) attribute the requisite mass quadrupole moment, $2 \times 10^{-7} I_{zz} (\dot{M}_{\rm a}/\dot{M}_{\rm Edd})^{1/2} (f/0.6\,{\rm kHz})^{-5/2}$, to lateral temperature gradients in the outer crust, which induce gradients in the electron capture rate and hence ρ.

Magnetic burial, acting in concert with the stalling effect, influences the rotational evolution of an accreting neutron star in two observationally testable ways. First, during the late stages of accretion, the instantaneous net torque is zero, because the gravitational wave and accretion torques balance (Bildsten 1998), but the average torque (on the time-scale $t_{\rm a}$) is effectively *negative*, because the gravitational wave torque increases with $M_{\rm a}$ as the polar mountain grows; that is, the instantaneous stall frequency $\Omega \propto \dot{M}_{\rm a}^{6/35} \mu (M_{\rm a})^{2/35} \epsilon (M_{\rm a})^{-2/5}$ decreases with $M_{\rm a}$. This effect ought to be detectable by X-ray timing experiments in progress (Galloway et al. 2002), although it may be masked if $\dot{M}_{\rm a}$ fluctuates stochastically on the time-scale $t_{\rm a}$, as commonly happens. Second, magnetic burial predicts a distinctive evolutionary relation between μ and Ω. During the early stages of accretion, before the star is spun up to the stall frequency, Ω increases while μ decreases due to burial, with $\Omega \propto R_{\rm a}^{1/2} M_{\rm a} \propto \dot{M}_{\rm a}^{-1/7} \mu^{-5/7}$ in the regime $\mu \propto M_{\rm a}^{-1}$. However, during the late stages of accretion, Ω and μ both decrease as explained above. Hence there exists a maximum spin frequency $\Omega/2\pi \lesssim 1\,{\rm kHz}$ bounding the population of accreting millisecond pulsars in the Ω-μ plane, and objects follow Λ-shaped evolutionary tracks in that plane.

Once accretion ends, do we expect to detect the neutron star as a radio millisecond pulsar? There are two arguments against this from the perspective of magnetic burial. First, the gravitational wave spin-down time, $t_{\rm g} \approx 5 \times 10^7 (\epsilon/10^{-7})^{-2} (\Omega/2\,{\rm krad\,s^{-1}})^{-4}\,{\rm yr}$, is shorter than the observed age, so the neutron star rapidly brakes below the radio pulsar death line ($\Omega/2\pi < 0.1\,{\rm kHz}$) and is extinguished as a radio source. Note that this occurs no matter what generates the quadrupole moment inferred from the stalling effect. Second, this rapid spin-down is interrupted if the stellar deformation relaxes quickly (compared to $t_{\rm g}$), for example if the buried, polar

magnetic field is resurrected on the Ohmic time-scale $t_{\rm d}$ of the outer crust, which satisfies $t_{\rm d} \sim t_{\rm a} = 6 \times 10^7 (M_{\rm a}/M_\odot)(\dot{M}_{\rm a}/\dot{M}_{\rm Edd})^{-1}\,{\rm yr}$ in the regime $M_{\rm a} \gtrsim 10^{-5} M_\odot$. However, the buried field is resurrected in stages; the steepest gradients are smoothed out ($L \propto t_{\rm a}^{1/2}$), but the natal field is not fully restored over the typical lifetime of a millisecond pulsar, because one has $\mu \propto L \propto t_{\rm a}^{1/2}$ and hence $B \sim 10^{9-10}\,{\rm G}$ after $\sim 10^9\,{\rm yr}$ (Cumming et al. 2001; Melatos and Phinney 2001). This scenario leaves the radio millisecond pulsars with the lowest fields unexplained unless they have low fields initially.

Chapter 6

Frequency spectrum of gravitational radiation from accreting neutron stars

6.1 Introduction

Nonaxisymmetric mountains on accreting neutron stars with millisecond spin periods are promising gravitational wave sources for long-baseline interferometers like the *Laser Interferometer Gravitational Wave Observatory* (LIGO). Such sources can be detected by coherent matched filtering without a computationally expensive hierarchical Fourier search (Brady et al. 1998), as they emit continuously at periods and sky positions that are known a priori from X-ray timing, at least in principle. Nonaxisymmetric mountains have been invoked to explain why the spin frequencies f_* of accreting millisecond pulsars, measured from X-ray pulses and/or thermonuclear burst oscillations (Chakrabarty et al. 2003; Wijnands et al. 2003b), are clustered in the range $0.27 \leq f_* \leq 0.62$ kHz. This is well below the centrifugal break-up frequency for most nuclear equations of state (Cook et al. 1994), suggesting that a gravitational wave torque balances the accretion torque, provided that the stellar ellipticity satisfies $\epsilon \sim 10^{-8}$ (Bildsten 1998). Already, the S2 science run on LIGO I has set upper limits on ϵ for 28 isolated radio pulsars, reaching as low as $\epsilon \leq 4.5 \times 10^{-6}$ for J2124−3358, following a coherent, multi-detector search synchronized to radio timing ephemerides (The LIGO Scientific Collaboration: B. Abbott et al. 2004b). Temperature

gradients (Bildsten 1998; Ushomirsky et al. 2000), large toroidal magnetic fields in the stellar interior (Cutler 2002), and polar magnetic burial, in which accreted material accumulates in a polar mountain confined by the compressed, equatorial magnetic field (Melatos and Payne 2005; Melatos and Phinney 2001; Payne and Melatos 2004), have been invoked to account for ellipticities as large as $\epsilon \sim 10^{-8}$. The latter mechanism is the focus of this chapter.

A magnetically confined mountain is not disrupted by ideal-magneto-hydrodynamic (ideal-MHD) instabilities, like the Parker instability, despite the stressed configuration of the magnetic field (Payne and Melatos 2005a). However, magnetospheric disturbances (driven by accretion rate fluctuations) and magnetic footpoint motions (driven by stellar tremors) induce the mountain to oscillate around its equilibrium position (Melatos and Payne 2005). In this chapter, we calculate the Fourier spectrum of the gravitational radiation emitted by the oscillating mountain. In section 6.2, we compute ϵ as a function of time by simulating the global oscillation of the mountain numerically with the ideal-MHD code ZEUS-3D. In section 6.3, we calculate the gravitational wave spectrum as a function of wave polarization and accreted mass. The signal-to-noise ratio (SNR) in the LIGO I and II interferometers is predicted in section 6.6 as a function of $M_{\rm a}$, for situations where the mountain does and does not oscillate, and for individual and multiple sources.

6.2 Magnetically confined mountain

6.2.1 Grad-Shafranov equilibria

During magnetic burial, material accreting onto a neutron star accumulates in a column at the magnetic polar cap, until the hydrostatic pressure at the base of the column overcomes the magnetic tension and the column spreads equatorward, compressing the frozen-in magnetic field into an equatorial magnetic belt or 'tutu' (Melatos and Phinney 2001; Payne and Melatos 2004). Figure 6.1 illustrates the equilibrium achieved for $M_{\rm a} = 10^{-5} M_{\odot}$, where $M_{\rm a}$ is the total accreted mass. As $M_{\rm a}$ increases, the equatorial magnetic belt is compressed further while maintaining its overall shape.

In the steady state, the equations of ideal MHD reduce to the force

balance equation (CGS units)

$$\nabla p + \rho \nabla \phi - (4\pi)^{-1} (\nabla \times \mathbf{B}) \times \mathbf{B} = 0, \tag{6.1}$$

where $\mathbf{B}$, ρ, $p = c_{\rm s}^2 \rho$, and $\phi(r) = GM_* r / R_*^2$ denote the magnetic field, fluid density, pressure, and gravitational potential respectively, $c_{\rm s}$ is the isothermal sound speed, M_* is the mass of the star, and R_* is the stellar radius. In spherical polar coordinates (r, θ, ϕ), for an axisymmetric field $\mathbf{B} = \nabla \psi(r, \theta) / (r \sin\theta) \times \hat{\mathbf{e}}_\phi$, (6.1) reduces to the Grad-Shafranov equation

$$\Delta^2 \psi = F'(\psi) \exp[-(\phi - \phi_0)/c_{\rm s}^2], \tag{6.2}$$

where Δ^2 is the spherical polar Grad-Shafranov operator, $F(\psi)$ is an arbitrary function of the magnetic flux ψ, and we set $\phi_0 = \phi(R_*)$. In this chapter, as in Payne and Melatos (2004), we fix $F(\psi)$ uniquely by connecting the initial and final states via the integral form of the flux-freezing condition, viz.

$$\frac{dM}{d\psi} = 2\pi \int_C \frac{ds\, \rho}{|\mathbf{B}|}, \tag{6.3}$$

where C is any magnetic field line, and the mass-flux distribution is chosen to be of the form $dM/d\psi \propto \exp(-\psi/\psi_{\rm a})$, where $\psi_{\rm a}$ is the polar flux, to mimic magnetospheric accretion (matter funneled onto the pole). We also assume north-south symmetry and adopt the boundary conditions $\psi =$ dipole at $r = R_*$ (line tying), $\psi = 0$ at $\theta = 0$, and $\partial\psi/\partial r = 0$ at large r. Equations (2) and (3) are solved numerically using an iterative relaxation scheme and analytically by Green functions, yielding equilibria like the one in Figure 6.1.

6.2.2 Global MHD oscillations

The magnetic mountain is hydromagnetically stable, even though the confining magnetic field is heavily distorted. Numerical simulations using ZEUS-3D, a multipurpose, time-dependent, ideal-MHD code for astrophysical fluid dynamics which uses staggered-mesh finite differencing and operator splitting in three dimensions (Stone and Norman 1992b), show that the equilibria from section 6.2.1 are not disrupted by growing Parker or interchange modes over a wide range of accreted mass ($10^{-7} M_\odot \lesssim M_{\rm a} \lesssim 10^{-3} M_\odot$) and intervals as long as 10^4 Alfvén crossing times (Payne and Melatos 2005a).

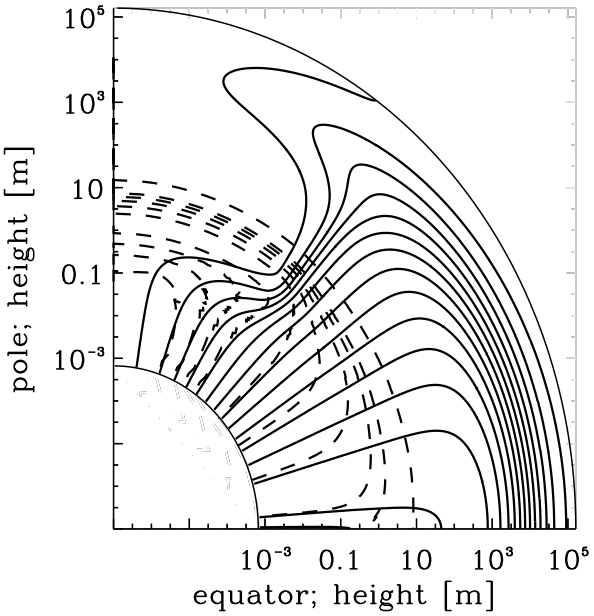

Figure 6.1: Equilibrium magnetic field lines (solid curves) and density contours (dashed curves) for $M_{\rm a} = 10^{-5} M_\odot$ and $\psi_{\rm a} = 0.1\psi_*$. Altitude is marked on the axes (log scale). [From Payne and Melatos (2004).]

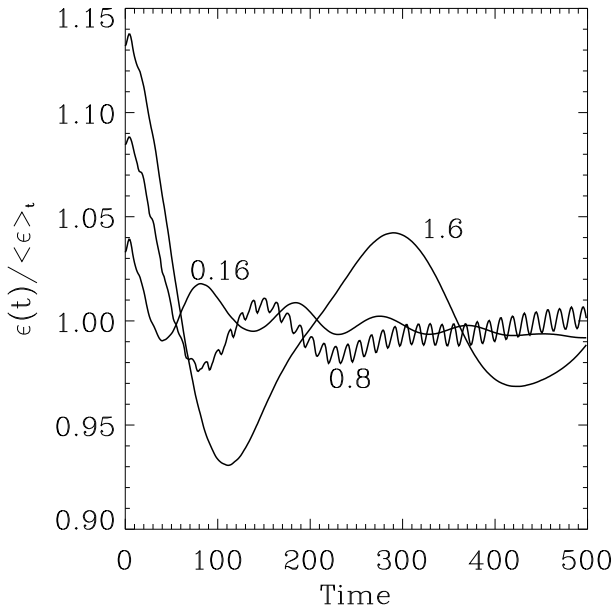

Figure 6.2: Normalized ellipticity $\epsilon(t)/\bar{\epsilon}$ for $M_{\rm a}/M_{\rm c} = 0.16, 0.80, 1.6$, with $\bar{\epsilon} = 8.0 \times 10^{-7}, 1.2 \times 10^{-6}, 1.3 \times 10^{-6}$ respectively for $b = 10$. Time is measured in units of the Alfvén crossing time, $\tau_{\rm A}$.

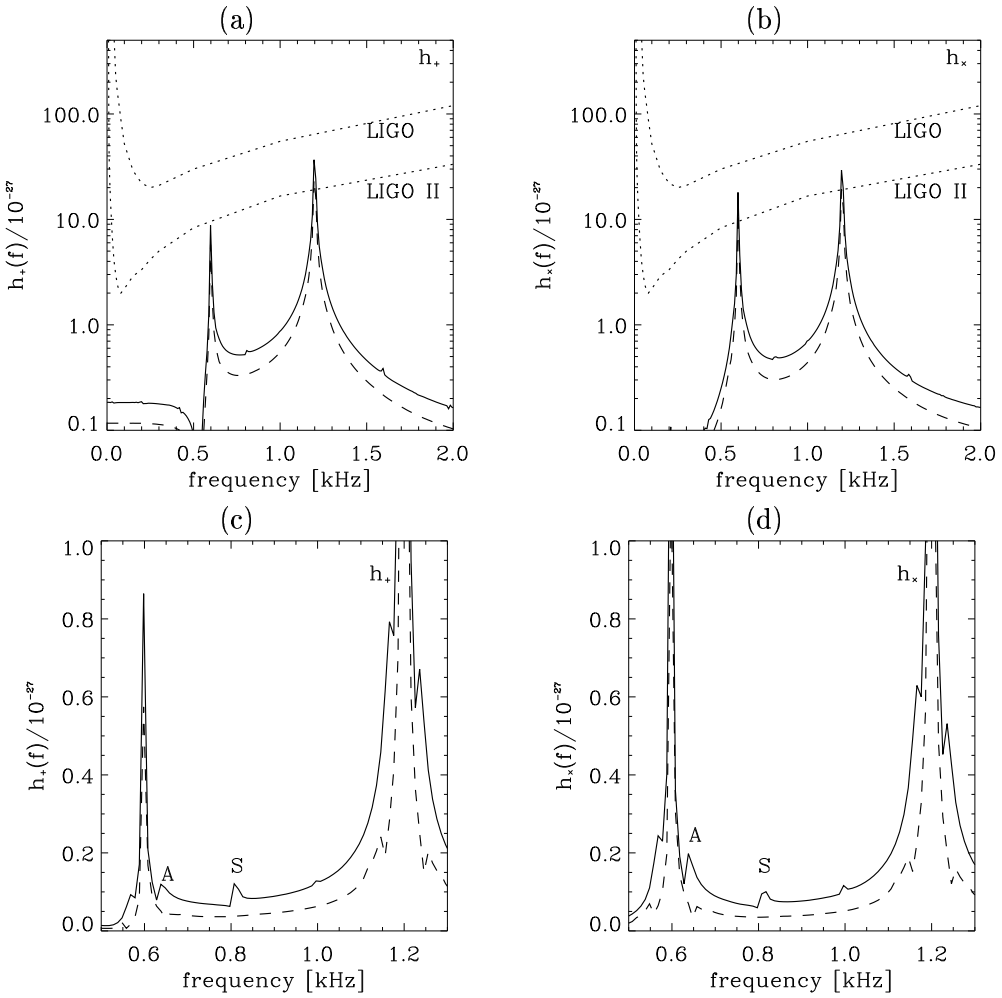

Figure 6.3: (*Top*) Fourier transforms of the wave strain polarization amplitudes $h_+(f)$ (*left*) and $h_\times(f)$ (*right*) for $M_a/M_c = 0.16$ (*dashed*) and 0.8 (*solid*), compared with the LIGO I and II noise curves $h_{3/yr}$ (see section 6.4) (*dotted*). The signals for $M_a/M_c = 0.16$ and 0.8 yield SNR = 2.9 and 4.4 respectively after 10^7 s. (*Bottom*). Zoomed-in view after reducing $h_{+,\times}(f_*)$ and $h_{+,\times}(2f_*)$ artificially by 90 per cent to bring out the sidebands. 'S' and 'A' label the signals induced by sound- and Alfvén-wave wobbles respectively. All curves are for $\alpha = \pi/3$, $i = \pi/3$, and $\psi_*/\psi_a = 10$.

However, the mountain does wobble when perturbed, as sound and Alfvén waves propagate through it (Payne and Melatos 2005a). Consequently, the ellipticity ϵ of the star oscillates about its mean value $\bar{\epsilon}$. The frequency of the oscillation decreases with $M_{\rm a}$, as described below. The mean value $\bar{\epsilon}$ increases with $M_{\rm a}$ up to a critical mass $M_{\rm c}$ and increases with $\psi_{\rm a}/\psi_*$, as described in section 6.3.1.

In ideal MHD, there is no dissipation and the oscillations persist for a long time even if undriven, decaying on the Alfvén radiation time-scale (which is much longer than our longest simulation run). In reality, the oscillations are also damped by ohmic dissipation, which is mimicked (imprecisely) by grid-related losses in our work.

To investigate the oscillations quantitatively, we load slightly perturbed versions of the Grad-Shafranov equilibria in section 6.2.1 into ZEUS-3D and calculate ϵ as a function of time t. Figure 6.2 shows the results of these numerical experiments. Grad-Shafranov equilibria are difficult to compute directly from (6.2) and (6.3) for $M_{\rm a} \gtrsim 1.6 M_{\rm c}$, because the magnetic topology changes and bubbles form, so instead we employ a bootstrapping algorithm in ZEUS-3D (Payne and Melatos 2005a), whereby mass is added quasistatically through the outer boundary and the magnetic field at the outer boundary is freed to allow the mountain to equilibrate. The experiment is performed for $r_0/R_* = c_{\rm s}^2 R_*/GM_* = 2 \times 10^{-2}$ (to make it computationally tractable) and is then scaled up to neutron star parameters ($r_0/R_* = 5 \times 10^{-5}$) according to $\epsilon \propto (R_*/r_0)^2$ and $\tau_{\rm A} \propto R_*/r_0$, where $\tau_{\rm A}$ is the Alfvén crossing time over the length-scale r_0 (Payne and Melatos 2005a).

The long-period wiggles in Figure 6.2 represent an Alfvén mode with phase speed $v_{\rm A} \propto M_{\rm a}^{-1/2}$; their period roughly triples from $100\tau_{\rm A}$ for $M_{\rm a}/M_{\rm c} = 0.16$ to $300\tau_{\rm A}$ for $M_{\rm a}/M_{\rm c} = 1.6$. Superposed is a shorter-period sound mode, whose phase speed $c_{\rm s}$ is fixed for all $M_{\rm a}$. Its amplitude is smaller than the Alfvén mode; it appears in all three curves in Figure 6.2 as a series of small kinks for $t \lesssim 50\tau_{\rm A}$, and is plainly seen at all t for $M_{\rm a}/M_{\rm c} = 0.8$. As $M_{\rm a}$ increases, the amplitude of the Alfvén component at frequency $f_{\rm A} \sim 17(M_{\rm a}/M_{\rm c})^{-1/2}$ Hz is enhanced. By contrast, the sound mode stays fixed at a frequency $f_{\rm S} \sim 0.4$ kHz, while its amplitude peaks at $M_{\rm a} \sim M_{\rm c}$ (Payne and Melatos 2005a).

6.3 Frequency spectrum of the gravitational radiation

In this section, we predict the frequency spectrum of the gravitational-wave signal emitted by freely oscillating and stochastically perturbed magnetic mountains in the standard orthogonal polarizations.

6.3.1 Polarization amplitudes

The metric perturbation for a biaxial rotator can be written in the transverse-traceless gauge as $h_{ij}^{\mathrm{TT}} = h_+ e_{ij}^+ + h_\times e_{ij}^\times$, where e_{ij}^+ and $e_{ij}^\times$ are the basis tensors for the + and × polarizations and the wave strains h_+ and $h_\times$ are given by (Bonazzola and Gourgoulhon 1996; Zimmermann and Szedenits 1979)

$$\begin{aligned} h_+ &= h_0 \sin\alpha[\cos\alpha \sin i \cos i \cos(\Omega t) \\ &\qquad - \sin\alpha(1+\cos^2 i)\cos(2\Omega t)]\,, \qquad (6.4) \\ h_\times &= h_0 \sin\alpha[\cos\alpha \sin i \sin(\Omega t) \\ &\qquad -2\sin\alpha\cos i \sin(2\Omega t)]\,, \qquad (6.5) \end{aligned}$$

with[1]

$$h_0 = 2GI_{zz}\epsilon\Omega^2/dc^4\,. \qquad (6.6)$$

Here, $\Omega = 2\pi f_*$ is the stellar angular velocity, i is the angle between the rotation axis $\mathbf{e}_z$ and the line of sight, α is the angle between $\mathbf{e}_z$ and the magnetic axis of symmetry, and d is the distance of the source from Earth.

The ellipticity is given by $\epsilon = |I_{zz} - I_{yy}|/I_0$, where I_{ij} denotes the moment-of-inertia tensor and $I_0 = \frac{2}{5}M_* R_*^2$. In general, ϵ is a function of t; it oscillates about a mean value $\bar{\epsilon}$, as in Figure 6.2. Interestingly, the oscillation frequency can approach Ω for certain values of M_{a} (see section 6.3.2), affecting the detectability of the source and complicating the design of matched filters. The mean ellipticity is given by (Melatos and Payne

[1] Our h_0 is half that given by Eq. (22) of Bonazzola and Gourgoulhon (1996).

2005)

$$\bar{\epsilon} = \begin{cases} 1.4 \times 10^{-6} \left(\dfrac{M_{\rm a}}{10^{-2} M_{\rm c}}\right) \left(\dfrac{B_*}{10^{12}\ {\rm G}}\right)^2 & M_{\rm a} \ll M_{\rm c} \\ \dfrac{5 M_{\rm a}}{2 M_*} \left(1 - \dfrac{3}{2b}\right) \left(1 + \dfrac{M_{\rm a} b^2}{8 M_{\rm c}}\right)^{-1} & M_{\rm a} \gtrsim M_{\rm c} \end{cases} \tag{6.7}$$

where $M_{\rm c} = G M_* B_*^2 R_*^2 / (8 c_{\rm s}^4)$ is the critical mass beyond which the accreted matter bends the field lines appreciably, $b = \psi_* / \psi_{\rm a}$ is the hemispheric to polar flux ratio, and B_* is the polar magnetic field strength prior to accretion. For $R_* = 10^6$ cm, $c_{\rm s} = 10^8$ cm s^{-1}, and $B_* = 10^{12}$ G, we find $M_{\rm c} = 1.2 \times 10^4 M_\odot$. The maximum ellipticity, $\bar{\epsilon} \to 20 M_{\rm c} / (M_* b^2) \sim 10^{-5} (b/10)^{-2}$ as $M_{\rm a} \to \infty$, greatly exceeds previous estimates, e.g. $\bar{\epsilon} \sim 10^{-12}$ for an undistorted dipole (Bonazzola and Gourgoulhon 1996; Katz 1989), due to the heightened Maxwell stress exerted by the compressed equatorial magnetic belt. Note that $\epsilon(t)$ is computed using ZEUS-3D for $b = 3$ (to minimize numerical errors) and scaled to larger b using (6.7).

6.3.2 Natural oscillations

We begin by studying the undamped, undriven oscillations of the magnetic mountain when it is "plucked", e.g. when a perturbation is introduced via numerical errors when the equilibrium is translated from the Grad-Shafranov grid to the ZEUS-3D grid (Payne and Melatos 2005a). We calculate $h_\times(t)$ and $h_+(t)$ for $f_* = 0.6$ kHz from (6.4) and (6.5) and display the Fourier transforms $h_\times(f)$ and $h_+(f)$ in Figure 6.3 for two values of $M_{\rm a}$. The lower two panels provide an enlarged view of the spectrum around the peaks; the amplitudes at f_* and $2f_*$ are divided by ten to help bring out the sidebands.

In the enlarged panels, we see that the principal carrier frequencies $f = f_*$, $2f_*$ are flanked by two lower frequency peaks arising from the Alfvén mode of the oscillating mountain (the rightmost of which is labelled 'A'). Also, there is a peak (labelled 'S') displaced by $\Delta f \sim 0.4$ kHz from the principal carriers which arises from the sound mode; it is clearly visible for $M_{\rm a}/M_{\rm c} = 0.8$ and present, albeit imperceptible without magnification, for $M_{\rm a}/M_{\rm c} = 0.16$. Moreover, ϵ diminishes gradually over many $\tau_{\rm A}$ (e.g. in Figure 6.2, for $M_{\rm a}/M_{\rm c} = 0.16$, ϵ drifts from $1.02\bar{\epsilon}$ to $0.99\bar{\epsilon}$ over $500\tau_{\rm A}$), causing the peaks at $f = f_*$, $2f_*$ to broaden. As $M_{\rm a}$ increases, this broadening increases; the frequency of the Alfvén component scales as $f_{\rm A} \propto M_{\rm a}^{-1/2}$ and

its amplitude increases $\propto M_{\rm a}^{1/2}$ (see section 6.2.2); and the frequency of the sound mode stays fixed at $f_{\rm S} \sim 0.4$ kHz (Payne and Melatos 2005a). Note that these frequencies must be scaled to convert from the numerical model ($r_0/R_* = 2 \times 10^{-2}$) to a realistic star ($r_0/R_* = 5 \times 10^{-5}$); it takes proportionally longer for the signal to cross the mountain (Payne and Melatos 2005a).

6.3.3 Stochastically driven oscillations

We now study the response of the mountain to a more complex initial perturbation. In reality, oscillations may be excited stochastically by incoming blobs of accreted matter (Wynn and King 1995) or starquakes that perturb the magnetic footpoints (Link et al. 1998). To test this, we perturb the Grad-Shafranov equilibria $\psi_{\rm GS}$ with a truncated series of spatial modes to obtain

$$\psi = \psi_{\rm GS}\{1 + \Sigma_n \delta_n \sin[m\pi(r - R_*)/(r_{\rm m} - R_*)] \sin(m\theta)\} \qquad (6.8)$$

at $t = 0$, with mode amplitudes scaling according to a power law $\delta_n = 0.25m^{-1}$, $m = 2n + 1$, $0 \leq n \leq 3$, as one might expect for a noisy process. Figure 6.4 compares the resulting spectrum to that of the free oscillations in section 6.3.2 for $M_{\rm a}/M_{\rm c} = 0.8$. The stochastic oscillations increase the overall signal strength at and away from the carrier frequencies f_* and $2f_*$. The emitted power also spreads further in frequency, with the full-width half-maximum of the principal carrier peaks measuring $\Delta f \approx 0.25$ kHz (c.f. $\Delta f \approx 0.2$ kHz in Figure 6.3). However, the overall shape of the spectrum remains unchanged. The Alfvén and sound peaks are partially washed out by the stochastic noise but remain perceptible upon magnification. The signal remains above the LIGO II noise curves in Figure 6.4; in fact, its detectability can (surprisingly) be enhanced, as we show below in section 6.4.

6.4 Signal-to-noise ratio

In this section, we investigate how oscillations of the mountain affect the SNR of such sources, and how the SNR varies with $M_{\rm a}$. In doing so, we generalize expressions for the SNR and characteristic wave strain $h_{\rm c}$ in the

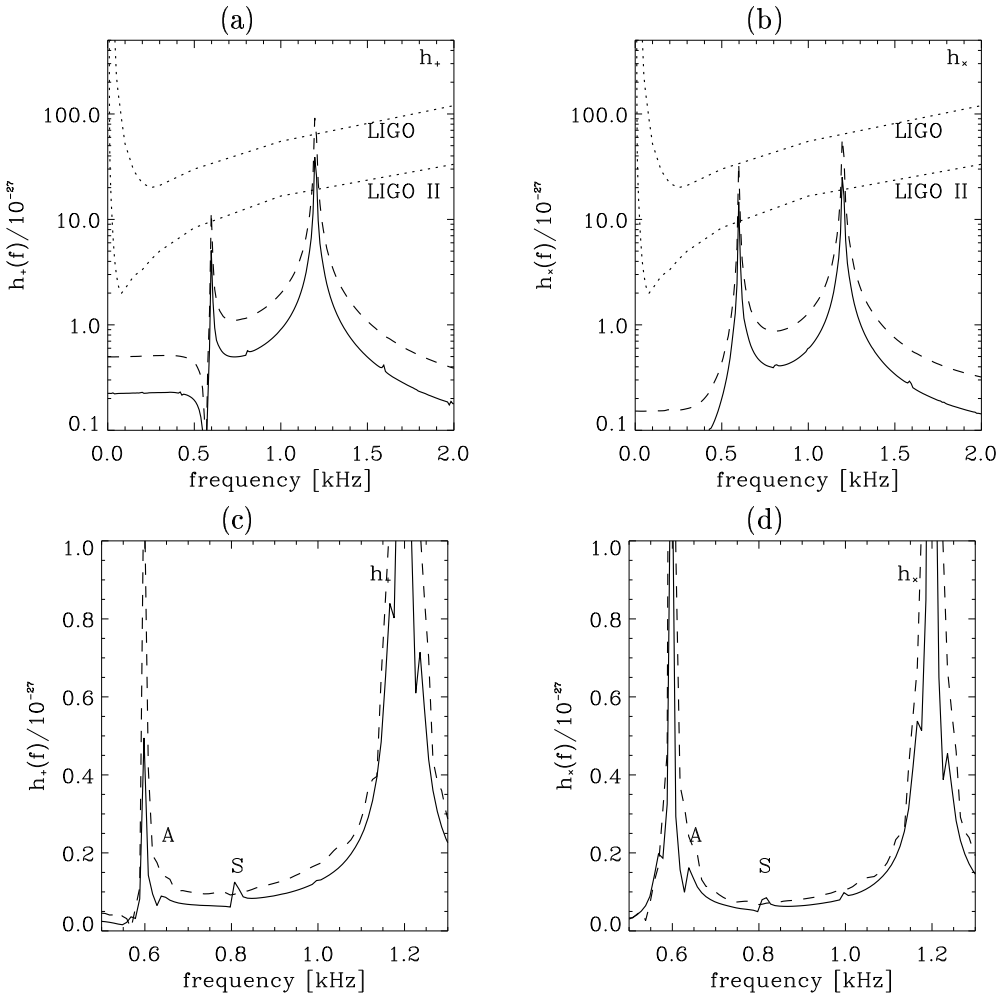

Figure 6.4: (*Top*) Fourier transforms of the wave strain polarization amplitudes $h_+(f)$ (*left*) and $h_\times(f)$ (*right*) for $M_\mathrm{a}/M_\mathrm{c} = 0.8$ with stochastic (*dashed*) and natural (*solid*), oscillations. compared with the LIGO I and II noise curves $h_{3/\mathrm{yr}}$ (see section 6.4) (*dotted*) corresponding to 99% confidence after 10^7 s. (*Bottom*) Zoomed in view with $h_{+,\times}(f_*)$ and $h_{+,\times}(2f_*)$ artificially reduced by 90 per cent to bring out the sidebands. 'S' and 'A' label the signal induced by sound- and Alfvén-wave wobbles respectively. All curves are for $\alpha = \pi/3$, $i = \pi/3$, and $\psi_*/\psi_\mathrm{a} = 10$.

literature to apply to nonaxisymmetric neutron stars oriented with arbitrary α and i.

6.4.1 Individual versus multiple sources

The signal received at Earth from an individual source can be written as $h(t) = F_+(t)h_+(t)+F_\times(t)h_\times(t)$, where F_+ and $F_\times$ are detector beam-pattern functions ($0 \leq |F_{+,\times}| \leq 1$) which depend on the sky position of the source as well as α and i (Thorne 1987). The squared SNR is then (Creighton 2003)[2]

$$\frac{S^2}{N^2} = 4\int_0^\infty df\,\frac{|h(f)|^2}{S_h(f)}\,, \tag{6.9}$$

where $S_h(f) = |h_{3/\mathrm{yr}}(f)|^2$ is the one-sided spectral density sensitivity function of the detector (Figures 6.3 and 6.4), corresponding to the weakest source detectable with 99 per cent confidence in 10^7 s of integration time, if the frequency and phase of the signal at the detector are known in advance (Brady et al. 1998).

A characteristic amplitude h_c and frequency f_c can also be defined in the context of periodic sources. For an individual source, where we know α, i, F_+ and $F_\times$ in principle, the definitions take the form

$$f_\mathrm{c} = \left[\int_0^\infty df\,\frac{|h(f)|^2}{S_h(f)}\right]^{-1}\,\left[\int_0^\infty df\,f\frac{|h(f)|^2}{S_h(f)}\right]\,, \tag{6.10}$$

and

$$h_\mathrm{c} = \frac{S}{N}[S_h(f_\mathrm{c})]^{1/2}\,. \tag{6.11}$$

These definitions are valid not only in the special case of an individual source with $\alpha = \pi/2$ (emission at $2f_*$ only) but also more generally for arbitrary α (emission at f_* and $2f_*$). Using (6.4), (6.5), (6.10) and (6.11), and assuming for the moment that ϵ is constant (i.e. the mountain does not oscillate), we obtain

$$f_\mathrm{c} = f_*(\chi A_1 + 2A_2)/(\chi A_1 + A_2)\,, \tag{6.12}$$

$$\frac{S}{N} = h_0[S_h(2f_*)]^{-1/2}(\chi A_1 + A_2)^{1/2}\sin\alpha \tag{6.13}$$

with $A_1 = \cos^2\alpha\sin^2 i(F_+\cos i+F_\times)^2$, $A_2 = \sin^2\alpha[F_+(1+\cos^2 i)+2F_\times\cos i]^2$, $\chi = S_h(2f_*)/S_h(f_*)$, and $\eta = S_h(f_c)/S_h(f_*)$. In the frequency range $0.2 \leq$

[2]This is twice the SNR defined in Eq. (29) of Thorne (1987).

$f \leq 3$ kHz, the LIGO II noise curve is fitted well by $h_{3/\mathrm{yr}}(f) = 10^{-26}(f/0.6\mathrm{kHz})$ $\mathrm{Hz}^{-1/2}$ (Brady et al. 1998), implying $\chi = 4$. As an example, for $(\alpha, i) = (\pi/3, \pi/3)$, we obtain $f_\mathrm{c} = 1.67 f_*$, $h_\mathrm{c} = 1.22 h_0$ and $S/N = 2.78(f_*/0.6\mathrm{kHz})(\epsilon/10^{-6})(d/10\mathrm{kpc})^{-1}$. In the absence of specific knowledge of the source position, we take $F_\times = F_+ = 1/\sqrt{5}$ (for motivation, see below).

If the sky position and orientation (α, i) of individual sources are unknown, it is sometimes useful to calculate the orientation- and polarization-averaged amplitude $\bar{h}_\mathrm{c}$ and frequency $\bar{f}_\mathrm{c}$. To do this, one cannot assume $\alpha = \pi/2$, as many authors do (Bildsten 1998; Brady et al. 1998; Thorne 1987); sources in an ensemble generally emit at f_* and $2f_*$. Instead, we replace $|h(f)|^2$ by $\langle |h(f)|^2 \rangle$ in (6.9), (6.10) and (6.11), defining the average as $\langle Q \rangle = \int_0^1 \int_0^1 Q \, d(\cos\alpha) \, d(\cos i)$. This definition is not biased towards sources with small α; we prefer it to the average $\langle Q \rangle_2 = \pi^{-1} \int_0^1 \int_0^\pi Q \, d\alpha \, d(\cos i)$, introduced in Eq. (87) of Jaranowski et al. (1998). Therefore, given an ensemble of neutron stars with mountains which are not oscillating, we take $\langle F_+^2 \rangle = \langle F_\times^2 \rangle = 1/5$ and $\langle F_+ F_\times \rangle = 0$ [Eq. (110) of Thorne (1987), c.f. Bonazzola and Gourgoulhon (1996); Jaranowski et al. (1998)], average over α and i to get $\langle A_1 \sin^2\alpha \rangle = 8/75$ and $\langle A_2 \sin^2\alpha \rangle = 128/75$, and hence arrive at $\bar{f}_\mathrm{c} = 1.80 f_*$, $\bar{h}_\mathrm{c} = 1.31 h_0$ and $\langle S^2/N^2 \rangle^{1/2} = 2.78(f_*/0.6\mathrm{kHz})(\epsilon/10^{-6})(d/10\mathrm{kpc})^{-1}$. This ensemble-averaged SNR is similar to the non-averaged value for $(\alpha, i) = (\pi/3, \pi/3)$, a coincidence of the particular choice.

Our predicted SNR, averaged rigorously over α and i as above, is $(2/3)^{1/2}$ times smaller than it would be for $\alpha = \pi/2$, because the (real) extra power at f_* does not make up for the (artificial) extra power that comes from assuming that all sources are maximal ($\alpha = \pi/2$) emitters. Our value of $\bar{h}_\mathrm{c}$ is 9/10 of the value of h_c quoted widely in the literature (Bildsten 1998; Brady et al. 1998; Thorne 1987). The latter authors, among others, assume $\alpha = \pi/2$ and average over i, whereas we average over α and i to account for signals at both f_* and $2f_*$; they follow Eq. (55) of Thorne (1987), who, in the context of *bursting* rather than continuous-wave sources, multiplies h_c by $(2/3)^{1/2}$ to reflect a statistical preference for sources with directions and polarizations that give larger SNRs (because they can be seen out to greater distances); and they assume $f_\mathrm{c} = 2f_*$ instead of $f_\mathrm{c} = 9f_*/5$ as required by (6.10).

6.4.2 Oscillations versus static mountain

We now compare a star with an oscillating mountain against a star whose mountain is in equilibrium. We compute (6.10) and (6.11) directly from $\epsilon(t)$ as generated by ZEUS-3D (see section 6.2 and 6.3.1), i.e. without assuming that $h_+(f)$ and $h_\times(f)$ are pure δ functions at $f = f_*$, $2f_*$.

Table 6.1 lists the SNR and associated characteristic quantities for three M_a values (and $b = 10$) for both the static and oscillating mountains. The case of a particular α and i ($\alpha = i = \pi/3$) is shown along with the average over α and i (Bildsten 1998; Brady et al. 1998; Thorne 1987). We see that the oscillations increase the SNR by up to $\sim$ 15 per cent; the peaks at $f = f_*$, $2f_*$ are the same amplitude as for a static mountain, but additional signal is contained in the sidebands. At least one peak exceeds the LIGO II noise curve in Figure 6.3 in each polarization.

6.4.3 Detectability versus M_a

The SNR increases with M_a, primarily because $\bar{\epsilon}$ increases. The effect of the oscillations is more complicated: although the Alfvén sidebands increase in amplitude as M_a increases, their frequency displacement from $f = f_*$ and $f = 2f_*$ decreases, as discussed in section 6.3.2, so that the extra power is confined in a narrower range of f. However, ϵ and hence the SNR plateau when M_a increases above M_c (see section 6.3.1). The net result is that increasing M_a by a factor of 10 raises the SNR by less than a factor of two. The SNR saturates at ~ 3.5 when averaged over α and i (multiple sources), but can reach ~ 6 for a particular source whose orientation is favorable. For our parameters, an accreting neutron star typically becomes detectable with LIGO II once it has accreted $M_\mathrm{a} \gtrsim 0.1 M_\mathrm{c}$.

6.5 Precession

The analysis in sections 6.3 and 6.4 applies to a biaxial star whose principal axis of inertia coincides with the magnetic axis of symmetry and is therefore inclined with respect to the angular momentum axis $\boldsymbol{J}$ in general (for $\alpha \neq 0$). Such a star precesses, a fact neglected in our analysis up to this point in order to maintain consistency with Bonazzola and Gourgoulhon (1996). In this section, we present a preliminary discussion of how precession modifies

Table 6.1: Signal-to-noise ratio quantities

f_* [kHz]	$M_a/10^{-4}M_\odot$	f_c[kHz]	$h_c/10^{-25}$	SNR
	Static	$\alpha = \pi/3$	$i = \pi/3$	
0.6	0.16	1.003	0.83	2.22
0.6	0.8	1.003	1.24	3.34
0.6	1.6	1.003	1.35	3.61
	Static	$\langle\rangle_\alpha$	$\langle\rangle_i$	
0.6	0.16	1.08	0.89	2.22
0.6	0.8	1.08	1.33	3.34
0.6	1.6	1.08	1.44	3.61
	Oscillating	$\alpha = \pi/3$	$i = \pi/3$	
0.6	0.16	1.008	1.40	2.63
0.6	0.8	1.003	2.15	4.02
0.6	1.6	1.004	2.27	4.25
	Oscillating	$\langle\rangle_\alpha$	$\langle\rangle_i$	
0.6	0.16	1.056	1.40	2.45
0.6	0.8	1.048	2.14	3.74
0.6	1.6	1.048	2.26	3.95

the gravitational wave spectrum $h_{+,\times}(f)$ emitted by a magnetically confined mountain.

Bonazzola and Gourgoulhon (1996) explicitly disregarded precession, arguing that most of the stellar interior is a fluid (crystalline crust $\lesssim 0.02M_*$), so that the precession frequency is reduced by $\sim 10^5$ relative to a rigid star (Pines and Shaham 1974). Equations (6.4) and (6.5) display this clearly. They are structurally identical to those that appear in the papers by Bonazzola and Gourgoulhon (1996) and Zimmermann and Szedenits (1979), but these two sets of authors differ markedly in their physical interpretations. In Zimmermann and Szedenits (1979), Ω differs from the pulsar spin frequency by the body-frame precession frequency, as expected for a precessing, rigid, Newtonian star, whereas in Bonazzola and Gourgoulhon (1996), Ω exactly equals the pulsar spin frequency, as expected for a (magnetically) distorted (but not precessing) fluid star. Moreover, θ (which replaces α) in Zimmermann and Szedenits (1979) is the angle between the angular momentum vector $\boldsymbol{J}$ (fixed in inertial space) and the principal axis of inertia $\mathbf{e}_3$, whereas α in Bonazzola and Gourgoulhon (1996) is the angle between the rotation axis $\boldsymbol{\Omega}$ and axis of symmetry $\boldsymbol{\mu}$ of the (magnetic) distortion. Both interpretations

Table 6.2: Four precession scenarios. Here, $\mathbf{e}_3$ is the principal axis of inertia, $\boldsymbol{\mu}$ is the axis of the magnetic dipole, $\boldsymbol{\Omega}$ is the spin axis, and f_* is the spin frequency. Entries containing f_* and/or $2f_*$ indicate gravitational wave emission at those frequencies; entries labelled 'zero' indicate no gravitational wave emission. We also specify whether or not each scenario admits X-ray pulsations.

	$\mathbf{e}_3 \parallel \boldsymbol{\Omega}$	$\mathbf{e}_3 \nparallel \boldsymbol{\Omega}$
$\mathbf{e}_3 \parallel \boldsymbol{\mu}$	$2f_*$ (triaxial)	$f_*, 2f_*$
	zero (biaxial)	
	no pulsar	pulsar
$\mathbf{e}_3 \nparallel \boldsymbol{\mu}$	$2f_*$ (triaxial)	$f_*, 2f_*$
	zero (biaxial)	
	pulsar	pulsar

match on time-scales that are short compared to the free precession time-scale $\tau_{\rm p} \approx (f_*\epsilon)^{-1}$, but the quadrupole moments computed in this chapter ($\epsilon \sim 10^{-7}$) and invoked by Bildsten (1998) to explain the spin frequencies of low-mass X-ray binaries ($10^{-8} \leq \epsilon \leq 10^{-7}$) predict $\tau_{\rm p}$ of order hours to days. The effect is therefore likely to be observable, unless internal damping proceeds rapidly; best estimates (Jones and Andersson 2002) of the dissipation time-scale give $\approx 3.2\,{\rm yr}\,(\kappa/10^4)(0.1{\rm kHz}/f_*)\ (I_0/10^{44}{\rm g\,cm^2})\ (10^{38}{\rm g\,cm^2}/I_{\rm d})$, where $I_{\rm d}$ is the piece of the moment of inertia that "follows" $\mathbf{e}_3$ (not $\boldsymbol{\Omega}$), and $400 \lesssim \kappa \lesssim 10^4$ (the Q of the free precession) parametrises the internal damping [e.g. from scattering of electrons off superfluid vortices (Alpar and Sauls 1988)].[3]

Four possible precession scenarios are summarised in table 6.2 (Melatos 2000). Unfortunately, none of them is completely satisfactory. If we attribute persistent X-ray pulsations to magnetic funnelling onto a polar hot spot, or to a magnetically anisotropic atmospheric opacity, then the angle between $\boldsymbol{\mu}$ and $\boldsymbol{\Omega}$ can be large, leading to precession with a large wobble angle, which would presumably be damped on short time-scales unless it is driven (cf. Chandler wobble). The pulsar would emit gravitational waves

[3]Precession has been detected in the isolated radio pulsar PSR B1828−11 (Link and Epstein 2001; Stairs et al. 2000). Ambiguous evidence also exists for long-period ($\sim$ days) precession in the Crab (Lyne et al. 1988), Vela (Deshpande and McCulloch 1996), and PSR B1642−03 (Shabanova et al. 2001). Of greater relevance here, it may be that Her X-1 precesses (e.g. Shakura et al. 1998). This object is an accreting neutron star where the precession may be continuously driven.

at a frequency near f_* (offset by the body-frame precession frequency) and $2f_*$. The relative orientations of $\boldsymbol{\mu}$, $\boldsymbol{\Omega}$ and $\mathbf{e}_3$ are determined when the crust of the newly born neutron star crystallizes after birth and subsequently by accretion torques. This is discussed in detail by Melatos (2000). If viscous dissipation in the fluid star forces $\boldsymbol{\Omega}$ to align with $\boldsymbol{\mu}$ before crystallization, and if the symmetry axis of the crust when it crystallizes is along $\boldsymbol{\Omega}$, then $\mathbf{e}_3$ (of the crystalline crust plus the subsequently accreted mountain), $\boldsymbol{\mu}$, and $\boldsymbol{\Omega}$ are all parallel and there is no precession (nor, indeed, pulsation). But if the crust crystallizes before $\boldsymbol{\Omega}$ has time to align with $\boldsymbol{\mu}$, then $\mathbf{e}_3$ and $\boldsymbol{\Omega}$ are not necessarily aligned (depending on the relative size of the rotation bulge and pre-accretion magnetic deformation) and there is precession. Moreover, this conclusion does not change when a mountain is subsequently accreted along $\boldsymbol{\mu}$; the new $\mathbf{e}_3$ (nearly, but not exactly, parallel to $\boldsymbol{\mu}$) is still misaligned with $\boldsymbol{\Omega}$ in general. Gravitational waves are emitted at f_* and $2f_*$. Of course, internal dissipation after crystallization (and, indeed, during accretion) may force $\boldsymbol{\Omega}$ to align with $\mathbf{e}_3$ (cf. Earth).[4,5] If this occurs, the precession stops and the gravitational wave signal at f_* disappears. The smaller signal at $2f_*$ persists if the star is triaxial (almost certainly true for any realistic magnetic mountain, even though we do not calculate the triaxiality explicitly in this thesis) and disappears if the star is biaxial (which is unlikely).

To compute the polarization waveforms with precession included, we employ the small-wobble-angle expansion for a nearly spherical star derived by Zimmermann (1980) and extended to quadratic order by Van Den Broeck

[4]Accreting millisecond pulsars like SAX J1808.4−3658 do not show evidence of precession in their pulse shapes, but it is not clear how stringent the limits are (Galloway, private communication).

[5]We do not consider the magnetospheric accretion torque here (Lai 1999).

(2005), viz.

$$
\begin{aligned}
h_+ &= -\frac{2GI_3\Omega_{\rm r}^2}{dc^4}\frac{(I_2-I_1)}{I_3}(1+\cos^2 i)\cos(2\Omega_{\rm r}t) \\
&\quad +\frac{GI_3\left(\Omega_{\rm r}+\Omega_{\rm p}\right)^2}{dc^4}\frac{2I_3-(I_1+I_2)}{2I_3}\left(\frac{I_1 a}{I_3 b}\right) \\
&\quad \times \sin 2i\,\cos[(\Omega_{\rm r}+\Omega_{\rm p})t]\,, \qquad (6.14) \\
h_\times &= -\frac{4GI_3\Omega_{\rm r}^2}{dc^4}\frac{(I_2-I_1)}{I_3}\cos i\,\sin(2\Omega_{\rm r}t) \\
&\quad +\frac{2GI_3\left(\Omega_{\rm r}+\Omega_{\rm p}\right)^2}{dc^4}\frac{2I_3-(I_1+I_2)}{2I_3}\left(\frac{I_1 a}{I_3 b}\right) \\
&\quad \times \sin i\,\sin[(\Omega_{\rm r}+\Omega_{\rm p})t]\,, \qquad (6.15)
\end{aligned}
$$

where subscripts 1,2, and 3 denote components along the principal axes of inertia. The fundamental angular frequencies in the problem are

$$
\begin{aligned}
\Omega_{\rm p} &= \frac{\pi b}{2K(m)}\left[\frac{(I_3-I_2)(I_3-I_1)}{I_1 I_2}\right]^{1/2}, \qquad (6.16) \\
\Omega_{\rm r} &= \frac{J}{I_1}-\left[1+\frac{i}{\pi}\frac{\vartheta_4'(i\pi\alpha)}{\vartheta_4(i\pi\alpha)}\right]\Omega_{\rm p}\,, \qquad (6.17)
\end{aligned}
$$

where

$$
\begin{aligned}
m &= \frac{(I_2-I_1)I_1 a^2}{(I_3-I_2)I_3 b^2}, \qquad (6.18) \\
\delta &= 1-\left[\frac{I_1(I_3-I_2)}{I_2(I_3-I_1)}\right]^{1/2}, \qquad (6.19)
\end{aligned}
$$

are small expansion parameters. The constants a and b are defined such that $\Omega_1 = a$ and $\Omega_3 = b$ at $t = 0$ (precession angle $\approx a/b \ll 1$), ϑ_4 is the fourth Jacobi theta function with nome[6]

$$
q = \exp\left[-\pi K(1-m)/K(m)\right], \qquad (6.20)
$$

and $K(m)$ is the complete elliptic integral of the first kind (Abramowitz and Stegun 1972). These formulae are valid for small a/b, small oblateness $(I_3-I_1)/I_1$, and small triaxiality $(I_2-I_1)/(I_3-I_2)$ (Zimmermann 1980). If these conditions are not met, e.g. if the triaxiality is significant, a more

[6]The nome of a Jacobi theta function is defined as $q = e^{\pi i\tau}$, where τ is the half-period ratio (Abramowitz and Stegun 1972).

general calculation is possible, for which Zimmermann (1980) provides an explicit recipe. This calculation lies outside the scope of this chapter, but constitutes important future work.

6.6 Discussion

A magnetically confined mountain forms at the magnetic poles of an accreting neutron star during the process of magnetic burial. The mountain, which is generally offset from the spin axis, generates gravitational waves at f_* and $2f_*$. Sidebands in the gravitational-wave spectrum appear around f_* and $2f_*$ due to global MHD oscillations of the mountain which may be excited by stochastic variations in accretion rate (e.g. disk instability) or magnetic footpoint motions (e.g. starquake). The spectral peaks at f_* and $2f_*$ are broadened, with full-widths half-maximum $\Delta f \approx 0.2$ kHz. We find that the SNR increases as a result of these oscillations by up to 15 per cent due to additional signal from around the peaks.

Recent coherent, multi-interferometer searches for continuous gravitational waves from nonaxisymmetric pulsars appear to have focused on the signal at $2f_*$, to the exclusion of the signal at f_*. Examples include the S1 science run of the LIGO and GEO 600 detectors, which was used to place an upper limit $\epsilon \leq 2.9 \times 10^{-4}$ on the ellipticity of the radio millisecond pulsar J1939+2134 (The LIGO Scientific Collaboration: B. Abbott et al. 2004c), and the S2 science run of the three LIGO I detectors (two 4-km arms and one 2-km arm), which was used to place upper limits on ϵ for 28 isolated pulsars with $f_* > 25$ Hz (The LIGO Scientific Collaboration: B. Abbott et al. 2004b). Our results indicate that these (time- and frequency-domain) search strategies must be revised to include the signal at f_* (if the mountain is static) and even to collect signal within a bandwidth Δf centred at f_* and $2f_*$ (if the mountain oscillates).

Our results suggest that sources such as SAX J1808.4−3658 may be detectable by next generation long-baseline interferometers like LIGO II. Note that, for a neutron star accreting matter at the rate $\dot{M} \approx 10^{-11} M_\odot \mathrm{yr}^{-1}$ (like SAX J1808.4−3658), it takes only 10^7 yr to reach $S/N > 3$. The characteristic wave strain $h_\mathrm{c} \sim 4 \times 10^{-25}$ is also comparable to that invoked by Bildsten (1998) to explain the observed range of f_* in low-mass X-ray binaries. An observationally testable scaling between h_c and the magnetic

dipole moment has been predicted (Melatos and Payne 2005).

The analysis in this chapter disregards the fact that LIGO II will be tunable. It is important to redo the SNR calculations with realistic tunable noise curves, to investigate whether the likelihood of detection is maximized by observing near f_* or $2f_*$. We also do not consider several physical processes that affect magnetic burial, such as sinking of accreted material, Ohmic dissipation, or Hall currents; their importance is estimated roughly by Melatos and Payne (2005). Finally, stellar precession (Cutler and Jones 2001) is neglected in this analysis, as are Doppler shifts due to the Earth's orbit and rotation (e.g. Bonazzola and Gourgoulhon 1996) and slow secular drifts in sensitivity during a coherent integration.

A fuller study of the waveforms emitted by a precessing neutron star with a magnetically confined mountain is essential. We plan to undertake it immediately upon completion of this thesis.

Chapter 7

Conclusion

This thesis began by asking what happens to the magnetic field of a neutron star when it accretes matter onto its magnetic poles from a binary companion. It has ended with a prediction of gravitational radiation from these "magnetic mountains", providing yet another testing ground for general relativity, now that a positive detection of gravitational waves is imminent after recent technical advances in long-baseline gravitational-wave interferometry. In this chapter, we summarise our main results (section 7.1) and discuss how they increase our understanding of certain astrophysical problems: magnetic field reduction in recycled compact objects (section 7.2), millisecond oscillations in type I X-ray bursts (section 7.3), and the range of millisecond pulsar spins (section 7.4). In section 7.5, suggestions are made regarding where the theory of magnetic burial needs to be developed further, and to what other astrophysical problems it can be profitably applied.

7.1 Synopsis of results

7.1.1 Magnetic burial

Magnetic burial or screening is one of three explanations for why the magnetic dipole moment of an accreting neutron star reduces from its birth in a supernova ($\sim 10^{30}$ G cm^3) to its death as an old millisecond pulsar ($\sim 10^{26}$ G cm^3). (The others are accelerated Ohmic decay and vortex-fluxoid spin interactions.) In this thesis, we rigorously calculate magnetostatic equilibria describing the mountains of material piled up at the magnetic poles of the star. Our calculations are novel in two respects: they treat properly the

magnetic stresses exerted by the equatorial magnetic field, which is compressed by, and "pushes back" against, the mountain; and they treat flux freezing self-consistently, so that the final state is realisable from the initial undistorted dipole by a continuous route in the ideal-MHD limit. We showed analytically (using a Green-function, small-$M_{\rm a}$ expansion) and numerically (by iteratively solving the Grad-Shafranov equation in tandem with a flux-freezing condition) that the magnetic dipole moment is not reduced significantly until $M_{\rm a} \sim 10^{-5} M_\odot$ has been accreted (chapter 2). This is markedly greater than previous estimates ($\lesssim 10^{-10} M_\odot$), which ignored equatorial magnetic stresses and mass-flux conservation.

Several numerical challenges, mainly associated with steep magnetic field gradients, were overcome in the course of this work. A customised, nonuniform numerical grid and optimised relaxation algorithm made it possible to compute Grad-Shafranov equilibria up to $M_{\rm a} \sim 10^{-4} M_\odot$ for the first time. Then, adopting a customised bootstrap approach, we managed to add more mass to these equilibria in the time-dependent, ideal-MHD code ZEUS-3D, reaching $M_{\rm a} \sim 10^{-3} M_\odot$ in the best case (chapter 3). This is significantly closer to realistic amounts of accreted mass than previous calculations. However, more (hard) work is needed to reach $M_{\rm a} \sim 0.1 M_\odot$, and to do so for realistic polar cap radii ($\psi_{\rm a}/\psi_* \sim 10^{-2}$). In this sense, the ultimate structure of the magnetic mountain in LMXBs remains unsolved despite our best efforts in this thesis.

The late stages of magnetic burial may be modelled either with or without velocity flow. In models with flow (e.g. Choudhuri and Konar 2002), the magnetic field evolves according to the induction equation with the velocity field prescribed (no Lorentz force). Polar cap widening can lessen the amount of screening caused by accreting matter (Konar and Choudhuri 2004). Models without flow, such as the one presented in this thesis, are justified because the local Alfvén time-scale is much shorter than the accretion flow time. Which scenario is correct in the later stages of magnetic burial? The definite answer is not provided by this thesis due to numerical difficulties. However, it is likely that a combination of both scenarios is required for a complete understanding.

Given the distorted magnetic structure of the mountains computed in chapter 2, it is natural to expect that these configurations are unstable. As it turns out, this is not true — a surprising result. We tested the issue

thoroughly in chapter 3 by evolving perturbed Grad-Shafranov equilibria in ZEUS-3D. Apart from some transient Parker-type modes, which quickly die away and affect μ at the level of just a few per cent, the equilibria are not disrupted. Indeed, after $\sim 10^5$ or more years of quasistatic accretion, they are already at their (nonlinear) Parker saturation state. On the other hand, when perturbed, the equilibria oscillate — a new result. The oscillation frequency $\propto M_{\rm a}^{-1/2}$ can reach close to f_* for $M_{\rm a} \sim 10^{-7} M_\odot$. It will be interesting to look for observable manifestations of this effect, e.g. in gravitational-wave signals (section 7.1.2).

To simplify our task in this thesis, we assumed perfect conductivity, which exaggerates how firmly the polar mountain is confined; an impenetrable stellar surface, which does not allow sinking of accreted material into the crust; and axisymmetry, which suppresses several hydromagnetic instabilities. Further work must lift these restrictions, as discussed in section 7.5.1.

7.1.2 Gravitational radiation

An accreting neutron star's quadrupole moment steadily increases as accreted matter piles up at the magnetic poles, saturating at $\sim 10^{-7} M_* R_*^2$ when matter starts spreading and Ohmic diffusion becomes important. Since the magnetic and spin axes are generally misaligned, gravitational waves are emitted. We predict that the resulting orientation- and polarization-averaged gravitational wave strain at Earth is $h \sim 6 \times 10^{24}$, detectable by LIGO II. Assuming a neutron star is an approximately rigid body, such large distortions give rise to a precession time-scale $\sim$ days for a LMXB with $f_* \sim 0.5$ kHz. The precession may decay due to internal dissipation, but its fate is unclear (see section 6.5) and needs to be investigated more completely. The magnetic burial model gives μ and ϵ as functions of $M_{\rm a}$. Eliminating $M_{\rm a}$, we predict a relation between h and μ, which is potentially testable. Magnetic mountains are therefore distinguishable from other types of deformation, once gravitational waves are detected directly.

Gravitational waves are emitted at both f_* and $2f_*$ — a point that is sometimes overlooked in the literature. Most authors focus on the emission at $2f_*$, inherently assuming that the distortion is perpendicular to the spin axis. The importance of the f_* component of the signal from a (nonoscillating) magnetic mountain is illustrated in figure 7.1, which compares the

signal-to-noise ratio for different values of the angles between the rotation axis and the line of sight (i) or the magnetic axis (α). For $i \gtrsim \pi/3$, the signal-to-noise ratio nearly doubles when both the f_* and $2f_*$ components are considered. The signal-to-noise ratio is between ~ 2 and ~ 6 for LIGO II. Mountain oscillations can enhance the signal-to-noise ratio, given a good matched filter, by up to 15 per cent. It is clear that accreting neutron stars are promising candidates for the first detection of gravitational waves by long-baseline interferometers after phase-coherent integration, particularly since their signal lies in a sensitivity sweet spot ($100 - 300$ Hz) and LIGO II will be tunable.

Global MHD oscillations, which may be excited stochastically (e.g. by accreting matter), cause the mountain to oscillate. This gives rise to sidebands of emission around f_* and $2f_*$ in the frequency spectrum of an accreting neutron star. We found the width of the emission band to be $\sim 0.2f_*$.

7.2 Magnetic fields of recycled compact objects

What observational signatures does the magnetic burial scenario explain and predict? And how can it be distinguished from other field reduction scenarios? One key point in this regard is that, in burial, the global μ is reduced, but the buried field is locally much more intense than the initial dipole, e.g. near the equator. This is quite unlike other scenarios (e.g. accelerated Ohmic decay, vortex-fluxoid interactions). The burial model is relevant for all neutron star binaries with a history of mass transfer and, assuming recycling is valid, all millisecond pulsars.

7.2.1 μ versus $M_{\rm a}$

The burial model predicts that μ is significantly reduced once $M_{\rm a} \sim 10^{-5} M_\odot$ is accreted, consistent with empirical scalings for $\mu(M_{\rm a})$ which fit data from objects whose μ is estimated from rotational spin-down models and $M_{\rm a}$ from binary evolution models. Figure 7.2 displays $\mu(M_{\rm a})$ for sources whose $M_{\rm a}$ can be estimated from binary evolution scenarios (listed in table 1.3). The theoretical curves of $\mu(M_{\rm a})$ predicted in this thesis are also plotted for initial moments of 10^{30} G cm^3 and 10^{31} G cm^3. These curves are of the form postulated by Shibazaki et al. (1989) and confirmed in the $M_{\rm a} \lesssim M_{\rm c}$ regime by our

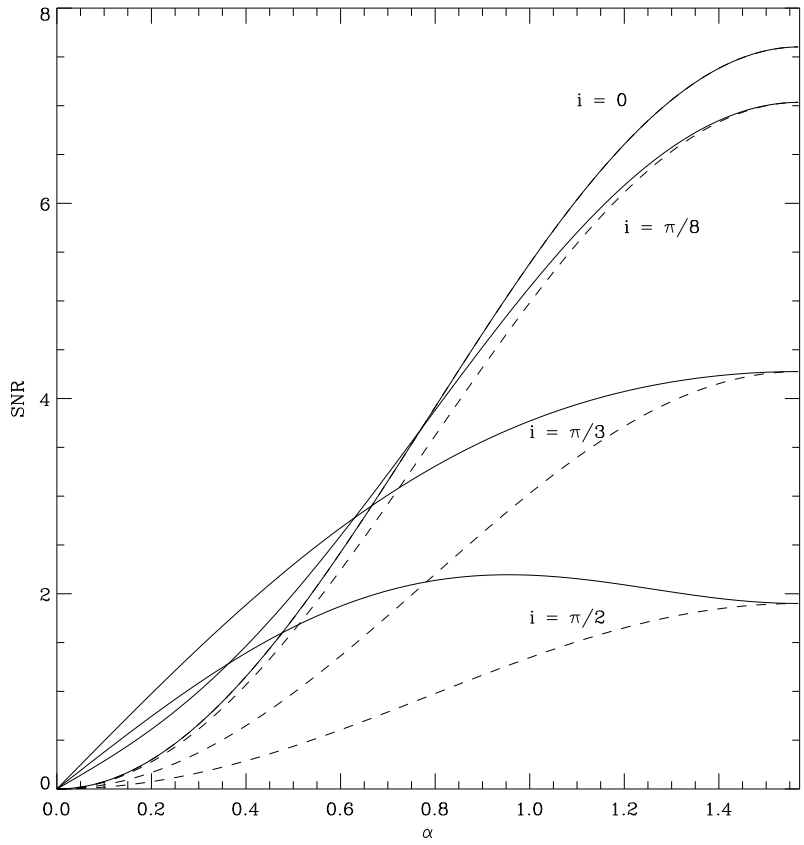

Figure 7.1: Signal-to-noise ratio as a function of α and i (in radians) for gravitational-wave emission from an accreting neutron star with a static mountain, including both f_* and $2f_*$ components (*solid*), and neglecting the f_* component (*dashed*).

Grad-Shafranov analysis (chapter 2), with M_c determined from (3.17). Allowing for a spread of initial magnetic field strengths, the data are reasonably fit by the burial model. Outliers include PSR B1821−00 which may have undergone accretion-induced collapse, PSR B1718−19 which is in a globular cluster, and PSR B0820+02 which has a large orbital eccentricity for a white dwarf binary) ($e = 0.012$) that points to an unusual evolutionary history. PSR B2303+46 and PSR J1141−6545 are young pulsars ($M_a \ll M_c$) with $\mu = 8 \times 10^{29}$ G cm^3 and 1.3×10^{30} G cm^3 respectively (Davies et al. 2002) in very eccentric orbits ($e = 0.66$ and 0.17 respectively) around carbon-oxygen white dwarfs (of masses $1.3M_\odot$ and $1.0M_\odot$ respectively).

Our numerical results in chapter 2 seem to imply a scaling $\mu/\mu_i \sim (M_a/5 \times 10^{-5}M_\odot)^{-2.2\pm0.2}$, for $M_a \gtrsim M_c$, where μ_i is the initial dipole moment, which falsely implies that μ decreases by $\sim 10^7$ times when $M_a \sim 0.1M_\odot$. However, this scaling does not include Ohmic dissipation. Ohmic dissipation allows field lines to slip through the accreted matter and acts to slow the reduction of μ. As the magnetic field gradients steepen, the rate of Ohmic diffusion becomes comparable to the rate of accretion once $M_a \gtrsim M_c$ (chapter 5). Roughly accounting for this, one finds $\mu/\mu_i \sim (1+3M_a/4M_c)^{-1}$ (the dashed and dotted lines in figure 7.2).

We have found that magnetic mountains are stable (in two dimensions) for $M_a \lesssim 10^{-3}M_\odot$, but have not ruled out instability for $M_a > 10^{-3}M_\odot$ (or in three dimensions). However, any instability that does occur for $M_a \gtrsim 10^{-3}M_\odot$, even if it disrupts the buried field and restores a dipole-like configuration, will be overcome very quickly within $\sim 10^5$ yr, when a further $10^{-3}M_\odot$ is accreted, again burying the field (cf. Braithwaite and Spruit 2004). This is an important point which is often neglected and merits further investigation.

7.2.2 Magnetars

Magnetars are ultramagnetized neutron stars with spin-down magnetic moments $10^{31}\,\mathrm{G\,cm^3} \leq \mu \leq 10^{33}\,\mathrm{G\,cm^3}$. As they may represent ~ 10 per cent of the neutron star population (e.g. Kouveliotou et al. 1998), some of them are sure to be born in binaries, where presumably they are spun up via the recycling scenario. What does this mean for magnetic burial?

The magnetic stress at the base of the polar mountain in a magnetar is $\sim 10^6$ times greater than for an ordinary pulsar and can confine a cor-

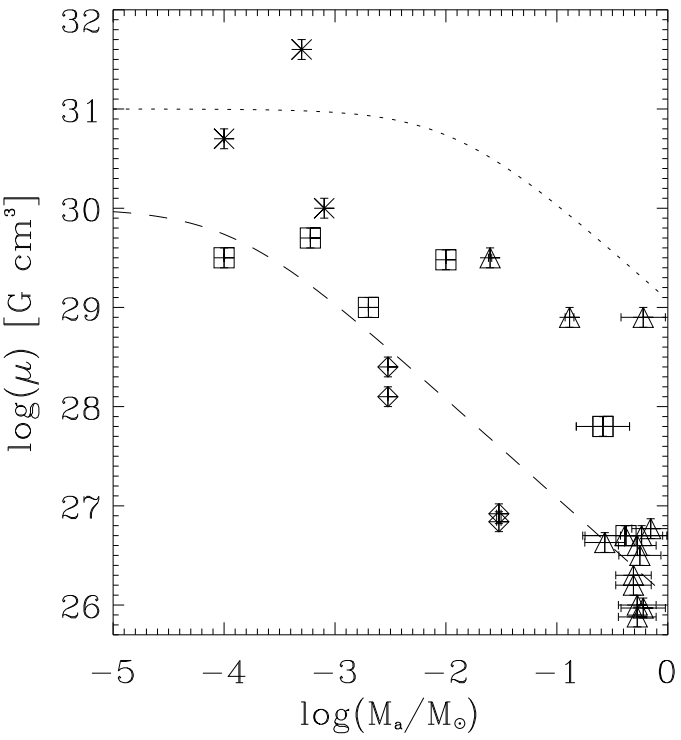

Figure 7.2: B_* as a function of M_a for low-mass radio binaries (triangles), high-mass radio binaries (diamonds), LMXBs (squares) and HMXBs (crosses). Without definite neutron star mass measurements (Thorsett and Chakrabarty 1999), M_a is estimated from the binary orbital parameters, the age of the system, and the accretion history (Taam and van den Heuvel 1986; van den Heuvel and Bitzaraki 1995). Binary radio pulsars with nearly circular orbits and low-mass white dwarf companions are plotted because they have a reasonably well-understood evolutionary history (Bhattacharya and van den Heuvel 1991).

respondingly larger amount of accreted matter ($M_{\rm c} \propto B_*^2$). For $B_* = 10^{15}$ G, we find $M_{\rm c} \sim 1 M_\odot$; that is, for typical values of $M_{\rm a}$, there is very little screening or equatorial hydromagnetic spreading. This represents a clear prediction of the burial scenario: any magnetar found in a binary in the future — no such object has been found to date — should still have the same μ as at birth. Two factors can interfere with this prediction: another process, (e.g. sinking, Ohmic dissipation, and Hall drift) may dominate over burial (Arras et al. 2004), or the magnetar's magnetic field may decay (as it emits X-rays) before accretion begins.

The lifetime of a magnetar as a pulsating source is so short (10^{4-5} yr) that we are unlikely to observe it as an accreting object (an X-ray pulsar's lifetime is typically $\sim 10^{5-8}$ yr and the time until accretion begins is comparable). However, there ought to be a population of former magnetars in binary systems. The best candidate for such a system is 2S 0114+650 (Li and van den Heuvel 1999). It has an extremely long spin period ($P = 9850$ s) and orbits around a B1 Ia star of mass $16 \pm 5 M_\odot$ with $P_{\rm b} = 11.6$ days. The long spin period cannot be reached via the propeller mechanism given $B_* \sim 10^{12-13}$ G, because the accretion rate $\dot{M}_{\rm a} \sim 10^{-13} - 10^{-12} M_\odot\,{\rm yr}^{-1}$ gives $P_{\rm spin-up} \lesssim 10^3$ s (centrifugal equilibrium). Thus an initial magnetic field $B_* \gtrsim 10^{14}$ G is required.

An alternative non-magnetar model of anomalous X-ray pulsars involves a fossil disk around a neutron star (with $B_* \leq 4 \times 10^{13}$ G) formed from the fallback of supernova ejecta, which rapidly spins down the star through a propeller torque (Rothschild et al. 2002). Magnetic burial occurs in this situation because the magnetic field of the young neutron star funnels the fall-back material onto its poles. Ghosh et al. (1997) argued that a young neutron star accretes $0.01 M_\odot - 0.05 M_\odot$ from a fossil disk, from which the magnetic burial model predicts $\mu \sim 10^{28}$ G cm^3 [cf. $\sim 10^{29}$ G cm^3 in Ghosh et al. (1997)].

7.2.3 Tangled multipolar fields

Magnetic burial predicts the existence of intense, localised, equatorial magnetic fields. Can we see any evidence for this? A direct probe of magnetic field strength at the stellar surface comes from cyclotron absorption features in the X-ray spectra of neutron stars. The magnetic field of 1E 1207.4−5209, $B_* \approx 1.4 \times 10^{14}$ G, estimated from atomic absorption features, is $\sim 10^2$ times

higher than its spin-down field, $2\mu/R_*^3 = (2-4)\times 10^{12}$ G (Pavlov et al. 2002). Likewise, the X-ray spectrum of PSR B1821−24 contains an emission line which could be interpreted as cyclotron emission from a corona above the pulsar's polar cap, with implied field strength $B_* \approx 2 \times 10^{11}$ G (Becker and Aschenbach 2002), whereas its spin-down field is $2\mu/R_*^3 \approx 2 \times 10^9$ G. These measurements provide evidence that the local magnetic fields at the stellar surface can be significantly larger than the dipolar field responsible for spin down (Bonanno et al. 2003). A factor of $\sim 10^2$ discrepancy can be reconciled by the magnetic burial mechanism presented in this thesis; in the equatorial belt, the magnetic field strength is increased by a factor $\sim 6\times 10^3 (M_{\rm a}/M_{\rm c})^{0.3}$ (an upper bound when Ohmic dissipation is neglected). Interestingly, Coburn et al. (2002) concluded from data on cyclotron line widths that a steady-state mountain with a "universal profile" forms at the polar caps irrespective of $\dot{M}_{\rm a}$.

Multipolar magnetic fields have been invoked in rotation-powered pulsars because a dipole cannot provide sufficient pair production in all pulsars. Ruderman and Sutherland (1975) argued that a radius of curvature $\lesssim R_*$ (too small for a dipole) is required for copious pair production. Arons (1993) and Hibschman and Arons (2001) invoked an offset dipole coupled with a Lense-Thirring model of the electric potential in the polar cap to explain the observed radio pulsar death line. Recently, Asseo and Khechinashvili (2002) invoked a multipolar magnetic topology to model the system of 20 isolated sub-beams observed in PSR B0943+10 by Deshpande and Rankin (2001).[1]

7.2.4 Magnetic white dwarfs

White dwarfs have magnetic field strengths in the range 3×10^4 G -1×10^9 G (Wickramasinghe and Ferrario 2000). Those objects that accrete from a binary companion may have their magnetic fields buried (Cumming 2002). Typical white dwarfs have $R_* \sim 10^9$ cm, $M_* \sim 1 M_\odot$, and $B_* \sim 10^7$ G, implying $M_{\rm c} \approx 10^{-8} (B_*/10^7\,{\rm G})^2 (R_*/10^9\,{\rm cm})^2 M_\odot$. The smaller value of $M_{\rm c}$ follows from the lower magnetic stresses at the magnetic pole of an accreting white dwarf. Since $r_{\rm A} \sim 4\times 10^{10}$ cm from (1.1) is greater than R_*, accreted

[1] Mitra et al. (1999) showed that the evolution of high-order multipoles ($\ell \leq 25$) under Ohmic dissipation is similar to a dipole, suggesting that, once the field is buried, its structure is maintained as the pulsar ages.

matter is funnelled towards the polar caps like in a neutron star (Hameury and Lasota 1985; Livio 1983). Significant reduction of μ occurs over just $1 - 10^3$ yr. Equatorial spreading limits the mass quadrupole moment to $\lesssim 10^{-8} M_* R_*^2$. Accelerated Ohmic decay (Cumming 2002), along with burial, may provide the missing evolutionary link between AM Her systems (with $1 \times 10^7 \leq B_* \leq 3 \times 10^8$ G and $\dot{M}_{\rm a} \approx 5 \times 10^{-11} M_\odot$ yr^{-1}) and intermediate polars [with $B_* \sim 10^{5-7}$ G and $\dot{M}_{\rm a} \approx (0.2-4) \times 10^{-9} M_\odot$ yr^{-1}]. Furthermore, magnetic burial (or accelerated Ohmic decay) might explain why accreting white dwarfs have $B_* \lesssim 2 \times 10^8$ G, whereas fields up to 10^9 G are observed for isolated white dwarfs (Cumming 2002).

Accretion-induced collapse of a white dwarf to a neutron star is invoked to explain why some neutron stars (e.g. PSR B1831−00) which have accreted $\sim 0.1 M_\odot$ still have high μ. However, this argument, which has an obvious fine-tuning weakness, also fails to acknowledge that magnetic burial will reduce μ in the white dwarf progenitor. How does this affect the initial μ of the resulting neutron star? Complicated multipolar magnetic field evolution during the collapse and supernova make it difficult to speculate; perhaps the neutron star's magnetic field is generated anew by a dynamo of some sort (Thompson and Duncan 1993).

7.2.5 Young stellar objects

Classical T Tauri stars have circumstellar disks and evidence for magnetospheric accretion exists (e.g. Hartmann 1998). Proto-stellar models invoke Ghosh and Lamb (1979) accretion onto the central object (Muzerolle et al. 1998). For typical parameters ($M_* \approx 0.5 M_\odot$, $R_* \sim 10^{11}$ cm, $\dot{M}_{\rm a} \sim 10^{-8} M_\odot$yr^{-1}, and $B_* \sim 10^3$ G), the magnetosphere is located at a few stellar radii. The smaller magnetic stresses at the polar caps lead to $M_{\rm c} \sim 10^{-12} M_\odot$, implying a substantial effect on μ in under a year. However, the physics of burial in protostars is very different from that in neutron stars: Ohmic diffusion, ambipolar diffusion (Basu and Mouschovias 1994), and complex, time-dependent, unstable magnetic field evolution modify the simple magnetic burial model. These modifications lie outside the scope of this thesis.

7.3 Thermonuclear burst oscillations

X-ray binaries provide a probe of the surface field structure of an accreting neutron star. Accreting millisecond pulsars, including those which only pulsate during thermonuclear X-ray bursts, probe the late stages of spin-up and magnetic burial. Does the buried field leave a signature in these thermonuclear burst oscillations? A surprising property of the burst oscillations is how sinusoidal they are: the fundamental constitutes over 90 per cent of the signal (Muno et al. 2002). Restriction of the burst to one hemisphere can explain this lack of harmonic content. In chapter 4, we show that the equatorial belt of intense magnetic field produced by burial can impede thermal transport between the hemispheres of the star. Estimates in chapter 4 indicate that the belt is sufficient to prevent thermal transfer via conduction, radiation, convection and ageostrophic shear flow. This idea meshes neatly with the scenario proposed by Spitkovsky et al. (2002), in which a cyclonic thermonuclear flame is driven by zonal shear drifts slowly across the stellar surface, explaining the $\sim$ Hz frequency drifts observed in the tails of type I X-ray bursts. Magnetic tension stabilizes ageostrophic shear, so when the cyclonic flame runs into the equatorial magnetic belt, it is reflected back into its own hemisphere, explaining why the bursts persist for tens of seconds.

MHD oscillations of the magnetic mountain (chapter 3), may be excited by the accretion process. The oscillations during thermonuclear bursts at frequency $\approx f_*$, may be modulated by the wobbling mountain, creating interesting electromagnetic signatures synchronised to the gravitational-wave signatures explored in chapter 6.

7.4 Rotational evolution

7.4.1 Maximum spin frequency of a millisecond pulsar

The spin frequency of a neutron star is limited above by centrifugal breakup (~ 2 kHz), yet observations imply $f_* \lesssim 0.7$ kHz. Stalling due to gravitational-wave emission is a likely reason for the spin frequency gap (Bildsten 1998). Burial models predict $\mu[M_{\rm a}(t)]$ and $\epsilon[M_{\rm a}(t)]$ as functions of time t, so the stalling hypothesis can be explored in more detail. The net torque on an accreting neutron star is the sum of torques: due to accretion, gravitational

radiation, and magnetic dipole radiation, giving the equation of motion

$$I\dot{\Omega}_* = \dot{M}_{\rm a}(\eta G M_* R_{\rm a})^{1/2} - \frac{2G\epsilon I^2\Omega_*^5}{5c^5}(16\sin^2\theta + \cos^2\theta)\sin^2\theta - \frac{2\mu^2\Omega_*^3}{3c^3}\sin^2\alpha \tag{7.1}$$

with $\eta \approx 0.5$ and the sign of the first term given by the Ghosh and Lamb (1979) prescription (Shapiro and Teukolsky 1983). The reduced μ affects not only the magnetic dipole torque but also the accretion torque, because the disk-magnetospheric boundary ($r_{\rm A}$) moves inwards as μ is reduced. The gravitational radiation torque is influenced by precession as described in section 6.5. The wobble angle θ decreases if precession decays, an open issue. Upon integrating (7.1) with constant θ, we find that f_* does not exceed ~ 0.8 kHz for most initial conditions, consistent with the observations. A fuller discussion of these results will be presented elsewhere.

7.4.2 Precession

If we presume that the magnetic symmetry axis must be misaligned with the spin axis for a recycled neutron star to pulse, and if a magnetic mountain is present, precession is expected. We neglect this throughout most of our gravitational-wave analysis, to remain consistent with the work of Bonazzola and Gourgoulhon (1996), but it is potentially important because ellipticities of order 10^{-7} imply a precession time-scale $\sim$ days. Most analyses of precession take limit of small wobble angle. A full analysis along the lines proposed by Zimmermann (1980) is required to resolve this issue.

7.5 Future directions

7.5.1 Extending the theory: Ohmic dissipation, sinking and three dimensions

Our magnetic burial model is based upon ideal MHD. Ohmic dissipation becomes important when the diffusion time becomes shorter than the accretion flow time when $M_{\rm a} \sim 4 \times 10^{-7} M_\odot$ has been accreted. It has been addressed semi-quantitatively in chapter 4 by calculating when the steepest magnetic field gradients cause the Ohmic diffusion time to becomes less than the accretion flow time (cf. Brown and Bildsten 1998). Diffusion allows the magnetic mountain at the polar caps to relax equatorward as magnetic field

lines slip through the resistive fluid. This is important when extrapolating the model to $M_{\rm a} \sim 0.1 M_\odot$. Further simulations, possibly with a ZEUS-3D Ohmic diffusion module, are required to confirm the detailed evolution with Ohmic dissipation.

Instead of a solid stellar surface, a Lane-Emden polytropic crust, can be implemented in ZEUS-3D to allow the accreted matter to sink into the deeper layers of the neutron star. Sinking reduces the magnetic field gradients, enabling numerical calculations to reach realistic accreted masses $M_{\rm a} \sim 0.1 M_\odot$. The quadrupole moment of the mountain can be modified significantly by sinking, affecting our gravity wave predictions.

Although we find that the buried fields are stable in two-dimensional ideal MHD, it is crucial to check their stability in three dimensions [cf. studies of the Parker instability (Kim et al. 1998)]. Work is underway in this regard using the FLASH code (Fryxell et al. 2000) which solves the fully compressible, reactive MHD equations with adaptive mesh refinement

7.5.2 Gravitational-wave and electromagnetic signatures

Sources of gravitational waves are likely to emit high energy photons. The link between these two types of emission in individual sources is only now starting to be explored. Examples include unpulsed X-rays from a hollow disk of circumnuclear gas relaxing viscously after a supermassive black hole merger (Milosavljević and Phinney 2005) and pulsed X-rays from r-modes in LMXBs (Wagoner 2004). If gravitational radiation can be detected from an accreting millisecond pulsar with a magnetic mountain (whose size depends on magnetic field strength and surface temperature), then its X-ray light curve can be related to the gravitational wave signal (which depends on the mass distribution). In this way, it will be possible to study how magnetic mountains respond to impulsive events (thermonuclear bursts, blobs of accreted matter), opening up a new window onto the thermonuclear physics of the bursts, and illuminating how much they are affected by magnetic fields.

7.5.3 Disk-magnetosphere interaction

This thesis has focused on the details of magnetic field evolution at the surface of an accreting neutron star, one aspect of the broader recycling scenario. The surface field evolution must be fed back into global models

of the disk-magnetosphere interaction during recycling. For example, as μ decreases, so does $r_{\rm A}$, increasing the size of the magnetic polar caps and slowing the rate at which μ decreases. The accretion torques are also affected by this interaction (Locsei and Melatos 2004), which feeds into the spin-up (spin-down) of the neutron star. By the same token, magnetic burial itself is affected by the structure of the magnetosphere, e.g. instabilities at the inner disk boundary can perturb the accretion column. A systems approach in which these diverse pieces of local physics are solved subject to local boundary conditions and then connected by global conservation laws is likely to pay dividends.

Bibliography

M. Abramowitz and I. A. Stegun. *Handbook of Mathematical Functions.* Handbook of Mathematical Functions, New York: Dover, 1972, 1972.

S. Akiyama, J. C. Wheeler, D. L. Meier, and I. Lichtenstadt. The Magnetorotational Instability in Core-Collapse Supernova Explosions. *Astroph. J.*, 584:954–970, February 2003.

B. Allen and R. Brustein. Detecting relic gravitational radiation from string cosmology with LIGO. *Phys. Rev. D*, 55:3260–3264, March 1997.

M. A. Alpar, P. W. Anderson, D. Pines, and J. Shaham. Vortex creep and the internal temperature of neutron stars. II - VELA pulsar. *Astroph. J.*, 278:791–805, March 1984.

M. A. Alpar, A. F. Cheng, M. A. Ruderman, and J. Shaham. A new class of radio pulsars. *Nature*, 300:728–730, December 1982.

M. A. Alpar and J. A. Sauls. On the dynamical coupling between the superfluid interior and the crust of a neutron star. *Astroph. J.*, 327:723–725, April 1988.

P. W. Anderson and N. Itoh. Pulsar glitches and restlessness as a hard superfluidity phenomenon. *Nature*, 256:25–27, July 1975.

N. Andersson. A New Class of Unstable Modes of Rotating Relativistic Stars. *Astroph. J.*, 502:708, August 1998.

J. R. P. Angel, E. F. Borra, and J. D. Landstreet. The magnetic fields of white dwarfs. *Astroph. J. Suppl. Ser.*, 45:457–474, March 1981.

N. V. Ardeljan, G. S. Bisnovatyi-Kogan, and S. G. Moiseenko. Magnetorotational supernovae. *Month. Notic. R. Astron. Soc.*, page 290, March 2005.

J. W. Armstrong, F. B. Estabrook, and M. Tinto. Time-Delay Interferometry for Space-based Gravitational Wave Searches. *Astroph. J.*, 527: 814–826, December 1999.

W. D. Arnett and R. L. Bowers. A Microscopic Interpretation of Neutron Star Structure. *Astroph. J. Suppl. Ser.*, 33:415, April 1977.

J. Arons. Magnetic field topology in pulsars. *Astroph. J.*, 408:160–166, May 1993.

J. Arons, D. J. Burnard, R. I. Klein, C. F. McKee, R. E. Pudritz, and S. M. Lea. Accretion onto magnetized neutron stars - magnetospheric structure and stability. In *High Energy Transients in Astrophysics*, page 215, 1984.

J. Arons and S. M. Lea. Accretion onto magnetized neutron stars - The fate of sinking filaments. *Astroph. J.*, 235:1016–1037, February 1980.

P. Arras, A. Cumming, and C. Thompson. Magnetars: Time Evolution, Superfluid Properties, and the Mechanism of Magnetic Field Decay. *Astroph. J. L.*, 608:L49–L52, June 2004.

P. Arras, E. E. Flanagan, S. M. Morsink, A. K. Schenk, S. A. Teukolsky, and I. Wasserman. Saturation of the r-Mode Instability. *Astroph. J.*, 591: 1129–1151, July 2003.

Z. Arzoumanian, D. F. Chernoff, and J. M. Cordes. The Velocity Distribution of Isolated Radio Pulsars. *Astroph. J.*, 568:289–301, March 2002.

E. Asseo and D. Khechinashvili. The role of multipolar magnetic fields in pulsar magnetospheres. *Month. Notic. R. Astron. Soc.*, 334:743–759, August 2002.

W. Baade and F. Zwicky. On Super-novae. *Proceedings of the National Academy of Science*, 20:254, 1934.

D. C. Backer, S. R. Kulkarni, C. Heiles, M. M. Davis, and W. M. Goss. A millisecond pulsar. *Nature*, 300:615–618, December 1982.

M. Bailes. The origin of pulsar velocities and the velocity-magnetic moment correlation. *Astroph. J.*, 342:917–927, July 1989.

M. Bailes, S. M. Ord, H. S. Knight, and A. W. Hotan. Self-Consistency of Relativistic Observables with General Relativity in the White Dwarf-Neutron Star Binary PSR J1141-6545. *Astroph. J. L.*, 595:L49–L52, September 2003.

S. A. Balbus and J. F. Hawley. A powerful local shear instability in weakly magnetized disks. I - Linear analysis. II - Nonlinear evolution. *Astroph. J.*, 376:214–233, July 1991.

S. A. Balbus and J. F. Hawley. Instability, turbulence, and enhanced transport in accretion disks. *Reviews of Modern Physics*, 70:1–53, January 1998.

L. Barack and C. Cutler. Confusion noise from LISA capture sources. *Phys. Rev. D*, 70(12):122002, December 2004.

M. M. Basko and R. A. Sunyaev. The role of the Alfvén surface in forming x-ray pulses in accreting pulsars. *SvA*, 20:537, October 1976.

S. Basu and T. C. Mouschovias. Magnetic braking, ambipolar diffusion, and the formation of cloud cores and protostars. 1: Axisymmetric solutions. *Astroph. J.*, 432:720–741, September 1994.

T. W. Baumgarte and S. L. Shapiro. Collapse of a Magnetized Star to a Black Hole. *Astroph. J.*, 585:930–947, March 2003.

A. Baykal, A. Alpar, and U. Kiziloglu. A shot noise model for a two-component neutron star. *Astron. and Astroph.*, 252:664–668, December 1991.

G. Baym, C. J. Pethick, and D. Pines. Superfluidity in Neutron Stars. *Nature*, 224:673, 1969.

W. Becker and B. Aschenbach. X-ray Observations of Neutron Stars and Pulsars: First Results from XMM-Newton. In *Neutron Stars, Pulsars, and Supernova Remnants*, page 64, 2002.

W. Becker, D. A. Swartz, G. G. Pavlov, R. F. Elsner, J. Grindlay, R. Mignani, A. F. Tennant, D. Backer, L. Pulone, V. Testa, and M. C. Weisskopf. Chandra X-Ray Observatory Observations of the Globular Cluster M28 and Its Millisecond Pulsar PSR B1821-24. *Astroph. J.*, 594: 798–811, September 2003.

K. Belczynski, V. Kalogera, and T. Bulik. A Comprehensive Study of Binary Compact Objects as Gravitational Wave Sources: Evolutionary Channels, Rates, and Physical Properties. *Astroph. J.*, 572:407–431, June 2002.

I. B. Bernstein, E.A Frieman, and M.D. Kruskal. An Energy Principle for hydromagnetic stability problems. *Proc. R. Soc. London A*, 244:17, 1958.

D. Bhattacharya. Models for the evolution of neutron star magnetic fields. In *Pulsar Timing, General Relativity and the Internal Structure of Neutron Stars*, page 235, 1999.

D. Bhattacharya and G. Srinivasan. On the implication of the recently discovered 5 millisecond binary pulsar PSR 1855+09. *Current Science*, 55:327–330, April 1986.

D. Bhattacharya and G. Srinivasan. Evolution of neutron star magnetic fields. In *in Lewin, W. H. G. and van Paradijs, J. and van den Heuvel, E. P. J. eds, X-ray Binaries*, page 235. Cambridge Astrophysics Series, Cambridge, MA: Cambridge University Press, —c1995, edited by Lewin, Walter H.G.; Van Paradijs, Jan; Van den Heuvel, Edward P.J., 1995.

D. Bhattacharya and E. P. J. van den Heuvel. Formation and evolution of binary and millisecond radio pulsars. *Physics Reports*, 203:1–124, 1991.

G. F. Bignami, P. A. Caraveo, A. D. Luca, and S. Mereghetti. The magnetic field of an isolated neutron star from X-ray cyclotron absorption lines. *Nature*, 423:725–727, June 2003.

L. Bildsten. Propagation of nuclear burning fronts on accreting neutron stars: X-ray bursts and sub-hertz noise. *Astroph. J.*, 438:852–875, January 1995.

L. Bildsten. Gravitational Radiation and Rotation of Accreting Neutron Stars. *Astroph. J. L.*, 501:L89, July 1998.

L. Bildsten, D. Chakrabarty, J. Chiu, M. H. Finger, D. T. Koh, R. W. Nelson, T. A. Prince, B. C. Rubin, D. M. Scott, M. Stollberg, B. A. Vaughan, C. A. Wilson, and R. B. Wilson. Observations of Accreting Pulsars. *Astroph. J. Suppl. Ser.*, 113:367, December 1997.

G. S. Bisnovatyi-Kogan and B. V. Komberg. Pulsars and close binary systems. *Soviet Astronomy*, 18:217, October 1974.

A. Blaauw. On the origin of the O- and B-type stars with high velocities (the "run-away" stars), and some related problems. *Bulletin of the Astronomical Institute of the Netherlands*, 15:265, May 1961.

R. D. Blandford, J. H. Applegate, and L. Hernquist. Thermal origin of neutron star magnetic fields. *Month. Notic. R. Astron. Soc.*, 204:1025–1048, September 1983.

R. D. Blandford, W. M. Decampli, and A. Konigl. Unsteady Accretion onto Magnetized Neutron Stars. *Bull. Am. Astron. Soc.*, 11:703, June 1979.

J. M. Blondin and K. Freese. Is the 1.5-ms pulsar a young neutron star? *Nature*, 323:786–788, October 1986.

J. M. Blondin, T. R. Kallman, B. A. Fryxell, and R. E. Taam. Hydrodynamic simulations of stellar wind disruption by a compact X-ray source. *Astroph. J.*, 356:591–608, June 1990.

A. Bonanno, L. Rezzolla, and V. Urpin. Mean-field dynamo action in protoneutron stars. *Astron. and Astroph.*, 410:L33–L36, October 2003.

S. Bonazzola and E. Gourgoulhon. Gravitational waves from pulsars: emission by the magnetic-field-induced distortion. *Astron. and Astroph.*, 312: 675–690, August 1996.

S. Bose. Search templates for stochastic gravitational-wave backgrounds. *Phys. Rev. D*, 71(8):082001, April 2005.

P. R. Brady and T. Creighton. Searching for periodic sources with LIGO. II. Hierarchical searches. *Phys. Rev. D*, 61:82001, April 2000.

P. R. Brady, T. Creighton, C. Cutler, and B. F. Schutz. Searching for periodic sources with LIGO. *Phys. Rev. D*, 57:2101–2116, February 1998.

J. Braithwaite and H. C. Spruit. A fossil origin for the magnetic field in A stars and white dwarfs. *Nature*, 431:819–821, October 2004.

E. F. Brown and L. Bildsten. The Ocean and Crust of a Rapidly Accreting Neutron Star: Implications for Magnetic Field Evolution and Thermonuclear Flashes. *Astroph. J.*, 496:915, March 1998.

G. E. Brown, A. Heger, N. Langer, C.-H. Lee, S. Wellstein, and H. A. Bethe. Formation of high mass X-ray black hole binaries. *New Astronomy*, 6:457–470, October 2001.

L. Burderi, A. Possenti, M. Colpi, T. di Salvo, and N. D'Amico. Neutron Stars with Submillisecond Periods: A Population of High-Mass Objects? *Astroph. J.*, 519:285–290, July 1999.

B. F. Burke and K. L. Franklin. Observations of a Variable Radio Source Associated with the Planet Jupiter. *J. Geophys. Res.*, 60(9):213, June 1955.

A. Burrows, J. Hayes, and B. A. Fryxell. On the Nature of Core-Collapse Supernova Explosions. *Astroph. J.*, 450:830, September 1995.

A. G. Cameron. Neutron Star Models. *Astroph. J.*, 130:884, November 1959.

S. Campana, M. Ravasio, G. L. Israel, V. Mangano, and T. Belloni. XMM-Newton Observation of the 5.25 Millisecond Transient Pulsar XTE J1807-294 in Outburst. *Astroph. J. L.*, 594:L39–L42, September 2003.

V. Canuto. Electrical Conductivity and Conductive Opacity of a Relativistic Electron Gas. *Astroph. J.*, 159:641, February 1970.

V. Cardoso and J. P. Lemos. Gravitational radiation from the radial infall of highly relativistic point particles into Kerr black holes. *Phys. Rev. D*, 67(8):084005, April 2003.

J. Chadwick. On the possible existence of the neutron. *Nature*, 129:312, January 1932.

D. Chakrabarty and E. H. Morgan. The two-hour orbit of a binary millisecond X-ray pulsar. *Nature*, 394:346–348, 1998.

D. Chakrabarty, E. H. Morgan, M. P. Muno, D. K. Galloway, R. Wijnands, M. van der Klis, and C. B. Markwardt. Nuclear-powered millisecond pulsars and the maximum spin frequency of neutron stars. *Nature*, 424: 42–44, July 2003.

P. Charbonneau and K. B. MacGregor. Magnetic Fields in Massive Stars. I. Dynamo Models. *Astroph. J.*, 559:1094–1107, October 2001.

K. Chen and M. Ruderman. Pulsar death lines and death valley. *Astroph. J.*, 402:264–270, January 1993.

K. Chen, M. Ruderman, and T. Zhu. Millisecond Pulsar Alignment: PSR J0437-4715. *Astroph. J.*, 493:397, January 1998.

K. S. Cheng and Z. G. Dai. On the Bimodal Magnetic Field Distribution of Binary Pulsars. *Astroph. J. L.*, 476:L39, February 1997.

K. S. Cheng and C. M. Zhang. Magnetic field evolution of accreting neutron stars. *Astron. and Astroph.*, 337:441–446, September 1998.

R. A. Chevalier and R. T. Emmering. Are pulsars born as slow rotators? *Astroph. J.*, 304:140–153, May 1986.

A. R. Choudhuri and S. Konar. Diamagnetic screening of the magnetic field in accreting neutron stars. *Month. Notic. R. Astron. Soc.*, 332:933, May 2002.

W. Coburn, W. A. Heindl, R. E. Rothschild, D. E. Gruber, I. Kreykenbohm, J. Wilms, P. Kretschmar, and R. Staubert. Magnetic Fields of Accreting X-Ray Pulsars with the Rossi X-Ray Timing Explorer. *Astroph. J.*, 580: 394–412, November 2002.

I. Contopoulos, D. Kazanas, and C. Fendt. The Axisymmetric Pulsar Magnetosphere. *Astroph. J.*, 511:351–358, January 1999.

G. B. Cook, S. L. Shapiro, and S. A. Teukolsky. Recycling Pulsars to Millisecond Periods in General Relativity. *Astroph. J. L.*, 423:L117, March 1994.

J. M. Cordes and D. F. Chernoff. Neutron Star Population Dynamics. II. Three-dimensional Space Velocities of Young Pulsars. *Astroph. J.*, 505: 315–338, September 1998.

F. V. Coroniti. Magnetically striped relativistic magnetohydrodynamic winds - The Crab Nebula revisited. *Astroph. J.*, 349:538–545, February 1990.

J. Cottam, F. Paerels, and M. Mendez. Gravitationally redshifted absorption lines in the X-ray burst spectra of a neutron star. *Nature*, 420:51–54, November 2002.

T. Creighton. Advanced LIGO: sources and astrophysics. *Classical and Quantum Gravity*, 20:853, September 2003.

A. Cumming. Magnetic field evolution in accreting white dwarfs. *Month. Notic. R. Astron. Soc.*, 333:589–602, July 2002.

A. Cumming, P. Arras, and E. Zweibel. Magnetic Field Evolution in Neutron Star Crusts Due to the Hall Effect and Ohmic Decay. *Astroph. J.*, 609: 999–1017, July 2004.

A. Cumming, E. Zweibel, and L. Bildsten. Magnetic Screening in Accreting Neutron Stars. *Astroph. J.*, 557:958–966, August 2001.

C. Cutler. Gravitational waves from neutron stars with large toroidal B fields. *Phys. Rev. D*, 66(8):084025, October 2002.

C. Cutler and É. E. Flanagan. Gravitational waves from merging compact binaries: How accurately can one extract the binary's parameters from the inspiral waveform? *Phys. Rev. D*, 49:2658–2697, March 1994.

C. Cutler and D. I. Jones. Gravitational wave damping of neutron star wobble. *Phys. Rev. D*, 63(2):024002, January 2001.

T. Damour. General relativity and experiment: a brief review . *Classical and Quantum Gravity*, 9:55, December 1992.

B. Datta. Recent Developments in Neutron Star Physics. *Fundamentals of Cosmic Physics*, 12:151–239, 1988.

M. B. Davies, H. Ritter, and A. King. Formation of the binary pulsars J1141-6545 and B2303+46. *Month. Notic. R. Astron. Soc.*, 335:369–376, September 2002.

A. A. Deshpande and P. M. McCulloch. Periodic Changes in Intensity and Arrival Time of Pulses from the VELA Pulsar: Evidence for Free Precession? In *ASP Conf. Ser. 105: IAU Colloq. 160: Pulsars: Problems and Progress*, page 101, 1996.

A. A. Deshpande and J. M. Rankin. The topology and polarization of sub-beams associated with the 'drifting' sub-pulse emission of pulsar B0943+10 - I. Analysis of Arecibo 430- and 111-MHz observations. *Month. Notic. R. Astron. Soc.*, 322:438–460, April 2001.

J. D. M. Dewi and O. R. Pols. The late stages of evolution of helium star-neutron star binaries and the formation of double neutron star systems. *Month. Notic. R. Astron. Soc.*, 344:629–643, September 2003.

S. V. Dhurandhar, D. G. Blair, and M. E. Costa. Possibility of detecting gravitational waves from millisecond pulsars by resonant bar antennas. *Astron. and Astroph.*, 311:1043–1048, July 1996.

R. C. Duncan and C. Thompson. Formation of very strongly magnetized neutron stars - Implications for gamma-ray bursts. *Astroph. J. L.*, 392: L9–L13, June 1992.

J.W. Dungey. A family of solutions of the magneto-hydrostatic problem in a conducting atmosphere in a gravitational field. *Month. Notic. R. Astron. Soc.*, 113:180, 1953.

A. Duquennoy and M. Mayor. Multiplicity among solar-type stars in the solar neighbourhood. II - Distribution of the orbital elements in an unbiased sample. *Astron. and Astroph.*, 248:485–524, August 1991.

R. T. Edwards, W. van Straten, and M. Bailes. A Search for Submillisecond Pulsars. *Astroph. J.*, 560:365–370, October 2001.

D. Eichler. A magnetospheric heating model for the evaporation of the companion to PSR 957+20. *Month. Notic. R. Astron. Soc.*, 254:11P–13P, January 1992.

E. Ergma and E. P. J. van den Heuvel. On the initial progenitor masses of stellar mass black holes and neutron stars. *Astron. and Astroph.*, 331: L29–L32, March 1998.

A. J. Farmer and E. S. Phinney. The gravitational wave background from cosmological compact binaries. *Month. Notic. R. Astron. Soc.*, 346:1197–1214, December 2003.

J. Faulkner. Ultrashort-Period Binaries, Gravitational Radiation, and Mass Transfer. I. The Standard Model, with Applications to WZ Sagittae and Z Camelopardalis. *Astroph. J. L.*, 170:L99, December 1971.

L. Ferrario and D. T. Wickramasinghe. Magnetic fields and rotation in white dwarfs and neutron stars. *Month. Notic. R. Astron. Soc.*, 356:615–620, January 2005.

D. A. Fischer and G. W. Marcy. Multiplicity among M dwarfs. *Astroph. J.*, 396:178–194, September 1992.

É. É. Flanagan and S. A. Hughes. Measuring gravitational waves from binary black hole coalescences. I. Signal to noise for inspiral, merger, and ringdown. *Phys. Rev. D*, 57:4535–4565, April 1998.

E. Flowers and M. A. Ruderman. Evolution of pulsar magnetic fields. *Astroph. J.*, 215:302–310, July 1977.

R. S. Foster and D. C. Backer. Constructing a pulsar timing array. *Astroph. J.*, 361:300–308, September 1990.

J. L. Friedman and S. M. Morsink. Axial Instability of Rotating Relativistic Stars. *Astroph. J.*, 502:714, August 1998.

J. L. Friedman, L. Parker, and J. R. Ipser. Rapidly rotating neutron star models. *Astroph. J.*, 304:115–139, May 1986.

C. L. Fryer, D. E. Holz, and S. A. Hughes. Gravitational Wave Emission from Core Collapse of Massive Stars. *Astroph. J.*, 565:430–446, January 2002.

C. L. Fryer, D. E. Holz, and S. A. Hughes. Gravitational Waves from Stellar Collapse: Correlations to Explosion Asymmetries. *Astroph. J.*, 609:288–300, July 2004.

B. Fryxell, K. Olson, P. Ricker, F. X. Timmes, M. Zingale, D. Q. Lamb, P. MacNeice, R. Rosner, J. W. Truran, and H. Tufo. FLASH: An Adaptive

Mesh Hydrodynamics Code for Modeling Astrophysical Thermonuclear Flashes. *Astroph. J. Suppl. Ser.*, 131:273–334, November 2000.

B. A. Fryxell and S. E. Woosley. A two-dimensional model for gamma-ray bursts. *Astroph. J.*, 258:733–739, July 1982.

D. K. Galloway, D. Chakrabarty, E. H. Morgan, and R. A. Remillard. Discovery of a High-Latitude Accreting Millisecond Pulsar in an Ultracompact Binary. *Astroph. J. L.*, 576:L137–L140, September 2002.

D. K. Galloway, C. B. Markwardt, E. H. Morgan, D. Chakrabarty, and T. E. Strohmayer. Discovery of the Accretion-powered Millisecond X-Ray Pulsar IGR J00291+5934. *Astroph. J. L.*, 622:L45–L48, March 2005.

U. Geppert, M. Küker, and D. Page. Temperature distribution in magnetized neutron star crusts. *Astron. and Astroph.*, 426:267–277, October 2004.

U. Geppert, D. Page, and T. Zannias. Submergence and re-diffusion of the neutron star magnetic field after the supernova. *Astron. and Astroph.*, 345:847–854, May 1999.

U. Geppert and M. Rheinhardt. Non-linear magnetic field decay in neutron stars. Theory and observations. *Astron. and Astroph.*, 392:1015–1024, September 2002.

U. Geppert and V. Urpin. Accretion-driven magnetic field decay in neutron stars. *Month. Notic. R. Astron. Soc.*, 271:490, November 1994.

P. Ghosh, L. Angelini, and N. E. White. The Nature of the "6 Second" and Related X-Ray Pulsars: Evolutionary and Dynamical Considerations. *Astroph. J.*, 478:713, March 1997.

P. Ghosh and F. K. Lamb. Accretion by rotating magnetic neutron stars. III - Accretion torques and period changes in pulsating X-ray sources. *Astroph. J.*, 234:296–316, November 1979.

P. Ghosh, C. J. Pethick, and F. K. Lamb. Accretion by rotating magnetic neutron stars. I - Flow of matter inside the magnetosphere and its implications for spin-up and spin-down of the star. *Astroph. J.*, 217:578–596, October 1977.

R. Giacconi, H. Gursky, E. Kellogg, E. Schreier, and H. Tananbaum. Discovery of Periodic X-Ray Pulsations in Centaurus X-3 from UHURU. *Astroph. J. L.*, 167:L67, July 1971.

R. Giacconi, H. Gursky, F. R. Paolini, and B. B. Rossi. Evidence for x Rays From Sources Outside the Solar System. *Physical Review Letters*, 9: 439–443, December 1962.

N. Glendenning. Internal Constitution of Neutron and Strange Stars. In *NATO ASIC Proc. 515: The Many Faces of Neutron Stars.*, page 15, 1998.

T. Gold. Rotating Neutron Stars and the Nature of Pulsars. *Nature*, 221: 25, 1969.

P. Goldreich and W. H. Julian. Pulsar Electrodynamics. *Astroph. J.*, 157: 869, August 1969.

P. Goldreich and A. Reisenegger. Magnetic field decay in isolated neutron stars. *Astroph. J.*, 395:250–258, August 1992.

P. L. Gonthier, M. S. Ouellette, J. Berrier, S. O'Brien, and A. K. Harding. Galactic Populations of Radio and Gamma-Ray Pulsars in the Polar Cap Model. *Astroph. J.*, 565:482–499, January 2002.

P.-A. Gourdain and J.-N. Leboeuf. Contour dynamics method for solving the Grad-Shafranov equation with applications to high beta equilibria. *Physics of Plasmas*, 11:4372, September 2004.

L. P. Grishchuk. The amplification of gravitational waves and creation of gravitons in the isotropic universes. *Nuovo Cimento Lettere*, 12:60–64, January 1975.

L. P. Grishchuk. Relic Gravitational Waves and Cosmology. *ArXiv General Relativity and Quantum Cosmology e-prints*, April 2005.

J. E. Gunn and J. P. Ostriker. Magnetic Dipole Radiation from Pulsars. *Nature*, 221:454, 1969.

O. H. Guseinov, A. Ankay, and S. O. Tagieva. The Strong Magnetic Field Decay and Evolution of Radio Pulsars on the P-a' Diagram. *International Journal of Modern Physics D*, 13:1805–1815, October 2004.

M. G. Haehnelt. Low-Frequency Gravitational Waves from Supermassive Black-Holes. *Month. Notic. R. Astron. Soc.*, 269:199, July 1994.

P. Haensel, J. P. Lasota, and J. L. Zdunik. On the minimum period of uniformly rotating neutron stars. *Astron. and Astroph.*, 344:151–153, April 1999.

P. Haensel, V. A. Urpin, and D. G. Iakovlev. Ohmic decay of internal magnetic fields in neutron stars. *Astron. and Astroph.*, 229:133–137, March 1990.

J. M. Hameury, S. Bonazzola, J. Heyvaerts, and J. P. Lasota. Magnetohydrostatics in the polar caps of the gamma-ray burst sources. *Astron. and Astroph.*, 128:369–374, December 1983.

J. M. Hameury and J. P. Lasota. Magnetohydrostatics in the polar caps of accreting magnetized white dwarfs. *Astron. and Astroph.*, 145:L10–L12, April 1985.

B. M. S. Hansen and E. S. Phinney. Stellar forensics. I - Cooling curves. *Month. Notic. R. Astron. Soc.*, 294:557, March 1998.

J. W. Hartman, D. Bhattacharya, R. Wijers, and F. Verbunt. A study of the evolution of radio pulsars through improved population synthesis. *Astron. and Astroph.*, 322:477–488, June 1997.

L. Hartmann. *Accretion processes in star formation.* Cambridge, UK ; New York : Cambridge University Press, 1998. (Cambridge astrophysics series ; 32) ISBN 0521435072., 1998.

A. Heger and S. E. Woosley. On the Progenitors of Collapsars. In *AIP Conf. Proc. 662: Gamma-Ray Burst and Afterglow Astronomy 2001: A Workshop Celebrating the First Year of the HETE Mission*, pages 214–216, April 2003.

A. Heger, S. E. Woosley, N. Langer, and H. C. Spruit. Presupernova Evolution of Rotating Massive Stars and the Rotation Rate of Pulsars (Invited Review). In *IAU Symposium*, page 591, June 2004.

A. Hewish, S. J. Bell, J. D. Pilkington, P. F. Scott, and R. A. Collins. Observation of a Rapidly Pulsating Radio Source. *Nature*, 217:709, 1968.

J. S. Heyl. Gravitational radiation from strongly magnetized white dwarfs. *Month. Notic. R. Astron. Soc.*, 317:310–314, September 2000.

J. S. Heyl. r-Modes on Rapidly Rotating, Relativistic Stars. I. Do Type I Bursts Excite Modes in the Neutron Star Ocean? *Astroph. J.*, 600: 939–945, January 2004.

J. A. Hibschman and J. Arons. Pair Production Multiplicities in Rotation-powered Pulsars. *Astroph. J.*, 560:871–884, October 2001.

G. Hobbs. Pulsars and Gravitational Wave Detection. *ArXiv Astrophysics e-prints*, December 2004.

W. Hua, R. Adhikari, D. B. DeBra, J. A. Giaime, G. D. Hammond, C. Hardham, M. Hennessy, J. P. How, B. T. Lantz, M. Macinnis, R. Mittleman, S. Richman, N. A. Robertson, J. Rollins, D. H. Shoemaker, and R. T. Stebbins. Low-frequency active vibration isolation for advanced LIGO. In *Optical Fabrication, Metrology, and Material Advancements for Telescopes. Edited by Atad-Ettedgui, Eli; Dierickx, Philippe. Proceedings of the SPIE, Volume 5500, pp. 194-205 (2004).*, pages 194–205, September 2004.

R. A. Hulse and J. H. Taylor. Discovery of a pulsar in a binary system. *Astroph. J. L.*, 195:L51–L53, January 1975.

A. I. Ibrahim, S. Safi-Harb, J. H. Swank, W. Parke, S. Zane, and R. Turolla. Discovery of Cyclotron Resonance Features in the Soft Gamma Repeater SGR 1806-20. *Astroph. J. L.*, 574:L51–L55, July 2002.

A. F. Illarionov and R. A. Sunyaev. Why the Number of Galactic X-ray Stars Is so Small? *Astron. and Astroph.*, 39:185, February 1975.

N. A. Inogamov and R. A. Sunyaev. Spread of matter over a neutron-star surface during disk accretion. *Astronomy Letters*, 25:269–293, May 1999.

K. Ioka. Magnetic deformation of magnetars for the giant flares of the soft gamma-ray repeaters. *Month. Notic. R. Astron. Soc.*, 327:639–662, October 2001a.

K. Ioka. Magnetic deformation of magnetars for the giant flares of the soft gamma-ray repeaters. *Month. Notic. R. Astron. Soc.*, 327:639–662, October 2001b.

N. Itoh and Y. Kohyama. Electrical and thermal conductivities of dense matter in the crystalline lattice phase. II - Impurity scattering. *Astroph. J.*, 404:268–270, February 1993.

M. Jahan-Miri. Fluxoid motion in neutron stars. *Phys. Rev. B*, 65(18): 184522, May 2002.

M. Jahan Miri and D. Bhattacharya. Magnetic Evolution of Neutron Stars in Wide Low-Mass Binary Systems. *Month. Notic. R. Astron. Soc.*, 269: 455, July 1994.

K. Jansky. Radio waves from outside the solar system. *Nature*, 132:66, 1933.

P. Jaranowski, A. Królak, and B. F. Schutz. Data analysis of gravitational-wave signals from spinning neutron stars: The signal and its detection. *Phys. Rev. D*, 58(6):063001, September 1998.

F. A. Jenet, S. B. Anderson, and T. A. Prince. Single-Pulse Characteristics of the Millisecond Radio Pulsar PSR B1937+21 at 430 MHZ. *Astroph. J.*, 546:394–400, January 2001.

F. A. Jenet, G. B. Hobbs, K. J. Lee, and R. N. Manchester. Detecting the stochastic gravitational wave background using pulsar timing. *ArXiv Astrophysics e-prints*, April 2005.

S. Johnston, L. Ball, N. Wang, and R. N. Manchester. Radio observations of PSR B1259-63 through the 2004 periastron passage. *Month. Notic. R. Astron. Soc.*, 358:1069–1075, April 2005.

D. I. Jones and N. Andersson. Gravitational waves from freely precessing neutron stars. *Month. Notic. R. Astron. Soc.*, 331:203–220, March 2002.

P. B. Jones. The alignment of the Crab pulsar magnetic axis. *Astrophys. Space. Sci.*, 33:215–230, March 1975.

P. B. Jones. Neutron star magnetic field decay - Hall drift and Ohmic diffusion. *Month. Notic. R. Astron. Soc.*, 233:875–885, August 1988.

P. B. Jones. Neutron superfluid spin-down and magnetic field decay in pulsars. *Month. Notic. R. Astron. Soc.*, 253:279–286, November 1991.

P. C. Joss. X-ray bursts and neutron-star thermonuclear flashes. *Nature*, 270:310–314, November 1977.

P. C. Joss and F. K. Li. Helium-burning flashes on accreting neutron stars - Effects of stellar mass, radius, and magnetic field. *Astroph. J.*, 238: 287–295, May 1980.

V. Kalogera, C. Kim, D. R. Lorimer, M. Burgay, N. D'Amico, A. Possenti, R. N. Manchester, A. G. Lyne, B. C. Joshi, M. A. McLaughlin, M. Kramer, J. M. Sarkissian, and F. Camilo. The Cosmic Coalescence Rates for Double Neutron Star Binaries. *Astroph. J. L.*, 601:L179–L182, February 2004.

D. L. Kaplan, S. R. Kulkarni, M. H. van Kerkwijk, and H. L. Marshall. X-Ray Timing of the Enigmatic Neutron Star RX J0720.4-3125. *Astroph. J. L.*, 570:L79–L83, May 2002.

V. M. Kaspi and F. P. Gavriil. (Anomalous) X-ray Pulsars. *Nuclear Physics B Proceedings Supplements*, 132:456–465, June 2004.

V. M. Kaspi, S. Johnston, J. F. Bell, R. N. Manchester, M. Bailes, M. Bessell, A. G. Lyne, and N. D'Amico. A massive radio pulsar binary in the Small Magellanic Cloud. *Astroph. J. L.*, 423:L43–L45, March 1994.

J. I. Katz. Do AM Hercules white dwarfs have toroidal internal fields? *Month. Notic. R. Astron. Soc.*, 239:751–758, August 1989.

J. Kim, S. S. Hong, D. Ryu, and T. W. Jones. Three-dimensional Evolution of the Parker Instability under a Uniform Gravity. *Astroph. J. L.*, 506: L139–L142, October 1998.

J. A. Klimchuk and P. A. Sturrock. Force-free magnetic fields - Is there a 'loss of equilibrium'? *Astroph. J.*, 345:1034–1041, October 1989.

Y. Kojima and T. Nakamura. Gravitational Radiation from a Particle with Orbital Angular Momentum Plunging into a Kerr Black Hole. *Progress of Theoretical Physics*, 71:79–90, January 1984.

K. D. Kokkotas and N. Andersson. Oscillation and instabilities of relativistic stars. In *Recent developments in general relativity. 14th SIGRAV Conference on General Relativity and Gravitational Physics, Genova, Italy,*

September 18-22, 2000, edited by R. Cianci, R. Collina, M. Francaviglia, P. Fré. Milano: Springer, ISBN 88-470-0162-5, 2002, p. 121 - 139, pages 121–139, 2002.

S. Konar and D. Bhattacharya. Magnetic field evolution of accreting neutron stars. *Month. Notic. R. Astron. Soc.*, 284:311–317, January 1997.

S. Konar and D. Bhattacharya. Magnetic field evolution of accreting neutron stars - II. *Month. Notic. R. Astron. Soc.*, 303:588–594, March 1999a.

S. Konar and D. Bhattacharya. Magnetic field evolution of accreting neutron stars - III. *Month. Notic. R. Astron. Soc.*, 308:795–798, September 1999b.

S. Konar and A. R. Choudhuri. Diamagnetic screening of the magnetic field in accreting neutron stars - II. The effect of polar cap widening. *Month. Notic. R. Astron. Soc.*, 348:661–668, February 2004.

D. Konenkov and U. Geppert. The effect of the neutron-star crust on the evolution of a core magnetic field. *Month. Notic. R. Astron. Soc.*, 313: 66–72, March 2000.

D. Konenkov and U. Geppert. The evolution of the core and surface magnetic fields in isolated neutron stars. *Month. Notic. R. Astron. Soc.*, 325: 426–434, July 2001.

K. Konno, T. Obata, and Y. Kojima. Flattening modulus of a neutron star by rotation and magnetic field. *Astron. and Astroph.*, 356:234–237, April 2000.

C. Kouveliotou, S. Dieters, T. Strohmayer, J. van Paradijs, G. J. Fishman, C. A. Meegan, K. Hurley, J. Kommers, I. Smith, D. Frail, and T. Murakami. An X-ray pulsar with a superstrong magnetic field in the soft gamma-ray repeater SGR 1806-20. *Nature*, 393:235–237, 1998.

M. Kramer. Determination of the Geometry of the PSR B1913+16 System by Geodetic Precession. *Astroph. J.*, 509:856–860, December 1998.

M.D. Kruskal and M Schwazschild. Some Instabilities of a Completely Ionized Plasma. *Proc. R. Soc. London A*, 223:348, 1954.

S. R. Kulkarni. Optical identification of binary pulsars - Implications for magnetic field decay in neutron stars. *Astroph. J. L.*, 306:L85–L89, July 1986.

D. Lai. Magnetically Driven Warping, Precession, and Resonances in Accretion Disks. *Astroph. J.*, 524:1030–1047, October 1999.

D. Lai, D. F. Chernoff, and J. M. Cordes. Pulsar Jets: Implications for Neutron Star Kicks and Initial Spins. *Astroph. J.*, 549:1111–1118, March 2001.

M. Landgraf, M. Hechler, and S. Kemble. Mission design for LISA Pathfinder. *Classical and Quantum Gravity*, 22:487, May 2005.

J. M. Lattimer and M. Prakash. Neutron Star Structure and the Equation of State. *Astroph. J.*, 550:426–442, March 2001.

Y. Levin. Runaway Heating by R-Modes of Neutron Stars in Low-Mass X-Ray Binaries. *Astroph. J.*, 517:328–333, May 1999.

A. Levinson and D. Eichler. Can neutron stars ablate their companions? *Astroph. J.*, 379:359–365, September 1991.

W. H. G. Lewin and P. C. Joss. X-Ray Bursters and the X-Ray Sources of the Galactic Bulge. In *Accretion-Driven Stellar X-ray Sources*, page 41, 1983.

X.-D. Li and E. P. J. van den Heuvel. Could 2S 0114+650 Be a Magnetar? *Astroph. J. L.*, 513:L45–L48, March 1999.

L. Lindblom, B. J. Owen, and S. M. Morsink. Gravitational Radiation Instability in Hot Young Neutron Stars. *Physical Review Letters*, 80: 4843–4846, June 1998.

B. Link and R. I. Epstein. Precession Interpretation of the Isolated Pulsar PSR B1828-11. *Astroph. J.*, 556:392–398, July 2001.

B. Link, L. M. Franco, and R. I. Epstein. Starquake-induced Magnetic Field and Torque Evolution in Neutron Stars. *Astroph. J.*, 508:838–843, December 1998.

V. M. Lipunov. *Astrophysics of neutron stars.* Berlin ; New York : Springer-Verlag, c1992., 1992.

C. Litwin, E. F. Brown, and R. Rosner. Ballooning Instability in Polar Caps of Accreting Neutron Stars. *Astroph. J.*, 553:788–795, June 2001.

Q. Z. Liu, J. van Paradijs, and E. P. J. van den Heuvel. A catalogue of high-mass X-ray binaries. *Astron. and Astroph.Suppl. Ser.*, 147:25–49, November 2000.

Q. Z. Liu, J. van Paradijs, and E. P. J. van den Heuvel. A catalogue of low-mass X-ray binaries. *Astron. and Astroph.*, 368:1021–1054, March 2001.

M. Livio. The influence of magnetic fields on nova outbursts. *Astron. and Astroph.*, 121:L7–L10, May 1983.

J. T. Locsei and A. Melatos. Torque bistability in the interaction between a neutron star magnetosphere and a thin accretion disc. *Month. Notic. R. Astron. Soc.*, 354:591–600, October 2004.

D. R. Lorimer. Binary and Millisecond Pulsars at the New Millennium. *Living Reviews in Relativity*, 4:5, June 2001.

B. C. Low. On magnetostatic equilibrium in a stratified atmosphere. *Sol. Phys.*, 65:147–165, February 1980.

A. G. Lyne, M. Burgay, M. Kramer, A. Possenti, R. N. Manchester, F. Camilo, M. A. McLaughlin, D. R. Lorimer, N. D'Amico, B. C. Joshi, J. Reynolds, and P. C. C. Freire. A Double-Pulsar System: A Rare Laboratory for Relativistic Gravity and Plasma Physics. *Science*, 303:1153–1157, February 2004.

A. G. Lyne, R. N. Manchester, and J. H. Taylor. The galactic population of pulsars. *Month. Notic. R. Astron. Soc.*, 213:613–639, April 1985.

A. G. Lyne and J. McKenna. PSR 1820-11 - A binary pulsar in a wide and highly eccentric orbit. *Nature*, 340:367–369, August 1989.

A. G. Lyne, R. S. Pritchard, and F. G. Smith. Crab pulsar timing 1982-87. *Month. Notic. R. Astron. Soc.*, 233:667–676, August 1988.

Y. Lyubarsky and J. G. Kirk. Reconnection in a Striped Pulsar Wind. *Astroph. J.*, 547:437–448, January 2001.

K. Makishima, T. Mihara, F. Nagase, and Y. Tanaka. Cyclotron Resonance Effects in Two Binary X-Ray Pulsars and the Evolution of Neutron Star Magnetic Fields. *Astroph. J.*, 525:978–994, November 1999.

K. Makishima, T. Ohashi, T. Sakao, T. Dotani, H. Inoue, H. Koyama, F. Makino, K. Mitsuda, F. Nagase, H. D. Thomas, M. J. L. Turner, T. Kii, and Y. Tawara. Spin-Down of the X-Ray Pulsar GX:1+4 during an Extended Low State. *Nature*, 333:746, June 1988.

R. Manchester, G. Hobbs, A Teoh, and M Hobbs. The ATNF Pulsar Catalogue. *ArXiv Astrophysics e-prints*, December 2004.

R. N. Manchester. Observational Properties of Pulsars. *Science*, 304:542–547, April 2004.

C. B. Markwardt, M. Juda, and J. H. Swank. XTE J1807-294. *IAU Circular*, 8095:2, March 2003.

C. B. Markwardt, J. H. Swank, T. E. Strohmayer, J. J. M. i. Zand, and F. E. Marshall. Discovery of a Second Millisecond Accreting Pulsar: XTE J1751-305. *Astroph. J. L.*, 575:L21–L24, August 2002.

S. Matt and R. E. Pudritz. The spin of accreting stars: dependence on magnetic coupling to the disc. *Month. Notic. R. Astron. Soc.*, 356:167–182, January 2005.

M. A. McLaughlin, D. R. Lorimer, D. J. Champion, Z. Arzoumanian, D. C. Backer, J. M. Cordes, A. S. Fruchter, A. N. Lommen, and K. M. Xilouris. New Binary and Millisecond Pulsars from Arecibo Drift-Scan Searches. *ArXiv Astrophysics e-prints*, April 2004.

M. A. McLaughlin, I. H. Stairs, V. M. Kaspi, D. R. Lorimer, M. Kramer, A. G. Lyne, R. N. Manchester, F. Camilo, G. Hobbs, A. Possenti, N. D'Amico, and A. J. Faulkner. PSR J1847-0130: A Radio Pulsar with Magnetar Spin Characteristics. *Astroph. J. L.*, 591:L135–L138, July 2003.

A. Melatos. Spin-down of an oblique rotator with a current-starved outer magnetosphere. *Month. Notic. R. Astron. Soc.*, 288:1049–1059, July 1997.

A. Melatos. Radiative precession of an isolated neutron star. *Month. Notic. R. Astron. Soc.*, 313:217–228, April 2000.

A. Melatos. Theory of Plerions. In *ASP Conf. Ser. 271: Neutron Stars in Supernova Remnants*, page 115, 2002.

A. Melatos and D. B. Melrose. Energy transport in a rotation-modulated pulsar wind. *Month. Notic. R. Astron. Soc.*, 279:1168–1190, April 1996.

A. Melatos and D. J. B. Payne. Gravitational Radiation from an Accreting Millisecond Pulsar with a Magnetically Confined Mountain. *Astroph. J.*, 623:1044–1050, April 2005.

A. Melatos and E. S. Phinney. Evolution of the Magnetic Field of a Neutron Star During Polar-Cap Accretion. In *ASP Conf. Ser. 202: IAU Colloq. 177: Pulsar Astronomy - 2000 and Beyond*, page 651, 2000.

A. Melatos and E. S. Phinney. Burial of the polar magnetic field of an accreting neutron star. I. Self-consistent analytic and numerical equilibria. *PASA*, 18:421, 2001.

M. Milosavljević and E. S. Phinney. The Afterglow of Massive Black Hole Coalescence. *Astroph. J. L.*, 622:L93–L96, April 2005.

D. Mitra, S. Konar, and D. Bhattacharya. Evolution of the multipolar magnetic field in isolated neutron stars. *Month. Notic. R. Astron. Soc.*, 307:459–462, August 1999.

P. M. Morse and H. Feshbach. *Methods of theoretical physics.* International Series in Pure and Applied Physics, New York: McGraw-Hill, 1953, 1953.

T.C. Mouschovias. Static Equilibria of the Interstellar Gas in the Presence of Magnetic and Gravitational Fields: Large-Scale Condensations. *Astroph. J.*, 192:37–50, August 1974.

T.C. Mouschovias. The Parker Instability in the interstellar medium. *in Solar and Astrophysical Magnetohydrodynamic Flows, ed. K. C. Tsinganos (NATO ASI Ser. C, 481) (Dordrecht: Kluwer)*, page 475, August 1996.

M. P. Muno, F. Özel, and D. Chakrabarty. The Amplitude Evolution and Harmonic Content of Millisecond Oscillations in Thermonuclear X-Ray Bursts. *Astroph. J.*, 581:550–561, December 2002.

T. Murakami, M. Fujii, K. Hayashida, M. Itoh, and J. Nishimura. Evidence for cyclotron absorption from spectral features in gamma-ray bursts seen with Ginga. *Nature*, 335:234, September 1988.

A. G. Muslimov and A. I. Tsygan. Neutron Star Superconductivity and Superfluidity and the Decay of Pulsar Magnetic Fields. *SvAL*, 11:80, March 1985.

J. Muzerolle, N. Calvet, and L. Hartmann. Magnetospheric Accretion Models for the Hydrogen Emission Lines of T Tauri Stars. *Astroph. J.*, 492: 743, January 1998.

F. Nagase. Accretion-powered X-ray pulsars. *pasj*, 41:1–79, 1989.

R. Narayan and J. P. Ostriker. Pulsar populations and their evolution. *Astroph. J.*, 352:222–246, March 1990.

R. Narayan, T. Piran, and A. Shemi. Neutron star and black hole binaries in the Galaxy. *Astroph. J. L.*, 379:L17–L20, September 1991.

G. Nelemans, L. R. Yungelson, and S. F. Portegies Zwart. The gravitational wave signal from the Galactic disk population of binaries containing two compact objects. *Astron. and Astroph.*, 375:890–898, September 2001.

R. W. Nelson, L. Bildsten, D. Chakrabarty, M. H. Finger, D. T. Koh, T. A. Prince, B. C. Rubin, D. M. Scott, B. A. Vaughan, and R. B. Wilson. On the Dramatic Spin-up/Spin-down Torque Reversals in Accreting Pulsars. *Astroph. J. L.*, 488:L117, October 1997.

J. R. Oppenheimer and G. M. Volkoff. On Massive Neutron Cores. *Physical Review*, 55:374–381, February 1939.

J. P. Ostriker and J. E. Gunn. On the Nature of Pulsars. I. Theory. *Astroph. J.*, 157:1395, September 1969.

B. J. Owen. Search templates for gravitational waves from inspiraling binaries: Choice of template spacing. *Phys. Rev. D*, 53:6749–6761, June 1996.

F. Pacini. Energy Emission from a Neutron Star. *Nature*, 216:567, 1967.

F. Pacini. Rotating Neutron Stars, Pulsars and Supernova Remnants. *Nature*, 219:145, 1968.

T. D. Padalia. Gravitational radiation and spiralling time of close binary systems (V). *Astrophys. Space. Sci.*, 202:63–68, April 1993.

C. Palomba. Gravitational radiation from young magnetars: Preliminary results. *Astron. and Astroph.*, 367:525–531, February 2001.

E.N. Parker. The Dynamical State of the Interstellar Gas and Field. *Astroph. J.*, 145:811, September 1966.

G. G. Pavlov, V. E. Zavlin, and D. Sanwal. Thermal Radiation from Neutron Stars: Chandra Results. In *Neutron Stars, Pulsars, and Supernova Remnants*, page 273, 2002.

D. J. B. Payne and A. Melatos. Burial of the polar magnetic field of an accreting neutron star - I. Self-consistent analytic and numerical equilibria. *Month. Notic. R. Astron. Soc.*, 351:569–584, June 2004.

D. J. B. Payne and A. Melatos. Burial of the polar magnetic field of an accreting neutron star. II. Stability of axisymmetric equilibria. *MNRAS, to be submitted*, 2005a.

D. J. B. Payne and A. Melatos. Magnetic burial and the harmonic content of millisecond oscillations in thermonuclear X-ray bursts. *ApJL, submitted*, 2005b.

C. J. Pethick. Topics in the Physics of High Magnetic Fields. In *Structure and Evolution of Neutron Stars*, page 115, 1992.

E. S. Phinney. Pulsars as probes of Newtonian dynamical systems. *Philos. Trans. Roy. Soc. London A*, 341:39, 1992.

E. S. Phinney and S. R. Kulkarni. Binary and Millisecond Pulsars. *Ann. Rev. Astron. Astrophys.*, 32:591–639, 1994.

E. S. Phinney and F. Verbunt. Binary pulsars before spin-up and PSR 1820 - 11. *Month. Notic. R. Astron. Soc.*, 248:21P–23P, February 1991.

D. Pines and J. Shaham. Free precession of neutron stars - Some plain truths, cautionary remarks, and assorted speculations. *Comments on Astrophysics and Space Physics*, 6:37–44, 1974.

A. L. Piro and L. Bildsten. Nonradial Oscillations on Bursting Neutron Stars. *AAS/High Energy Astrophysics Division*, 8, August 2004.

P. Podsiadlowski, N. Langer, A. J. T. Poelarends, S. Rappaport, A. Heger, and E. Pfahl. The Effects of Binary Evolution on the Dynamics of Core Collapse and Neutron Star Kicks. *Astroph. J.*, 612:1044–1051, September 2004.

P. Podsiadlowski and S. Rappaport. Cygnus X-2: The Descendant of an Intermediate-Mass X-Ray Binary. *Astroph. J.*, 529:946–951, February 2000.

R. Popham and R. Sunyaev. Accretion Disk Boundary Layers around Neutron Stars: X-Ray Production in Low-Mass X-Ray Binaries. *Astroph. J.*, 547:355–383, January 2001.

A. Possenti, M. Colpi, N. D'Amico, and L. Burderi. Population Synthesis of Millisecond and Submillisecond Pulsars. *Astroph. J. L.*, 497:L97, April 1998.

A. Y. Potekhin. Electron conduction in magnetized neutron star envelopes. *Astron. and Astroph.*, 351:787–797, November 1999.

W. H. Press, S. A. Teukolsky, W. T. Vetterling, and B. P. Flannery. *Numerical recipes in C. The art of scientific computing.* Cambridge: University Press, 2nd ed., 1992.

J. E. Pringle and M. J. Rees. Accretion Disc Models for Compact X-Ray Sources. *Astron. and Astroph.*, 21:1, October 1972.

D. Psaltis and D. Chakrabarty. The Disk-Magnetosphere Interaction in the Accretion-powered Millisecond Pulsar SAX J1808.4-3658. *Astroph. J.*, 521:332–340, August 1999.

E. H. P. Pylyser and G. J. Savonije. The evolution of low-mass close binary systems with a compact component. II - Systems captured by angular momentum losses. *Astron. and Astroph.*, 208:52–62, January 1989.

H. Quaintrell, A. J. Norton, T. D. C. Ash, P. Roche, B. Willems, T. R. Bedding, I. K. Baldry, and R. P. Fender. The mass of the neutron star in Vela X-1 and tidally induced non-radial oscillations in GP Vel. *Astron. and Astroph.*, 401:313–323, April 2003.

F. J. Raab. Overview of LIGO instrumentation. In *Optical Fabrication, Metrology, and Material Advancements for Telescopes. Edited by Atad-Ettedgui, Eli; Dierickx, Philippe. Proceedings of the SPIE, Volume 5500, pp. 11-24 (2004).*, pages 11–24, September 2004.

S. M. Ransom, J. W. T. Hessels, I. H. Stairs, P. C. C. Freire, F. Camilo, V. M. Kaspi, and D. L. Kaplan. Twenty-One Millisecond Pulsars in Terzan 5 Using the Green Bank Telescope. *Science*, 307:892–896, February 2005.

F. A. Rasio, E. D. Pfahl, and S. Rappaport. Formation of Short-Period Binary Pulsars in Globular Clusters. *Astroph. J. L.*, 532:L47–L50, March 2000.

L. Rastätter and K. Schindler. Magnetized Accreting Stars: Studies of the Inner Accretion Disk Edge by a Magnetohydrodynamical Approach. I. Construction and Analysis of Magnetopause Equilibria. *Astroph. J.*, 519: 658–666, July 1999.

T. Regimbau and J. A. de Freitas Pacheco. Population synthesis of pulsars: Magnetic field effects. *Astron. and Astroph.*, 374:182–188, July 2001.

A. Reisenegger. Magnetic Fields of Neutron Stars: an Overview. In *ASP Conf. Ser. 248: Magnetic Fields Across the Hertzsprung-Russell Diagram*, page 469, 2001.

M. Rheinhardt, D. Konenkov, and U. Geppert. The occurrence of the Hall instability in crusts of isolated neutron stars. *Astron. and Astroph.*, 420: 631–645, June 2004.

K. J. Rhook and J. S. B. Wyithe. Realistic Event Rates for Detection of Supermassive Black Hole Coalescence by LISA. *ArXiv Astrophysics e-prints*, March 2005.

N. A. Robertson, B. Abbott, R. Abbott, R. Adhikari, G. S. Allen, H. Armandula, S. M. Aston, A. Baglino, M. Barton, B. Bland, R. Bork, J. Bogenstahl, G. Cagnoli, C. Campbell, C. A. Cantley, K. Carter, D. Cook, D. Coyne, D. R. Crooks, E. J. Daw, D. B. DeBra, E. Elliffe, J. Faludi, P. Fritschel, A. Ganguli, J. A. Giaime, S. Gossler, A. Grant, J. Greenhalgh, M. Hammond, J. Hanson, C. Hardham, G. M. Harry, A. Heptonstall, J. Heefner, J. Hough, D. Hoyland, W. Hua, L. Jones, R. Jones, J. E.

Kern, J. LaCour, B. T. Lantz, K. Lilienkamp, N. Lockerbie, H. Lück, M. MacInnis, K. Mailand, K. Mason, R. Mittleman, S. A. Nayfeh, J. Nichol, D. J. Ottaway, H. Overmier, M. Perreur-Lloyd, J. Phinney, M. V. Plissi, W. Rankin, D. I. Robertson, J. Romie, S. Rowan, R. Scheffler, D. H. Shoemaker, P. Sarin, P. H. Sneddon, C. C. Speake, O. Spjeld, G. Stapfer, K. A. Strain, C. I. Torrie, G. Traylor, J. van Niekerk, A. Vecchio, S. Wen, P. Willems, I. Wilmut, H. Ward, M. Zucker, and L. Zuo. Seismic isolation and suspension systems for Advanced LIGO. In *Optical Fabrication, Metrology, and Material Advancements for Telescopes. Edited by Atad-Ettedgui, Eli; Dierickx, Philippe. Proceedings of the SPIE, Volume 5500, pp. 81-91 (2004).*, pages 81–91, September 2004.

K. A. Romani, R. W. in van Riper, R. Epstein, and C. Ho. *Isolated Pulsars.* Isolated Pulsars, ISBN 0521434297, Cambridge University Press, 1993., 1993.

R. W. Romani. A unified model of neutron-star magnetic fields. *Nature*, 347:741–743, October 1990.

R. W. Romani. Neutron Star Magnetic Fields. In *ASP Conf. Ser. 72: Millisecond Pulsars. A Decade of Surprise*, page 288, 1995.

M. M. Romanova, G. V. Ustyugova, A. V. Koldoba, and R. V. E. Lovelace. The Propeller Regime of Disk Accretion to a Rapidly Rotating Magnetized Star. *Astroph. J. L.*, 616:L151–L154, December 2004.

R. E. Rothschild, D. Marsden, and E. Lingenfelter. Fossil disks and propeller spindown of SGR/AXPs. *Memorie della Societa Astronomica Italiana*, 73: 508–515, 2002.

M. Ruderman. Neutron star crustal plate tectonics. I - Magnetic dipole evolution in millisecond pulsars and low-mass X-ray binaries. *Astroph. J.*, 366:261–269, January 1991a.

M. Ruderman. Neutron star crustal plate tectonics. II - Evolution of radio pulsar magnetic fields. III - Cracking, glitches, and gamma-ray bursts. *Astroph. J.*, 382:576, December 1991b.

M. Ruderman. Neutron Star Crustal Plate Tectonics. III. Cracking, Glitches, and Gamma-Ray Bursts. *Astroph. J.*, 382:587, December 1991c.

M. Ruderman. Spin-Driven Changes in Neutron Star Magnetic Fields. *Journal of Astrophysics and Astronomy*, 16:207, June 1995.

M. A. Ruderman and P. G. Sutherland. Theory of pulsars - Polar caps, sparks, and coherent microwave radiation. *Astroph. J.*, 196:51–72, February 1975.

Y. Sang and G. Chanmugam. Ohmic decay of crustal neutron star magnetic fields. *Astroph. J. L.*, 323:L61–L64, December 1987.

Y. Sang and G. Chanmugam. Pulsar statistics with nonexponential magnetic field decay. *Astroph. J.*, 363:597–602, November 1990.

D. Sanwal, G. G. Pavlov, V. E. Zavlin, and M. A. Teter. Discovery of Absorption Features in the X-Ray Spectrum of an Isolated Neutron Star. *Astroph. J. L.*, 574:L61–L64, July 2002.

R. Schneider, V. Ferrari, S. Matarrese, and S. F. Portegies Zwart. Low-frequency gravitational waves from cosmological compact binaries. *Month. Notic. R. Astron. Soc.*, 324:797–810, July 2001.

E. Schreier, R. Levinson, H. Gursky, E. Kellogg, H. Tananbaum, and R. Giacconi. Evidence for the Binary Nature of Centaurus X-3 from UHURU X-Ray Observations. *Astroph. J. L.*, 172:L79, March 1972.

B. F. Schutz. Gravitational wave astronomy . *Classical and Quantum Gravity*, 16:A131–A156, December 1999.

M. Schwarzschild and R. Härm. Therma Instability in Non-Degenerate Stars. *Astroph. J.*, 142:855, October 1965.

A. D. Schwope, V. Hambaryan, F. Haberl, and C. Motch. The pulsed X-ray light curves of the isolated neutron star RBS1223. *ArXiv Astrophysics e-prints*, May 2005.

S. Sengupta. Evolution of Crustal Magnetic Fields in Isolated Neutron Stars: Combined Effects of Cooling and Curvature of Spacetime. *Astroph. J.*, 501:792, July 1998.

T. V. Shabanova, A. G. Lyne, and J. O. Urama. Evidence for Free Precession in the Pulsar B1642-03. *Astroph. J.*, 552:321–325, May 2001.

C. A. Shain. Location on Jupiter of a source of radio noise. *Nature*, 176: 836, 1955.

N. I. Shakura, K. A. Postnov, and M. E. Prokhorov. On some features of free precession of a triaxial body: the case of HER X-1. *Astron. and Astroph.*, 331:L37–L40, March 1998.

S. L. Shapiro and S. A. Teukolsky. *Black holes, white dwarfs, and neutron stars: The physics of compact objects.* Research supported by the National Science Foundation. New York, Wiley-Interscience, 1983, 663 p., 1983.

N. Shibazaki, T. Murakami, J. Shaham, and K. Nomoto. Does mass accretion lead to field decay in neutron stars? *Nature*, 342:656–658, December 1989.

I. S. Shklovskii. The Nature of the X-Ray Source Sco X-1. *Astronomicheskii Zhurnal*, 44:930, 1967.

S. Sigurdsson, H. B. Richer, B. M. Hansen, I. H. Stairs, and S. E. Thorsett. A Young White Dwarf Companion to Pulsar B1620-26: Evidence for Early Planet Formation. *Science*, 301:193–196, July 2003.

F. G. Smith. *Pulsars.* Cambridge and New York, Cambridge University Press, 1977. 249 p., 1977.

W. V. Snyder. Algorithm 531, Contour Plotting [J6]. *ACM Trans. Math. Soft.*, 4(3):290–294, September 1978.

A. Spitkovsky, Y. Levin, and G. Ushomirsky. Propagation of Thermonuclear Flames on Rapidly Rotating Neutron Stars: Extreme Weather during Type I X-Ray Bursts. *Astroph. J.*, 566:1018–1038, February 2002.

H. C. Spruit. Dynamo action by differential rotation in a stably stratified stellar interior. *Astron. and Astroph.*, 381:923–932, January 2002.

H. C. Spruit and E. S. Phinney. Birth kicks as the origin of pulsar rotation. *Nature*, 393:139, May 1998.

G. Srinivasan. The maximum mass of neutron stars. *The Astronomy and Astrophysics Review*, 11:67–96, 2002.

G. Srinivasan, D. Bhattacharya, A. Muslimov, and A. Tsygan. A novel mechanism for the decay of neutron star magnetic fields. *Curr. Sci.*, 59: 31, 1990.

I. H. Stairs. Pulsars in Binary Systems: Probing Binary Stellar Evolution and General Relativity. *Science*, 304:547–552, April 2004.

I. H. Stairs, Z. Arzoumanian, F. Camilo, A. G. Lyne, D. J. Nice, J. H. Taylor, S. E. Thorsett, and A. Wolszczan. Measurement of Relativistic Orbital Decay in the PSR B1534+12 Binary System. *Astroph. J.*, 505: 352–357, September 1998.

I. H. Stairs, A. G. Lyne, and S. L. Shemar. Evidence for free precession in a pulsar. *Nature*, 406:484–486, August 2000.

I. H. Stairs, R. N. Manchester, A. G. Lyne, V. M. Kaspi, F. Camilo, J. F. Bell, N. D'Amico, M. Kramer, F. Crawford, D. J. Morris, A. Possenti, N. P. F. McKay, S. L. Lumsden, L. E. Tacconi-Garman, R. D. Cannon, N. C. Hambly, and P. R. Wood. PSR J1740-3052: a pulsar with a massive companion. *Month. Notic. R. Astron. Soc.*, 325:979–988, August 2001.

G. M. Stollman. Pulsar statistics. *Astron. and Astroph.*, 178:143–152, May 1987.

J. M. Stone and M. L. Norman. ZEUS-2D: A radiation magnetohydrodynamics code for astrophysical flows in two space dimensions. I - The hydrodynamic algorithms and tests. *Astroph. J. Suppl. Ser.*, 80:753–790, June 1992a.

J. M. Stone and M. L. Norman. ZEUS-2D: A radiation magnetohydrodynamics code for astrophysical flows in two space dimensions. I - The hydrodynamic algorithms and tests. *Astroph. J. Suppl. Ser.*, 80:753–790, June 1992b.

J. M. Stone and M. L. Norman. ZEUS-2D: A Radiation Magnetohydrodynamics Code for Astrophysical Flows in Two Space Dimensions. II. The Magnetohydrodynamic Algorithms and Tests. *Astroph. J. Suppl. Ser.*, 80: 791, June 1992c.

T. E. Strohmayer and L. Bildsten. New views of thermonuclear bursts. *To appear in Compact Stellar X-Ray Sources, eds. W.H.G. Lewin and M. van der Klis, Cambridge University Press*, 2003.

T. E. Strohmayer, K. Jahoda, A. B. Giles, and U. Lee. Millisecond Pulsations from a Low-Mass X-Ray Binary in the Galactic Center Region. *Astroph. J.*, 486:355, September 1997.

T. E. Strohmayer, C. B. Markwardt, J. H. Swank, and J. in't Zand. X-Ray Bursts from the Accreting Millisecond Pulsar XTE J1814-338. *Astroph. J. L.*, 596:L67–L70, October 2003.

P. A. Sturrock. A Model of Pulsars. *Astroph. J.*, 164:529, March 1971.

R. E. Taam, A. Fu, and B. A. Fryxell. Accretion in wind-driven X-ray sources. *Astroph. J.*, 371:696–707, April 1991.

R. E. Taam and E. P. J. van den Heuvel. Magnetic field decay and the origin of neutron star binaries. *Astroph. J.*, 305:235–245, June 1986.

T. M. Tauris and S. Konar. Torque decay in the pulsar (P,$\dot{P}$) diagram. Effects of crustal ohmic dissipation and alignment. *Astron. and Astroph.*, 376:543–552, September 2001.

T. M. Tauris and R. N. Manchester. On the Evolution of Pulsar Beams. *Month. Notic. R. Astron. Soc.*, 298:625–636, August 1998.

T. M. Tauris and G. J. Savonije. Formation of millisecond pulsars. I. Evolution of low-mass X-ray binaries with $P_b > 2$ days. *Astron. and Astroph.*, 350:928–944, October 1999.

T. M. Tauris, E. P. J. van den Heuvel, and G. J. Savonije. Formation of Millisecond Pulsars with Heavy White Dwarf Companions:Extreme Mass Transfer on Subthermal Timescales. *Astroph. J. L.*, 530:L93–L96, February 2000.

The LIGO Scientific Collaboration: B. Abbott, M. Kramer, and A. G. Lyne. Analysis of LIGO data for gravitational waves from binary neutron stars. *Phys. Rev. D*, 69(12):122001, June 2004a.

The LIGO Scientific Collaboration: B. Abbott, M. Kramer, and A. G. Lyne. Limits on gravitational wave emission from selected pulsars using LIGO data. *ArXiv General Relativity and Quantum Cosmology e-prints*, October 2004b.

The LIGO Scientific Collaboration: B. Abbott, M. Kramer, and A. G. Lyne. Setting upper limits on the strength of periodic gravitational waves from PSR J1939+2134 using the first science data from the GEO 600 and LIGO detectors. *Phys. Rev. D*, 69(8):082004, April 2004c.

C. Thompson and R. C. Duncan. Neutron star dynamos and the origins of pulsar magnetism. *Astroph. J.*, 408:194–217, May 1993.

C. Thompson and R. C. Duncan. The soft gamma repeaters as very strongly magnetized neutron stars - I. Radiative mechanism for outbursts. *Month. Notic. R. Astron. Soc.*, 275:255–300, July 1995.

K. S. Thorne. *Gravitational radiation, in Three Hundred Years of Gravitation, edited by W. W. Hawking and W. Israel* . Cambridge, MA: Cambridge University Press, 1987, 1987.

S. E. Thorsett and D. Chakrabarty. Neutron Star Mass Measurements. I. Radio Pulsars. *Astroph. J.*, 512:288–299, February 1999.

Y. M. Toropin, O. D. Toropina, V. V. Savelyev, M. M. Romanova, V. M. Chechetkin, and R. V. E. Lovelace. Spherical Bondi Accretion onto a Magnetic Dipole. *Astroph. J.*, 517:906–918, June 1999.

J. Trümper, W. Pietsch, C. Reppin, W. Voges, R. Staubert, and E. Kendziorra. Evidence for strong cyclotron line emission in the hard X-ray spectrum of Hercules X-1. *Astroph. J. L.*, 219:L105–L110, February 1978.

A. V. Tutukov and A. V. Fedorova. Evolution of Close Stellar Binaries with Black Holes under the Action of Gravitational Radiation and Magnetic and Induced Stellar Winds of the Donor. *Astronomy Reports*, 46:765–778, September 2002.

Y. Uchida and B. C. Low. Equilibrium configuration of the magnetosphere of a star loaded with accreted magnetized mass. *JA&A*, 2:405–419, December 1981.

V. Urpin. Instabilities, turbulence, and mixing in the ocean of accreting neutron stars. *ArXiv Astrophysics e-prints*, April 2005.

V. Urpin and U. Geppert. Accretion and evolution of the neutron star magnetic field. *Month. Notic. R. Astron. Soc.*, 275:1117–1124, August 1995.

V. Urpin and D. Konenkov. Spin and magnetic evolution of accreting neutron stars in close binaries. *Month. Notic. R. Astron. Soc.*, 284:741–748, January 1997.

V. A. Urpin, S. A. Levshakov, and D. G. Iakovlev. Generation of neutron star magnetic fields by thermomagnetic effects. *Month. Notic. R. Astron. Soc.*, 219:703–717, April 1986.

V. A. Urpin and A. G. Muslimov. Crustal magnetic field decay and neutron star cooling. *Month. Notic. R. Astron. Soc.*, 256:261–268, May 1992.

V. A. Urpin and D. G. Yakovlev. Thermogalvanomagnetic Effects in White Dwarfs and Neutron Stars. *Soviet Astronomy*, 24:425, August 1980.

G. Ushomirsky, C. Cutler, and L. Bildsten. Deformations of accreting neutron star crusts and gravitational wave emission. *Month. Notic. R. Astron. Soc.*, 319:902–932, December 2000.

V. V. Usov and D. B. Melrose. Pulsars with Strong Magnetic Fields - Polar Gaps Bound Pair Creation and Nonthermal Luminosities. *Australian Journal of Physics*, 48:571, 1995.

D. A. Uzdensky. Magnetic Interaction Between Stars And Accretion Disks. *Astrophys. Space. Sci.*, 292:573–585, 2004.

D. A. Uzdensky, A. Königl, and C. Litwin. Magnetically Linked Star-Disk Systems. I. Force-free Magnetospheres and Effects of Disk Resistivity. *Astroph. J.*, 565:1191–1204, February 2002.

C. Van Den Broeck. The gravitational wave spectrum of non-axisymmetric, freely precessing neutron stars. *Classical and Quantum Gravity*, 22:1825–1839, May 2005.

E. P. van den Heuvel, J. A. van Paradijs, and R. E. Taam. Evidence for an asymptotic lower limit to the surface dipole magnetic field strengths of neutron stars. *Nature*, 322:153–155, July 1986.

E. P. J. Van Den Heuvel and O. Bitzaraki. X-ray binaries and recycled pulsars. *Memorie della Societa Astronomica Italiana*, 65:237, 1994.

E. P. J. van den Heuvel and O. Bitzaraki. The magnetic field strength versus orbital period relation for binary radio pulsars with low-mass companions: evidence for neutron-star formation by accretion-induced collapse? *Astron. and Astroph.*, 297:L41, May 1995.

M. van der Klis, R. A. D. Wijnands, K. Horne, and W. Chen. Kilohertz Quasi-Periodic Oscillation Peak Separation Is Not Constant in Scorpius X-1. *Astroph. J. L.*, 481:L97, June 1997.

M. H. van Kerkwijk, J. van Paradijs, and E. J. Zuiderwijk. On the masses of neutron stars. *Astron. and Astroph.*, 303:497, November 1995.

J. van Paradijs. Neutron Stars and Black Holes in X-Ray Binaries. In *NATO ASIC Proc. 515: The Many Faces of Neutron Stars.*, page 279, 1998.

W. van Straten, M. Bailes, M. Britton, S. R. Kulkarni, S. B. Anderson, R. N. Manchester, and J. Sarkissian. A test of general relativity from the three-dimensional orbital geometry of a binary pulsar. *Nature*, 412: 158–160, July 2001.

F. Verbunt and G. Nelemans. Binaries for LISA . *Classical and Quantum Gravity*, 18:4005–4011, October 2001.

F. Verbunt, R. A. M. J. Wijers, and H. M. G. Burm. Evolutionary scenarios for the X-ray binary pulsars 4U 1626-67 and Hercules X-1, and their implications for the decay of neutron star magnetic fields. *Astron. and Astroph.*, 234:195–202, August 1990.

R. V. Wagoner. Gravitational radiation from accreting neutron stars. *Astroph. J.*, 278:345–348, March 1984.

R. V. Wagoner. A Timing Signature of Gravitational Radiation from LMXB Neutron Stars. In *AIP Conf. Proc. 714: X-ray Timing 2003: Rossi and Beyond*, pages 224–227, July 2004.

S. Wakatsuki, A. Hikita, N. Sato, and N. Itoh. The nonexponential evolution of pulsar magnetic fields. *Astroph. J.*, 392:628–636, June 1992.

J. C. Weatherall and J. A. Eilek. Are There Two Pulsar Emission Mechanisms? *Astroph. J.*, 474:407, January 1997.

R. F. Webbink, S. Rappaport, and G. J. Savonije. On the evolutionary status of bright, low-mass X-ray sources. *Astroph. J.*, 270:678–693, July 1983.

J. Weber. Detection and Generation of Gravitational Waves. *Physical Review*, 117:306–313, January 1960.

C. E. Wendell, H. M. van Horn, and D. Sargent. Magnetic field evolution in white dwarfs. *Astroph. J.*, 313:284–297, February 1987.

N. E. White and W. Zhang. Millisecond X-Ray Pulsars in Low-mass X-Ray Binaries. *Astroph. J. L.*, 490:L87, November 1997.

D. T. Wickramasinghe and L. Ferrario. Magnetism in Isolated and Binary White Dwarfs. *Publ. Astron. Soc. Pac.*, 112:873–924, July 2000.

D. T. Wickramasinghe and L. Ferrario. The origin of the magnetic fields in white dwarfs. *Month. Notic. R. Astron. Soc.*, 356:1576–1582, February 2005.

R. A. M. J. Wijers. Evidence against field decay proportional to accreted mass in neutron stars. *Month. Notic. R. Astron. Soc.*, 287:607–614, May 1997.

R. Wijnands and M. van der Klis. A millisecond pulsar in an X-ray binary system. *Nature*, 394:344–346, 1998.

R. Wijnands, M. van der Klis, J. Homan, D. Chakrabarty, C. B. Markwardt, and E. H. Morgan. Quasi-periodic X-ray brightness fluctuations in an accreting millisecond pulsar. *Nature*, 424:44–47, July 2003a.

R. Wijnands, M. van der Klis, J. Homan, D. Chakrabarty, C. B. Markwardt, and E. H. Morgan. Quasi-periodic X-ray brightness fluctuations in an accreting millisecond pulsar. *Nature*, 424:44–47, July 2003b.

A. Wolszczan. Confirmation of Earth Mass Planets Orbiting the Millisecond Pulsar PSR:B1257+12. *Science*, 264:538, April 1994.

A. Wolszczan, O. Doroshenko, M. Konacki, M. Kramer, A. Jessner, R. Wielebinski, F. Camilo, D. J. Nice, and J. H. Taylor. Timing Observations of Four Millisecond Pulsars with the Arecibo and Effelsberg Radio Telescopes. *Astroph. J.*, 528:907–912, January 2000.

S. E. Woosley and R. K. Wallace. The thermonuclear model for gamma-ray bursts. *Astroph. J.*, 258:716–732, July 1982.

G. A. Wright and E. D. Loh. Companion star of a binary millisecond pulsar. *Nature*, 324:127, November 1986.

G. A. Wynn and A. R. King. Diamagnetic accretion in intermediate polars - I. Blob orbits and spin evolution. *Month. Notic. R. Astron. Soc.*, 275: 9–21, July 1995.

E. J. Young and G. Chanmugam. Postaccretion magnetic field evolution of neutron stars. *Astroph. J. L.*, 442:L53–L56, April 1995.

M. D. Young, R. N. Manchester, and S. Johnston. A radio pulsar with an 8.5-second period that challenges emission models. *Nature*, 400:848–849, 1999.

V. E. Zavlin, G. G. Pavlov, and D. Sanwal. Variations in the Spin Period of the Radio-quiet Pulsar 1E 1207.4-5209. *Astroph. J.*, 606:444–451, May 2004.

Y. B. Zeldovich and O. H. Guseynov. Collapsed Stars in Binaries. *Astroph. J.*, 144:840, May 1966.

B. Zhang, A. K. Harding, and A. G. Muslimov. Radio Pulsar Death Line Revisited: Is PSR J2144-3933 Anomalous? *Astroph. J. L.*, 531:L135–L138, March 2000.

C. M. Zhang. Accretion induced crust screening for the magnetic field decay of neutron stars. *Astron. and Astroph.*, 330:195–200, February 1998.

C. M. Zhang and Y. Kojima. Neutron star bottom magnetic field and magnetosphere evolution in low mass X-ray binary. *ArXiv Astrophysics e-prints*, October 2004.

C.-M. Zhang, X.-J. Wu, and G.-C. Yang. The crust screen model for the magnetic field of binary X-ray sources. *Astron. and Astroph.*, 283:889, March 1994.

M. Zimmermann. Gravitational waves from rotating and precessing rigid bodies. II - General solutions and computationally useful formulas. *Phys. Rev. D*, 21:891–898, February 1980.

M. Zimmermann and E. Szedenits. Gravitational waves from rotating and precessing rigid bodies - Simple models and applications to pulsars. *Phys. Rev. D*, 20:351–355, July 1979.

M. Zingale, F. X. Timmes, B. Fryxell, D. Q. Lamb, K. Olson, A. C. Calder, L. J. Dursi, P. Ricker, R. Rosner, P. MacNeice, and H. M. Tufo. Helium Detonations on Neutron Stars. *Astroph. J. Suppl. Ser.*, 133:195–220, March 2001.

E. G. Zweibel and A. J. Hundhausen. Magnetostatic atmospheres - A family of isothermal solutions. *Sol. Phys.*, 76:261–299, March 1982.